



Delft University of Technology

Diamond Nanophotonic Devices for Quantum Networks Experiments

Codreanu, N.

DOI

[10.4233/uuid:e1c789d7-d71e-42b8-a9a8-23fafdaea22e](https://doi.org/10.4233/uuid:e1c789d7-d71e-42b8-a9a8-23fafdaea22e)

Publication date

2025

Document Version

Final published version

Citation (APA)

Codreanu, N. (2025). *Diamond Nanophotonic Devices for Quantum Networks Experiments*. [Dissertation (TU Delft), Delft University of Technology]. <https://doi.org/10.4233/uuid:e1c789d7-d71e-42b8-a9a8-23fafdaea22e>

Important note

To cite this publication, please use the final published version (if applicable).
Please check the document version above.

Copyright

Other than for strictly personal use, it is not permitted to download, forward or distribute the text or part of it, without the consent of the author(s) and/or copyright holder(s), unless the work is under an open content license such as Creative Commons.

Takedown policy

Please contact us and provide details if you believe this document breaches copyrights.
We will remove access to the work immediately and investigate your claim.

The background features a complex, abstract pattern of coral-like or dendritic structures in shades of pink, orange, and purple. Overlaid on this are several semi-transparent, isometric images of diamond microchips, showing their intricate surface patterns and rectangular shapes.

DIAMOND NANOPHOTONIC DEVICES

FOR QUANTUM NETWORKS EXPERIMENTS

NINA
CODREANU

DIAMOND NANOPHOTONIC DEVICES FOR QUANTUM NETWORKS EXPERIMENTS

DIAMOND NANOPHOTONIC DEVICES FOR QUANTUM NETWORKS EXPERIMENTS

Dissertation

for the purpose of obtaining the degree of doctor
at Delft University of Technology
by the authority of the Rector Magnificus Prof.dr.ir. T.H.J.J. van der Hagen
chair of the Board for Doctorates
to be defended publicly on
Monday 29 September 2025 at 12:30 o'clock

by

Nina CODREANU

Master of Science in Engineering Physics,
Politecnico di Milano, Italy

born in Leuseni, Republic of Moldova.

This dissertation has been approved by the promotor:
Prof.dr.ir. R. Hanson and Prof.dr. S. Gröblacher

Composition of the doctoral committee:

| | |
|------------------------|--|
| Rector Magnificus | chairperson |
| Prof.dr.ir. R. Hanson | Technische Universiteit Delft, <i>promotor</i> |
| Prof.dr. S. Gröblacher | Technische Universiteit Delft, <i>promotor</i> |

Independent members:

| | |
|----------------------------|---|
| Prof.dr. P. Barclay | University of Calgary, Canada |
| Dr. S.C. Conesa Boj | Technische Universiteit Delft |
| Prof.dr. A. High | University of Chicago, United States of America |
| Prof.dr.ir. T. van der Sar | Technische Universiteit Delft |

Reserve member:

| | |
|--------------------------------|-------------------------------|
| Prof.dr.ir. L.M.K. Vandersypen | Technische Universiteit Delft |
|--------------------------------|-------------------------------|



QuTech



TU Delft

Delft
University of
Technology



KAVLI INSTITUTE
of Nanoscience Delft

| | |
|---------------|--------------------------------|
| Copyright | ©2025 Nina Codreanu |
| Cover design: | Nina Codreanu and Stefan Huber |
| Printed by: | Gildeprint |
| ISBN | 978-94-6518-130-1 |

An electronic copy of this dissertation is available at
<https://repository.tudelft.nl>

A tutte le bambine del mondo

CONTENTS

| | |
|---|-------------|
| Summary | xi |
| Samenvatting | xiii |
| 1 Introduction | 1 |
| 1.1 Quantum networks with color centers in diamond | 1 |
| 1.1.1 NV centers | 2 |
| 1.1.2 Group-IV color centers | 3 |
| 1.2 SnV centers in diamond as spin-photon interfaces | 5 |
| 1.3 Brief history walk on development of diamond material | 11 |
| 1.4 Fabrication of diamond devices | 12 |
| 1.4.1 Why is diamond challenging to nano-structure? | 12 |
| 1.4.2 Nanophotonic devices in diamond: fabrication methods | 14 |
| 1.5 Outline of the thesis | 18 |
| 1.6 References | 19 |
| 2 Fabrication of Diamond Nanophotonic Structures for Quantum Networks | |
| Applications | 29 |
| 2.1 Introduction | 30 |
| 2.2 QIE-based fabrication process | 31 |
| 2.2.1 General fabrication steps | 31 |
| 2.2.2 Crystallographic diamond etch | 32 |
| 2.3 QIE-based process requirements | 33 |
| 2.4 Design: Nanophotonic structures layout | 37 |
| 2.4.1 65 °C QIE-based variant compatible devices layout and designs | 39 |
| 2.4.2 250 °C QIE-based variant compatible devices layout and designs | 42 |
| 2.5 Methods | 44 |
| 2.5.1 Baseline QIE-based process development | 44 |
| 2.5.2 Complementary Si / Si _x N _y etch tests | 49 |
| 2.6 Results: 65 °C QIE-based process variant | 51 |
| 2.6.1 Si _x N _y hard mask | 51 |
| 2.6.2 Telecom-wavelength diamond cavity devices | 55 |
| 2.6.3 Transfer pattern | 55 |
| 2.6.4 Vertical sidewall passivation | 59 |
| 2.6.5 Quasi-isotropic undercut | 60 |
| 2.6.6 Conclusions | 62 |
| 2.7 Methods: 250 °C QIE-based process variant | 63 |
| 2.7.1 250 °C QIE ICP-RIE recipe | 63 |
| 2.7.2 Pattern transfer bias | 66 |
| 2.7.3 Optimizing transfer pattern: low aspect-ratio and ICPCVD Si _x N _y | 70 |

| | | |
|----------|--|------------|
| 2.8 | Results: 250 °C QIE-based variant SnV center integrated diamond PCCs. . . | 74 |
| 2.8.1 | Transfer pattern | 76 |
| 2.8.2 | Vertical sidewall passivation | 77 |
| 2.8.3 | Quasi-isotropic undercut | 77 |
| 2.8.4 | Aspect-ratio dependency | 79 |
| 2.8.5 | Conclusions | 81 |
| 2.9 | References | 84 |
| 3 | Fabrication of Tin-Vacancy Centers in Diamond: Surface-Protected Annealing Method and Graphitization Analysis | 87 |
| 3.1 | Introduction | 88 |
| 3.2 | Color centers in diamond: generation methods. | 88 |
| 3.2.1 | In-growth synthesis | 88 |
| 3.2.2 | Post-growth incorporation: ion implantation. | 89 |
| 3.3 | Group-IV color centers in diamond creation and activation. | 92 |
| 3.3.1 | SnV centers generation methods | 93 |
| 3.3.2 | Implantation damage and high temperature low pressure thermal annealing | 95 |
| 3.3.3 | Challenge: High temperature low pressure annealing surface graphitization. | 96 |
| 3.3.4 | Why is surface graphitization a challenge?. | 97 |
| 3.4 | Methods: high energy Sn implantation and high temperature thermal annealing | 98 |
| 3.4.1 | Pre-implantation substrate preparation. | 98 |
| 3.4.2 | Ion implantation parameters | 100 |
| 3.4.3 | Conventional annealing process | 101 |
| 3.4.4 | Surface-protected method for high temperature annealing | 102 |
| 3.4.5 | Analysis methods | 103 |
| 3.5 | Results: Conventional high temperature annealing method. | 105 |
| 3.6 | Results: Surface-protected method for high temperature annealing. | 108 |
| 3.6.1 | Scanning Electron Microscopy investigation | 110 |
| 3.6.2 | Raman spectroscopy investigation | 113 |
| 3.6.3 | Atomic force microscopy investigation. | 117 |
| 3.6.4 | X-ray photoelectron spectroscopy investigation | 122 |
| 3.7 | Conclusions and Outlook. | 126 |
| 3.8 | References | 129 |
| 4 | Nonlinear Quantum Photonics with a Tin-Vacancy Center Coupled to a One-Dimensional Diamond Waveguide | 133 |
| 4.1 | Introduction | 134 |
| 4.2 | Device and experiment. | 135 |
| 4.3 | Optical transition stability | 135 |
| 4.4 | Spectroscopy of the waveguide-SnV system | 136 |
| 4.5 | Photon statistics of transmitted field | 141 |
| 4.6 | Reflected signal and photon statistics. | 141 |
| 4.7 | Conclusions | 142 |

| | | |
|-----------------|--|------------|
| 4.8 | Methods | 142 |
| 4.8.1 | Sample and device fabrication | 142 |
| 4.8.2 | Inhomogeneous Distribution in the Waveguide Devices | 144 |
| 4.8.3 | Experimental setup. | 144 |
| 4.8.4 | Measurement sequences | 146 |
| 4.8.5 | PLE and CR-Checked Linescans | 147 |
| 4.9 | References | 149 |
| 5 | Tin-Vacancy Embedded All-Diamond Photonic Crystal Cavities | 153 |
| 5.1 | Introduction | 154 |
| 5.2 | Nanophotonic cavity devices | 154 |
| 5.2.1 | Cavity design and layout | 155 |
| 5.2.2 | Fabricated devices geometry evaluation | 156 |
| 5.3 | Cavity optical performance: devices statistics | 160 |
| 5.4 | Towards cavity-SnV centers coupling | 167 |
| 5.5 | Conclusions | 171 |
| 5.5.1 | Fabricated devices and geometry | 171 |
| 5.5.2 | Cavity optical performance. | 172 |
| 5.5.3 | Towards cavity-SnV centers coupling | 173 |
| 5.6 | Methods | 173 |
| 5.6.1 | Fabrication. | 173 |
| 5.6.2 | Room-temperature characterization setup | 176 |
| 5.6.3 | Measurement sequences | 177 |
| 5.6.4 | Experimental setup. | 177 |
| 5.7 | References | 179 |
| 6 | Conclusions and Outlook | 181 |
| 6.1 | Summary. | 182 |
| 6.2 | SnV centers as spin-photon interfaces | 183 |
| 6.2.1 | Optical and spin properties. | 183 |
| 6.2.2 | Nanophotonic integration | 184 |
| 6.2.3 | Current challenges | 186 |
| 6.3 | Future prospects | 188 |
| 6.3.1 | SnV center generation | 189 |
| 6.3.2 | Nano-devices fabrication | 190 |
| 6.4 | Epilogue | 191 |
| 6.5 | Data availability | 191 |
| 6.6 | References | 192 |
| Appendix | | 197 |
| A.1 | Annealing fabrication steps and tri-acid clean | 198 |
| A.2 | 65 °C QIE-based fabrication process parameters | 200 |
| A.3 | 250 °C QIE-based fabrication process parameters | 202 |
| A.4 | AlO _x mask for QIE-inspired fabrication process | 204 |
| A.5 | References | 207 |

| | |
|-----------------------------|------------|
| Gallery | 211 |
| Acknowledgments | 219 |
| List of Publications | 227 |
| Curriculum Vitæ | 229 |

SUMMARY

In this thesis, we explore the fabrication methods aimed at engineering integrated spin-photon interfaces based on SnV centers in diamond nanostructures for future quantum networks. We first introduce the group-IV color centers, elaborating on their spin and optical properties as future quantum networks end-node candidates. Specifically, the inversion symmetry of these color centers opens the path towards nanophotonic integration, a key step to enable scalability. However, integration of tin-vacancy (SnV) color centers in diamond and fabrication of suspended nanophotonic devices is challenging.

In Chapter 2, we focus on the crystal-plane-dependent quasi-isotropic-etch based fabrication, and present the extensive development of two fabrication process variants: we present the optimization of the fabrication protocols and discuss in depth the requirements and the fabrication process parameter space such that successful fabrication of suspended nanophotonic structures in diamond is achieved. The methods and optimized process parameters developed here are then used for fabrication of suspended nanophotonic structures with integrated SnV centers in diamond.

Integration of SnV centers in diamond is typically realized via ion implantation and high temperature annealing activation. In Chapter 3, we explore the graphitization phenomenon that occurs at the diamond surface upon high temperature low pressure annealing. Here we investigate the graphitization phenomenon with complementary diagnostic methods and find that this significantly affects and modifies the diamond surface properties. We then propose an alternative surface-protected high temperature annealing fabrication method and demonstrate graphitization-free activation of SnV centers. The developed methods and fabrication protocol are then used to systematically and reliably integrate SnV centers in bulk diamond.

In Chapter 4, we investigate the interaction between a single SnV center and a weak coherent light field in a single-mode nanophotonic waveguide. We perform spectroscopy of the transmitted and reflected signals, and demonstrate the single-photon nature of the interaction by measuring the effect on the photon statistics in both fields. These results highlight SnV centers integrated in diamond waveguides as a promising platform for the realization of efficient spin-photon interfaces, with significantly reduced fabrication overhead inherent to the waveguide design.

Finally, with the fabrication methods developed in this thesis, in Chapter 5 we present the successful integration of SnV centers in diamond photonic crystal cavities. Here we show a systematic analysis and estimate the geometry of the fabricated device, evaluating the performance of the developed and optimized fabrication process. We then show the statistics of the fabricated devices optical performance at room temperature and present the results on the cryogenic-temperature SnV-cavity spectroscopy experiments. These results open the path towards further SnV-cavity interaction in the weak cavity regime and demonstrate the potential of such a platform as an efficient light-matter interface to unlock high entanglement rates in modern quantum networks.

SAMENVATTING

In dit proefschrift verkennen we de fabricagemethodes gericht op het ontwerpen en creëren van geïntegreerde spin-foton interfaces gebaseerd op tin-holtecentra voor toekomstige kwantumnetwerken. We introduceren eerst de groep-IV kleurcentra en gaan dieper in op hun spin- en optische eigenschappen als toekomstig eindknooppunt kandidaat voor kwantumnetwerken. De inversie-symmetrie van deze centra opent de deur naar nanofotonische integratie, een grote stap richting schaalbaarheid. De integratie van tin-holte (SnV) kleurcentra in diamant en fabricage van zwevende nanofotonische structuren blijft echter uitdagend.

In Hoofdstuk 2 focussen we op de fabricagemethode gebaseerd op de kristal-vlak-afhankelijke quasi-isotrope-ets en presenteren we de omvangrijke ontwikkeling van twee varianten van het fabricageproces: we presenteren de optimalisatie van de fabricage protocollen zien en bespreken diepgaand de vereisten en parameterruimte van het fabricageproces om succesvolle fabricage van vrijdragende nanofotonische structuren in diamant te bereiken. De methodes en procesparameters die we hier ontwikkeld hebben worden vervolgens gebruikt voor de fabricage van zwevende nanofotonische structuren geïntegreerd met SnV kleurcentra in diamant.

De integratie van SnV kleurcentra in diamant wordt normaliter gerealiseerd door ionen-implantatie en activatie door gloeien bij hoge temperatuur. In Hoofdstuk 3 verkennen we het grafitiseringfenomeen dat zich voordoet op het oppervlak van diamant tijdens gloeien bij hoge temperatuur en lage druk. We onderzoeken hier het grafitisering fenomeen met complementaire diagnostische methodes en ondervinden dat dit fenomeen de eigenschappen van het diamant oppervlak significant aantast. We stellen een alternatieve methode voor die het oppervlak beschermt tijdens de hoge-temperatuur lage-druk gloei methode en demonstreren we grafitisering-vrije activatie van SnV kleurcentra. De ontwikkelde methodes en fabricageprotocollen worden vervolgens gebruikt voor het systematisch en betrouwbaar integreren van SnV kleurcentra in bulk diamant.

In Hoofdstuk 4 onderzoeken we de interactie tussen een enkel SnV kleurcentrum en een zwak coherent lichtveld in een enkele modus nanofotonische golfgeleider. We voeren spectroscopie uit op de doorgelaten en gereflecteerde signalen en laten de eigenschappen van een enkel foton zien tijdens de interactie door het meten van de fotonstatistieken in beide lichtvelden. Deze resultaten benadrukken dat SnV kleurcentra in diamanten golfgeleiders een veelbelovend platform zijn voor de realisatie van efficiënte spin-foton interfaces, met aanzienlijk lagere fabricage-inspanning die inherent zijn aan het golfgeleider ontwerp.

Tot slot, met de fabricagemethodes ontwikkeld in dit proefschrift presenteren we in Hoofdstuk 5 de succesvolle integratie van SnV kleurcentra in diamanten fotonische kristalholtes. We laten hier een systematische analyse zien en schatten de geometrie van de gefabriceerde structuren om de kwaliteit van het ontwikkelde fabricageproces te evalueren. Vervolgens presenteren wij de statistieken van de optische prestatie bij kamertemperatuur

van de gefabriceerde structuren, gevolgd door de resultaten van SnV-holte experimenten bij cryogene temperaturen. Deze resultaten banen de weg naar verdere SnV-holte interactie experimenten in het zwakke holte regime en tonen de potentiaal van een dergelijk platform aan als efficiënt licht-materie interface voor hogere verstrengeling snelheden in moderne kwantumnetwerken.

1

INTRODUCTION

1.1 QUANTUM NETWORKS WITH COLOR CENTERS IN DIAMOND

The purpose of a quantum internet is to enable applications that are fundamentally beyond the reach of the classical internet, with future quantum networks opening the path to secure communication, distributed quantum computing, and quantum enhanced sensing [1].

Optically active spins in diamond represent a promising building block for the realization of future quantum networks [2, 3]. Color centers in diamond represent promising candidates as end-nodes for photon mediated entanglement distribution, where the spin-state is the realization of the qubit. In order to classify as suitable candidates for a quantum network, such end-nodes must fulfill a series of requirements.

The first is the ability to create entanglement between the spin state of the electron (localized in the defect) and the quantum state of the emitted photon. This is a key ingredient to enable quantum information transfer from a stationary qubit (spin) to a flying qubit (photon). The second is the capability of storing the quantum states during entanglement generation, that is, the qubit coherence times under full network activity must be longer than the required time to generate entanglement between individual nodes. The third is the capability to store several entangled states per node while at the same time guaranteeing high-fidelity operations between them [4].

These three fundamental requirements translate into a series of requirements for the spin-photon interface. For color centers in diamond, generally, the above requirements can be satisfied. First, the color center contains an optically active spin, which can be individually addressed and controlled. The internal level structure of the color center is suitable for spin-photon entanglement generation owing to the ability to address spin-state-selective optical transitions. Second and third, the color center electron spin can be

interfaced with surrounding long-lived nuclear spins. In turn, nuclear spins can act as memory qubits that can be manipulated with a high degree of fidelity. Therefore, quantum state storage becomes possible in the memory qubit(s), freeing up the communication qubit for further network activity [4].

Thus, in a quantum network, where communication is established via photon-mediated entanglement, the remote parties are connected via photonic links, the end nodes require both access to long-lived memory qubit registers that can be operated with high fidelity, and bright spin-selective optical transitions with good coherence properties [1]. Recently, several promising photonic platforms [5–8] have been investigated as potential compatible candidates.

By leveraging this ability over multiple stationary distant qubits, such resource allows to link distant nodes, eventually realizing remote spin-spin entanglement over multiple distant end-nodes.

In this thesis, we focus primarily on the reliable fabrication, design and characterization of such building block. The focus is directed towards a specific color center, namely the negatively charged the tin-vacancy (SnV) in diamond, although the fabrication methods and general underlying principles are valid for the frequently encountered nitrogen-vacancy centers (NV), as well as group-IV color centers.

1.1.1 NV CENTERS

Nitrogen vacancy centers (NV) in diamond have been and are currently among the leading platforms, with milestone achievements such as the first loophole-free Bell test [9], entanglement distillation [10], a local 10-qubit quantum register [11], the first demonstration of a heralded generation of a multipartite entangled state across a 3 node quantum network [12] and most recently metropolitan-scale heralded entanglement [13]. However, further scaling of the network is hindered by a low spin-photon entanglement generation rate. The low entanglement generation rate can be attributed to two main limitations: a physically intrinsic limitation of low fraction of optical emission at the zero-phonon line (ZPL) only 3 % and the extrinsic limited collection efficiency. These two limitations combined currently restrict local entanglement generation rates to < 100 Hz [14]. The limited ZPL emission is an inherent physical constraint to the system itself arising from the strong electron-phonon coupling between the system and the diamond lattice, whereas the limited collection efficiency arises from the internal reflection at diamond-environment (typically vacuum or air) due to the high refractive index contrast.

A viable route to address the challenge of low emission rate of coherent ZPL photons and increase it is to enhance the spontaneous emission rate through approaches such as embedding the color center in an optical cavity. Embedding NV centers in an optical cavity allows to leverage the Purcell effect, thus enhance the ZPL emission. At the same time, optical cavities address as well the challenge associated with the poor collection efficiency, enabling collection of the emitted photons into a well defined output mode. As a result, spin-photon entanglement generation rate can be increased, as well as improving the collection and efficient routing of the entangled photons for further spin-spin entanglement.

Promising strategies for coupling color centers in diamond to optical resonators can be broadly categorized into two main approaches. The first involves positioning a diamond sample hosting the activated color center within fiber-based open microcavities. The sample

hosting the color center may be nanodiamonds [15–17], or micrometer-thin diamond membranes [18–22]. This approach allows for tunability and high-quality optical coupling. In the case of NV centers, employing micrometer-thin diamond membranes is beneficial to maintain good optical coherence, [23, 24]. Purcell-enhanced ZPL photons from NV centers in open optical cavities have been shown, demonstrating a potential increase of the entanglement rates of 3 orders of magnitude [25].

The second approach entails fabricating nanophotonic cavities directly in the diamond substrate, around the color centers, thereby integrating the color center into a monolithic cavity structure with enhanced optical confinement and stability. The integration of NV centers in nanophotonic optical cavities remains challenging [26], the reason being that optical transitions of the NV center are detrimentally affected when positioned in the vicinity of surfaces [27, 28]. In fact, NV centers embedded in nanophotonic cavities showed substantially broadened transition linewidths, induced by surface effects [27]. Due to the presence of a permanent electric dipole moment, the NV centers are affected by charge-noise [29]. The reason is in the atomic structure of the color center itself: the NV system is constituted by a nitrogen atom replacing a carbon atom of the diamond lattice, next to a lattice vacancy, which gives rise to a C_{3v} point group symmetry. This renders the NV center a system that possesses a permanent electric dipole moment. As a consequence, NV centers are highly susceptible to electric fields, to first order [4]. Although this allowed a high degree of optical control of the NV centers, enabling Stark tuning of optical transitions, at the same time this prevented NV centers from high optical coherence when embedded in nanophotonic cavities [23].

Thus, open Fabry-Pérot microcavities remain particularly appealing for the NV centers in diamond for several reasons, among these most relevant being the bulk-like properties of NV centers preserved in micrometer-thick membranes [30], as already demonstrated in previous works. Open microcavities present the advantage of full spectral and spatial tunability, photon emission into a well-collectible cavity output mode [31], as well as quality factors (of the order of $\sim 10^6$) [32]. Nevertheless, this comes at the cost of a higher mode volume [33] with respect to typical mode volumes, for example, of nanophotonic crystal cavities and challenging cavity vibration isolation [21].

1.1.2 GROUP-IV COLOR CENTERS

The research field has become fervent in recent years in the search of alternative good candidates with excellent properties that could fulfill the requirements of suitable platforms for the realization of a quantum network. In this framework, of great interest are the group-IV (Si, Ge, Sn, and Pb) color centers, which represent a promising alternative to the widely studied NV centers. For a comprehensive review of optical and spin properties and control, as well as their applications to quantum technologies, we refer the reader to Refs. [34, 35].

The atomic structure of the group-IV color centers is substantially different from the NV centers: the group-IV atom takes an interstitial lattice site between two lattice vacancies, resulting in a D_{3d} point group symmetry [36], rendering these a zero permanent dipole moment, meaning that, to first order, the group-IV color centers are insensitive to electric field fluctuations [4, 37]. While frequency tuning of the emission line of interest via the Stark effect for these systems is limited [37–39], the first-order insensitivity to the

local charge environment offers the advantage of robustness to charge noise, rendering nanophotonic integration a viable route towards efficient extraction of emitted photons [40, 41].

To date, the most mature group-IV color center has been the negatively charged silicon vacancy center (SiV), including groundbreaking quantum networks experiments such as a two-node quantum network composed of multi-qubit registers based on SiV centers in nanophotonic diamond cavities [42] and universal distributed blind quantum computing [43].

The key limitation of the SiV center is that it requires operational temperatures in the mK-regime in order to enable sufficient ground-state spin coherence, thereby necessitating the experimental overhead related to employment of dilution refrigerators. In the case of SnV center, exceptional optical properties are guaranteed, at the same time the higher ground-state splitting guarantees spin coherence at higher temperature in the \sim K regime (See Table 1.1). The measured $\Delta_{\text{GS}} \approx 850$ GHz) is higher than e.g. SiV center (measured $\Delta_{\text{GS}} \approx 50$ GHz). The ground state splitting determines the phonon-limited coherence which is $\propto \frac{\Delta_{\text{GS}}^3}{e^{\Delta_{\text{GS}}/k_{\text{B}}T} - 1}$ [44], therefore a higher ground state splitting is desirable in order to suppress the exponential factor and allow operation at higher temperatures. The SnV higher ground-state splitting limits the phonon population which in turn limits the coherence of the spin qubit [45, 46] at a higher temperature. Ultimately, for large-scale integration, aiming for operational temperatures in the \sim K regime results in less experimental overhead.

At the same time, compared to other group-IV (e.g. SiV), SnV centers are characterized by higher quantum efficiency (η) and Debye-Waller factor (β_0).

SPIN PROPERTIES

As mentioned in Section 1.1, high fidelity quantum control of the ground-state spin (where the qubit is encoded) is paramount for the realization of an efficient spin-photon interface. Until recently, this key capability has not been demonstrated in the case of the SnV centers. The first demonstration of spin control has been demonstrated via all-optical multi-axis coherent control of the SnV spin qubit with microwave modulated laser fields [47], with moderate fidelity. Most recently, high fidelity microwave spin control [48–51] and control of single nuclear spins [52] have been successfully demonstrated. Thus, this capability motivates further advances to research and improve SnV-based spin-photon interfaces.

OPTICAL PROPERTIES

Evidence of Sn-related single-photon emitters in single-crystal diamond has been reported for the first time in 2017, including the negatively charged SnV centers in diamond [53, 54]. In the following years, the properties of the SnV have been actively studied, where a detailed spectroscopic study and analysis of the phonon sideband and Debye–Waller factor have been shown, as well Fourier limited linewidths and stability of the charge state of single emitters [45, 46].

Furthermore, by embedding SnV centers in diamond nanophotonic waveguides, despite the heavy fabrication process of the nanostructures, SnV zero phonon line (ZPL) linewidth as narrow as 36 ± 3 MHz has been reported for free-hanging waveguide integrated nanophotonic waveguides [55], values comparable to those previously reported for nanopillar integrated SnV [41], and in both cases reported values are close to the

| color center | λ [nm] | η | β_0 | τ [ns] | Δ_{GS} [GHz] |
|--------------|----------------|---------|------------|-------------|---------------------|
| SiV | 737 | 0.1~0.3 | (0.65-0.9) | 1.8 | 50 |
| GeV | 602 | ~0.2 | ~0.6 | 5 | 170 |
| SnV | 620 | ~0.8 | 0.57 | (4.5~8) | 830 |
| PbV | 520 | / | ~0.34 [62] | 4.4 [63] | ~ 6000 [63] |

Table 1.1: Main properties of group-IV - Vacancy centers in diamond. Data adapted from Refs. [4, 64]. λ : ZPL wavelength of the C transition; η : Quantum Efficiency; β_0 : Debye-Waller factor; τ : excited state lifetime.

lifetime-limited linewidth of around 32 MHz [54]. Taking into account the high quantum efficiency (η), Debye-Waller factor (β_0), and higher operating temperature regime, these characteristics represent a strong motivation to pursue nanophotonic integration of SnV centers in broadband devices (e.g. one-dimensional photonic waveguides) in order to both increase collection efficiency of the ZPL emitted photons and to leverage non-linear quantum effects [21, 56].

Recently, Purcell enhancement of SnV centers in diamond photonic crystal cavities has been demonstrated, with SnV-cavity devices showing an average Purcell factors up to ~ 37 [57–59]. Efficient spin-photon interfaces that implement SnV centers with improved collection efficiency and enhanced coherent ZPL emission by resonant SnV to cavity coupling have the potential to enable next-generation quantum networks beyond the current state of art [60, 61].

In this thesis work, integration of SnV color centers in diamond substrates, in nanophotonic waveguides, and photonic crystal cavities is investigated, realized, and presented in Chapters 3, 2, 4 and 5, respectively. The objective of this work is to develop robust methods aimed at systematic and reliable integration of SnV centers in diamond substrates, as well as to design, engineer, and optimize nanophotonic optical interfaces for efficient photon collection into well-defined modes, suitable as single-photon sources for quantum network experiments.

1.2 SnV CENTERS IN DIAMOND AS SPIN-PHOTON INTERFACES

The negatively charged tin vacancy (SnV) center in diamond is a group-IV color center, in a *split-vacancy configuration* aligned with $\langle 111 \rangle$ equivalent crystallographic axis, of which a schematic is illustrated in Figure 1.1 (a). The symmetry of this class of defects belongs to the D_{3d} symmetry point group [36], in particular, displaying an inversion symmetry point centered on the position of the impurity atom.

SNV ELECTRONIC LEVEL STRUCTURE AND OPTICAL TRANSITIONS

The unperturbed electronic structure can, in principle, be predicted by group theory [36], with the energy ordering of the states calculated by density functional theory (DFT) [65]. The electronic structure can be determined from the defect molecule model: Each neighboring carbon atom presents one unsaturated dangling bond, from which the 6

orbitals in the D_{3d} symmetry emerge. Each orbital can host two electrons, due to spin degeneracy, for a total of twelve electrons. The negatively charged SnV center hosts eleven electrons: six electrons from each nearest-neighbor carbon atom, four electrons from the interstitial Sn atom, and one electron captured from a donor in the diamond lattice. This results in spin and orbital dynamics, effectively, of a spin 1/2 system [65]. The electronic structure (schematically illustrated in Figure 1.1 (b)) exhibits a ground state and an excited state with opposite wavefunction parity: even (g) for the ground state (GS) and odd (u) for the excited state (ES). In the unperturbed case, both GS and ES are four-fold degenerate. In the absence of any interaction, the ground state and the excited state are split by an optical transition at 619 nm. We will indicate the spin-1/2 electron with $|\uparrow\rangle$ and $|\downarrow\rangle$ to indicate $|m_s = +1/2\rangle$ and $|m_s = -1/2\rangle$, respectively, and the orbital states described in the bases $|e_+\rangle$ and $|e_-\rangle$ (in which the spin-orbit interaction Hamiltonian is diagonal) [36].

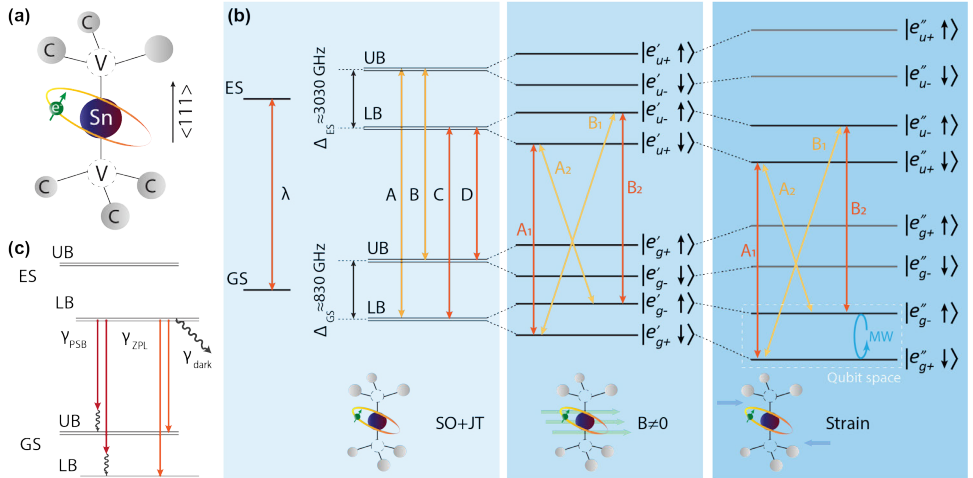


Figure 1.1: Tin-Vacancy (SnV) center in diamond | (a) Schematic illustration of the negatively charged SnV center; (b) Schematic illustration of the electronic energy levels: (left) spin-orbit (SO) and Jahn-Teller (JT) interaction lift the orbital degeneracy of the ground state (GS) and excited state (ES) onto two-fold degenerate states in the GS and ES respectively, lower branch (LB) and upper branch (UB); the energy splitting between LB and UB scales as $\Delta = \sqrt{\lambda^2 + 4\gamma^2}$; (center) Zeeman effect (for $B \neq 0$) and (right) Strain lift the spin degeneracy; C and D transitions split into spin-conserving transitions (A_1 and B_2 , allowed by selection rules) and spin-flipping transitions (A_2 and B_1 , allowed in the presence of an off-axis static magnetic field) (c) Decay paths: direct transition in the zero-phonon-line (ZPL, orange) and indirect phonon-assisted transitions phonon-sideband (PSB, red). Figure adapted from Ref. [48, 64].

In presence of spin-orbit (SO) coupling and the Jahn-Teller (JT) effect, the ground states and the excited states are split into a set of two-fold degenerate branches each, respectively, lower branch (LB) and upper branch (UB) (Figure 1.1 (b), left panel). The set of two-fold degenerate ground and excited states gives rise to four optical transitions. The energy splitting in the ground (Δ_{GS}) and the excited state (Δ_{ES}) scales as $\Delta = \sqrt{\lambda^2 + 4\gamma^2}$, where γ is the magnitude of the Jahn-Teller effect and λ is the spin-orbit coupling factor [36]. The splitting is $\Delta_{GS} \approx 830\text{GHz}$ in the ground state, whereas in the excited state $\Delta_{GS} \approx 3030\text{GHz}$. When taking into account inherent interactions to the system, such as spin-orbit coupling and the Jahn-Teller effect (and lattice strain), the ground state and excited state are split

into A, B, C and D transitions: B and C transitions are linearly polarized, whereas those of A and D are circularly polarized. At cryogenic temperatures ($\lesssim 100$ K), the upper branch of the excited state is characterized by a low occupation population and fast relaxation to the lower branch of the excited state. As a result, optical transitions from the excited state upper branch are suppressed and prevalent optical transitions involve the C and D transitions, respectively [45].

Next, the population of the upper branch of the ground state is temperature dependent: for temperatures $\lesssim 10$ K the phonon transition rate to the upper branch of the ground state is negligible compared to the fast phonon decay rate in the lower branch of the ground state [64]. As a consequence, the short lifetime of the ground state UB renders the respective states (Figure 1.1 (b), center panel, states indicated as UB $|e'_{g+} \uparrow\rangle$ and $|e'_{g-} \downarrow\rangle$, respectively) impractical to use.

In the presence of a static magnetic field, the spin degeneracy is lifted revealing eight spin-orbital levels (Figure 1.1 (b) center) due to Zeeman interaction, revealing A_1 , A_2 , B_1 and B_2 transitions (A_1 and B_2 spin-conserving transitions, A_2 and B_1 spin-flipping). In the presence of additional external strain, the energy levels are further shifted (Figure 1.1 (b) right), enabling spectral tuning of the ZPL emission of interest [66–68].

SnV AS SPIN-PHOTON INTERFACE

The features that render SnV a promising spin-photon interface are the efficiency of the optical transition (high quantum efficiency (η), Debye-Waller factor (β_0) and branching ratio (α)), the spin control at temperatures higher than 2K and the inversion symmetry.

The qubit states of the SnV center are defined as the spin-down and spin-up states (Figure 1.1 (b), states indicated as $|e'_{g+} \downarrow\rangle$ and $|e'_{g-} \uparrow\rangle$, respectively) of the lower branch in the ground state (Figure 1.1 (b), center and right panels). These two states are the lowest-energy states, with the orbital part of the wavefunction mutually orthogonal. Driving between these two states is forbidden according to the selection rules due to the orthogonality of the orbital components. This challenge can be overcome via two possible approaches: one is to alter the orbital component of the states e.g. via crystal strain, relaxing the orthogonality between the two states (thus relaxing the selection rules). In such case, microwave driving between the two states (Figure 1.1 (b), right panel, states indicated as $|e''_{g+} \downarrow\rangle$ and $|e''_{g-} \uparrow\rangle$, respectively) becomes possible [48, 50, 52]. Another approach is the stimulated-Raman scattering [47], where coherent population transfer between the two states with a two-photon process through a common (virtual) excited state (detuned from the excited state) is employed with two driving fields in a "lambda scheme" configuration [47].

The optical initialization of the SnV qubit state involves spin-dependent resonant excitation schemes, driving the cycling spin-conserving transition (e.g. A_1 or B_2) and a non-cycling spin-flipping transition (e.g. A_2 or B_1) used for qubit initialization (optical pumping into the down state) [64].

The relevant decay paths of the SnV center are schematically illustrated in Figure 1.1 (c). Within the radiative channels, the decay from the excited state can occur through a direct transition (zero-phonon line, ZPL) or through phonon-assisted processes: the electric dipole transitions are associated with a change in the wavefunction, in turn linked to a change in the charge distribution. A variation in the charge distribution causes a change

in the positions of the nuclei in the vicinity of the defect, inducing lattice vibrations, hence the electronic and vibronic structures are linked [36, 44]. Phonon-assisted decay processes result in a spectrally broad phonon sideband (PSB, for SnV $\gtrsim 630$ nm).

Quantum efficiency (η) is defined as the ratio between the radiative decay rate (γ_{rad}) over the total decay rate ($\gamma_{\text{rad}} + \gamma_{\text{nonrad}}$). The Debye-Waller (β_0) factor quantifies the ratio of ZPL to ZPL+PSB, while the branching ratio (α) quantifies the efficiency of the ZPL decay of interest to the total ZPL. Thus, quantum efficiency (η), Debye-Waller factor (β_0) and branching ratio (α) are each defined respectively as

$$\eta = \frac{\gamma_{\text{rad}}}{\gamma_{\text{rad}} + \gamma_{\text{nonrad}}}, \quad (1.1)$$

$$\beta_0 = \frac{\gamma_{\text{ZPL}}}{\gamma_{\text{ZPL}} + \gamma_{\text{PSB}}}, \quad (1.2)$$

$$\alpha = \frac{\gamma_{\text{C}}}{\gamma_{\text{ZPL}}}. \quad (1.3)$$

where $\gamma_{\text{rad}} = \gamma_{\text{ZPL}} + \gamma_{\text{PSB}}$ and $\gamma_{\text{ZPL}} = \gamma_{\text{C}} + \gamma_{\text{D}}$. The total efficiency of the SnV center can be quantified in the product between the above terms as follows

$$\eta \cdot \beta_0 \cdot \alpha \simeq 0.36. \quad (1.4)$$

This value shows improvement over SiV centers total efficiencies, as well as an order of magnitude improvement over the NV centers [21].

EMBEDDING SnV CENTERS IN OPTICAL CAVITIES

As highlighted in Section 1.1, in the context of color centers in diamond as end-nodes for long-distance quantum networks, a key goal is to increase the entanglement generation rate. To achieve this, we focus on improving both the photon collection efficiency from the color center and enhancing its spontaneous emission rate. Embedding the color center in a nanophotonic structure, such as a photonic crystal cavity, offers a promising approach to simultaneously address both objectives.

In the context of nanofabrication, one can identify two simple ways to enhance quantum systems interaction with light, that is, the integration of SnV in nanophotonic waveguides and in resonant cavity systems (e.g. photonic crystal cavities). In the following, the aim is to introduce the main figures of merit to quantify the emitter to cavity interaction.

The use of optical cavities to enhance the quantum system interaction with light is a well-studied subject, for which we refer the reader to other literature references [69–71], while below a brief overview of key figures of merit is introduced [64]. Considering a two-level system (linked by an electric dipole transition) located inside a single-mode optical cavity resonantly interacting with the cavity light field, the interaction between the two is described by the Jaynes-Cummings model. From the resulting Hamiltonian, if the emitter is in resonance with the cavity and the cavity mode is occupied by one photon (more photons lead to faster energy exchange), it follows that the rate at which the two-level system exchanges energy with the optical field is quantified by $2g$, where g is the emitter-cavity coupling. The coupling constant g is defined as

$$g = \sqrt{\frac{\omega \mu_{eg}^2}{2\hbar\epsilon_0\epsilon_r V}}, \quad (1.5)$$

where ω is the transition frequency between two eigenstates of the dipole emitter, $\vec{\mu}_{eg} = \mu_{eg} \cdot \hat{d}$ is the electric dipole moment of the emitter, V is the vacuum field quantization volume, ϵ_0 and ϵ_r are the vacuum and relative electric permittivity, respectively [30].

In the case of solid-state defects, in addition to the optical transition of interest coupled to the cavity, there are several additional decay channels (non-radiative decays, phonon sideband emission, and D-transition emission). These decay channels affect the coupling factor g between the transition of interest and the cavity mode, as the transition dipole moment effectively decreases when the other decay channels are taken into account. The cooperativity C compares the rate of radiation via the cavity to all emitter decay mechanisms. Taking into account the efficiency of the solid-state defect, the cooperativity follows [21]

$$C = F_P \beta_0 \eta \alpha \zeta \epsilon, \quad (1.6)$$

where β_0 is the Debye-Waller factor, η quantum efficiency, α is the branching ratio into the C transition, ζ overlap of cavity polarization with the emitter dipole and ϵ the spatial overlap of cavity mode and emitter. An important figure of merit is the Purcell factor F_P , defined as:

$$F_P = \frac{3}{4\pi^2} \left(\frac{\lambda}{n} \right)^3 \frac{Q}{V}, \quad (1.7)$$

where λ is the cavity resonance wavelength, n the refractive index of diamond, Q is the cavity quality factor (defined as $Q = \omega/\Delta\omega$ with frequency ω and cavity linewidth $\Delta\omega$) and V is the cavity mode volume. Equation 1.6 expresses the efficiency of a spin-photon interface [72], which can be expressed as

$$C = \frac{4g^2}{\kappa(\gamma_{\text{rad}} + \gamma_{\text{nonrad}})}. \quad (1.8)$$

where $\kappa = \kappa_{\text{in/out}} + \kappa_{\text{loss}}$ is the total decay rate of the cavity and $\gamma = \gamma_{\text{rad}} + \gamma_{\text{nonrad}}$ is the total decay rate of the transition. For the SnV center the radiative component $\gamma_{\text{rad}} = \gamma_{\text{ZPL}} + \gamma_{\text{PSB}}$, with a further split of the ZPL component in the C and D transitions $\gamma_{\text{ZPL}} = \gamma_C + \gamma_D$ [21]. Here we focus on the cavity resonant with the C transition of the SnV center.

The cavity-induced increased C transition decay rate (γ_P) with respect to its initial value γ_C is determined as follows

$$\gamma_P = F_P \epsilon \zeta \gamma_C + \gamma, \quad (1.9)$$

Taking into account $\gamma_C = \eta \beta_0 \alpha \gamma$, from Eq. 1.1, 1.2 and 1.3 we obtain:

$$C = F_P \frac{\gamma_C}{\gamma} \zeta \epsilon, \quad (1.10)$$

$$\gamma_P = \gamma(C + 1), \quad (1.11)$$

which yields for $\gamma = 1/(2\pi\tau)$

$$C = \frac{\gamma_P}{\gamma} - 1 = \frac{\tau}{\tau_P} - 1. \quad (1.12)$$

Thus, cooperativity C can be determined by measuring the Purcell-reduced excited state lifetime τ_P and the natural excited state lifetime τ [21].

Next, taking into account broadening effects of the optical transition, such as dephasing, the linewidth-broadened emitter decay rate is $\gamma' = \gamma + \gamma_d$ and the comprehensive metric quantifying the emitter-cavity interaction is the *coherent cooperativity* [72]

$$C_{\text{coh}} = C \frac{\gamma}{\gamma'} = \frac{\gamma_P'}{\gamma'} - 1. \quad (1.13)$$

Therefore, coherent cooperativity can be determined by measuring the emitter linewidth and Purcell-enhanced linewidth.

Finally, in the case of nanophotonic cavity devices, the probability of emission in the cavity mode (β_{cav}) and the overcoupling of the cavity to the waveguide $\frac{\kappa_w}{\kappa_w + \kappa_s}$ (κ_s includes all unwanted cavity scattering loss with $\kappa = \kappa_w + \kappa_s$) determine the efficiency of the outcoupled ZPL emission (η_{out}) [73] defined, respectively, as

$$\beta_{\text{cav}} = \frac{C}{C+1}, \quad (1.14) \quad \eta_{\text{out}} = \frac{\kappa_w}{\kappa_w + \kappa_s} \cdot \beta_{\text{cav}}. \quad (1.15)$$

The cavity-emitter coupling strength regimes can be roughly divided into two regimes. In the weak coupling regime ($\kappa, \gamma \gg g$ and $C \lesssim 1$) the emitter properties are modified by the increased photonic density of states at the cavity resonance. The optical transition of the emitter in resonance with the cavity is enhanced via the Purcell effect and is associated with a decrease in the excited-state lifetime in the cavity τ_P compared to the natural excited-state lifetime τ . In this regime the cavity and emitter decay are faster than the coupling rate; therefore, the probability that the emitter interacts with a photon in the cavity mode is low. In the case of a "lossy" cavity regime ($\kappa \gg g \gg \gamma$ and $C \gtrsim 1$) Purcell enhancement scales with cooperativity C : for increasing cooperativity, Purcell enhancement is stronger. Although cavity decay is still faster than the coupling rate and emitter decay, the probability of emitter interaction with a cavity field is increased; therefore, although the interaction probability is modest, coherent interaction between the emitter and the cavity field can be observed.

In the strong coupling regime ($g \gg \kappa, \gamma$ and $C \gg 1$) the interaction rate between the cavity photon and the emitter is much faster than the decay rate of the cavity and the total decay rate of the emitter, leading to a high probability of cavity-photon interaction with the emitter several times before the cavity photon is lost. In this regime, ($C \gg 1$ high cooperativity) near-deterministic interactions between the emitter and the photon are enabled [72] and allows implementation of reflection-based schemes to realize entanglement by using the spin-dependent reflection amplitude of the cavity, as demonstrated in the case of SiV embedded in a nanophotonic cavity [40].

In practice, Purcell enhancement is leveraged to increase spontaneous emission in the cavity mode or using coherent interaction with input photons to realize spin-dependent

single-photon gates. For color centers in diamond, two types of optical cavities are promising candidates [70]: nanophotonic cavities, which can be fabricated directly into the bulk diamond crystal host environment and the open Fabry-Pérot microcavities (previously discussed in Section 1.1.1).

Integrated nanophotonic cavities are appealing due to their small optical mode volumes $V < (\lambda/n_{\text{diamond}})^3$ [74] and the inherent cavity spectral stability [75]. In fact, from Eq. 1.7, the ratio Q/V is entirely determined by the cavity design, with the objective of maximizing Q and minimizing V in order to maximize F_p .

In case of the SnV center, taking into account the non-radiative decay (quantum efficiency), phonon sideband emission (PSB) and emission in the C-transition (branching ratio, α), the efficiency $\eta \cdot \beta_0 \cdot \alpha \approx 0.36$ is higher compared to other color centers in diamond [21]. Therefore, given a defined cavity performance as a result of fabrication imperfections, for an optimally coupled SnV center to the cavity mode, the resulting cooperativity is higher when compared to other group-IV (Table 1.1). On the other hand, the C transition ZPL line is blue-shifted with respect to e.g. SiV color centers, rendering the nanocavity design more challenging to fabricate, as the cavity geometry is as a consequence smaller.

1.3 BRIEF HISTORY WALK ON DEVELOPMENT OF DIAMOND MATERIAL

Diamond is an exceptional material with a unique combination of outstanding properties, making it a compelling focus of scientific inquiry. It exhibits remarkable mechanical strength, including unparalleled hardness, as well as superior thermal conductivity. Its broad optical transparency, chemical inertness, biocompatibility, and favorable electronic characteristics further contribute to its appeal. This rare convergence of attributes positions diamond as a highly versatile platform for diverse technological and engineering applications.

In the context of this work, diamond material is of interest mainly due to the wide optical window transparency and the variety of hosted color centers. Diamond is a semiconductor material, with a large indirect optical bandgap of $E_{\text{gap}}=5.5$ eV, while the direct energy bandgap is $E_{\Gamma}=7.3$ eV (at the Γ in the center of the irreducible Brillouin zone). This large energy bandgap of diamond renders the material transparent to an optical window from ultraviolet to far infrared [76]. At the same time, a plethora of optically active impurities that can lead to absorption of light in the visible spectrum are possibly hosted in the diamond crystalline lattice. The peculiarity of such optically active systems is that the energy levels of impurities lie within the diamond energy bandgap, effectively rendering them optically isolated systems in a solid state environment. Such systems, in analogy with e.g. trapped atoms, offer the advantage of optical control, while being embedded in a solid-state environment that effectively acts as a vacuum. This eliminates the need for experimental overhead, such as trapping potentials, which is typically required in atomic systems. A great deal of effort and interest has been directed toward the study of such complexes, establishing over hundreds of species, which have been studied, characterized, and summarized in Ref. [76, 77].

The underlying basic scientific principles aimed at the development and control of color centers in diamond for quantum technologies began to take shape in the previous century.

It was in 1951 that William G. Eversole reported the first successful artificial diamond synthesis [78, 79]. Only a few years later, in an equally rapidly advancing field of physics, the laser was invented by Theodore Maiman in 1960. Together, these two breakthroughs laid the foundation for quantum experiments involving color centers in diamond.

We refer the reader to the complete historical scientific endeavor of chemical vapor deposition synthesis efforts over the past century [78], while here we report on the very first milestone experiments investigating diamond chemical composition and artificial synthesis efforts.

The first scientific studies on diamond material date back to 1694 at the Accademia del Cimento in Florence, where diamond combustion studies have been conducted by Averani and Targioni [78]. Fast forward, in 1797, it was concluded that "diamond consisted entirely of charcoal, differing from it only by its crystallized form" [79]. The discovery that diamond is fully constituted by carbon has raised interest in research on artificial synthesis.

As early as 1915, G.N. Lewis and M. Randall determined that under room temperature, diamond and graphite are in equilibrium at 10000 atm. It was until 1949 that serious concerns were held valid with respect to the growth of diamond at low pressures. The first documented diamond growth reports at low pressures have been documented by William G. Eversole at the Linde Division of the Union Carbide Corporation in 1949: carbon monoxide was proposed to be used as a source gas to precipitate diamond on a diamond crystal seed. The growth of these has been achieved in January 1953, with fast conclusive proof in February of the same year. This discovery precedes the high pressure synthesis of diamond, reported by the General Electric Company in 1954 [78].

In the following decade, extensive efforts have been dedicated towards the investigation of reliable diamond growth, with fervent developments and rapid implementation of new techniques, which mainly involved laboratories across the United States (Union Carbide, General Electric, Case Western Reserve University), Soviet Union (Physical Chemistry Institute) and Japan (National Institute for Research in Inorganic Materials). These efforts confirmed that diamond synthesis can be achieved successfully at low pressures and relatively moderate temperatures (of the order of 1000 K) employing mainly CH_4/H_2 gas mixture.

To date, artificial diamond synthesis is enabled by mainly three processes, namely high-pressure high-temperature (HPHT), detonation, and chemical vapor deposition (CVD).

Although the potential of diamond as a semiconducting material was clear, until the 1990s its optical technology applications remained limited, the main reason being a restricted availability of high purity and crystal size. The advent and development of diamond CVD growth has changed this scenario, making readily available optical CVD grades that rapidly found a variety of technological applications, including e.g. high energy radiation detectors [79, 80], and, very recently, quantum applications.

1.4 FABRICATION OF DIAMOND DEVICES

1.4.1 WHY IS DIAMOND CHALLENGING TO NANO-STRUCTURE?

Diamond lattice (constituted by carbon atoms in a crystal), consists of two interpenetrating face-centered cubic Bravais lattices. Each constituting atom has its four nearest neighbors positioned to form the vertices of a tetrahedron [81]. In this spatial configuration, the

spatial electronic distribution of each constituent atom is localized and preferred along certain directions (typical of covalent crystals), giving rise to sigma bonds (154 pm long) in a three-dimensional configuration. Therefore, in this configuration, both the atomic position within the crystal lattice and the electron wavefunction distribution give rise to the sp^3 configuration.

CHEMICAL REACTIVITY

At the same time, diamond is chemically inert and is not affected by any acid or other chemical solutions [80, 82]. Moreover, controlled chemical modification of the diamond surface has proven challenging, with the surface generally being inert to most chemical reagents. Ref. [83] reports that the first major factor responsible for the low reactivity of diamond surfaces is the steric bulk of the diamond surface. This constrains the attack trajectory of a potential reagent to a near-surface normal vector. The second factor relies on the crystalline structure of the lattice: the bulk sp^3 hybridization, combined with surface carbon-hydrogen termination is inherently characterized by low reactivity [83]. Thus, the outstanding chemical stability of diamond in the sp^3 configuration and the high binding energy of the C-C bonds render the wet chemical etch ineffective: wet chemical etch solutions do not provide sufficient energy to break the C-C bonds [84]. This makes diamond a challenging material to shape, by mechanical means or wet etching.

There are several exceptions to the generally low reactivity of diamond surfaces. The first and most notable one is the graphitization (to which we dedicated a great deal of attention in this thesis, Chapter 3) and the second (and most important) exception is represented by surface oxidation.

Wet etching of diamond surfaces is made possible by strongly oxidizing agents at high temperatures under ambient pressure that efficiently attack the surface of the diamond [80, 82, 83]. Such oxidizing agents are mainly constituted by molten alkali nitrates (e.g. $KClO_3$, $KMnO_4$, K_2CrO_7 and $NaClO_4$ wet etch of {111} oriented diamond at 653 K [85] and KNO_3 wet etch of {100} oriented diamond at 800 K to 1100 K [86]) [82]. The other possible chemical attack form is composed of two groups of metals: At high temperatures, metals such as tungsten, tantalum, titanium and zirconium react chemically with diamond to form respective carbides, whereas metals such as iron, cobalt, manganese, nickel, chromium and platinum group of metals, in the molten state, act as solvents for carbon [80, 82].

The severe wet etching conditions of diamond employing the above chemical attack methods, combined with the resulting typical etched pattern (triangularly shaped cavities, in case of {111} oriented surfaces [85]) and squared etched pits (in case of {100} oriented surfaces [86]), made diamond wet etching significantly challenging for future micro- or nano-structuring purposes. In addition, these methods are highly aggressive, technically challenging to implement, and not compatible with cleanroom fabrication processes or with the safety regulations of typical cleanroom facilities. Therefore, even though in the above exceptions wet etching of diamond is in principle possible, it is not a viable route for micro- and nano-fabrication of devices.

DRY ETCHING

The high chemical inertness renders the diamond a challenging substrate material for alternative reactive ion etching (RIE), with few candidate etchants that effectively etch

diamond in chemistry processes involving oxygen plasma. At the same time, the strong bonding nature of the carbon lattice makes physical etching quite challenging [77].

The dry etching mechanism is fundamentally different from the chemical wet etch, which involves mainly four major steps: (1) reactive species (radicals and ions) are generated in the plasma; (2) the species are brought in proximity to the substrate of interest and adsorb on the target; (3) chemical reactions occur at the surface of the target; (4) etch byproducts desorb from the surface [87]. In addition, sputtering of ions occurs (physically removing ions from the target substrate) for sufficiently energetic plasma radicals.

Efforts directed at the dry reactive ion etch date back as early as 1961, where experiments of etching diamond surfaces in air at high temperatures have been conducted [88]. Most of the efforts in the study of reactive ion etching stem from research conducted in the context of diamond CVD growth. Hence, hydrogen and oxygen etching are by far the most common etching mechanisms. The reason for the high etch rates in the case of an oxygen-based plasma is the reactivity of the diamond surface upon oxidation [82]. Atomic oxygen strongly oxidizes the diamond surface, chemically removing surface carbon atoms, resulting in CO and CO₂, whereas atomic hydrogen etch yields CH₄ volatile byproducts [89].

Although diamond is known to be an inert material, extensive surface functionalization research has recently been conducted for a variety of applications, of particular interest for molecular sensing and biosensing [90].

1.4.2 NANOPHOTONIC DEVICES IN DIAMOND: FABRICATION METHODS

With the advent and potential of optically active color centers in diamond for quantum communication applications and quantum sensing, photonic integration has gained significant interest. Diamond material offers the advantage as both a solid-state platform hosting potentially high performance spin-qubits, while at the same time offering the possibility of engineering high efficiency optical nanophotonic devices. These ultimately have the potential for nanophotonic integration with conventional integrated photonic circuits, offering the advantage of on chip routing and signal processing [91]. In the context of quantum communications, the above features open the possibility to overcome experimental challenges hindering scalability due to low photon collection efficiency.

In recent decades, diamond fabrication has seen tremendous development, characterized by several landmark application-driven fabrication processes being successfully developed. We refer to several comprehensive literature review articles exploring this subject [77, 84, 92], here we focus on the main fabrication processes aimed at nanophotonic integration with NV and group-IV color centers for quantum communications.

Conventional methods for structuring diamond material involve cutting and fine polishing, yielding flat sub-nanometer surface roughness Single Crystal Diamond (SCD) plates. Structuring diamond beyond this dimensionality is notoriously challenging, with several methods developed in order to engineer curved surfaces, such as focused ion beam milling and ultrashort pulse laser micro-structuring [93]. Additionally, methods relying on lithography patterning and reactive ion etching enabled a top-down approach towards diamond structuring, yielding successful fabrication of micro and nano devices. To date, a method for wet-etch undercutting of nanophotonic structures by means of a wet etch of a sacrificial layer, as conventionally adopted strategy in the traditional silicon photonics (i.e. silicon on

Overview of fabrication processes

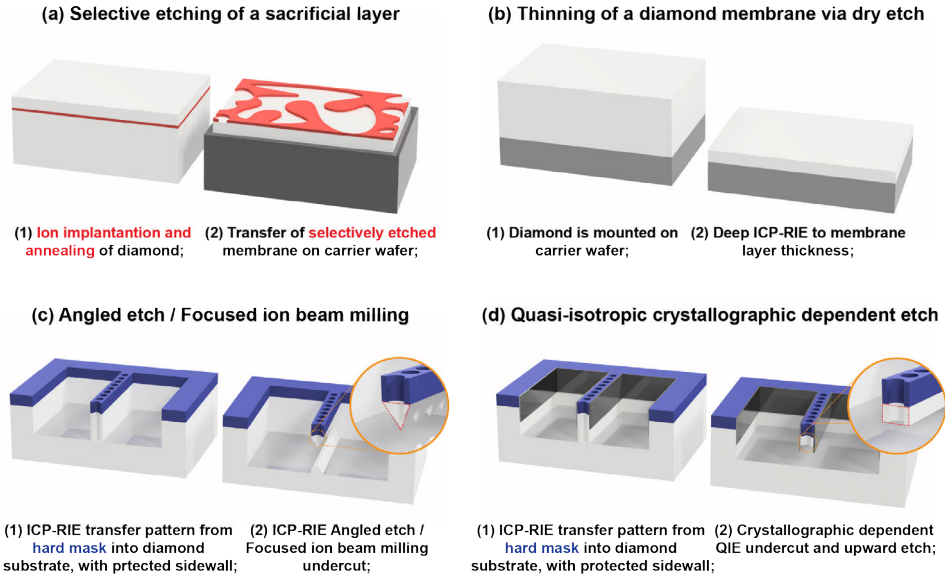


Figure 1.2: **Overview of common fabrication methods:** | (a) Schematic illustration of selective etching of a sacrificial amorphous carbon layer, obtained via ion implantation and subsequent high temperature annealing; (b) Deep ICP-RIE of a several tens of micrometer thick diamond membrane, to few micrometer device layer thickness; (c) ICP-RIE Angled ion etch / Focused ion beam milling: a hard mask material is used for nanophotonic device transfer pattern; (d) QIE crystallographic dependent based fabrication process. Figure adapted from Ref. [4].

insulator (SOI) platform) has emerged [94], although not widely available yet. The majority of developed diamond fabrication processes start from bulk SCD substrates and typically rely on lithography combined with dry reactive ion etching, where common fabrication methods can be roughly divided into four approaches.

SELECTIVE ETCHING OF A SACRIFICIAL LAYER

This method is based on high energy ion implantation of the SCD above a critical damage threshold at a depth dictated by the ion beam energy. This yields a highly damaged buried layer inside the SCD at a precise depth. Subsequently, a thin layer of high quality diamond (i.e. a low concentration of crystalline defects and non-native impurity atoms) is overgrown via CVD. In order to incorporate non-native impurities, typically delta doping takes place in the overgrowth phase (as in the case of subsequent NV or SiV center creation), or ion implantation of dopants is carried out in a following step. The substrate is then annealed at high temperature, both activating the color centers and migrating the vacancies in the overgrown layer, as well as converting the damaged layer into chemically non-inert amorphous carbon. Next, in order to release the diamond thin film from the parent substrate, the amorphous carbon layer is chemically or electrochemically etched and transferred to a carrier wafer chip, the damaged layer being further dry etched (RIE or ICP-RIE) and for further post thin-film release fabrication [94–104]. Typically, this method yields ultra low surface roughness (few hundreds of picometers), high uniformity (wedge-free), thin-film

layer thickness ≤ 200 nm (typical dimension for visible wavelength waveguiding structures) diamond films. Nanophotonic diamond devices fabricated with this method have shown the highest Purcell enhancement of color centers in diamond to date [103, 105].

THINNING OF A DIAMOND MEMBRANE VIA DRY ETCH

Starting from a commercially available diamond membrane of few micrometer thick, directly hosted by a carrier wafer chip (for example, silicon), the membrane is thinned down by means of relatively long RIE etching (typically argon / chlorine and oxygen-based) to a device layer compatible with nanophotonic devices fabrication (typically up to ~ 200 nm thick). Next, dry etching is performed to undercut the host wafer chip and suspend the diamond devices [27, 106–108]. Similarly, micrometer thick diamond film layers can be fabricated via deep RIE employing a positioned mask placed atop the substrate. In this case, the mask opening allows for deep etching of diamond substrates, whereas the masked areas preserve the original substrate thickness. This method demonstrated the advantage of user-efficient handling while preserving the structural integrity of the resulting thin film. On the other hand, thickness uniformity across the etched area has resulted in a challenge to guarantee, ultimately hindering the ability to reach the nanophotonic device layers of ~ 200 nm typically required for optimal optical mode waveguiding [109–111].

ANGLED ETCH / MILLING

Starting from a commercially available SCD, typically a few hundred micrometers thick, the fabrication process begins by patterning a high etch-selectivity hard mask using standard lithography techniques. Nanophotonic device structures are then defined and undercut to form fully suspended geometries through an angled reactive ion etch (RIE) process, or focused ion beam milling process, in which ions are directed toward the substrate surface at a well-controlled angle. This approach enables the realization of free-standing devices with triangular cross-sections, as demonstrated using both focused ion beam (FIB) milling [112] and angled RIE. The latter can be achieved by employing a Faraday cage to steer plasma radicals relative to the surface normal [113], or by direct reactive ion beam angled etching [114, 115]. State-of-the-art quality factors photonic crystal cavity devices, starting from bulk SCD substrates have been demonstrated with this method as well as demonstration of probabilistic entanglement generation between two SiV centers in the same waveguide [116] (showing coherent cavity-SiV interaction for the first time), strong interaction between two SiV centers placed in the same nanocavity [117], demonstration of a memory-enhanced quantum communication employing a nanophotonic diamond resonator with cooperativity of $C=105 \pm 11$ [118].

QUASI-ISOTROPIC CRYSTALLOGRAPHIC DEPENDENT ETCH (QIE)

In analogy with the crystallographic-dependent wet etch in silicon, where crystallographic planes with different Miller indices exhibit different etch rates when exposed to the same wet etch conditions, diamond crystallographic etch was demonstrated in dry reactive ion etch plasma under specific etch conditions for the first time by Ref. [119]. The combination of crystallographic etch selectivity with single-crystal reactive ion etching and metallization (SCREAM) process principles [120] has enabled fabrication of high quality nanophotonic devices in diamond, such as microdisk resonators [119], one-dimensional nanophotonic

waveguides [55, 56, 91], one- and two-dimensional photonic crystal cavities [26, 121, 122], as well as nanomechanical resonators [123].

In this thesis, we focus primarily on the development of the latter fabrication process, establishing experimental methods and fully characterizing the process parameters that allow the reliable fabrication of nanophotonic devices with SnV centers in diamond.

1.5 OUTLINE OF THE THESIS

This thesis presents the progress on the development and methods for the realization of spin-photon interfaces based on tin-vacancy (SnV) centers in diamond nanophotonic devices, and is organized as follows:

- **Introduction** gave a brief overview of quantum networks, color centers in diamond and the properties of SnV centers. We then motivated the advantages of SnV-embedded nanophotonic devices as spin-photon interfaces for next generation quantum networks. Challenges associated with diamond nanofabrication methods were introduced and a brief overview of state-of-the-art fabrication processes with the goal of realizing free-hanging all-diamond nanophotonic one-dimensional nanophotonic waveguides and photonic crystal cavities was given.
- **Chapter 2** presents and discusses in detail the quasi-isotropic-etch (QIE) based nanofabrication process and presents the two process variants we developed. Next, we present the optimized process parameters and nanophotonic devices designs. We then show successful fabrication of all-diamond photonic crystal cavity devices operating in the telecommunications regime and all-diamond photonic crystal cavities operating at the SnV emission wavelength.
- **Chapter 3** gives a brief overview of state-of-the-art generation and activation of color centers in diamond. We investigated the graphitization challenge associated with the activation of SnV implanted color centers upon high-temperature vacuum annealing. We then propose and present an alternative surface-protected high temperature annealing discussing the analysis of the graphitization phenomenon via complementary inspection methods. The analysis confirms the efficacy of the proposed method in preventing the diamond surface graphitization phenomenon.
- **Chapter 4** presents a detailed investigation of a diamond SnV center coupled to a nanophotonic waveguide. We present the integration of SnV centers in a diamond waveguide, showing the successful fabrication of free-hanging diamond nanophotonic devices with the 65 °C QIE-based fabrication process variant. We then investigate the interaction between a single SnV in a single-mode fabricated waveguide and a coherent input field and demonstrate strong non-linear interaction.
- **Chapter 5** presents the results of fabricated SnV-embedded photonic crystal cavity devices with the surface-protected high temperature vacuum annealing (development and methods in Chapter 3) and 250 °C QIE-based variant fabrication process (development and methods presented in Chapter 2). Here we show the results of optically characterized cavity devices and show cavity resonance tuning at cryogenic temperature.
- **Chapter 6** summarizes the findings of this thesis and outlines the prospects for further development of SnV-embedded all-diamond nanophotonic devices as the next generation of diamond-based quantum network nodes.

1.6 REFERENCES

1. Wehner, S., Elkouss, D. & Hanson, R. Quantum internet: A vision for the road ahead. *Science* **362** (2018).
2. Kimble, H. J. The Quantum Internet. *Nature* **453**, 1023–1030 (2008).
3. Vardoyan, G., Skrzypczyk, M. & Wehner, S. On the quantum performance evaluation of two distributed quantum architectures. *ACM SIGMETRICS PER* **49**, 30–31 (2022).
4. Ruf, M., Wan, N. H., Choi, H., Englund, D. & Hanson, R. Quantum Networks Based on Color Centers in Diamond. *Journal of Applied Physics* **130**, 070901 (2021).
5. Bernien, H., Hensen, B., Pfaff, W., Koolstra, G., Blok, M. S., Robledo, L., Taminiau, T. H., Markham, M., Twitchen, D. J., Childress, L. & Hanson, R. Heralded Entanglement between Solid-State Qubits Separated by Three Metres. *Nature* **497**, 86–90 (2013).
6. Knaut, C. M., Suleymanzade, A., Wei, Y.-C., Assumpcao, D. R., Stas, P.-J., Huan, Y. Q., Machielse, B., Knall, E. N., Sutula, M., Baranes, G., *et al.* Entanglement of nanophotonic quantum memory nodes in a telecom network. *Nature* **629**, 573–578 (2024).
7. Ruskuc, A., Wu, C.-J., Green, E., Hermans, S., Pajak, W., Choi, J. & Faraon, A. Multiplexed entanglement of multi-emitter quantum network nodes. *Nature*, 1–6 (2025).
8. Afzal, F., Akhlaghi, M., Beale, S. J., Bedroya, O., Bell, K., Bergeron, L., Bonsma-Fisher, K., Bychkova, P., Chaisson, Z. M., Chartrand, C., *et al.* Distributed quantum computing in silicon. *arXiv preprint arXiv:2406.01704* (2024).
9. Hensen, B., Bernien, H., Dréau, A. E., Reiserer, A., Kalb, N., Blok, M. S., Ruitenberg, J., Vermeulen, R. F., Schouten, R. N., Abellán, C., *et al.* Loophole-free Bell inequality violation using electron spins separated by 1.3 kilometres. *Nature* **526**, 682–686 (2015).
10. Kalb, N., Reiserer, A. A., Humphreys, P. C., Bakermans, J. J., Kamerling, S. J., Nickerson, N. H., Benjamin, S. C., Twitchen, D. J., Markham, M. & Hanson, R. Entanglement distillation between solid-state quantum network nodes. *Science* **356**, 928–932 (2017).
11. Bradley, C., Randall, J., Abobeih, M., Berrevoets, R., Degen, M., Bakker, M., Markham, M., Twitchen, D. & Taminiau, T. A ten-qubit solid-state spin register with quantum memory up to one minute. *Physical Review X* **9**, 031045 (2019).
12. Pompili, M., Hermans, S. L., Baier, S., Beukers, H. K., Humphreys, P. C., Schouten, R. N., Vermeulen, R. F., Tiggeleman, M. J., dos Santos Martins, L., Dirkse, B., *et al.* Realization of a multinode quantum network of remote solid-state qubits. *Science* **372**, 259–264 (2021).
13. Stolk, A. J., van der Enden, K. L., Slater, M.-C., te Raa-Derckx, I., Botma, P., van Rantwijk, J., Biemond, J. B., Hagen, R. A., Herfst, R. W., Koek, W. D., *et al.* Metropolitan-scale heralded entanglement of solid-state qubits. *Science advances* **10**, eadp6442 (2024).
14. Humphreys, P. C., Kalb, N., Morits, J. P., Schouten, R. N., Vermeulen, R. F., Twitchen, D. J., Markham, M. & Hanson, R. Deterministic delivery of remote entanglement on a quantum network. *Nature* **558**, 268–273 (2018).

15. Albrecht, R., Bommer, A., Deutsch, C., Reichel, J. & Becher, C. Coupling of a Single Nitrogen-Vacancy Center in Diamond to a Fiber-Based Microcavity. *Phys. Rev. Lett.* **110**, 243602 (2013).
16. Kaupp, H., Deutsch, C., Chang, H.-C., Reichel, J., Hänsch, T. W. & Hunger, D. Scaling laws of the cavity enhancement for nitrogen-vacancy centers in diamond. *Phys. Rev. A* **88**, 053812 (2013).
17. Johnson, S., Dolan, P. R., Grange, T., Trichet, A. A. P., Hornecker, G., Chen, Y. C., Weng, L., Hughes, G. M., Watt, A. A. R., Auffèves, A. & Smith, J. M. Tunable cavity coupling of the zero phonon line of a nitrogen-vacancy defect in diamond. *New J. Phys.* **17**, 122003 (2015).
18. Yurgens, V., Fontana, Y., Corazza, A., Shields, B. J., Maletinsky, P. & Warburton, R. J. Cavity-assisted resonance fluorescence from a nitrogen-vacancy center in diamond. *npj Quantum Inf* **10**, 112 (2024).
19. Zifkin, R., Rodríguez Rosenblueth, C. D., Janitz, E., Fontana, Y. & Childress, L. Lifetime reduction of single germanium-vacancy centers in diamond via a tunable open microcavity. *PRX Quantum* **5**, 030308 (2024).
20. Berghaus, R., Sachero, S., Bayer, G., Heupel, J., Herzig, T., Feuchtmayr, F., Meijer, J., Popov, C. & Kubanek, A. Cavity-enhanced emission and absorption of color centers in a diamond membrane with selectable strain. *Phys. Rev. Appl.* **23**, 034050 (2025).
21. Herrmann, Y., Fischer, J., Brevoord, J. M., Sauerzapf, C., Wienhoven, L. G., Feije, L. J., Pasini, M., Eschen, M., Ruf, M., Weaver, M. J., *et al.* Coherent coupling of a diamond tin-vacancy center to a tunable open microcavity. *Physical Review X* **14**, 041013 (2024).
22. Herrmann, Y., Brevoord, J. M., Fischer, J., Scheijen, S., Sauerzapf, C., Codreanu, N., Wienhoven, L. G. C., van der Graaf, Y. M. Q., Wolfs, C. F. J., Méjard, R., Ruf, M., de Jong, N. & Hanson, R. Laser-cut patterned, micrometer-thin diamond membranes with coherent color centers for open microcavities. *Materials for Quantum Technology* **5**, 035001 (2025).
23. Ruf, M., Ijspeert, M., Van Dam, S., De Jong, N., Van Den Berg, H., Evers, G. & Hanson, R. Optically coherent nitrogen-vacancy centers in micrometer-thin etched diamond membranes. *Nano letters* **19**, 3987–3992 (2019).
24. Yurgens, V., Corazza, A., Zuber, J., Gruet, M., Kasperczyk, M., Shields, B., Warburton, R., Fontana, Y. & Maletinsky, P. Spectrally stable nitrogen-vacancy centers in diamond formed by carbon implantation into thin microstructures. *Applied Physics Letters* **121** (2022).
25. Bogdanović, S., van Dam, S. B., Bonato, C., Coenen, L. C., Zwerver, A.-M. J., Hensen, B., Liddy, M. S., Fink, T., Reiserer, A., Lončar, M., *et al.* Design and low-temperature characterization of a tunable microcavity for diamond-based quantum networks. *Applied Physics Letters* **110**, 171103 (2017).
26. Mouradian, S., Wan, N. H., Schröder, T. & Englund, D. Rectangular Photonic Crystal Nanobeam Cavities in Bulk Diamond. *Applied Physics Letters* **111**, 021103 (2017).

27. Faraon, A., Santori, C., Huang, Z., Acosta, V. M. & Beausoleil, R. G. Coupling of nitrogen-vacancy centers to photonic crystal cavities in monocrystalline diamond. *Phys. Rev. Lett.* **109**, 033604 (2012).
28. Jung, T., Görlitz, J., Kambs, B., Pauly, C., Raatz, N., Nelz, R., Neu, E., Edmonds, A. M., Markham, M., Mücklich, F., *et al.* Spin measurements of NV centers coupled to a photonic crystal cavity. *Apl Photonics* **4** (2019).
29. Doherty, M. W., Manson, N. B., Delaney, P., Jelezko, F., Wrachtrup, J. & Hollenberg, L. C. The nitrogen-vacancy colour centre in diamond. *Physics Reports* **528**, 1–45 (2013).
30. Ruf, M. *Cavity-enhanced quantum network nodes in diamond* PhD thesis (Delft University of Technology, 2021).
31. Benedikter, J., Kaupp, H., Hümmer, T., Liang, Y., Bommer, A., Becher, C., Krueger, A., Smith, J. M., Hänsch, T. W. & Hunger, D. Cavity-enhanced single-photon source based on the silicon-vacancy center in diamond. *Phys. Rev. Appl.* **7**, 024031 (2017).
32. Hunger, D., Steinmetz, T., Colombe, Y., Deutsch, C., Hänsch, T. W. & Reichel, J. A fiber Fabry–Perot cavity with high finesse. *New Journal of Physics* **12**, 065038 (2010).
33. Riedel, D., Söllner, I., Shields, B. J., Starsielec, S., Appel, P., Neu, E., Maletinsky, P. & Warburton, R. J. Deterministic enhancement of coherent photon generation from a nitrogen-vacancy center in ultrapure diamond. *Physical Review X* **7**, 031040 (2017).
34. Bradac, C., Gao, W., Forneris, J., Trusheim, M. E. & Aharonovich, I. Quantum Nanophotonics with Group IV Defects in Diamond. *Nature Communications* **10**, 5625 (2019).
35. Orphal-Kobin, L., Torun, C. G., Bopp, J. M., Pieplow, G. & Schröder, T. Coherent microwave, optical, and mechanical quantum control of spin qubits in diamond. *Advanced Quantum Technologies* **8**, 2300432 (2025).
36. Hepp, C. *Electronic structure of the silicon vacancy color center in diamond* PhD thesis (Universität des Saarlandes, 2014).
37. Aghaeimeibodi, S., Riedel, D., Rugar, A. E., Dory, C. & Vučković, J. Electrical Tuning of Tin-Vacancy Centers in Diamond. *Phys. Rev. Appl.* **15**, 064010 (2021).
38. De Santis, L., Trusheim, M. E., Chen, K. C. & Englund, D. R. Investigation of the stark effect on a centrosymmetric quantum emitter in diamond. *Phys. Rev. Lett.* **127**, 147402 (2021).
39. Bushmakina, V., von Berg, O., Sauerzapf, C., Jayaram, S., Denisenko, A., Tarín, C., Anders, J., Vorobyov, V., Gerhardt, I., Liu, D., *et al.* Two-Photon Interference of Photons from Remote Tin-Vacancy Centers in Diamond. *arXiv preprint arXiv:2412.17539* (2024).
40. Nguyen, C., Sukachev, D., Bhaskar, M., Machielse, B., Levonian, D., Knall, E., Stroganov, P., Chia, C., Burek, M., Riedinger, R., *et al.* An integrated nanophotonic quantum register based on silicon-vacancy spins in diamond. *Physical Review B* **100**, 165428 (2019).

41. Trusheim, M. E., Pingault, B., Wan, N. H., Gündoğan, M., De Santis, L., Debroux, R., Gangloff, D., Purser, C., Chen, K. C., Walsh, M., *et al.* Transform-limited photons from a coherent tin-vacancy spin in diamond. *Phys. Rev. Lett.* **124**, 023602 (2020).
42. Knaut, C. M., Suleymanzade, A., Wei, Y.-C., Assumpcao, D. R., Stas, P.-J., Huan, Y. Q., Machielse, B., Knall, E. N., Sutula, M., Baranes, G., *et al.* Entanglement of nanophotonic quantum memory nodes in a telecom network. *Nature* **629**, 573–578 (2024).
43. Wei, Y.-C., Stas, P.-J., Suleymanzade, A., Baranes, G., Machado, F., Huan, Y. Q., Knaut, C. M., Ding, S. W., Merz, M., Knall, E. N., *et al.* Universal distributed blind quantum computing with solid-state qubits. *Science* **388**, 509–513 (2025).
44. Stramma, A. M. *The tin-vacancy centre in diamond: a coherent spin-photon interface for quantum network nodes* PhD thesis (2024).
45. Görlitz, J., Herrmann, D., Thiering, G., Fuchs, P., Gandil, M., Iwasaki, T., Taniguchi, T., Kieschnick, M., Meijer, J., Hatano, M., Gali, A. & Becher, C. Spectroscopic Investigations of Negatively Charged Tin-Vacancy Centres in Diamond. *New Journal of Physics* **22**, 013048 (2020).
46. Trusheim, M. E. *et al.* Transform-Limited Photons From a Coherent Tin-Vacancy Spin in Diamond. *Phys. Rev. Lett.* **124**, 023602 (2020).
47. Debroux, R., Michaels, C. P., Purser, C. M., Wan, N., Trusheim, M. E., Arjona Martínez, J., Parker, R. A., Stramma, A. M., Chen, K. C., De Santis, L., *et al.* Quantum control of the tin-vacancy spin qubit in diamond. *Physical Review X* **11**, 041041 (2021).
48. Rosenthal, E. I., Anderson, C. P., Kleidermacher, H. C., Stein, A. J., Lee, H., Grzesik, J., Scuri, G., Rugar, A. E., Riedel, D., Aghaeimeibodi, S., *et al.* Microwave spin control of a tin-vacancy qubit in diamond. *Physical Review X* **13**, 031022 (2023).
49. Rosenthal, E. I., Biswas, S., Scuri, G., Lee, H., Stein, A. J., Kleidermacher, H. C., Grzesik, J., Rugar, A. E., Aghaeimeibodi, S., Riedel, D., *et al.* Single-Shot Readout and Weak Measurement of a Tin-Vacancy Qubit in Diamond. *Physical Review X* **14**, 041008 (2024).
50. Guo, X., Stramma, A. M., Li, Z., Roth, W. G., Huang, B., Jin, Y., Parker, R. A., Arjona Martínez, J., Shofer, N., Michaels, C. P., *et al.* Microwave-based quantum control and coherence protection of tin-vacancy spin qubits in a strain-tuned diamond-membrane heterostructure. *Physical Review X* **13**, 041037 (2023).
51. Karatzakis, I., Resch, J., Schrodin, M., Fuchs, P., Kieschnick, M., Heupel, J., Kussi, L., Sürgers, C., Popov, C., Meijer, J., *et al.* Microwave control of the tin-vacancy spin qubit in diamond with a superconducting waveguide. *Physical Review X* **14**, 031036 (2024).
52. Beukers, H. K., Waas, C., Pasini, M., Van Ommen, H. B., Ademi, Z., Iuliano, M., Codreanu, N., Brevoord, J. M., Turan, T., Taminiau, T. H., *et al.* Control of solid-state nuclear spin qubits using an electron spin-1/2. *Physical Review X* **15**, 021011 (2025).

53. Tchernij, S. D., Herzig, T., Forneris, J., Küpper, J., Pezzagna, S., Traina, P., Moreva, E., Degiovanni, I. P., Brida, G., Skukan, N., Genovese, M., Jakšić, M., Meijer, J. & Olivero, P. Single-Photon-Emitting Optical Centers in Diamond Fabricated upon Sn Implantation. *ACS Photonics* **4**, 2580–2586 (2017).
54. Iwasaki, T., Miyamoto, Y., Taniguchi, T., Siyushev, P., Metsch, M. H., Jelezko, F. & Hatano, M. Tin-Vacancy Quantum Emitters in Diamond. *Phys. Rev. Lett.* **119**, 253601 (2017).
55. Rugar, A. E., Dory, C., Aghaeimeibodi, S., Lu, H., Sun, S., Mishra, S. D., Shen, Z.-X., Melosh, N. A. & Vučković, J. Narrow-Linewidth Tin-Vacancy Centers in a Diamond Waveguide. *ACS Photonics* **7**, 2356–2361 (2020).
56. Pasini, M., Codreanu, N., Turan, T., Riera Moral, A., Primavera, C. F., De Santis, L., Beukers, H. K., Brevoord, J. M., Waas, C., Borregaard, J., *et al.* Nonlinear quantum photonics with a tin-vacancy center coupled to a one-dimensional diamond waveguide. *Phys. Rev. Lett.* **133**, 023603 (2024).
57. Kuruma, K., Pingault, B., Chia, C., Renaud, D., Hoffmann, P., Iwamoto, S., Ronning, C. & Lončar, M. Coupling of a Single Tin-Vacancy Center to a Photonic Crystal Cavity in Diamond. *Applied Physics Letters* **118**, 230601 (2021).
58. Rugar, A. E., Aghaeimeibodi, S., Riedel, D., Dory, C., Lu, H., McQuade, P. J., Shen, Z.-X., Melosh, N. A. & Vučković, J. Quantum photonic interface for tin-vacancy centers in diamond. *Physical Review X* **11**, 031021 (2021).
59. Chen, K. C., Christen, I., Raniwala, H., Colangelo, M., De Santis, L., Shtyrkova, K., Starling, D., Murphy, R., Li, L., Berggren, K., *et al.* A scalable cavity-based spin-photon interface in a photonic integrated circuit. *Optica Quantum* **2**, 124–132 (2024).
60. Pompili, M., Hermans, S. L. N., Baier, S., Beukers, H. K. C., Humphreys, P. C., Schouten, R. N., Vermeulen, R. F. L., Tiggelman, M. J., Dos Santos Martins, L., Dirkse, B., Wehner, S. & Hanson, R. Realization of a Multinode Quantum Network of Remote Solid-State Qubits. *Science* **372**, 259–264 (2021).
61. Hermans, S. L. N., Pompili, M., Beukers, H. K. C., Baier, S., Borregaard, J. & Hanson, R. Qubit Teleportation between Non-Neighbouring Nodes in a Quantum Network. *Nature* **605**, 663–668 (2022).
62. Wang, P., Kazak, L., Senkalla, K., Siyushev, P., Abe, R., Taniguchi, T., Onoda, S., Kato, H., Makino, T., Hatano, M., *et al.* Transform-limited photon emission from a lead-vacancy center in diamond above 10 K. *Phys. Rev. Lett.* **132**, 073601 (2024).
63. Abe, R., Chen, Y., Wang, P., Taniguchi, T., Miyakawa, M., Onoda, S., Hatano, M. & Iwasaki, T. Narrow Inhomogeneous Distribution and Charge State Stabilization of Lead-Vacancy Centers in Diamond. *Advanced Functional Materials*, e12412 (2025).
64. Pasini, M. *Nanophotonics with Diamond Color Centers: Quantum Optics and Entanglement Protocols* PhD thesis (Delft University of Technology, 2024).
65. Thiering, G. & Gali, A. Ab initio magneto-optical spectrum of group-IV vacancy color centers in diamond. *Physical Review X* **8**, 021063 (2018).

66. Brevoord, J. M., Wienhoven, L. G., Codreanu, N., Ishiguro, T., van Leeuwen, E., Iuliano, M., De Santis, L., Waas, C., Beukers, H. K., Turan, T., *et al.* Large-Range Tuning and Stabilization of the Optical Transition of Diamond Tin-Vacancy Centers by In-Situ Strain Control. *Appl. Phys. Lett.* **126** (2025).
67. Wan, N. H., Lu, T.-J., Chen, K. C., Walsh, M. P., Trusheim, M. E., De Santis, L., Bersin, E. A., Harris, I. B., Mouradian, S. L., Christen, I. R., *et al.* Large-scale integration of artificial atoms in hybrid photonic circuits. *Nature* **583**, 226–231 (2020).
68. Li, L., Santis, L. D., Harris, I. B., Chen, K. C., Gao, Y., Christen, I., Choi, H., Trusheim, M., Song, Y., Errando-Herranz, C., *et al.* Heterogeneous integration of spin–photon interfaces with a CMOS platform. *Nature* **630**, 70–76 (2024).
69. Reiserer, A. & Rempe, G. Cavity-based quantum networks with single atoms and optical photons. *Reviews of Modern Physics* **87**, 1379–1418 (2015).
70. Janitz, E., Bhaskar, M. K. & Childress, L. Cavity quantum electrodynamics with color centers in diamond. *Optica* **7**, 1232–1252 (2020).
71. González-Tudela, A., Reiserer, A., García-Ripoll, J. J. & García-Vidal, F. J. Light–matter interactions in quantum nanophotonic devices. *Nature Reviews Physics* **6**, 166–179 (2024).
72. Borregaard, J., Sørensen, A. S. & Lodahl, P. Quantum networks with deterministic spin–photon interfaces. *Advanced Quantum Technologies* **2**, 1800091 (2019).
73. Knall, E. N., Knaut, C. M., Bekenstein, R., Assumpcao, D. R., Stroganov, P. L., Gong, W., Huan, Y. Q., Stas, P.-J., Machielse, B., Chalupnik, M., *et al.* Efficient source of shaped single photons based on an integrated diamond nanophotonic system. *Phys. Rev. Lett.* **129**, 053603 (2022).
74. Schröder, T., Trusheim, M. E., Walsh, M., Li, L., Zheng, J., Schukraft, M., Sipahigil, A., Evans, R. E., Sukachev, D. D., Nguyen, C. T., *et al.* Scalable focused ion beam creation of nearly lifetime-limited single quantum emitters in diamond nanostructures. *Nature communications* **8**, 1–7 (2017).
75. Nguyen, C., Sukachev, D., Bhaskar, M., Machielse, B., Levonian, D., Knall, E., Stroganov, P., Riedinger, R., Park, H., Lončar, M., *et al.* Quantum network nodes based on diamond qubits with an efficient nanophotonic interface. *Phys. Rev. Lett.* **123**, 183602 (2019).
76. Zaitsev, A. M. *Optical properties of diamond: a data handbook* (Springer Science & Business Media, 2013).
77. Shandilya, P. K., Flågan, S., Carvalho, N. C., Zohari, E., Kavatamane, V. K., Losby, J. E. & Barclay, P. E. Diamond integrated quantum nanophotonics: spins, photons and phonons. *Journal of Lightwave Technology* **40**, 7538–7571 (2022).
78. Paoletti, A. & Tucciarone, A. *The physics of diamond* (Ios Press, 1997).
79. Mildren, R. P. Intrinsic optical properties of diamond. *Optical engineering of diamond*, 1–34 (2013).
80. Field, J. E. *The properties of diamond* ISBN: 0122553500 (Academic Press, 1979).

81. Ashcroft, N. W. & Mermin, N. D. *Solid state physics* ISBN: 0-03-083993-9 (Saunders College Publishing, 1976).
82. Pierson, H. O. *Handbook of carbon, graphite, diamonds and fullerenes: processing, properties and applications* (William Andrew, 2012).
83. Miller, J. B. & Brown, D. W. Photochemical modification of diamond surfaces. *Langmuir* **12**, 5809–5817 (1996).
84. Mi, S., Kiss, M., Graziosi, T. & Quack, N. Integrated photonic devices in single crystal diamond. *Journal of Physics: Photonics* **2**, 042001 (2020).
85. Patel, A. & Ramanathan, S. Etch pits on diamond surfaces. *Philosophical Magazine* **7**, 1305–1314 (1962).
86. Tolansky, S., Miller, R. & Punglia, J. Changes in orientation of etch pits produced on the cubic faces of diamond. *Philosophical Magazine* **26**, 1275–1280 (1972).
87. Nojiri, K. *Dry etching technology for semiconductors* (Springer, 2015).
88. Evans, T. & Sauter, D. H. Etching of diamond surfaces with gases. *Philosophical Magazine* **6**, 429–440 (1961).
89. Sandhu, G. & Chu, W. Reactive ion etching of diamond. *Applied physics letters* **55**, 437–438 (1989).
90. Janitz, E., Herb, K., Völker, L. A., Huxter, W. S., Degen, C. L. & Abendroth, J. M. Diamond surface engineering for molecular sensing with nitrogen–vacancy centers. *Journal of Materials Chemistry C* **10**, 13533–13569 (2022).
91. Wan, N. H., Lu, T.-J., Chen, K. C., Walsh, M. P., Trusheim, M. E., De Santis, L., Bersin, E. A., Harris, I. B., Mouradian, S. L., Christen, I. R., Bielejec, E. S. & Englund, D. Large-Scale Integration of Artificial Atoms in Hybrid Photonic Circuits. *Nature* **583**, 226–231 (2020).
92. Schröder, T., Mouradian, S. L., Zheng, J., Trusheim, M. E., Walsh, M., Chen, E. H., Li, L., Bayn, I. & Englund, D. Quantum nanophotonics in diamond. *JOSA B* **33**, B65–B83 (2016).
93. Toros, A., Kiss, M., Graziosi, T., Sattari, H., Gallo, P. & Quack, N. Precision micro-mechanical components in single crystal diamond by deep reactive ion etching. *Microsystems & nanoengineering* **4**, 12 (2018).
94. Guo, X., Deegan, N., Karsch, J. C., Li, Z., Liu, T., Shreiner, R., Butcher, A., Awschalom, D. D., Heremans, F. J. & High, A. A. Tunable and transferable diamond membranes for integrated quantum technologies. *Nano Letters* **21**, 10392–10399 (2021).
95. Parikh, N., Hunn, J., McGucken, E., Swanson, M., White, C., Rudder, R., Malta, D., Posthill, J. & Markunas, R. Single-crystal diamond plate liftoff achieved by ion implantation and subsequent annealing. *Applied physics letters* **61**, 3124–3126 (1992).
96. Fairchild, B. A., Olivero, P., Rubanov, S., Greentree, A. D., Waldermann, F., Taylor, R. A., Walmsley, I., Smith, J. M., Huntington, S., Gibson, B. C., *et al.* Fabrication of ultrathin single-crystal diamond membranes. *Advanced Materials* **20**, 4793–4798 (2008).

97. Gaathon, O., Hodges, J., Chen, E., Li, L., Bakhru, S., Bakhru, H., Englund, D. & Osgood Jr, R. Planar fabrication of arrays of ion-exfoliated single-crystal-diamond membranes with nitrogen-vacancy color centers. *Optical Materials* **35**, 361–365 (2013).
98. Lee, J. C., Bracher, D. O., Cui, S., Ohno, K., McLellan, C. A., Zhang, X., Andrich, P., Alemán, B., Russell, K. J., Magyar, A. P., *et al.* Deterministic coupling of delta-doped nitrogen vacancy centers to a nanobeam photonic crystal cavity. *Applied Physics Letters* **105** (2014).
99. Lee, J. C., Magyar, A. P., Bracher, D. O., Aharonovich, I. & Hu, E. L. Fabrication of thin diamond membranes for photonic applications. *Diamond and related materials* **33**, 45–48 (2013).
100. Piracha, A. H., Ganesan, K., Lau, D. W., Stacey, A., McGuinness, L. P., Tomljenovic-Hanic, S. & Prawer, S. Scalable fabrication of high-quality, ultra-thin single crystal diamond membrane windows. *Nanoscale* **8**, 6860–6865 (2016).
101. Piracha, A. H., Rath, P., Ganesan, K., Kühn, S., Pernice, W. H. & Prawer, S. Scalable fabrication of integrated nanophotonic circuits on arrays of thin single crystal diamond membrane windows. *Nano letters* **16**, 3341–3347 (2016).
102. Guo, X., Xie, M., Addhya, A., Linder, A., Zvi, U., Wang, S., Yu, X., Deshmukh, T. D., Liu, Y., Hammock, I. N., *et al.* Direct-bonded diamond membranes for heterogeneous quantum and electronic technologies. *Nature communications* **15**, 8788 (2024).
103. Ding, S. W., Haas, M., Guo, X., Kuruma, K., Jin, C., Li, Z., Awschalom, D. D., Deegan, N., Heremans, F. J., High, A. A., *et al.* High-Q cavity interface for color centers in thin film diamond. *nature communications* **15**, 6358 (2024).
104. Basso, L., Titze, M., Henshaw, J., Kehayias, P., Cong, R., Ziabari, M. S., Lu, T.-M., Lilly, M. P. & Mounce, A. M. Fabrication of thin diamond membranes by Ne⁺ implantation. *Giant* **17**, 100238 (2024).
105. Ding, S. W., Jin, C., Kuruma, K., Guo, X., Haas, M., Korzh, B., Beyer, A., Shaw, M. D., Sinclair, N., Awschalom, D. D., *et al.* Purcell-enhanced emissions from diamond color centers in slow light photonic crystal waveguides. *Nano Letters* (2025).
106. Riedrich-Moller, J., Arend, C., Pauly, C., Mucklich, F., Fischer, M., Gsell, S., Schreck, M. & Becher, C. Deterministic coupling of a single silicon-vacancy color center to a photonic crystal cavity in diamond. *Nano letters* **14**, 5281–5287 (2014).
107. Li, L., Schröder, T., Chen, E. H., Walsh, M., Bayn, I., Goldstein, J., Gaathon, O., Trusheim, M. E., Lu, M., Mower, J., *et al.* Coherent spin control of a nanocavity-enhanced qubit in diamond. *Nature communications* **6**, 6173 (2015).
108. Cady, J. V., Michel, O., Lee, K. W., Patel, R. N., Sarabalis, C. J., Safavi-Naeini, A. H. & Jayich, A. C. B. Diamond optomechanical crystals with embedded nitrogen-vacancy centers. *Quantum Science and Technology* **4**, 024009 (2019).
109. Heupel, J., Pallmann, M., Körber, J., Merz, R., Kopnarski, M., Stöhr, R., Reithmaier, J. P., Hunger, D. & Popov, C. Fabrication and characterization of single-crystal diamond membranes for quantum photonics with tunable microcavities. *Micromachines* **11**, 1080 (2020).

110. Appel, P. *Scanning nanomagnetometry: Probing magnetism with single spins in diamond* PhD thesis (University of Basel, 2017).
111. Challier, M., Sonusen, S., Barfuss, A., Rohner, D., Riedel, D., Koelbl, J., Ganzhorn, M., Appel, P., Maletinsky, P. & Neu, E. Advanced fabrication of single-crystal diamond membranes for quantum technologies. *Micromachines* **9**, 148 (2018).
112. Bayn, I., Meyler, B., Salzman, J. & Kalish, R. Triangular nanobeam photonic cavities in single-crystal diamond. *New Journal of Physics* **13**, 025018 (2011).
113. Burek, M. J., De Leon, N. P., Shields, B. J., Hausmann, B. J., Chu, Y., Quan, Q., Zibrov, A. S., Park, H., Lukin, M. D. & Loncar, M. Free-standing mechanical and photonic nanostructures in single-crystal diamond. *Nano letters* **12**, 6084–6089 (2012).
114. Atikian, H. A., Latawiec, P., Burek, M. J., Sohn, Y.-I., Meesala, S., Gravel, N., Kouki, A. B. & Lončar, M. Freestanding nanostructures via reactive ion beam angled etching. *APL Photonics* **2** (2017).
115. Chia, C., Machielse, B., Shams-Ansari, A. & Lončar, M. Development of hard masks for reactive ion beam angled etching of diamond. *Optics Express* **30**, 14189–14201 (2022).
116. Sipahigil, A., Evans, R. E., Sukachev, D. D., Burek, M. J., Borregaard, J., Bhaskar, M. K., Nguyen, C. T., Pacheco, J. L., Atikian, H. A., Meuwly, C., *et al.* An integrated diamond nanophotonics platform for quantum-optical networks. *Science* **354**, 847–850 (2016).
117. Evans, R. E., Bhaskar, M. K., Sukachev, D. D., Nguyen, C. T., Sipahigil, A., Burek, M. J., Machielse, B., Zhang, G. H., Zibrov, A. S., Bielejec, E., *et al.* Photon-mediated interactions between quantum emitters in a diamond nanocavity. *Science* **362**, 662–665 (2018).
118. Bhaskar, M. K., Riedinger, R., Machielse, B., Levonian, D. S., Nguyen, C. T., Knall, E. N., Park, H., Englund, D., Lončar, M., Sukachev, D. D. & Lukin, M. D. Experimental Demonstration of Memory-Enhanced Quantum Communication. *Nature* **580**, 60–64 (2020).
119. Khanaliloo, B., Mitchell, M., Hryciw, A. C. & Barclay, P. E. High-Q/V Monolithic Diamond Microdisks Fabricated with Quasi-isotropic Etching. *Nano Letters* **15**, 5131–5136 (2015).
120. Shaw, K. A., Zhang, Z. L. & MacDonald, N. C. SCREAM I: a single mask, single-crystal silicon, reactive ion etching process for microelectromechanical structures. *Sensors and Actuators A: Physical* **40**, 63–70 (1994).
121. Rugar, A. E., Aghaeimeibodi, S., Riedel, D., Dory, C., Lu, H., McQuade, P. J., Shen, Z.-X., Melosh, N. A. & Vučković, J. Quantum Photonic Interface for Tin-Vacancy Centers in Diamond. *Physical Review X* **11**, 031021 (2021).
122. Wan, N. H., Mouradian, S. & Englund, D. Two-dimensional photonic crystal slab nanocavities on bulk single-crystal diamond. *Applied Physics Letters* **112** (2018).
123. Joe, G., Haas, M., Kuruma, K., Jin, C., Kang, D. D., Ding, S., Chia, C., Warner, H., Pingault, B., Machielse, B., *et al.* Observation of the acoustic Purcell effect with a color-center and a nanomechanical resonator. *arXiv preprint arXiv:2503.09946* (2025).

2

FABRICATION OF DIAMOND NANOPHOTONIC STRUCTURES FOR QUANTUM NETWORKS APPLICATIONS

Future quantum networks require end nodes that combine excellent qubit control and coherence with efficient spin-photon interfaces. Further scaling of such systems requires higher entanglement rates combined with excellent spin-qubit control and coherence with efficient spin-photon interfaces. Diamond Tin-Vacancy (SnV) centers have recently emerged as prime node candidates thanks to their long spin coherence times and strong optical coherence even when integrated in photonic nanostructures. Such integration enables engineering of quantum light matter interactions for efficient spin-photon interfaces. Fabrication of free-standing diamond nanostructures is in itself a challenge. Here we present the quasi-isotropic etch (QIE) undercut-based fabrication process flow, where we show our development and optimization of two variants of the process, with which we achieve successful fabrication of free-standing nanophotonic structures, such as one-dimensional waveguides (operating at the SnV center zero-phonon line (ZPL) emission) and photonic crystal cavities (PCCs) (operating both at the telecom and SnV center ZPL emission wavelengths). The successful integration of quantum emitters in nanophotonic structures opens the path toward integration in photonic circuitry.

2.1 INTRODUCTION

Diamond crystallographic etch was demonstrated in dry reactive ion etch plasma under specific etch conditions for the first time by the authors in Ref. [1]. High etch selectivity along crystallographic planes, combined with the principles of the single-crystal reactive ion etching and metallization (SCREAM) process [2] have proved excellent ingredients for the development of the diamond quasi-isotropic undercut fabrication process. This has enabled fabrication of high quality nanophotonic devices in diamond [1, 3–11], operating in both the visible and the telecom regimes, and demonstrating the robustness and versatility of the proposed process.

In this chapter, we present the methods and fabrication protocols we developed, aimed at systematic and reliable fabrication of suspended diamond nanophotonic devices for quantum network experiments. In this work, we develop two variants of the Quasi-Isotropic Etch (QIE) based fabrication process. First, we show the 65 °C QIE-based process variant, used for the successful fabrication of free-standing nanophotonic structures, such as one-dimensional waveguides (operating at the SnV center zero-phonon line (ZPL) emission) and photonic crystal cavities (PCCs) (operating at the telecom wavelength). Second, we show the development of the 250 °C QIE-based process variant, demonstrating successful fabrication of one-dimensional PCCs operating at the SnV center ZPL emission.

In Section 2.2 we introduce the general steps of QIE-based fabrication process flow, with a brief overview of the crystallographic-dependent etch mechanism. Section 2.3 enumerates and discusses the requirements of the main fabrication parameters aimed at developing a robust process flow. Section 2.4 presents and elaborates on the main nanophotonic device designs and the overall chiplet layout variants developed, calibrated, and tailored for the two QIE-based variants. In Section 2.5 we present and discuss the baseline design of QIE-based process, elaborating on the process development and parameters, as well as the complementary Si / Si_xN_y etch tests protocol, necessary for monitoring the main fabrication process. Section 2.6 presents the results of the 65 °C QIE-based process variant performance. This process variant shows the successful fabrication of free-hanging one-dimensional nanophotonic waveguides (results presented in Chapter 4) and PCCs (operating at the telecom wavelength).

Next, in Section 2.7 we elaborate on the methods aimed at the development and optimization of the 250 °C QIE-based process variant. Here, we focus primarily on the development of the ICP-RIE quasi-isotropic etch recipe at 250 °C table temperature (methods in Section 2.7.1) and the high-fidelity device geometry layout transfer pattern (methods in Sections 2.7.2 and 2.7.3).

Finally, we conclude with presenting the successful fabrication of one-dimensional free-hanging photonic crystal cavity devices operating at the SnV center ZPL emission in the QIE-based variant 2.8 achieving high control over the process parameters, as well as evaluating the performance of the newly developed 250 °C.

2.2 QIE-BASED FABRICATION PROCESS

2.2.1 GENERAL FABRICATION STEPS

Quasi-Isotropic Etch (QIE) based fabrication process is an example of a diamond nanophotonic fabrication which foresees starting from a bulk diamond substrate. In the context of the development and optimization of this fabrication process in Kavli Nanolab Delft, we have converged to two variants of the QIE-based process, both of which rely on the main fabrication steps schematically illustrated in Figure 2.1.

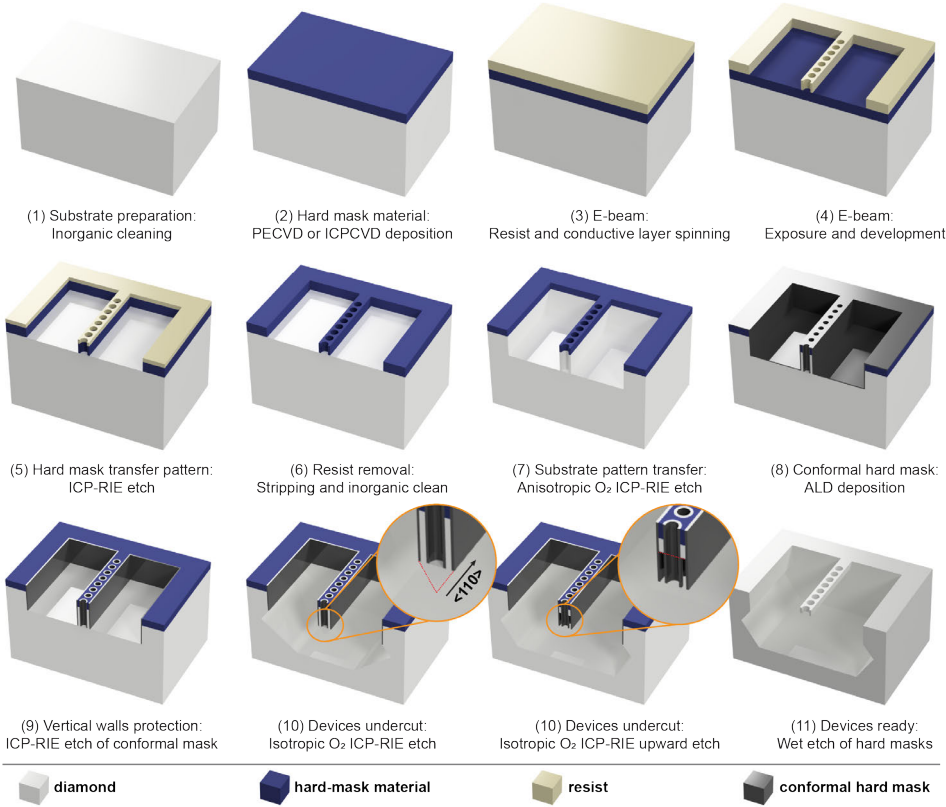


Figure 2.1: **Quasi-isotropic undercut ICP-RIE etch based fabrication process: Schematics of the fabrication steps** Fabrication process flow variant adapted from [1, 5–7, 12, 13], developed in Kavli Nanolab Delft. The optional second oxygen anisotropic etch between steps (9) and (10), which allows for faster undercut etch of nanophotonic devices is omitted here [1, 12].

The general process steps are schematically illustrated in Figure 2.1 and can be roughly divided into three process phases: I. Design transfer pattern (steps (1) to (7)): nanophotonic design pattern is electron-beam (e-beam) written onto a positive resist, followed by inductively coupled plasma reactive ion etch pattern transfer into the hard mask material and downstream into the diamond substrate; II. Vertical sidewalls passivation (steps (8) to (9)): patterned vertical sidewall are conformally coated with a second hard mask material,

followed by clearance of the former from the horizontal sample plane to open plasma access to diamond substrate; III. Quasi-isotropic undercut etch (steps (10)): undercut of patterned devices, resulting in free-hanging structures, followed by upward etching to reach the design target thickness. Lastly, hard mask materials are wet etched (step (11))

The core of such a fabrication process is the method with which the devices are eventually undercut, such that fully suspended, free-hanging devices are obtained. For this purpose, a particular oxygen-based chemistry plasma regime is utilized: reactive ion etching (RIE) at a highly inductively coupled plasma in combination with a high substrate temperature has been shown to produce crystallographic-dependent etching of diamond [1]. The authors of Ref. [1] have successfully demonstrated that under zero substrate Radio Frequency (RF) power, dense O_2 plasma with 3000 W Inductively Coupled Plasma (ICP) power and 250 °C table temperature, diamond substrates exhibit crystallographic-dependent etch rate, hence a quasi-isotropic etch.

The QIE-based fabrication process is inspired by the single-crystal reactive ion etching and metallization (SCREAM) process, developed in the 1990s [2]. The SCREAM process emerged as a breakthrough in bulk micromachining for fabricating high-aspect-ratio single-crystal silicon beams. The development of this process was driven in the context of microelectromechanical systems (MEMS), which required high-aspect ratio structures to enhance performance in applications such as motors, gears, and accelerometers. In addition to addressing the challenge of creating high-aspect-ratio features, the SCREAM process enabled the effective undercutting of silicon MEMS structures through dry etching methods, using only one lithographic step and conventional RIE processes. This advancement overcame the limitations of wet chemical etching, which often proved problematic to achieve precision at sub-micrometer scales, as successfully shown in Ref. [2].

The backbone concepts underlying the SCREAM process, combined with the crystal-dependent etch rate of diamond substrates, have proved to be excellent ingredients for the development of the diamond quasi-isotropic undercut fabrication process.

2.2.2 CRYSTALLOGRAPHIC DIAMOND ETCH

RIE is mainly characterized by two phenomena occurring during the exposure of a material to a certain plasma chemistry. Specifically, etching of the substrate occurs as a result of chemical susceptibility of the substrate to free radicals of the plasma and physical ion bombardment. The major factors controlling the etch mechanism include the ion flux impinging the surface, kinetic energy of the impinging ions, and the energy barrier for chemical reactions to take place. Crystallographic-dependent etching in diamond has been thoroughly investigated by the authors in Ref. [14]. In this study, the etching principle underlying the crystal-dependent etching in diamond is presented, where the authors find that crystallographic etching in diamond can be observed by finely tuning the plasma regime between the purely chemical region and purely anisotropic region. A high etch selectivity along crystallographic planes emerges only when the ion energy is tuned to the chemical energy barrier and the chemical reaction limits the etching process.

By fine-tuning the kinetic energy of the impinging plasma ions, a crystallographic-dependent diamond etch rate can be observed. Authors of Ref. [14] find this energy barrier threshold to be 60 eV. The kinetic energy of the impinging plasma ions can be controlled by controlling the RF power of the plasma itself, thus, for RF powers lower than ~ 40 W

(corresponding to the chemical energy barrier threshold), crystallographic etching was shown to be achieved. The degree of anisotropy achieved (i.e. the exposed crystallographic $\{hkl\}$ Miller indices planes) is proportional to the applied RF power. Depending on the alignment orientation of the patterned features, combined with the value of the RF bias power, different $\{hkl\}$ Miller indices crystallographic planes can be revealed upon quasi-isotropic etch. In Xie et al. [14], linear edges aligned with $\langle 110 \rangle$ direction show a decreasing angle between faceted surfaces etched at different bias power (Table 1 in Xie et al. [14]) for increasing RF power, with corresponding $\{hkl\}$ planes revealed, respectively from $\{111\}$ (0 W RF power) to $\{331\}$ (40 W RF power). Therefore, in principle, crystal planes with different Miller indices can be revealed by varying the substrate power. The resulting shapes of etched features strongly depend on the alignment of the edges of the mask, combined with the RF power of the plasma.

Given $\{001\}$ surface exposed diamond substrates, $\{111\}$ planes are exposed with zero RF power and patterned structures aligned with $\langle 110 \rangle$ crystallographic direction, depending on the width of the window exposed to plasma between the linear edges, V-shaped grooves can be obtained. Considering, for example, the aligned 1D patterned waveguide $\langle 110 \rangle$ aligned (relevant in the context of this work), positioned in the middle of two adjacent rectangular patterned openings, with the advancement of the etch time, $\{111\}$ planes in a V-shaped groove configuration will present. Advancing the etch process by prolonging the etch time, V shapes from the opposite longitudinal side of the waveguide will recess in the vertical $\langle 001 \rangle$ direction, causing eventually $\{111\}$ planes to converge, resulting in a full undercut of the waveguide device. This etch mechanism is shown in Ref. [14] for both $\langle 110 \rangle$ and $\langle 110 \rangle$ mask aligned edges, as well as in previous work in Ref. [1] for round microdisk resonators.

2.3 QIE-BASED PROCESS REQUIREMENTS

In this Section, we elaborate on the requirements of each of the three phases foreseen by the QIE-based fabrication process.

I. TRANSFER PATTERN AND HARD MASK MATERIAL

This phase comprises the fabrication steps aimed at the successful top-down transfer of the pattern from the intended device geometry computer-aided design (CAD) of the nanophotonic devices into the bulk diamond substrate. This phase is composed by a two-step pattern transfer, where the CAD design is first transferred into an e-beam resist via electron beam lithography (e-beam), followed by a highly anisotropic dry ICP-RIE step which transfers the intended design into a hard mask material. The design features are then transferred from the patterned hard mask material to the bulk diamond material through a top-down O_2 anisotropic plasma etch. We opt for a 2-step transfer pattern as it offers the advantages of versatility in the high resolution transfer pattern onto the electron beam lithography resist, combined with the high resistivity of the patterned hard mask material, thus satisfying the requirements listed below. In order to reliably and successfully execute the aforementioned steps, a series of requirements over the process parameters must be satisfied, which, in turn translate in the below listed:

Requirements

1. **Robustness of the mask to overall QIE-based process:** the first primary requirement for a patterned mask, is that it must withstand with minimal etch rate and erosion all the sequential etch steps foreseen by the overall QIE process itself. This fundamental requirement translates into high selectivity for all involved ICP-RIE plasma chemistries foreseen by the QIE process.
2. **Versatility and high resolution pattern transfer:** highest resolution, combined with high accuracy pattern transfer, e.g. e-beam, are desirable, allowing to achieve resolution compatible with the fabrication of nanophotonic structures tailored to SnV center emission wavelength. Current state-of-the-art patterning tools with resolutions on the order of tens of nanometers include electron beam (E-beam) lithography, commonly available, or less than tens of nanometers such as extreme ultraviolet (EUV) lithography, not commonly available. E-beam lithography is a powerful tool and, therefore, widely adopted in the research community. Generally, in the development phase, e-beam lithography offers the advantage of rapid customized patterning, offering flexibility over design of chiplets and layouts, whereas EUV exposure requires ad-hoc preparation of exposure mask.
3. **Low vertical sidewall surface roughness:** sidewall surface roughness of the patterned hard mask features is directly transferred to the surface roughness of the etched nanophotonic devices pattern in the diamond substrate. Low surface roughness of vertical (and horizontal) nanophotonic devices is desirable, as this limits propagation scattering losses. This is a fundamental requirement for efficient guiding and in-coupling exciting laser source and out-coupling and extraction of the light emitted by the integrated into the photonic structure color centers. For resonant cavities, surface roughness is a well-known detrimental factor, lowering the quality factor of such, therefore limiting it.
4. **Good surface properties, e.g. high adhesion to the substrate:** low stress of the hard mask material limits undesired effects such as contraction of the deposited film upon higher thicknesses of the deposited material. High stress in the film may cause delamination or buckling of the film, which can cause poor adhesion to the substrate, which is an undesired effect. The mask material should also have high surface adhesion, such that a good adhesion of the e-beam resist is guaranteed.
5. **Easy to remove at end of process:** a high selective wet etch rate of the mask material is desired, such that an e.g. wet or vapor inorganic clean is enabled.
6. **Compatibility of material with processing and inspection cleanroom equipment:** the mask material should be compatible with the overall equipment of the fabrication process foreseen by subsequent QIE fabrication steps. This is a practical requirement which allows for both parallelization of the process (reducing processing overall fabrication time) and compatibility of the fabrication process with available cleanroom equipment (avoiding cross-contamination of the sample with co-living different fabrication processes in the cleanroom).

The combination of the first two requirements listed above, generally determine whether the transfer of the pattern takes place in a one-step pattern transfer (typically soft e-beam resists or flowable hydrogen silsesquioxane (HSQ or FOX series)) or in a two-step pattern transfer (typically a combination of soft e-beam resists with deposited thin film hard mask materials).

In the general context of QIE-based variants fabrication processes, the most common approach is a two-step transfer pattern. The first advantage is that high-resolution e-beam resists can be exploited to pattern tens of nanometer sized features: this represents a stringent requirement criterion when considering visible range nanophotonic structures. Second advantage of the two-step transfer pattern is that regardless of the selectivity of the e-beam resist, the hard mask material choice is relatively independent of the latter. Thus, a material with the most adequate process parameters can be chosen regardless of the chosen e-beam patterning resist.

In a two-step transfer pattern approach of the intended design, thus, one should prioritize a high resolution e-beam resist, in combination with a high selectivity hard mask material. While the first step should consider a careful calibration of e-beam exposure set of parameters in order to allow for highest possible accuracy pattern transfer onto the resist, the next critical step is to transfer such pattern into the hard mask material. Next, the successfully e-beam developed resist pattern is transferred into a pre-deposited hard mask material characterized by high selectivity to both quasi-isotropic and anisotropic diamond O₂ ICP-RIE plasma chemistry, as well as to the ICP-RIE plasma chemistry necessary in the vertical sidewall passivation phase II.

The one-step transfer pattern has been proven successful as well in the case of micrometer-sized dimension nanophotonic devices, such as telecom wavelength operating range optomechanical crystal cavities. The work of Ref. [15] explores in detail the possibility of one-step pattern transfer comparing different mask materials performance both with the QIE-based fabrication process and reactive ion beam angled etching (RIBAE). In this work, the HSQ resist in combination with the alumina adhesion layer as the hard mask has demonstrated the best performance for the fabrication of 1550 nm PCCs with RIBAE process[15]. Same approach transfer pattern has been demonstrated successful in the context of QIE-based fabrication of 1550 nm optomechanical crystals, showing high optical quality factor devices in Ref. [16]. However, authors of Ref. [16] report on switching to two-step transfer pattern for nanodevices of smaller dimensions such as phononic crystals (PnC) slabs due to requirements on higher resolution. The developed QIE-based fabrication processes in the research community typically rely on two-step transfer pattern, as it generally satisfy the above listed requirements alongside the listed advantages.

II. VERTICAL SIDEWALLS PASSIVATION

This phase comprises the fabrication steps required to passivate and cover the vertical sidewalls of the top down etched patterned devices in the diamond substrate. For this, a fully conformal coating of the substrate is desirable, which can be achieved by Atomic Layer Deposition (ALD) deposition method. Following the conformal coating, a highly anisotropic plasma etch is required to fully etch the horizontal thin-film coated substrate, while fully preserving the vertical sidewalls coverage.

Requirements

1. **Conformal coating the diamond walls:** a uniform and high selectivity material to quasi-isotropic O_2 ICP-RIE plasma chemistry is required. This ensures minimal etch during the undercut phase of the devices. A high selectivity thin film material is preferable in order to allow for full coverage and robustness over the downstream process etch steps, such that the thickness of the film is low enough to allow for SEM transparency imaging through it. This in turn enables high contrast at the diamond interface, allowing real-time monitoring of the undercut process progress. At the same time, such material is desirable to have high adhesion to the diamond and low film stress to prevent delamination from the passivated sidewalls.
2. **High anisotropy of the clearing plasma:** the deposited thin film layer mask should be efficiently etched and fully cleared out of the diamond interface. No micromasking is preferable so that subsequent QIE plasma access to the diamond substrate is uniformly guaranteed. The ICP-RIE clearing plasma should be characterized by a high degree of anisotropy such that high top-down etch rates are ensured, along with preferably no lateral etch to prevent undesired exposure of vertical sidewalls of the patterned nanobeams to the downstream QIE steps.

QIE-based fabrication process variants typically rely on Plasma Enhanced Chemical Vapor Deposition (PECVD) of Si_xN_y , or, most commonly, ALD deposition of AlO_x . A decent conformality of PECVD deposition can be achieved for a moderate aspect ratio, although the degree of conformality is strongly dependent on the chamber deposition conditions. On the other hand, ALD is inherently conformal thanks to self-limiting surface reactions through sequential deposition cycles. This ensures precise and uniform deposited thin film layers regardless of the aspect ratio and orientation of the substrate features. Therefore, the thickness of the material on the vertical sidewalls is equal to the thickness of the material on the horizontal plane of the sample. This makes the characterization of the fabrication step (9) reliable and reproducible in simple flat-etch tests. For our process, taking into account the above considerations, we chose ALD as deposition method for vertical sidewalls passivation.

III. QUASI-ISOTROPIC UNDERCUT ETCH

This phase comprises multiple iterative steps, depending on the progression of the undercut etch process, aimed at fully undercutting and suspending the intended nanophotonic devices, followed by a QIE 'upward-etch' step with the goal of flattening the bottom surface of the suspended devices, rendering preferably rectangular cross-section of devices.

Requirements

1. **Etch rate of {111} vs. {100} crystallographic planes :** the etch rate of {111} planes is generally higher than the etch rate of {100} planes. Hence, typically a full undercut of $\langle 110 \rangle$ aligned nanophotonic devices will be achieved for $\langle 110 \rangle$ aligned patterned devices as a result of convergence of peripheral adjacent {111} planes underneath the patterned devices and recess of these in the $\langle 100 \rangle$ direction with respect to the

surface of the diamond substrate. The ICP-RIE QIE recipe parameters should be calibrated at an optimal working point such that the overall recess of the resulting bottom plane underneath the suspended devices extends to depths compatible with post-QIE fabrication, e.g. patterning of electrodes in close proximity to the suspended nanobeams. Thus, a relatively low $\langle 100 \rangle$ direction recess rate of the crystallographic planes is desirable, such that the vertical gap between devices and bulk diamond is compatible with RF and MW fields extents for efficient qubit driving.

2. **Short overall etch time:** first, the total duration of the QIE step should not exceed the total robustness lifetime of the protection top and sidewall hard mask materials; second, the total etch time should be compatible with practical operability in terms of etch duration and stability of plasma in the reactor chamber.

2.4 DESIGN: NANOPHOTONIC STRUCTURES LAYOUT

In this Section, we present and elaborate on the main nanophotonic device designs and the overall chiplet layout variants developed, calibrated and tailored for the two QIE-based variants (**65 °C QIE-based variant** and **250 °C QIE-based variant**) fabrication processes within the context of this work.

Although the principles of single device designs are the same for different operating wavelengths for both waveguides and photonic crystals, the physical geometric dimensions of such are dependent on the former. Therefore, based on the geometric dimensions of the devices, we divide the designs fabricated in this work into two categories: Section 2.4.1 presents the devices designs and layouts, which have proven compatible with the **65 °C QIE-based variant fabrication process**, while Section 2.4.2 presents the devices designs and layouts, which have proven compatible with the **250 °C QIE-based variant fabrication process**.

As mentioned in the Introduction, with the inversion symmetry of group-IV color centers comes the advantage of their resilience to noisy charge environment, hence the great advantage of integrating these color centers in nanophotonic diamond structures. The latter method of improving light-matter interaction, namely using optical cavities to enhance the interaction of a quantum system with light, is a well-studied subject [17] and mainly relies on the Purcell effect to increase the spontaneous emission rate in the strongly confined colocalized cavity mode. The former method of enhancing light-matter interaction is to use a single traveling optical mode in a waveguide [18].

In practice, the two approaches branch out into the two types of nanophotonic diamond devices hereafter presented: waveguides and photonic crystal cavities.

| | Rectangular hole-based PCC | | | | Rectangular $\langle 110 \rangle$ waveguide | |
|------------|----------------------------|-------|-----|-------|---|----------|
| Parameter | a_n | w_n | r | t_n | w_{wg} | t_{wg} |
| Value [nm] | 206 | 275 | 71 | 230 | 250 | 160 |

Table 2.1: **Zero-phonon line emission (ZPL) frequency of SnV centers compatible devices designs parameters** | Left: Unit cell parameter values used to simulate rectangular hole-based PCCs bandstructure, based on which the defect functional form from Refs. [13, 19] is implemented to obtain PCC devices, illustrated in Figure 2.3 (b) and (c); | Right: optimal waveguide parameters, maximizing the SnV center electric dipole coupling to a $\langle 110 \rangle$ oriented structure, from Refs. [18, 20], to obtain waveguide devices illustrated in Figure 2.2 (b) and Figure 2.3 (a).

Waveguide device

A waveguide is a device where the light field is confined in two dimensions and allowed to propagate in the third. The chosen geometry of the waveguide is a simple rectangular cross-section, aligned with $\langle 110 \rangle$ (or $\langle 100 \rangle$) diamond crystallographic directions respectively, typically compatible with the QIE-based fabrication process. The dimensions of the waveguide structure are determined as a result of coupling maximization between the emitter C-transition and the rectangular cross section air-cladded geometry, taking into account the relative orientation of the emitter along $\langle 111 \rangle$ direction with respect to the $\langle 110 \rangle$ oriented waveguide.

Using COMSOL[®] Multiphysics, the coupling between the electric dipole of the emitter to the waveguide is simulated, following the approach in Ref. [21]. As a result, the coupling between the emitter and the $\langle 100 \rangle$ and $\langle 110 \rangle$ oriented waveguides with different dimensions is obtained, as detailed in Refs. [18, 20]. $\langle 110 \rangle$ orientation of waveguide structures is preferred, as higher emitter to waveguide coupling is obtained in this case. Table 2.1 details the values of the optimal waveguide parameters, aligned with $\langle 110 \rangle$ crystallographic direction, fabricated subsequently in this work.

Photonic crystal cavity (PCC) device

Compared to the propagation in a simple cross-section rectangular waveguide, where the rectangular cross-section is uniformly maintained along the propagation direction, in a photonic crystal cavity device, the propagation of the electromagnetic field is altered by a periodic modulation of the refractive index between air and diamond. In this case, the periodic modulation of the refractive index is guaranteed by physically removing parts of the diamond slab in a periodic fashion along the longitudinal propagation direction. Pragmatically, this concept translates into a variety of available designs such as fishbone cavities [22] and hole-based design [6, 7], to name a few.

For a detailed introduction to the topic of photonic crystals, we refer the reader to Refs. [23, 24]. For a detailed description of the photonic crystal cavity devices hereafter described, we refer the reader to Refs. [13, 19, 25].

In this work, we adopt the hole-based cavity design, where in COMSOL[®] Multiphysics we simulate the nanobeam unit cell, parametrized by hole radius r , beam thickness t_n , lattice period a_n and beam width w_n . By introducing a perturbation to the nominal lattice period a_n , in combination with fixed values of all aforementioned parameters, the lowest TE mode frequency is raised into the TE modes bandgap to the target frequency, here corresponding to the C-transition of the SnV centers. The perturbation to the lattice period a_n is introduced adiabatically, in a functional form introduced by Ref. [19], in order to minimize coupling to radiation modes.

Once the nanobeam parameters are determined, the nanophotonic cavity structure results as a structure formed by two opposite symmetric mirror regions over M unit cells of lattice period a_n , where the lowest TE mode is localized in the band-gap by introducing the altered correspondingly lattice period a_n over N unit cells, forming the full symmetric cavity region over $2N$ unit cells.

A full description of the nanobeam parameters optimization herein adopted can be found in Ref. [13].

Table 2.1 details the values of the unit cell parameters based on which the bandstructure

has been simulated and on which the PCCs fabricated in this work are constructed.

Diamond chiplets layout

Once the optimal operating parameters of the nanophotonic device are determined in COMSOL[®] Multiphysics, the next step is to embody these structures into a chiplet body layout, typically integrating several PCCs and / or waveguides within the same body-frame. In Section 2.4.1 and Section 2.4.2, the chiplet layout integration configurations are presented, along with the light coupling method to the integrated devices.

2.4.1 65 °C QIE-BASED VARIANT COMPATIBLE DEVICES LAYOUT AND DESIGNS

This Section presents and describes the diamond chiplet designs developed in Hanson Group, compatible with the first 65 °C QIE-based variant fabrication process developed in Kavli Nanolab Delft.

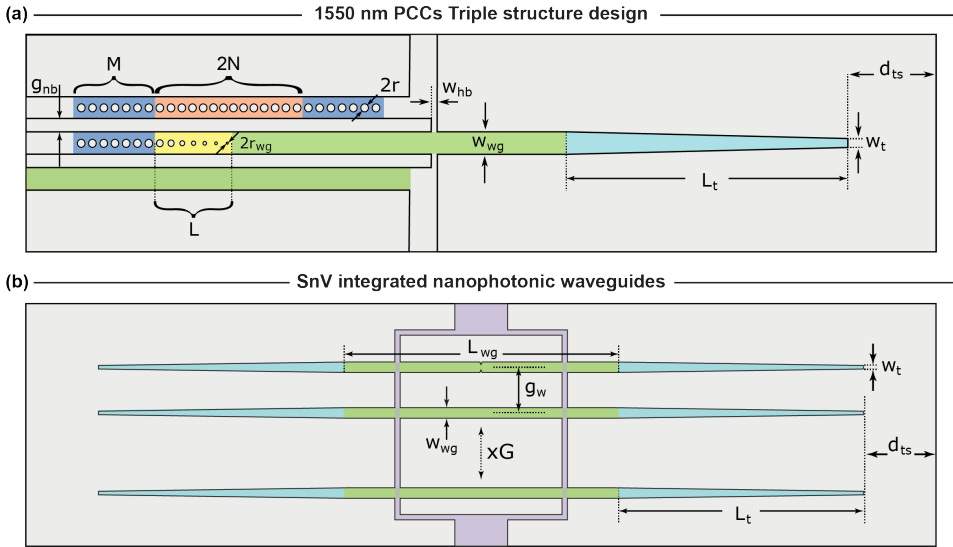


Figure 2.2: 65 °C QIE-based variant compatible devices layout and designs | (a) 1550 nm Nanophotonic cavities Triple structure device design Figure here modified and adapted from Ruf M. PhD Thesis [13]. | (b) SnV center tailored nanophotonic waveguides: schematic of the waveguide chiplet.

(a) 1550 nm triple structure devices chiplet in diamond

Figure 2.2 (a) schematically illustrates the design of the triple structure devices chiplet (adapted from Ruf M. PhD Thesis [13]), compatible with the fabrication process described in Section 2.5.1. Details on the device parameters can be found in Chapter 7 of Ruf M. PhD Thesis [13]. The simulated design of the nanophotonic crystal cavity with parameters listed in Ruf M. PhD Thesis [13] show a quality factor $Q = 1 \times 10^6$ and a resonant wavelength $\lambda_c = 1531$ nm. For the purpose of developing and optimizing the QIE-based fabrication process, relevant device parameters are detailed in Table 2.2. Taking into account the en-

semble of geometric parameters characterizing the triple structure chiplet design presented below, these allow for thorough evaluation of the first QIE-based variant (65 °C QIE-based variant) fabrication process and subsequent optimization.

2

| | Rectangular hole-based PCC | | | | Coupling mirror / holding bar / taper | | | | |
|------------|----------------------------|-------|-----|-------|---------------------------------------|----------|----------|----------|-------|
| Parameter | a_n | w_n | r | t_n | w_{wg} | r_{wg} | g_{nb} | w_{hb} | w_t |
| Value [nm] | 507 | 690 | 169 | 568 | 690 | 30 | Var. | Var. | Var. |

Table 2.2: 1550 nm PCCs Triple structure design devices parameters, adapted from Ref. [13]; g_{nb} , w_{hb} and w_t are varied.

The device geometry is composed of (top) one photonic crystal cavity (symmetric mirrors over M unit cells each, regions shaded in blue, cavity region over $2N$ unit cells shaded in orange), (middle) coupling waveguide (shaded in green, waveguide width w_{wg} , minimum taper width w_t), and (bottom) simple waveguide (shaded in green).

The (middle) coupling waveguide terminates into a Bragg mirror (M unit cells, shaded in blue), which allows to probe and transfer the waveguide field to the adjacent structures via evanescent field coupling. This transfer efficiency depends on the distance g_w between the waveguide and the lateral devices. In order to avoid scattering of light into leaky modes, the hole radius of the terminating mirror waveguide gradually changes from waveguiding region of width w_{wg} (shaded in green), starting with a hole of minimum tapered radius of r_{wg} to the mirror hole size r , while keeping the lattice spacing a_n throughout the hole radius variation constant (shaded in yellow, changed over L unit cells). To allow structural integrity, waveguides are anchored to the diamond frame via narrow holding bars: the value of the width of the holding bars w_{hb} is an optimal trade-off between structural stability of the entire structure and minimization of scattering losses.

Next, the (middle) coupling waveguide can be coupled to a single-sided tapered single-mode optical fiber in a tapered waveguide region (shaded cyan) to a minimum taper width w_t . Such tapered optical fibers are typically fabricated in house via wet etching in HF 40% controlled velocity fiber pulling [26]. By achieving high control over the axial direction pulling axis, the taper radius of the optical fiber is virtually reduced to zero and angle of the fiber can be achieved as low as few degrees. This is particularly favorable for achieving high degree adiabaticity in mode transfer from fiber to waveguide taper, with coupling efficiencies as high as 90% [27, 28].

Finally, the spacing between the waveguide taper end and the diamond substrate d_{ts} should be high enough to allow comfortable positioning of the optical fiber upon tapered contact coupling. This is a desirable feature because it prevents the fiber length from contacting the bulk diamond substrate, hindering unwanted sliding and mechanical vibrations from the substrate itself. At the same time, this allows for accurate positioning and alignment of the fiber to the coupling waveguide taper. In our triple structure chiplet device layout, we typically use $d_{ts} \approx 80 \mu\text{m}$.

As a first step of the process development and optimization, resulting in the 65 °C QIE-based variant fabrication process, the triple structure features dimensions allow us to evaluate the performance of the fabrication process for waveguiding structures of width, length, and hole radius twice the typical dimensions of devices for SnV center ZPL designed nanophotonic structures.

Next, pragmatically, the already available telecom wavelength test setups in Gröblacher

Lab in Delft allowed us to evaluate the performance of the QIE-based fabrication process on 1550 nm nanophotonic cavities. By evaluating the experimentally evaluated quality factor of the fabricated devices, we can evaluate whether the accuracy of the obtained devices with respect to the CAD designs, combined with the surface roughness, would eventually allow us to scale-down the aforementioned nanophotonic structures to much shorter operating wavelengths, compatible with the SnV center emission.

The triple structure device chiplet has been modified and optimized to host waveguides and PCCs with devices parameters detailed in Table 2.1, for which a schematic is shown in Figure 2.8. The same working principles as described above apply in the scaled-down version of the chiplet. As it will be shown in Section 2.7.3, the narrow design features typical of hole-based 620 nm PCCs are challenging to accurately pattern with the fabrication recipes developed in the context of **65 °C QIE-based variant**. Hence, the nanofabrication feasibility of this design variant is investigated subsequently in the context of **250 °C QIE-based variant**.

(b) 620 nm SnV center integrated waveguides chiplet in diamond

Figure 2.2 (b) illustrates the schematic of a SnV center emission tailored designed nanophotonic waveguides chiplet. The typical suspended chiplet layout is attached to the diamond substrate via the rectangular holding frame (lille, holding bar width w_{hb}). The SnV center emission tailored nanophotonic waveguides can be probed in both transmission and reflection via input and output fiber coupling: the total waveguide length L_{wg} (green) terminates in double-sided tapers (cyan) of length L_t each and the end taper minimum width w_t . The spacing of the waveguide taper end to the diamond substrate d_{ts} (not to scale) and the inter-waveguide distance gap g_w are designed so that the fiber-to-waveguide taper coupling is spatially comfortably hosted. For this purpose we experiment two configurations: in the first layout configuration $d_{ts} \sim 35 \mu m$ and $g_w = 4 \mu m$, whereas in the second configuration we experiment with an in-line positioning of chiplets with a fully etched unified inter-chiplet trench of taper-to-taper distance $d_{tt} \sim 100 \mu m$ and $g_w = 4 \mu m$. The second configuration proved the most suitable for fiber coupling, both in-contact and in lensed-fiber configuration.

Typical values of waveguide length L_{wg} are implemented as a result of semi-quantitative considerations on the statistics of the SnV centers, namely considering the average number of SnV center per unit volume of waveguide length. Thus, with typical implantation parameters and conversion yield in this work, we typically sweep L_{wg} between $10 \mu m$ to $20 \mu m$. Next, in order to maximize the fiber to waveguide taper coupling, we sweep L_t from $\sim 10 \mu m$ to $15 \mu m$ and fix w_t to $\sim 50 nm$, the minimum value width compatible with the QIE-based fabrication process. g_w and d_{ts} are design parameters adopted as a trade-off between maximization of the number of waveguides per chiplet and fiber-to-waveguide taper coupling spatial optimization.

The waveguide chiplet layout of diamond nanophotonic waveguides described here is adopted for the fabrication of arrays of SnV center integrated nanophotonic waveguides, results and experiments of which are presented in Chapter 4.

2.4.2 250 °C QIE-BASED VARIANT COMPATIBLE DEVICES LAYOUT AND DESIGNS

This Section presents and describes the diamond chiplet designs, compatible with the second **250 °C QIE-based variant** fabrication process developed in Kavli Nanolab Delft. In order to fully characterize the QIE-based process and more specifically the 250 °C QIE etch recipe aspect-ratio dependency, we experiment with different aspect-ratio chiplet layouts in combination with different surrounding opening in the diamond substrates (schematically illustrated in Figure 2.3, single-standing nanophotonic devices combined with narrow opening, double structure layout combined with narrow opening and single standing devices combines with wide opening).

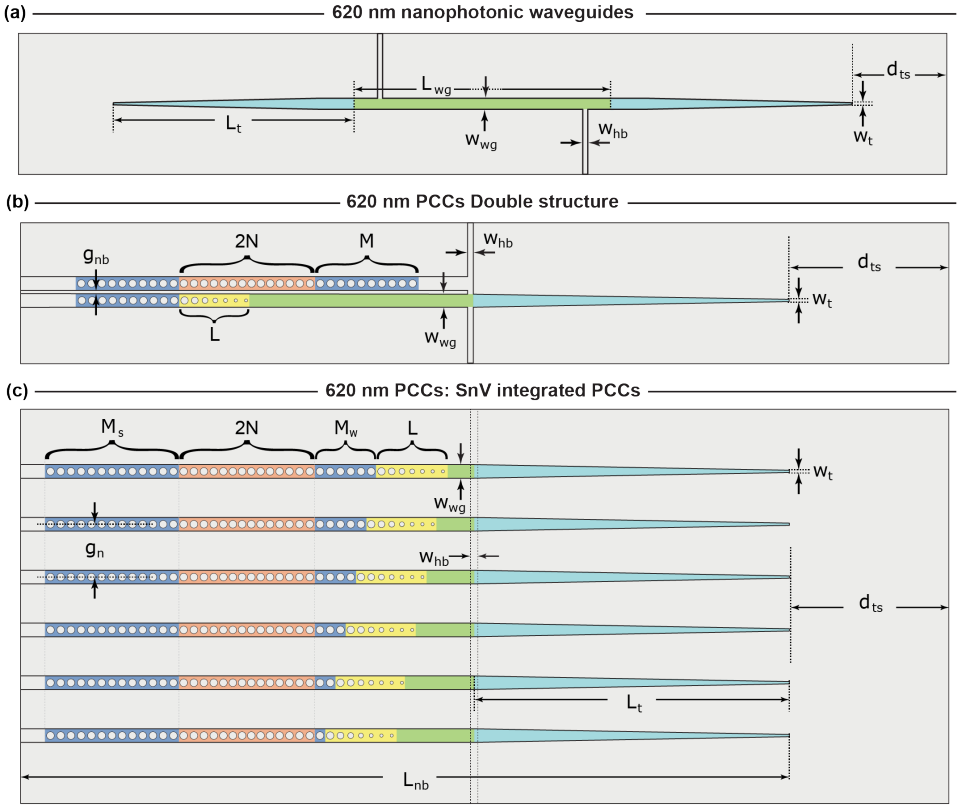


Figure 2.3: **250 °C QIE-based variant compatible devices layout and designs SnV center integrated PCCs: SnV center emission tailored nanophotonic waveguides and cavities:** | (a) Single standing nanophotonic waveguide; | (b) Photonic crystal cavity double structure design, similar to the triple structure device chiplet in Ref. [13]; | (c) Suspended single standing asymmetric one-sided PCCs.

(a) 620 nm SnV center integrated single standing waveguides in diamond

The rectangular cross section waveguide designs presented in Section 2.4.1 are, naturally, compatible with the finer tuned **250 °C QIE-based variant** fabrication process, as this process addresses the more stringent fabrication process parameters requirements dictated

by the more complex geometry of the devices, alongside denser patterns. Figure 2.3 (a) shows a schematic illustration of the revisited waveguide design. Here, double-sided waveguides are single-standing, fixed to the diamond substrate via two holding bars of width w_{hb} at an angle 90° with respect to the axial direction of the waveguide. The holding bars here presented are positioned on alternative sides with respect to the substrate border (although the same side is equally effective), so that the torsional motion in all three directions of the waveguide is minimized upon fiber coupling from both taper ends. Typical values of waveguide length L_{wg} , taper length L_t , waveguide width w_{wg} , waveguide thickness t_w , end taper width w_t , and end-to-substrate distance d_{ts} have the same values as in Section 2.4.1 waveguide chiplet design.

The design presented in Figure 2.2 (b) has been optimized and modified, first taking into account the total number of optical scattering points per waveguide: each point where the waveguide encounters the holding bar, if w_{hb} value deviates from the nominal design, within the fabrication process, increases the total amount of scattering losses. Therefore, instead of four holding bars per waveguide as characteristic for the chiplets in Figure 2.2 (b), the number of scattering points here is reduced to only two.

At the same time, the number of waveguides per chiplet has been reduced to one in order to guarantee systematic and equal thermal link of the waveguide to the diamond substrate, such that a closer and more efficient thermal dissipation of the heat generated upon optical excitation is dispersed in the substrate via the holding bars.

(b) 620 nm **double structure PCCs**

Similarly to the triple-structure chiplet design presented in Section 2.4.1, Figure 2.3 (b) shows a schematic illustration of the double-structure chiplet design. Here, the structure of the nanophotonic crystal cavity follows the same hole-based symmetric cavity principles as in Ref. [13], where (top) the nanobeam is composed of two symmetric mirror regions (blue-shaded, lattice spacing a_n each over M unit cells) and a central cavity region (red-shaded, over total $2N$ unit cells) where the defect is adiabatically introduced over N unit cells by varying a_n with the functional form introduced by Ref. [19]. The PCC is evanescently coupled via the (central) coupling waveguide region, placed at a distance g_{nb} , terminating in a Bragg mirror (blue-shaded, over M unit cells), adiabatically tapered down from the r radius hole to the $r_{min, wg}$ minimum radius hole (yellow-shaded, over L unit cells), keeping the lattice spacing constant a_n . The waveguide of width w_{wg} is tapered down (shaded with cyan) from w_{wg} to the end taper width of width w_t . Again, the end taper to substrate distance d_{ts} (not scale) value is designed such that the one-sided tapered optical fiber coupling is comfortably hosted and allows for accurate positioning on the waveguide taper. The structure is attached to the substrate through holding bars of width w_{hb} .

(c) 620 nm **Single standing one-sided SnV center integrated PCCs**

Figure 2.3 (c) shows a schematic illustration of the single standing one-sided asymmetric photonic crystal cavity design, in an array chiplet configuration. In contrast to the evanescent field lateral coupling via the central waveguide presented so far, here the coupling of the optical field takes place by leveraging the designed input weak-coupling mirror. The design of the nanophotonic structure hereby presented is inspired by the design introduced in Ref. [29].

Taking into account a single nanobeam from the presented array, the asymmetric PCC design is articulated as follows: From left to right, the photonic crystal cavity is terminated

in a strong mirror region (blue shaded, constant lattice spacing a_n over M_s unit cells), followed by the cavity region (red shaded, over a total of $2N$ unit cells) where the defect is introduced adiabatically over N unit cells by varying a_n with the functional form introduced by Ref. [19]. Next to the cavity region, the weak mirror region (blue-shaded, constant lattice spacing a_n over M_w unit cells) is positioned. This is adiabatically tapered down from r radius hole to $r_{\min, \text{wg}}$ minimum radius hole (yellow shaded, over L unit cells) to the waveguide region (green shaded, width w_{wg} same as nanobeam width). The waveguide region is next tapered down from w_{wg} to end taper minimum width w_t , over L_t taper length (cyan). The end taper to substrate distance d_{ts} , is designed similarly as in all previous tapered optical fiber couplings.

The difference in the design parameters with respect to Ref. [30] is that here the weak mirror over M_s unit cells maintains a constant lattice spacing a_n . Therefore, in this case, the weak mirror allows coupling of the input field via leaking the input TE mode through a poorly reflective in-coupling mirror. Given that the expected coupling efficiency to the nanobeam cavity is not optimized, we sweep the number of M_s unit cells from a minimum of one to a maximum of six.

In contrast to all chiplets designs presented so far, the single standing one-sided PCCs here presented are fully suspended and free-hanging, where the holding bars are optionally implemented (holding bar width w_{hb}). The devices are fixed to the diamond substrate via an end waveguide region distanced from the strong mirror $\sim 2 \mu\text{m}$. Therefore, in order to guarantee structural stability, a careful trade-off between the overall length of the nanobeam and the L_t taper length is considered.

2.5 METHODS

In this Section, we present the development and optimization of the QIE-based diamond fabrication process in Kavli Nanolab Delft, schematically illustrated in Figure 2.1. We have adapted this fabrication process in two different variants, according to the specific devices design requirements. Specifically, we have adapted this process with the quasi-isotropic ICP-RIE at 65°C temperature and further optimized and developed a second variant of this process with the quasi-isotropic ICP-RIE at 250°C temperature. This fabrication process, including optimization of the entire parameter space, is developed and for $\{100\}$ oriented surface diamond substrates. The baseline methods and protocols presented here are generally valid for both QIE-based process variants, unless otherwise mentioned. All SEM quantitative measurements are corrected for tilted angled view.

2.5.1 BASELINE QIE-BASED PROCESS DEVELOPMENT

Referring to Figure 2.1 the fabrication steps of the QIE-based fabrication process are discussed below in detail, for which the process parameters are listed in Appendix A.4, Table A.3 and Appendix A.4, Table A.4 for the **65°C QIE-based variant** and **250°C QIE-based variant** respectively.

SUBSTRATE PREPARATION: FABRICATION STEP (1)

The cleaning procedure is detailed in Table A.3 step (1), where we first perform a room temperature hydrofluoric acid clean (HF, 40 % concentration), followed by two subsequently performed piranha mixture (ratio 3:1 of H_2SO_4 (95%) : H_2O_2 (31%)) inorganic cleanings

at 80 °C. The purpose of this extensive inorganic cleaning is to ensure a free of organic contaminants substrate prior to any following fabrication steps.

First, a fully cleaned uniform substrate surface ensures good adhesion of the hard mask material.

Second, the presence of point macro-sized impurities may constitute nucleation points for the PECVD (or ICPCVD) growth, resulting in a non-uniform thin film layer (hard mask). This effect is undesirable, as it can negatively impact the resist spin coating (fabrication step (2)), causing an uneven thickness of the spun resist, which in turn is detrimental for subsequent e-beam exposure in fabrication step (3).

HARD MASK MATERIAL DEPOSITION: FABRICATION STEP (2)

65 °C QIE-based variant: plasma-enhanced chemical vapor deposition (PECVD) of Si_xN_y for a thickness of ~200 nm, deposition parameters in Table A.3 step (2).

250 °C QIE-based variant: inductively coupled plasma chemical vapour deposition (ICPCVD) of Si_xN_y for a thickness of ~85 nm, deposition parameters in Table A.4 step (2).

Once the real-time Si_xN_y deposition rate is determined (methods described in Section 2.5.2), we proceed with material deposition on both target diamond substrates and additional twin Si test samples, all in the same deposition chamber, in the same deposition run. After deposition, we repeat the spectroscopic ellipsometry to confirm that the design thickness is achieved in the Si_xN_y deposition process.

E-BEAM RESIST AND CONDUCTIVE LAYER SPINNING: FABRICATION STEP (3)

Before proceeding with the e-beam resist spin coating, one has to ensure that the surface of the deposited Si_xN_y does not undergo significant surface modification, e.g. oxidation. Exposure of Si_xN_y to O_2 plasma, as well as ambient oxygen, causes oxidation of Si_xN_y at the surface, resulting in the formation of a thin layer of non-stoichiometric silicon oxynitride [31, 32]. As a consequence of prolonged exposure of Si_xN_y to ambient conditions, the adhesion of the surface may change. Therefore, one should proceed with the following spin coating step of the e-beam resist at a fast pace, so that modifications of the Si_xN_y adhesion are contained.

Typically, diamond substrates with which we experiment have different areas, for example 2 mm × 2 mm, 3 mm × 3 mm and 4 mm × 4 mm and a typical thickness of 500 μm. The dimension of the diamond plates represents a challenge per se, as for dimensions as small as the above expressed, spin coating of resist is severely affected by resist reflow. During the spin coating, the liquid resist suffers from edge-beating effect, resulting in a post-spin effective resist thickness considerably higher than that designed by experiment.

In order to mitigate for the edge-beating effect, one possible solution is to artificially expand the effective spin-coating area. Pragmatically, by extending the effective spin-coating area, the edge-beating phenomenon still takes place on the diamond / Si_xN_y edges, though to a lesser extent.

We artificially expand the effective spin coating area by positioning Si / Si_xN_y (with same thickness as the diamond / Si_xN_y and dimensions 5 mm × 5 mm) in the immediate vicinity at the diamond / Si_xN_y edges. The deposited Si_xN_y (within the same deposition

session as the diamond substrate) on the surrounding Si coupons guarantees the same adhesion as the target diamond sample, while the same height of the surrounding Si / Si_xN_y coupons alleviate the edge-beating effect at the edges of the diamond. The diamond and surrounding artificial spin-coating area are all glued to a silicon carrier coupon for easy handling. In order to ensure a uniform spin coating of the resist layer, the overall system, prioritizing the diamond substrate position, should be central with respect to the spin-coating chuck such that the resist experiences a centrifugal force centered on the diamond sample center. This method allows us to obtain consistently and reproducibly a uniform resist layer of resist at the center of the diamond / Si_xN_y stack, presenting reflowed resist only on the four edges of the sample.

The preparation of the diamond substrate for e-beam exposure is articulated in two main steps: first, a positive e-beam resist is spin coated, followed by conductive polymer spin-coating to prevent the sample substrate from charging effects throughout e-beam exposure.

65 °C QIE-based variant: AR-P-6200.13 positive e-beam resist of ~ 400 nm, followed by AR-PC-5090 conductive polymer of ~ 40 nm, parameters in Table A.3 step (3).

250 °C QIE-based variant: AR-P-6200.09 positive e-beam resist of ~ 220 nm, followed by the AR-PC-5090 conductive polymer of ~ 40 nm, parameters in Table A.4 step (3).

E-BEAM EXPOSURE AND DEVELOPMENT: FABRICATION STEP (4)

Once the optimal clearing exposure dose is determined (implementing ad-hoc dose tests), the e-beam writing set of parameters is optimized.

Specifically, we optimize over the following:

- **Beam spot size and Beam Step Size (BSS):** the beam spot size d_s and BSS are related roughly as $d_s = 1.2 \times \text{BSS}$ to $d_s = 1.5 \times \text{BSS}$. This ensures a continuous exposure of the beam spot size in the e-beam raster scan exposure of the pattern, as an optimal exposure of adjacent points; We choose a beam spot size of $d_s = 2.3$ nm (closer to the smallest available on our exposure tool EBPG 5200) and a BSS = 3 nm (closer to the highest resolution possible to the grid size of the pattern);
- **Pattern fracture:** among the possible options, we test the Large Rectangle Fine Trapezoid (LRFT), conventional and curved. We find that the curved setting yields the highest accuracy of the design pattern in the case of circular features, as this fracturing mode offers the finest writing trapezoids (in good agreement with the results of the fracturing test patterns for ellipsoidal shapes in Ref. [33]).
- **Writing order:** among the conventional combinations possible (array no compaction and follow geometry), the follow geometry option yielded the highest accuracy.
- **Proximity Effect Correction (PEC):** we Monte Carlo simulate in the TRACER software the stack of materials constituted by diamond / Si_xN_y / AR.P.6200, combined with the adopted d_s and acceleration voltage (100 keV) to obtain the Point Spread Function (PSF) of energy density. We then implemented the PSF into the PEC module in BEAMER and obtained a design calibrated local exposure dose, hence, pattern

density calibrated with respect to the clearing optimal dose. As mentioned above, the optimal clearing dose is determined in a dose test beforehand. TRACER simulations parameters for the stack of materials systems of two variants of the process are:

500 μm **diamond** / 200 nm Si_xN_y / 400 nm **AR.P.6200.13**, 65 °C **QIE-based variant**
 500 μm **diamond** / 85 nm Si_xN_y / 220 nm **AR.P.6200.09**, 250 °C **QIE-based variant**

- **Lateral development compensation:** in order to compensate for exposure bias on the design geometric parameters, a lateral development compensation is implemented in order to compensate for resist over-exposure by secondary electrons lateral spread.

The exposure is first tested on Si / Si_xN_y coupon twin test samples by patterning benchmark test designs.

Before the resist development step, the conductive polymer is removed: a gentle H_2O water rinse is performed for 1 min at room temperature. The sample must then be thoroughly N_2 dried. An optical microscope inspection before developing the underlying resist is strongly recommended to ensure the absence of H_2O on top of the sample. H_2O and the wet development solutions are immiscible liquids; therefore, H_2O droplet residues eventually act as a mask on top of the exposed pattern on the resist, preventing it from developing. Since complete development of the exposed pattern is essential, total removal of H_2O is strongly recommended.

The development of the pattern follows a standard recipe developed in Kavli Nanolab Delft (parameters in Table A.3, step (4)). An optical microscope inspection of the developed pattern is followed in order to ensure that the exposed resist is fully cleared out.

TRANSFER PATTERN IN THE HARD MASK MATERIAL: FABRICATION STEP (5)

The developed pattern is transferred into the Si_xN_y hard mask material via a top-down anisotropic CHF_3/O_2 ICP-RIE plasma chemistry.

The etching process and performance are first tested on Si / Si_xN_y coupon twin samples prepared at step (2) and exposed at step (4), as described in Section 2.5.2. Once the real-time etch rate, transfer pattern geometry and RIE lag are determined, we proceed with the CHF_3/O_2 etch on diamond samples. In order to compensate for RIE lag, we overetch with a $\sim 25\%$ to 30% tolerance.

RESIST REMOVAL: FABRICATION STEP (6)

The resist removal is articulated in the following two steps:

1. **Course resist stripping:** Coarse resist stripping is carried out employing a PRS-3000 resist stripper solution, detailed in Tables A.3 and A.4. This allows for bulk removal of the residual post-etch resist layer from the extended non-exposed areas of the sample.
2. **Fine inorganic cleaning:** intensive and highly reactive acid cleaning enables fine chemical wet etching of fine resist traces, ensuring complete resist cleaning even in the case of dense design pattern features. For this purpose, since, typically, the Piranha solution is highly effective within the first ~ 10 min after adding the H_2O_2 to the H_2SO_4 , we chose a double sequential inorganic Piranha mixture cleaning (parameters detailed in Table A.3 and A.4) in au-bain Marie at 80 °C, over a longer

duration one-step cleaning. Residues from resist traces negatively affect the transfer pattern into the diamond substrate in the fabrication step (7), causing micromasking (e.g., nano and micro pillars or pits). In turn, micromasking may potentially act as nucleation points for the ALD step (8), resulting in a variable thickness AlO_x film across the sample. This further exacerbates micromasking in the fabrication step (9). QIE etch (step (10)) takes place along the diamond crystallographic planes; therefore, micromasking on a starting diamond surface translates into an irregular etch, enhancing surface roughness on the bottom surface of suspended nanophotonic devices. Efficient removal of masking sources rules out possible sources of micromasking; therefore, it is critical to ensure thorough inorganic cleaning of the diamond sample in this fabrication step.

SUBSTRATE PATTERN TRANSFER: FABRICATION STEP (7)

The design patterns are transferred from the Si_xN_y hard mask top-down to the diamond substrate via anisotropic O_2 ICP-RIE. The vertical spatial extent is $\sim 2\times$ to $3\times$ the design thickness of the nanophotonic devices. The extent of the etch allows sufficient room for the QIE etch at step (10) to undercut the patterned devices, as well as to allow for an efficient upward etch of the devices.

CONFORMAL HARD MASK ALD [FABRICATION STEP (8)] AND ETCHING [FABRICATION STEP (9)]

The passivation of vertical sidewalls is ensured by the inherently conformal ALD method. We deposit a thin layer of ~ 20 nm AlO_x , verifying the target thickness by spectroscopic ellipsometry on Si / AlO_x ALD deposited twin coupon samples (within the same deposition session).

The AlO_x mask is then removed from the horizontal facets of the sample via anisotropic BCl_3/Cl_2 ICP-RIE. We etch with a $\sim 25\%$ to 30% tolerance in order to both compensate for RIE lag effect, as well as to remove the excess thickness-variable AlO_x , which may possibly result in micromasking nucleation points otherwise. The tolerance is compatible with the BCl_3/Cl_2 ICP-RIE (as lateral etch is significantly limited, since the ICP-RIE plasma is strongly anisotropic), anisotropic O_2 ICP-RIE, and the overall QIE undercut consecutive steps (as an overetch does not affect the underlying diamond substrate, because the etch rate of diamond is close to zero in BCl_3/Cl_2 plasma).

Once BCl_3/Cl_2 ICP-RIE is completed, the reactor chamber is pumped down for a considerably longer duration compared to conventional post-etch pump-down to efficiently evacuate any possible residues of volatile reaction byproducts. The diamond sample is then kept within the reactor chamber for the next etching steps without breaking the vacuum. Preventing a vacuum break, and hence maintaining low pressure in the chamber, avoids possible sources of organic contamination from the environment, therefore reducing the risk of micromasking.

QIE ICP-RIE UNDERCUT: FABRICATION STEP (10)

QIE ICP-RIE undercut etch steps are executed in sequential steps. Each QIE step is interleaved by SEM inspection sessions of the diamond sample. Typically SEM inspection takes place at an inspection tilt angle of 65° tilt: this allows for a precise monitoring of the etch progress on the diamond photonic structures.

The sample must be inspected for a brief period of time, up to ~ 30 min each session: This provides us with the possibility to contain the carbon contamination from the electron beam raster scan during imaging.

WET ETCH OF HARD MASK MATERIALS: FABRICATION STEP (11)

Once the target thickness on diamond nanophotonic devices is reached, the substrate undergoes an inorganic wet cleaning step. The wet cleaning time should be determined according to the wet etch rate of Si_xN_y and AlO_x in HF 40%. Reported etch rates of PECVD Si_xN_y and evaporated AlO_x in Piranha solution are respectively zero and ~ 19 nm/min [34]. Reported etch rates of PECVD Si_xN_y and evaporated AlO_x in diluted 5:1 HF are respectively ~ 8.2 nm to 60 nm/min and ~ 160 nm/min [34]. Although the wet etch rate of such materials depend on their respective stoichiometry and deposition parameters, the above literature gives a rough estimation of the expected etch rates in the respective inorganic solutions. We observe a zero etch rate of Si_xN_y and a high etch rate of AlO_x in the Piranha solution and a very high etch rate of both materials in HF 40%. To ensure that no traces of these mask materials are left on the diamond samples, we overshoot and perform double cleaning in HF 40% at room temperature for 20 minutes each, followed by a Piranha mixture at 80°C for ~ 20 minutes.

As the fabricated photonic structures have dimensions of a few hundreds of nanometers in thickness, it is strongly suggested to avoid mechanical vibrations of the sample throughout the entire procedure.

Finally, it is beneficial to avoid blowing dry N_2 of the sample, as such operation may lead to the breaking of fragile suspended nanophotonic devices.

2.5.2 COMPLEMENTARY Si / Si_xN_y ETCH TESTS

Typically, the CAD design transfer pattern is tested first on Si / Si_xN_y coupon samples. Prior to the Si_xN_y deposition on diamond substrates, we routinely pre-characterize the real-time Si_xN_y deposition rate on silicon (Si) substrate test samples. This protocol allows us to monitor fluctuations in the deposition rate of the material, which may be caused by the real-time deposition chamber conditions.

Before deposition of Si_xN_y , we prepare the pristine Si coupon substrate thoroughly cleaning the surface: a pristine silicon (Si) coupon test sample is thoroughly cleaned at room temperature in 10 min ethanol ultrasonic bath, followed by 10 min acetone ultrasonic bath and 5 min Isopropyl Alcohol (IPA) ultrasonic bath, concluding with blow drying N_2 .

The spectroscopic ellipsometry method is used to determine the thickness of native silicon dioxide (ntve SiO_2): the ellipsometry data analysis of the Si / ntve SiO_2 material stack is performed by modeling the stack with oscillator models of the aforementioned materials (using J.A. Woollam software and data analysis tool), thus extracting the optical constants (refractive index n and absorption coefficient k) and the thickness of ntve SiO_2 .

The test sample is then used as the substrate for the Si_xN_y test deposition with an arbitrary deposition time.

The thickness of the deposited Si_xN_y material is measured by spectroscopic ellipsometry: the ellipsometry data analysis of the Si / ntve SiO_2 / Si_xN_y material stack system is performed by modeling the system, this time fixing the previously determined optical constants and thickness of ntve SiO_2 , while the optical constants and thickness of Si_xN_y

are fitted. The fitting is carried out by minimizing the Mean Squared Error (MSE) and comparing the obtained values of optical constants of the Si_xN_y with both the literature and values from previous deposition rounds. The real-time deposition rate is obtained by dividing the estimated thickness by the deposition time.

Next, we deposit the target thickness Si_xN_y on Si substrates (Figure 2.4, step (2)), preferably in the same deposition run as the diamond substrate. Subsequent spectroscopic ellipsometry confirms the deposition rate and the target thickness of Si_xN_y .

Figure 2.4 schematically illustrates the fabrication protocol we have developed for Si / Si_xN_y etch tests. The protocol presented here allows us to determine the real-time deposition rate of Si_xN_y , the etch rate of Si_xN_y under the CHF_3/O_2 ICP-RIE plasma and, as will be presented in Section 2.6.1 the performance of Si_xN_y under anisotropic O_2 ICP-RIE plasma. Close monitoring of these parameters and preventive measurements allow for accurate control over the fabrication process, regardless of the deposition and etching reactor chamber conditions.

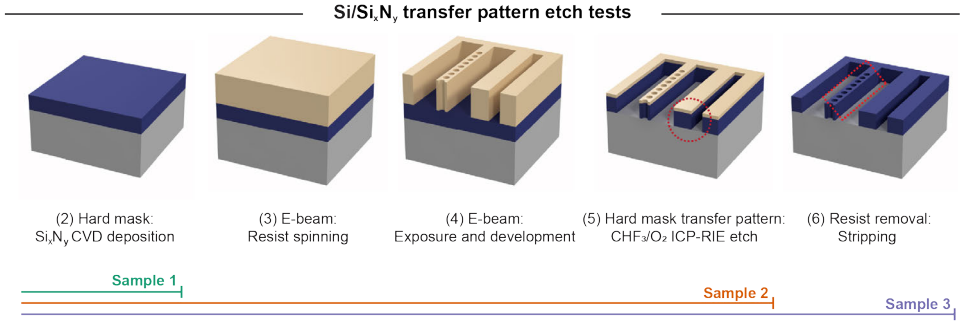


Figure 2.4: **Si / Si_xN_y etch tests:** fabrication steps foreseen for the preparation of test samples.

The etch tests transfer pattern are carried out on two types of Si / Si_xN_y test samples: 1. Non-patterned Si / Si_xN_y twin samples allow us to first determine the real-time etch rate; 2. E-beam patterned Si / Si_xN_y test samples are constituted by a combination of benchmark test design devices and simple geometry trench lines of varying width.

Thus, based on the above categories of test samples available, we developed the following protocol:

1. **Real-time etch rate:** on non-patterned Si / Si_xN_y test samples (Figure 2.4, Sample 1), the thickness of Si_xN_y is measured via spectroscopic ellipsometry before and after the CHF_3/O_2 ICP-RIE is performed. This allows to determine the net real-time etch rate.
2. **Geometry of devices and RIE lag:** patterned Si / Si_xN_y test samples are etched under CHF_3/O_2 ICP-RIE. The etched test sample is cleaved in correspondence of the trench lines into 2 parts.

The part of the sample containing the trench lines (Figure 2.4, Sample 2) is further SEM inspected under 85° tilt angle. An analysis of vertical sidewalls is carried out, allowing to determine the resist to Si_xN_y selectivity. At the same time, we analyze

the vertical sidewall angle, surface roughness, and re-deposition of the material. Next, by inspecting trenches of various widths, we determine the effect of RIE lag [35] for dimensions typical for our nanophotonic devices.

The sample part containing the benchmark photonic structures design (Figure 2.4, Sample 3) undergoes fabrication step (6), after which an SEM inspection at 0° tilt angle is carried out. This allows us to evaluate the geometric mismatch between patterned devices and CAD design. Thus, we determine if any systematic bias (consistent dimensions mismatch between design values and fabrication etched obtained values) and/or geometry-dependent bias (inconsistent dimensions mismatch, variable according to pattern density and geometry) is present, so that it can be compensated with the next fabrication optimization iteration.

2.6 RESULTS: 65 °C QIE-BASED PROCESS VARIANT

2.6.1 Si_xN_y HARD MASK

Before proceeding with presenting the results of the overall QIE-based 65 °C temperature variant of the fabrication process on diamond substrate, in this section we focus on briefly showing the design transfer pattern in the Si_xN_y hard mask, evaluating systematic bias and / or geometry-dependent bias, as well as evaluating the robustness of the mask under downstream O₂ ICP-RIE, foreseen by the QIE-based fabrication process.

For this, we first carry out a series of Si / Si_xN_y etch tests, following the methods described in Section 2.5.2. We iterate over several test rounds and optimize the thickness of resist and Si_xN_y, e-beam exposure parameters, etch duration, and tolerance over the process parameters. The benchmark test design chiplet used during the development and optimization process is the design of the triple structure layout device schematically illustrated in Figure 2.2 (a). In the following, we present the results with the best set of parameters determined, detailed in Appendix A.2, Table A.3.

Transfer pattern into the Si_xN_y mask

As described in Methods (Section 2.5.2), the steps of the fabrication process that lead us to test the transfer of the pattern from the CAD design to top-down etching in the hard mask Si_xN_y are schematically illustrated in Figure 2.5 (a). Typically, for the 65 °C QIE-based variant of the process, pattern transfer is executed using a stack of materials composed of 400 nm CSAR-13 spin coated on top of 200 nm PECVD Si_xN_y. The benchmark test design layout is then the e-beam exposed, developed, and top down etched (the same process parameters as in Table A.3 for the corresponding fabrication steps) design.

SEM inspection (85° tilt view) enables inspection of the etched trenches vertical sidewalls (Figure 2.5 (b.1)): the sidewalls of the etched mask show a ~90° sidewall angle, with a surface roughness that cannot be quantitatively resolved by SEM inspection. For the telecom frequency regime tailored and operating photonic devices, as detailed in Table 2.2, typical dimensions are ≥100 nm and relatively low pattern density. Hence, we do not identify the RIE lag effects. At the same time, we determine that CSAR-13 to Si_xN_y is ~3:2, confirming that the 400 nm CSAR-13 is sufficient for a full breakthrough of the 200 nm Si_xN_y mask.

The e-beam writing parameters and the etch rate of Si_xN_y in CHF₃/O₂ ICP-RIE plasma have been optimized to improve the accuracy of the transfer pattern. Top-down SEM inspec-

tion (0° tilt, top view) enables inspection of the patterned devices, allowing for an evaluation of systematic bias and geometry-dependent bias. Triple structure telecom frequency tailored devices, etched in Si_xN_y , can be observed in the SEM pictogram (Figure 2.5 (b.2)) (left) coupling waveguide terminating in a mirror and (right) photonic crystal cavity. The systematic bias in the transfer pattern is ≤ 25 nm, whereas no geometry-dependent bias can be identified. We also observe that the constant exposure dose (the same) on Si / Si_xN_y and diamond / Si_xN_y produces a different systematic bias on the two different substrates; therefore, here we present the systematic bias on diamond / Si_xN_y , for which the nominal exposure dose is calibrated with respect to Si / Si_xN_y .

The quantified systematic bias is then compensated in the design phase of the SnV center emission tailored nanophotonic waveguides (Figure 2.5 (b.3)): SEM inspection (0° tilt, top view) allows to quantify the compensated systematic bias to amount to ≤ 10 nm, hence a one-to-one transfer pattern from CAD design to hard mask.

From these etch test, we conclude that the Methods described in Section 2.5.1, according to the process parameters detailed in Appendix A.2 Table A.3 are the optimal ones for a reliable transfer pattern onto the Si_xN_y hard mask material.

Si_xN_y erosion in anisotropic O_2 ICP-RIE

The challenges associated with the robustness of the Si_xN_y mask in the QIE-based fabrication process are frequently addressed. Specifically, the Si_xN_y mask often breaks during the several ICP-RIE steps foreseen by the QIE-based variants of the process, compromising the result of the sample fabrication. QIE plasma acquires access to the protected diamond slab of material, etching the diamond structures via the broken open access points, thus yielding severely altered cross-section suspended devices, characterized by both high surface roughness in correspondence to the broken mask areas and fully etched through devices.

In Ruf M., PhD Thesis [13], Chapter 8, we demonstrated that anisotropic O_2 plasma etching significantly alters the profile of the Si_xN_y hard mask. We found that subjecting the PECVD Si_xN_y mask to 5 minutes of continuous anisotropic etching in O_2 ICP-RIE plasma leads to edge erosion, resulting in rounded sidewalls and material re-deposition. This suggests that the primary mechanism responsible for mask degradation is the erosion effect induced by O_2 ICP-RIE plasma.

Here, we show that the erosion mechanism becomes more pronounced when anisotropic O_2 etching is performed in two separate steps. Furthermore, we demonstrate the mask breaking process, providing direct confirmation of the previously proposed hypothesis.

This study aims to replicate the performance of the Si_xN_y mask under the exact 2-step anisotropic O_2 etch QIE-based fabrication process. The key benefit of the optional second O_2 etch step is its ability to reduce the overall quasi-isotropic undercut etch time. As reported in Ref. [8], this approach can shorten the total undercut etch duration to approximately 8 hours. However, since anisotropic O_2 etching accelerates edge erosion of the Si_xN_y mask, the additional etch step may increase the risk of mask failure.

Building on the previous sample preparation (Figure 2.5 (a)), the sample undergoes an extensive inorganic cleaning process (fabrication step (7)). For inspection, we focus on the benchmark etch test lines composed of nominally 200 nm Si_xN_y . The profile of these patterned etch lines (Figure 2.5 (a)) exhibits a 90° sidewall angle, with a measured width of approximately 235 nm, which is close to the intended design width of 200 nm.

To assess the impact of O_2 etching, the sample is subjected to two sequential anisotropic O_2 etch steps: the first lasting 2 minutes and 15 seconds, and the second lasting 3 minutes (Figure 2.5 (d) and Figure 2.5 (e), respectively).

After the first anisotropic O_2 etch, the thickness of the Si_xN_y is reduced from 200 nm (starting thickness) to ~174 nm, resulting in an etch rate ~11 nm/min, thus a selectivity of ~27, to 1, as expected. From top to bottom, the sidewall angle changes from ~45° (over ~70 nm thickness) to ~90° (over ~105 nm thickness).

After the second anisotropic O_2 etch (additional 3 min, Figure 2.5 (e)), the thickness of the Si_xN_y is reduced from 174 nm to ~123 nm with respectively sidewall angle ~45° (over ~94 nm thickness) and ~73° (over ~29 nm thickness).

However, significant re-deposition can be observed (highlighted in pink false color), which affects the accuracy of the sidewall angle estimation. This is due to Si_xN_y redepositing directly within the etched trench line, particularly near the Si / Si_xN_y interface. As a result, the previously estimated sidewall angle at the interface represents an optimistic value. To obtain a more precise measurement of the angle of the sidewall after anisotropic etching O_2 , we repeat the etch test directly on a diamond substrate.

Repeating the same etch procedure on a diamond / Si_xN_y test sample, the first anisotropic O_2 etch (2 min 15 sec) confirms the characteristic erosion of Si_xN_y on the diamond substrate, demonstrating that this effect arises solely from the O_2 anisotropic etch. Unlike in Si / Si_xN_y tests, no re-deposition of Si_xN_y is observed at the diamond / Si_xN_y interface, making the sidewall angle estimation unequivocal. As expected, the erosion of the Si_xN_y mask is more pronounced compared to previous observations, with a sidewall angle estimation of ~53° (over ~98 nm thickness), with a remaining ~78° (over ~71 nm thickness). The increased angling observed in the diamond / Si_xN_y test sample further reinforces the severity of mask degradation, providing additional evidence in support of the mask breaking mechanism hypothesis.

To evaluate the robustness of the mask, the sample containing the triple-structure device layout undergoes 5 hours + 11 hours of QIE etching at a table temperature of 65 °C. Following the extended QIE sequential steps, clear signs of hard mask failure emerge at the interface (highlighted by red circles, Figure 2.5 (g)), evident in the SEM contrast between the vertical coverage of AlO_x and the progressively etched underlying diamond.

Upon examination of the same device after removal of the hard mask materials (Figure 2.5 (i)), a direct one-to-one correlation is observed between the regions previously suspected of mask failure and the final post-fabrication features. This further substantiates the breakdown of the mask, reinforcing the hypothesis of its progressive degradation during the etching process.

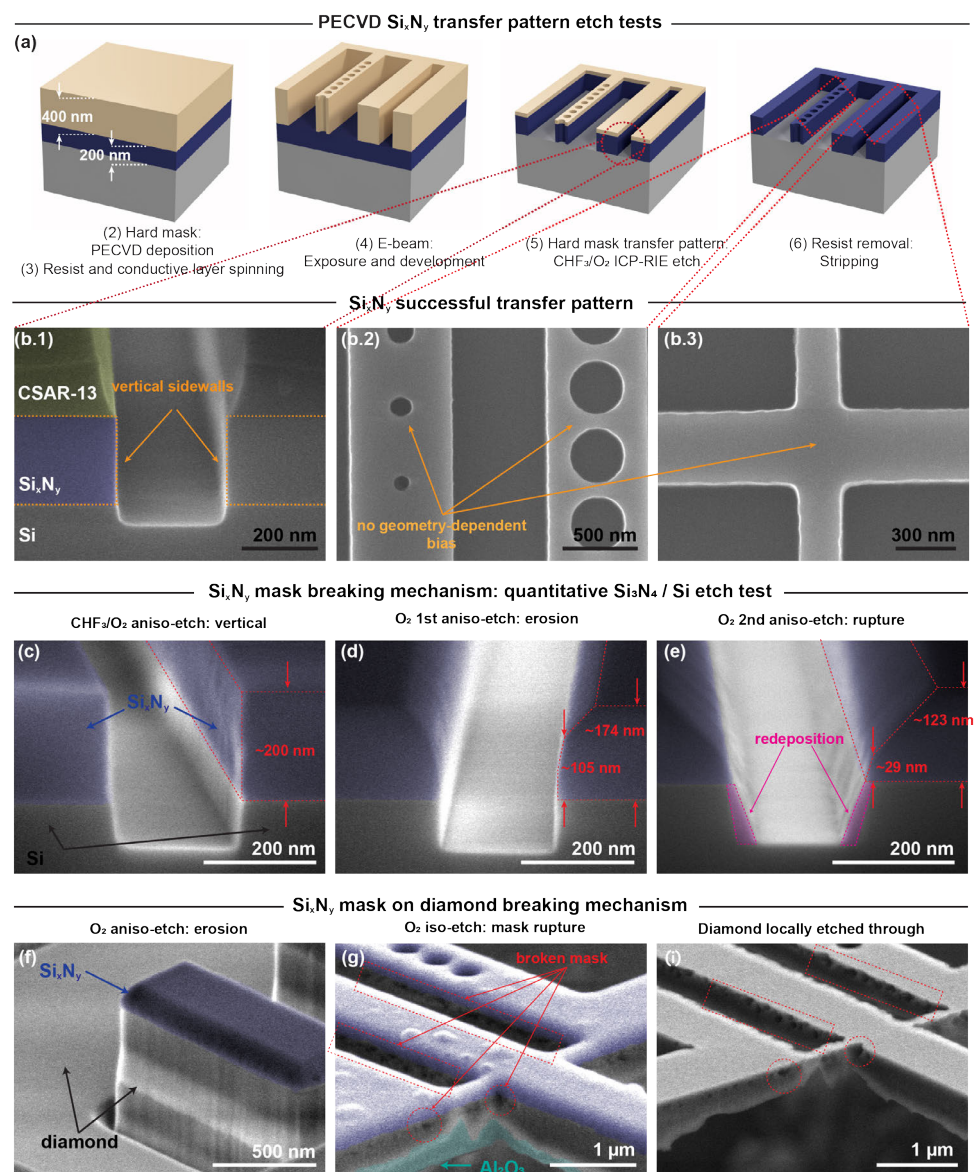


Figure 2.5: Si_xN_y Hard Mask Performance and Etch Tests | **Top panel:** PECVD Si / Si_xN_y transfer pattern etch tests: (a) Etch test fabrication steps for 400 nm CSAR-13 / 200 nm Si_xN_y ; (b.1) Cross-section SEM (85° tilt) of benchmark etched trench lines; (b.2) Top-view SEM (0° tilt) of telecom-wavelength designed patterned structures: coupling waveguide tapered mirror holes (left) and photonic crystal cavity (right); (b.3) Cross-bar structure for SnV center tailored nanophotonic waveguide. | **Middle panel:** Si / Si_xN_y anisotropic O₂ ICP-RIE tests: (c) Same as (b.1), after resist removal; (d) First O₂ anisotropic etch: significant edge erosion, leaving 105 nm vertical sidewall mask material; (e) Second O₂ anisotropic etch: further mask erosion, nearly no sidewall protection at the interface. | **Bottom panel:** Mask failure and correlation with etched-through diamond devices: (f) Etch test on diamond confirms Si_xN_y erosion after anisotropic O₂ ICP-RIE; (g) Triple-structure suspended devices after O₂ QIE steps: mask rupture observed (red circles); (i) One-to-one correlation between broken mask areas and etched-through diamond regions.

CONCLUSIONS

In this section, we have demonstrated that anisotropic O₂ ICP-RIE etching causes severe erosion of the Si_xN_y hard mask. Notably, the erosion effects are more pronounced when the etch is performed in consecutive separate steps rather than a single continuous etch of equivalent total duration. In the two-step anisotropic O₂ ICP-RIE etch variant of the QIE-based fabrication process, the residual protective Si_xN_y hard mask exhibits a severe sidewall angle of approximately 45°, resulting in a lower overall sidewall angle and residual Si_xN_y at the substrate interface. Consequently, the remaining 29 nm thick Si_xN_y layer may continue to erode during the extended quasi-isotropic diamond etch, ultimately leading to mask failure.

To further investigate this degradation mechanism, anisotropic O₂ etch tests are conducted on diamond / Si_xN_y samples, confirming significant erosion at the interface. Additionally, QIE etching of diamond photonic devices at 65 °C table temperature reveals that Si_xN_y breaks during the undercut process. As a result, the etched diamond devices exhibit reduced mechanical stability at the edges, often leading to breakage at the holding bars. Furthermore, the increased surface roughness at the edges is suspected to contribute to high optical losses. The quality factor of the fabricated devices is measured to be lower than the simulated values, as reported in Ruf M., PhD Thesis [13].

In conclusion, due to the enhanced erosion of Si_xN_y, the second anisotropic O₂ etch step (after BCl₃/Cl₂ ICP-RIE) is omitted from 65 °C QIE-based variant fabrication process. This adjustment mitigates the hard mask erosion effects caused by anisotropic O₂ ICP-RIE, ensuring the robustness of the mask throughout the fabrication process. This modification of the process, nevertheless, comes with the trade-off of a slower overall quasi-isotropic undercut etch during fabrication step (10).

2.6.2 TELECOM-WAVELENGTH DIAMOND CAVITY DEVICES

In the following Section 2.6.3, 2.6.4 and 2.6.5 we present the results of the overall 65 °C QIE-based variant, developed following the methods described in Section 2.5.1, for which the optimized final set of parameters are detailed in Appendix A.2, Table A.3. This variant of the QIE-based variant fabrication process showed a successful fabrication of telecom-wavelength PCCs (for which representative results are shown in Figure 2.6 and Figure 2.7) and 620 nm photonic waveguides (for which representative results are shown in Chapter 4. Consequently, the benchmark test design chiplets employed through the development and optimization process are the design of the triple structure device and the waveguide chiplets schematically illustrated in Figure 2.2 (a) and (b)).

2.6.3 TRANSFER PATTERN

Referring to Figure 2.1 for the fabrication steps, this section presents and discusses the optimized results achieved after multiple rounds of refinement of the process parameters. To demonstrate the robustness of the developed fabrication process, SEM inspections are performed at key fabrication stages (Figure 2.6 and Figure 2.7), ensuring that interleaved imaging does not introduce cross-contamination or compromise the final result.

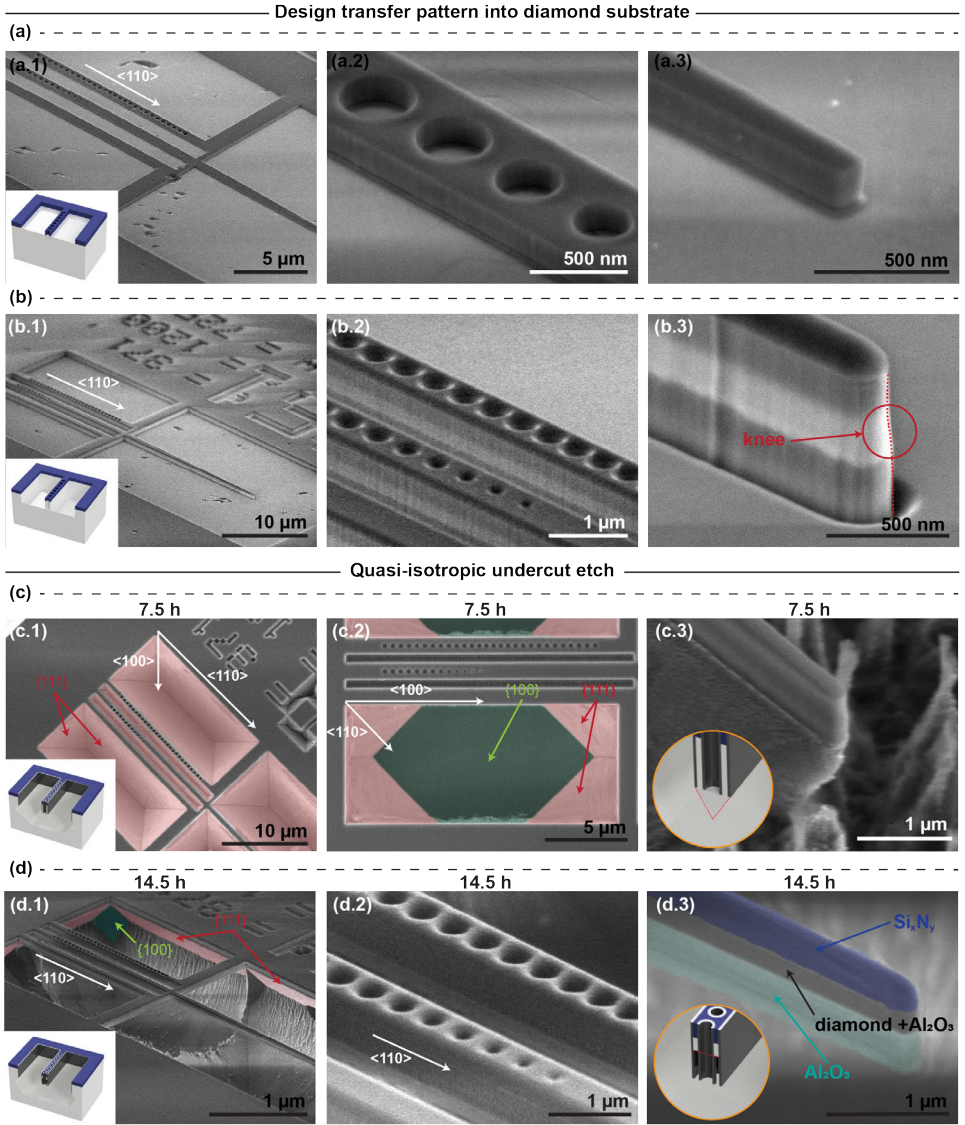


Figure 2.6: 65 °C QIE-based fabrication process: telecom-wavelength tailored nanophotonic devices | Upper panel: design transfer pattern into the diamond substrate: | (a) After fabrication step (6): (a.1) Overview of the patterned $\langle 110 \rangle$ aligned triple structure in Si_xN_y hard mask; (a.2) Zoom in of the cavity region inspection of the circular holes and sidewalls; (a.3) Zoom in of the coupling waveguide taper end; | (b) After fabrication step (7): (b.1) Same device as in (a.1), after anisotropic O_2 ICP-RIE; (b.2) Zoom in of the coupling waveguide (center) and cavity defect region (right); (b.3) Same as in (a.3), after O_2 etch: Si_xN_y mask erosion at the tip due to anisotropic O_2 ICP-RIE; Bottom panel: 65 °C QIE sequential steps (c) After 7.5 h QIE | (c.1) Same device as in (a.1) and (b.1): exposed $\{111\}$ family of planes, parallel to the $\langle 110 \rangle$ aligned devices; (c.2) Same device as in (c.1) but $\langle 100 \rangle$ aligned; (c.3) Same as in (a.3) and (b.3), after first QIE step; | (d) After additional 7 h QIE, second QIE step; | (d.1) Same device as in (a.1), (b.1) and (c.1); (d.2) Same device as in (b.2); (d.3) Same as in (a.3), (b.3) and (c.3): the thickness of the diamond devices can be monitored through the thin AlO_x hard mask during upward-etch.

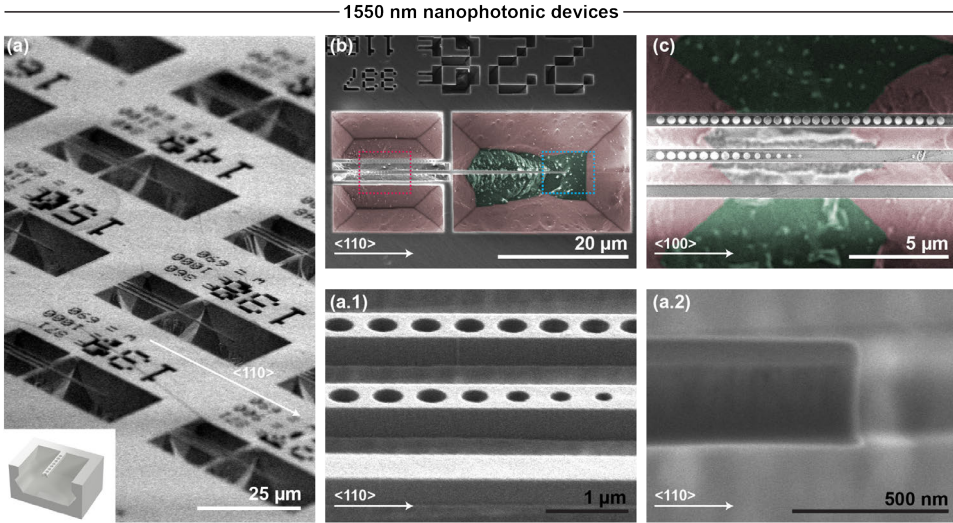


Figure 2.7: 65 °C QIE-based fabrication process: telecom-wavelength tailored nanophotonic devices Total QIE duration 15 h 10 min | (a) SEM sample overview (62° tilt view); (b) <110> aligned and (c) <100> aligned devices (top-down view, 0° tilt); (a.1) Zoom in on <110> aligned devices cavity defect region; (a.2) coupling central waveguide taper (62° tilt view).

Fabrication steps (1) to (6): hard mask transfer pattern

The transfer pattern of the design of the layout of the triple structure device (schematically illustrated in Figure 2.4.1 (a)) is achieved on diamond substrates (Figure 2.6 (a)) with optimized process parameters (Appendix A.2, Table A.3). This confirms the reliability of the Si / Si_xN_y developed etch test protocol (Section 2.5.2).

SEM inspection at 55° tilt angle enables evaluation of vertical sidewall angle and qualitative evaluation of the Si_xN_y sidewall surface roughness. The design of the triple structure device is aligned with <110> diamond crystallographic direction. From the general inspection (Figure 2.6 (a.1)), it can be seen that the Si_xN_y hard mask is fully etched and removed from the surrounding area in the vicinity of the device.

A higher SEM magnification of the PCC in the cavity region (Figure 2.6 (a.2)) allows evaluating the sidewalls of the cavity edges, finding a ~90° sidewall angle, linear and uniform edge profile. At the same time, the patterned circular holes maintain the circular aspect and are fully etched through. From this SEM inspection, no RIE lag is identified. The same high magnification SEM inspection of the coupling waveguide taper (Figure 2.6 (a.3)) confirms that the rectangular taper shape is fully transferred into the mask material Si_xN_y in a reliable top-down transfer pattern, one-to-one for the respective dimensions of the features. The surface roughness of the Si_xN_y vertical sidewalls is not quantitatively resolved at the respective SEM magnification. However, the finite magnitude of the roughness of the Si_xN_y vertical sidewalls is transferred directly to the diamond substrate at the next fabrication step, for which the effects can be identified correspondingly.

Fabrication step (7): anisotropic O₂ ICP-RIE

In this fabrication step, anisotropic O₂ ICP-RIE in diamond transfers top-down the layout chiplet pattern from the Si_xN_y into the diamond substrate.

An SEM inspection of the device (the same as in Figure 2.6 (a.1)) after the ICP-RIE step confirms the absence of micromasking on the planar etched diamond surfaces (Figure 2.6 (b.1)). This validates the effectiveness of the organic and inorganic resist wet etch methods detailed in Section 2.5.1. Notably, all e-beam resist residues are completely removed. Together with full clearance of the Si_xN_y mask material in the previous etch step, prevent the formation of unwanted nanopillars in the open areas surrounding the diamond device.

At higher SEM magnification, the PCC cavity region and the coupling waveguide (Figure 2.6 (b.2)) reveal that anisotropic O₂ ICP-RIE produces sidewalls with no significant deviation from vertical alignment at 90°. However, SEM inspection shows that the diamond vertical sidewalls exhibit surface roughness higher than sub-nanometer scale. This roughness originates from the roughness of the Si_xN_y mask surface, which is transferred top-down with high accuracy upon anisotropic O₂ ICP-RIE. The surface roughness of the diamond sidewalls observed here may ultimately degrade the quality factor of the devices.

In the regions corresponding to the circular etched holes, the Si_xN_y mask does not maintain fully vertical sidewalls at this stage of fabrication. As discussed in Section 2.6.1, the Si_xN_y mask undergoes severe erosion under high-power ICP-RIE O₂ etching. This effect is particularly evident around the circular holes, where the remaining Si_xN_y layer exhibits significant thickness inhomogeneity. This yields tapered circular holes in the diamond substrate.

At high SEM magnification, the device taper (Figure 2.6 (b.3)) clearly reveals the impact of anisotropic O₂ ICP-RIE etching on both the top-down etched diamond profile and the Si_xN_y mask. Close examination of the Si_xN_y thickness shows that the mask profile is significantly altered. As demonstrated in the Si / Si_xN_y anisotropic O₂ etch tests (Section 2.6.1), the estimated angling of Si_xN_y due to O₂ etch erosion is approximately 45° on each edge of the taper. Given the minimal taper widths of 50 nm to 100 nm, an extended O₂ anisotropic etch causes the angled sidewalls from the three taper edges to converge. This leads to a significant reduction in mask thickness in the taper region compared to wider sections of the taper and waveguide.

The Si_xN_y mask thickness, initially aligned with the nominal values observed in the waveguide region, gradually decreases toward the taper tip, following the taper's design profile. This poses a fabrication challenge, as it indicates that narrow-width waveguides experience accelerated mask erosion due to enhanced edge degradation. To counteract this, an adequate initial Si_xN_y mask thickness is required to compensate for the erosion effect.

The second consequence of this effect is that this enhanced mask erosion leads to an overall Si_xN_y thickness reduction over the longitudinal taper profile. This results in a potential mask failure site, which allows QIE plasma penetration during fabrication step (10), which could lead to unintended protective mask deterioration and etching of the entire taper structure.

Furthermore, this erosion-induced thinning of the mask in the taper region translates into a non-vertical diamond taper tip sidewall profile, as evident in the knee profile observed in Figure 2.6 (b.2) (marked in red circles). This knee profile presents a vulnerability in process robustness: Following passivation with AlO_x, the subsequent BCl₃/Cl₂ highly

anisotropic ICP-RIE step may etch through the AlO_x layer at the knee, breaking the protective coverage and exposing the underlying diamond. This exposure could lead to unintended etching of the entire taper structure, further compromising the fabrication process.

Nevertheless, we identify a Si_xN_y ~ 200 nm starting thickness, combined with an O_2 ICP-RIE etch yielding a $\times 2.5$ final device thickness, as an optimal trade-off. This approach ensures that a sufficient vertical mask thickness remains post-etch, maintaining structural integrity. In contrast to QIE-based fabrication methods reported in the literature [5, 7], where O_2 etch erosion is not explicitly accounted for, we omit a second anisotropic O_2 ICP-RIE step to mitigate excessive mask erosion and enhance the stability of our devices, with the disadvantage of QIE undercut steps in fabrication step (10) that require considerably longer etching duration.

2.6.4 VERTICAL SIDEWALL PASSIVATION

At this stage, as described in Section 2.5.1, next fabrication step is vertical sidewalls of the patterned diamond device passivation (step (8)): we find ALD of AlO_x for ~ 20 nm to 25 nm, similar to Ref. [7] to be the optimal value, preserving the integrity of the sidewalls. Next, in fabrication step (9), while Ref. [7] removes the top layer of AlO_x with a CF_4 ICP-RIE plasma chemistry; in our case we employ a BCl_3/Cl_2 plasma chemistry (parameters detailed in Appendix A.2, Table A.3). The challenge associated with the BCl_3/Cl_2 etch recipe lies in its relatively high etch rate for the AlO_x , combined plasma instability.

Slight variations in plasma stability significantly impact the effectiveness of the overall BCl_3/Cl_2 ICP-RIE of AlO_x horizontal coverage. This aspect is exacerbated in case of high etching rate plasma, i.e. short etching duration. Without an adequate tolerance margin for the etch step, under-etching of the AlO_x film from the planar diamond interface may occur as a result. Such under-etching compromises the O_2 QIE ICP-RIE undercut process, as the O_2 QIE plasma cannot reach the underlying diamond substrate. Additionally, AlO_x exhibits relatively high selectivity to O_2 QIE plasma, preventing AlO_x mask breakthrough regardless of the total duration of the O_2 QIE undercut steps.

On the other hand, excessive BCl_3/Cl_2 overetching can lead to unwanted lateral etching, which may thin the vertical AlO_x film coverage and expose the sidewalls of the patterned devices to subsequent etch steps. Thus, in order to decide the maximum overetch value, etch tests in ICP-RIE BCl_3/Cl_2 of ALD AlO_x on Si / Si_xN_y test samples (prepared following methods described in Section 2.6.1) are conducted. The tests carried out do not show significant lateral etching of AlO_x .

Thus, in order to ensure efficient and full clearance of the AlO_x film from the planar diamond interface, we systematically implement a $\sim 25\%$ to 30% overetch, without compromising the vertical coverage integrity of the protective film.

Fabrication steps (8) and (9) are monitored by spectroscopic ellipsometry on Si / AlO_x twin test samples, while direct SEM inspection is deliberately avoided to prevent cross-contamination, which is highly likely at this stage of the fabrication process.

2.6.5 QUASI-ISOTROPIC UNDERCUT

Fabrication step (10): QIE undercut

Once both top protective Si_xN_y and the sidewall AlO_x layers are prepared, the diamond substrate undergoes O_2 QIE (parameters detailed in Appendix A.2, Table A.3) iterative steps after the fabrication step (9). In the 65°C QIE-based variant, QIE etch is distinguished by an extended etch duration, typically several hours. Here we show the results of typical two-step long QIE iterative undercut.

The SEM-overview inspection of the triple structure device layout (same as in (c), (b) and (a)) upon the first O_2 ICP-RIE QIE step of 7.5 h duration, at table temperature 65°C is shown in Figure 2.6 (c). The $\langle 110 \rangle$ crystallographic direction (Figure 2.6 (c.1)) and $\langle 100 \rangle$ crystallographic direction aligned devices show different undercut etch as a result. As expected from the QIE etch mechanism for 0 RF forward power (described in Section 2.2.2), $\{111\}$ planes (red false colored) and $\{100\}$ planes (green false colored) are revealed.

The $\langle 110 \rangle$ direction aligned devices exhibit $\{111\}$ planes parallel to the longitudinal direction of the devices. For prolonged QIE etch, the $\{111\}$ planes etch further recessing in the $\langle 100 \rangle$ direction, eventually converging underneath the triple structure device layout. In the case of $\langle 110 \rangle$ alignment of devices, given that $\{111\}$ planes recess at the same rate in the $\langle 100 \rangle$ direction longitudinally to the patterned longitudinal device cross section, this enables a uniform longitudinal undercut of devices. As a result, $\langle 110 \rangle$ aligned devices show the same cross section and thickness throughout the whole length.

In the $\langle 100 \rangle$ direction aligned devices case, as the etch rate along $\{100\}$ crystallographic planes is higher than the etch rate along $\{111\}$ crystallographic planes, the undercut mechanism is different with respect to the alignment of devices along $\langle 110 \rangle$ direction.

Specifically, $\{001\}$ planes are revealed by the QIE etch along with $\{111\}$ planes recessing in the $\langle 111 \rangle$ direction at a lower speed from the center of the device and the $\{001\}$ planes recess at a faster speed in the $\langle 001 \rangle$ direction. As a result, the $\langle 100 \rangle$ aligned devices start to undercut faster in the longitudinal center ($\langle 001 \rangle$ etch rate higher than $\langle 111 \rangle$) progressing towards the edges of the devices at a rate equal to the $\langle 111 \rangle$ equivalent direction of the receding $\{111\}$ planes. For a sufficiently long QIE duration, the resulting undercut devices present a rectangular cross section throughout the device length.

However, if the undercut etch is not completed, the resulting devices will present a center device of rectangular cross section, with a transition to triangular cross section and higher thickness towards devices edge: this effect is detrimental for both waveguide devices (increasing thickness of the device allows multimodal propagation) and photonic crystal cavities (mirror regions with a higher thickness affects the bandgap of allowed resonating modes).

Finally, a higher SEM magnification inspection of the $\langle 110 \rangle$ aligned (the same as in (a.3) and (b.3)) coupling waveguide taper end (Figure 2.6 (c.3)) shows a triangular cross section of the undercut taper end. For the same duration of the QIE etch, it can be observed that the stage of the undercut of the device taper is considerably more advanced with respect to both $\langle 100 \rangle$ aligned and $\langle 110 \rangle$ aligned triple structure, where the $\langle 110 \rangle$ aligned is the slowest.

Considering the $\langle 110 \rangle$ aligned triple structure and the taper device, this can be explained as follows: Based on the mechanism of QIE etching along the crystallographic planes, a complete undercut is obtained when recessing $\{111\}$ in the $\langle 100 \rangle$ direction converge

underneath the patterned devices. Therefore, a full undercut of an effective width of the triple structure (lateral device distance $2 \times g_w$ + waveguide width $2 \times w_{wg}$ + PCC width w_{wg}) requires a longer etch time with respect to an effective width of the taper (effective width of w_{wg} , narrowed to the minimum taper width w_t). Therefore, higher-width devices require longer QIE undercut duration compared to their narrower-width counterparts. Hence, in the QIE undercut, we observe [device aspect-ratio dependent undercut etch](#).

Next, SEM inspection of the triple structure device layout after the second 7 h O₂ ICP-RIE QIE step is shown in Figure 2.6 (d). The SEM overview of the <110> aligned triple structure device (Figure 2.6 (d.1), same as in (a.1), (b.1) and (c.1)) shows that after the second QIE step, the device layout is fully undercut. Notice the {100} and {111} planes revealed at the edge of the aperture. A higher SEM magnification inspection of the cavity region of the PCC and coupling waveguide terminating mirror (Figure 2.6 (d.2), same as in (a.2) and (b.2)) shows full suspension of both devices from the diamond substrate, as well as 'upward-etch'.

Next, a high SEM magnification inspection of the taper end (Figure 2.6 (d.3), same as in (a.3), (b.3) and (c.3)) shows the advancement of the upward etch. This can be clearly observed as the thickness of the diamond is decreased relative to the etched diamond in the fabrication step (7). Assuming there is no significant erosion of the surrounding AlO_x and no significant erosion of the upper Si_xN_y, the diamond taper device can be estimated from the SEM contrast obtained between Si_xN_y (false blue), diamond + AlO_x coverage (not colored) and the AlO_x skirt (false cyan colored). Considering the indirect measured thickness of the taper end with the thickness of the PCC and coupling waveguide, we observe that the taper end has a lower thickness with respect to the nanophotonic devices (paired in the triple structure layout device configuration), again indicating that the QIE undercut is device geometry aspect-ratio dependent.

Fabrication step (11): protective hard mask wet etch

Once the QIE undercut is completed at step (10), the sample undergoes inorganic clean: the masking materials are wet etched in HF 40% (methods Section 2.5.1). This fabrication step completes the fabrication process and the SEM inspection of the diamond devices is carried out (Figure 2.7).

The SEM overview of the diamond sample (Figure 2.7 (a)) shows typical large-scale fabrication of one-dimensional diamond nanophotonic waveguides and PCCs.

The SEM (top view) overview of the devices aligned with <110> and <100> crystallographic directions (Figure 2.7 (b) and Figure 2.7 (c), respectively) shows the topography of the diamond plane etched below: This is characterized by the presence of the {100} and {111} planes (green and red false colored, respectively). QIE-based process with the 65 °C table temperature yields an etched bottom plane characterized by a non-flat topography. In the eventuality of post-fabrication patterning of e.g. microwave driving electrode lines, the resulting bottom-plane topography represents a constraint, as this prevents a successful patterning (disrupted metal thin film deposition) on top of it.

In order to evaluate the thickness of adjacently placed 1D waveguide, coupling waveguide and PCC in the triple structure configuration layout, a higher SEM magnification inspection of the aforementioned devices is carried out at a 62° view tilt angle (Figure 2.7 (a.1)): the thickness of cavity region of the PCC, the coupling waveguide terminating mirror and the adjacent waveguide all present roughly the same thickness.

Same high SEM magnification inspection of the taper end (Figure 2.7 (a.2)) allows to evaluate the measured thickness of the taper at this stage of fabrication process: comparison of the measured value at this stage with indirect thickness estimation in the previous fabrication step shows in good agreement. Thus, we conclude that the sequential SEM inspection throughout the QIE undercut in the previous fabrication step is reliable for accurate estimate of upward etch.

2.6.6 CONCLUSIONS

The 65 °C QIE-based variant fabrication process has been extensively optimized through numerous Si / Si_xN_y etch tests and diamond / Si_xN_y evaluations, leading to the identification of an optimal parameter space, as detailed in Appendix A.2, Table A.3. The presented methods have proven effective in reliably fabricating telecom-wavelength tailored nanophotonic devices, including as 1D waveguides and PCCs. Additionally, this fabrication process has been successfully applied to the fabrication of SnV center emission tailored operating regime of nanophotonic waveguides, as it will be shown in Chapter 4.

In particular, the omission of the second anisotropic O₂ etch step in this QIE-based process variant ensures mask integrity throughout the entire fabrication sequence, enabling the successful long-duration QIE sequential steps. The process parameters are well-controlled, as demonstrated by interleaved SEM inspection monitoring at key fabrication stages (Figure 2.6 and Figure 2.7), ensuring that interleaved imaging does not introduce cross-contamination or compromise the final result.

This process is well-suited for fabricating large-scale devices with simple geometries. However, it presents two main limitations:

1. Challenging pattern transfer for smaller geometric dimensions and denser pattern, typical of SnV center emission tailored hole-based PCC designs.
2. Extended etch duration of QIE undercut phase, limited by the low QIE etch rates typical of the 65 °C QIE etch recipe.

So far, in the 65 °C QIE-based fabrication process variant, the O₂ QIE ICP-RIE recipe has been developed and optimized [13] on an Oxford Plasmalab 100 system, converging to recipe parameters detailed in Table A.3 (step (10)). Although successful undercut and fabrication of SnV center integrated photonic waveguides has been demonstrated with the QIE ICP-RIE at 65 °C, this low temperature variant of the process often exhibited relatively long quasi-isotropic etch duration steps. In fact, a complete undercut and upward etch of nanophotonic waveguides (results in Chapter 4) amounted to a total of ~ 18 h QIE ICP-RIE. A duration of this extent often results in challenges associated with stability of the plasma over a long duration of the etch, as well as extremely long etch duration times eroding the mask materials, eventually compromising the coverage robustness. Last but nonetheless important are pragmatic challenges associated with the availability of the tool and long processing times.

Despite these constraints, the developed methods and protocols serve as a strong foundation for the second process variant (250 °C QIE-based variant), which specifically addresses the above main limitations, as presented in the following sections.

2.7 METHODS: 250 °C QIE-BASED PROCESS VARIANT

As shown in Section 2.6.2, telecom-wavelength operating regime PCCs successful fabrication can be achieved with 65 °C QIE-based variant fabrication process. This variant of the fabrication process has also been suitable for the fabrication of SnV centers integrated nanophotonic waveguides, for which the results and the experiment are presented and discussed in Chapter 4.

Besides the main limitations of the 65 °C QIE-based variant listed in the conclusions of Section 2.6.2, this variant presents additional challenges such as non-uniform flat bottom diamond plane (underneath the fabricated chiplets). All of the previous combined investigations have incentivized us to develop a second variant of the QIE fabrication process, which would allow us to solve the aforementioned challenges.

In this Section, we present the development of the O₂ ICP-RIE QIE undercut etch recipe at a 250 °C table temperature (Section 2.7.1). Following, we present the challenges associated with the transfer pattern of the SnV center integrated PCCs (Section 2.7.2) and the optimization of the aspect-ratio of resist / Si_xN_y materials stack, demonstrating the efficacy of the developed methods, guaranteeing up to ~5 nm accuracy transfer pattern (Section 2.7.3). Next, we present the results on the performance of the optimized **250 °C QIE-based variant** fabrication process flow, demonstrating the reliable and systematically robust fabrication of PCCs in diamond (Section 2.8).

The benchmark test design chiplets used through the development and optimization process are the triple structure device design (Figure 2.8 (a)), the single standing waveguide chiplets, the double structure device chiplet, and single standing one-sided PCCs, schematically illustrated in respectively Figure 2.3 (a), (b) and (c).

2.7.1 250 °C QIE ICP-RIE RECIPE

In order to tackle the challenges previously discussed in Section 2.6.6, we have shifted focus and developed a higher temperature QIE recipe on an alternative ICP-RIE system (Oxford PlasmaPro Cobra).

The QIE crystallographic-dependent etch rates and principles have been studied in Ref. [14], demonstrating crystallographic dependent etch at 10 °C table temperature. A brief literature study of typical QIE ICP-RIE recipe variants parameters is presented in Table 2.3. As elaborated in Section 2.6.2, in order to preserve the integrity of the Si_xN_y hard mask through the 65 °C QIE-based fabrication process, we have opted to omit the optional second O₂ anisotropic etch step, at the expense of long duration of the full QIE devices undercut. This strategy is in contrast to the positive results reported by the authors in Ref. [8], introducing a second O₂ anisotropic etch step, which reduces the overall QIE undercut of two-dimensional PCCs to ~8 h. Considering that the full undercut of diamond devices is strongly dependent on the aspect ratio of patterned devices (Section 2.2.2 and Section 2.6.2), the duration of full undercut of one-dimensional PCCs is likely lower than in the reported case of two-dimensional PCCs. Although this duration is significantly shorter than the typical overall undercut etch times in our 65 °C QIE variant, the reported duration is still several hours, for which considerations on hard mask integrity throughout the etch process still hold.

| Literature | O ₂ precursor flow [sccm] | RF / ICP power [W] | Pressure [μ bar] | Temperature [$^{\circ}$ C] | Devices |
|-------------------------|--------------------------------------|--------------------|-----------------------|-----------------------------|--|
| Ref. [14] | 40 | Var / 900 | 13.3 | 10 | Study on QIE |
| Ref. [13], This work | 50 | 0 / 2500 | 15 | 65 | Telecom 1D PCCs, 620 nm 1D waveguides |
| Ref. [16] | 40 | 0 / 1100 | 13.3 | 150 | Telecom 1D OMCs, 2D PnCs |
| Ref. [7], Ref. [8] | N/A | 0 / 900 | 30 | 200 | 630 nm 1D and 2D PCCs |
| Ref. [22] | 99 | 0 / 2000 | 100 | N/A | 620 nm 1D PCCs |
| Ref. [1] | N/A | 0 / 3000 | 20 | 250 | 1550 nm Microdisk resonators |
| This work | 50 | 0 / 3000 | 20 | 250 | 620 nm 1D PCCs, 1D waveguides |
| Ref. [6], Ref. [36] | N/A | 0 / 3000 | N/A | 300 | 620 nm 1D PCCs, 1D waveguides |

Table 2.3: **O₂ QIE ICP-RIE etch recipes variants**: etch recipe variants parameters developed in and reported in literature. **Blue**: recipe parameters of the QIE ICP-RIE etch developed for the 65 $^{\circ}$ C QIE ICP-RIE in this work and in Ref. [13]; **Green**: variant reported for completeness, parameters published after we established **Burgundy**: recipe parameters of the QIE ICP-RIE etch developed for the 250 $^{\circ}$ C QIE ICP-RIE in this work based on parameters available from Ref. [1].

In general, to ignite the 0 RF forward power QIE plasma in a systematic and reproducible way, we insert an a priori ignition step. The ignition step recipe parameters are the same as the anisotropic O₂ ICP-RIE (detailed in Table A.4) for a duration of 15 seconds, where 90 W RF power is sufficient to efficiently ignite and stabilize the plasma in the reactor chamber. The additional advantage in using the same recipe parameters in the ignition step as the ones in the anisotropic O₂ ICP-RIE are that this etch recipe is fully characterized, a top-down etch rate of ~ 220 nm/min, which for a total ignition step duration of 15 s yields 55 nm etched extent. This ensures a short etch of the diamond material, at the same time not impacting the integrity of the mask materials aspect ratio. Next, a switching from 90 W RF / 1100 W ICP directly to 0 W RF / 3000 W ICP guarantees a smooth transition from anisotropic to QIE regime. The 15 s duration of the ignition step results as a trade-off between plasma stabilization and the diamond anisotropic etch rate.

As reported by the authors in Ref. [7], increased table temperature and pressure produces an increase in the chemical interaction rate with the diamond. This results in an overall increase in the etch rate of both {111} and {100} crystallographic planes.

Thus, with respect to the 65 $^{\circ}$ C QIE recipe, we decided to increase ICP power, pressure and table temperature recipe parameters to the respective values reported in Ref. [1], namely 3000 W ICP power, 20 μ bar chamber pressure and 250 $^{\circ}$ C table temperature. At the same time, in our new QIE recipe parameters variant, we keep a relatively high O₂ gas precursor flow of 50 standard cubic centimeters per minute (sccm). Last but not least, we keep the same reactor chamber temperature (60 $^{\circ}$ C) as in the 65 $^{\circ}$ C QIE recipe variant.

A calibrated combination of increased ICP power, pressure, and table temperature combined with a high precursor flow should yield significantly higher chemical interaction rates with the exposed diamond substrate, when compared to QIE recipe variants reported in literature (except for Ref. [22], published a-posteriori to our recipe development) to our knowledge (see Table 2.3). Our etch recipe has been tested on {100} oriented diamond substrates, on which the triple structure, double structure, single-standing one sided devices and nanophotonic waveguides chiplets benchmark layouts have been patterned with the

methods described in Section 2.5.1. The undercut and upward etch have been characterized, for which results will be presented in the following results Section 2.8.

The combination of parameters listed above has resulted in the **250 °C QIE recipe 3 major advantages:**

1. **Short full QIE undercut etch duration:** In contrast to full undercut of single-standing SnV center integrated nanophotonic waveguides (Chapter 4) of a total duration of 18 hours QIE at 65 °C, same design nanophotonic waveguides have been fully undercut and reached the design thickness for an etch duration of 1 hour and 20 minutes with this QIE recipe variant. Thus, by changing the recipe parameters from the 65 °C QIE recipe variant to the 250 °C QIE recipe variant, we observed a 13-fold reduction in the QIE undercut duration.
2. **Flexibility over Si_xN_y mask thickness:** The established 250 °C QIE recipe has been first implemented in the 65 °C QIE-based process variant in order to quantify the etch rates of Si_xN_y and AlO_x materials. We did not observe a significant quantitative difference between the etch rates determined with the 65 °C QIE recipe and the newly established 250 °C QIE recipe. However, the advantage of the considerably shorter duration of QIE undercut for full undercut and upward etching of nanophotonic devices offers now the advantage of optimizing the aspect ratio of the resist / Si_xN_y : under similar erosion etch rates for Si_xN_y , compared to the 65 °C QIE recipe, in the lower total undercut etch duration of the 250 °C QIE recipe, a thinner film of protective Si_xN_y hard mask material is now required. This is an advantage, as it allows a higher accuracy transfer pattern of CAD design into the Si_xN_y hard mask material, as will be shown in Section 2.7.3.
3. **Uniform {100} oriented etched and exposed bottom plane:** As will be presented in Section 2.8, as a result of enhanced chemical etching of the diamond substrate, the undercut bottom plane of the QIE etched surface exposed fully the {100} crystallographic plane, yielding close to perfectly flat bottom etched diamond plane underneath the patterned devices layout chiplets. This offers the advantage of post-QIE additional sequential fabrication of additional electric circuitry, necessary for e.g. microwave driving or Stark tuning of embedded into nanophotonic structures SnV centers. The {100} oriented bottom plane at a depth of $\sim 2\text{ }\mu\text{m}$ (dependent on the duration of the upward etch) offers the advantage of straightforward electrode patterning (uniform resist spin coating and metal deposition) as well as relatively close $\langle 100 \rangle$ distance from the integrated SnV centers into the suspended nanophotonic devices.

In conclusion, in this Section we presented the development of the newly developed 250 °C QIE recipe, as a result of the fine tuning of the recipe parameters between the previously developed (Section 2.6.2 and Ref. [13]) 65 °C QIE recipe and the QIE recipe variant developed by the authors of Ref. [1].

The recipe developed and presented here has been adopted as standard recipe for the diamond QIE-based fabrication process in Kavli Nanolab Delft.

Up to date, in addition to the nanophotonic devices presented in this work, this etch recipe has been successfully employed for the fabrication of diamond nanophotonic can-

tilevers for large-range tuning and stabilization of the optical transition of diamond SnV centers by in-situ strain control [10].

2.7.2 PATTERN TRANSFER BIAS

As discussed and shown in previous sections, the optimization on the transfer pattern (Figure 2.1 fabrication steps (2) to (6)) with high aspect ratio 400 nm CSAR-13 on 200 nm Si_xN_y, in the **65 °C QIE-based variant** fabrication process has demonstrated accurate transfer pattern for higher wavelength operation regime nanophotonic devices, as well as for relatively simple SnV center ZPL tailored nanophotonic waveguides fabrication (devices designs discussed in Section 2.4.1 schematically illustrated in Figure 2.2).

On the other hand, the aspect ratio stack 400 nm CSAR-13 on 200 nm has proven to be highly inaccurate in the case of pattern transfer of more complex design features, characteristic for hole-based design nanophotonic crystal cavities operating at the SnV center ZPL emission frequency (device designs discussed in Section 2.4.2 schematically illustrated in Figure 2.3).

In fact, when implementing the aforementioned set of parameters in the hole-based PCC design, tailored to the SnV center emission wavelength, the results of the transfer pattern etch test on Si / Si_xN_y test samples (prepared following the Methods described in Section 2.5.2, process parameters detailed in Appendix A.2 Table A.3), with this high aspect ratio stack 400 nm CSAR-13 on 200 nm Si_xN_y yields a poor accuracy transfer pattern, as shown in Figure 2.8.

Here, we first start by testing the transfer pattern of the triple structure device layout (Figure 2.8 (a)), adapted to operating ZPL SnV center frequency (structure design adapted from the benchmark triple structure design chiplet of 1550 nm PCC, **65 °C QIE-based variant**, adapted from Ref. [13]) As in the 1550 nm PCC case, the structure includes (top, green shaded) a nanophotonic waveguide, (middle) coupling waveguide and (bottom) an operating ZPL SnV center frequency photonic crystal cavity.

We investigate the chiplet transfer pattern (Figure 2.8 (b)) via SEM inspection (0° tilt view angle) of the test samples Si / (200 nm) Si_xN_y (fabricated following the methods described in Section 2.5.2), where no e-beam optimization is implemented (as in the case of **65 °C QIE-based variant**). The transfer pattern with such high aspect ratio stack shows high inaccuracy of the patterned devices compared to the design parameters. The poor accuracy between the obtained results and the design can be attributed to the effect of bias in the transfer pattern, which can be categorized roughly into types:

1. **Systematic bias:** this is a systematic constant bias over the dimensions of devices post transfer pattern phase, regardless of the pattern density or geometry.

In the case of ZPL SnV center operating frequency nanophotonic waveguides, this systematic bias can be easily compensated in the design phase of the devices: the systematic bias can be determined empirically from Si / (200 nm) Si_xN_y transfer pattern etch tests, following the discrepancy bias between the obtained dimensions (waveguide width w_{wg}) and the design one can be compensated with the following fabrication round on the diamond target substrate. This strategy has proven remarkably successful in the case of ZPL SnV center operating frequency nanophotonic waveguides, as demonstrated in Chapter 4.

In the case of ZPL SnV center operating frequency PCCs, this systematic bias can also be compensated in the design phase of the devices by varying the scaling of the devices (lattice constant a_n , hole radius r and nanobeam width w_{nb}). In principle, the consistent bias in the geometry of the devices can be compensated by varying the scaling of the devices (varying values of a_n , r and w_{nb} around the nominal values by $\pm 10\%$). Taking into account that the thickness of the devices is challenging to control and results the same across the entire diamond substrate for minimal variation in devices parameters, the thickness and the systematic bias are both compensated by e-beam writing different scalings of the parameters listed above.

2. **Geometry dependent bias:** The second aspect of the poor accuracy in the transfer pattern is the additional bias which is dependent on the geometry of the devices design. In the case of relatively simple geometry ZPL SnV center operating frequency nanophotonic waveguides, this bias is not empirically measurable. In the case of ZPL SnV center operating frequency PCCs this effect is strongly affecting the aspect of the patterned designs: distortions of both circular shape and nanobeam sidewalls of the devices are present, yielding an overall nanobeam shape quantitatively different from the designed one. This bias may be caused by e-beam writing effects, such as proximity effect and charging, which are exacerbated when exposing dense pattern designs, or other effects due to resist resolution. This type of bias is challenging to be systematically predicted and compensated in the design phase a priori, therefore in order to eliminate, an optimization in the fabrication process is necessary.

From a high magnification (underlying) SEM inspection image (Figure 2.8 (b.1), 0° angle tilt view) of the defect region and the tapered circular holes radius of the coupling mirror, overlaying (to scale) the design of the device geometry, clear systematic and geometry-dependent bias can be noticed.

We evaluated both the systematic bias on the nanophotonic (top) waveguide, and the geometry-dependent transfer pattern bias on the nanophotonic cavity (bottom). The systematic bias on waveguide-like structures amounts to ~ 30 nm to 35 nm. Next, the geometry-dependent bias is more challenging to evaluate, for which a zoom-in (underlying) SEM pictogram of the cavity region (overlying in green the design, to scale) is shown in Figure 2.8 (b.2). Here, the combination of typical small dimensions circular holes (142 nm optimal value) with narrow cavity width (275 nm optimal value) yields a highly inaccurate transfer pattern. First, the shape of the (in design, perfectly circular) holes in fabrication yields distorted rhomboidal openings, while the peripheral sidewall of the nanobeam (in design, perfectly linear) in fabrication yields a severely corrugated profile. Second, given the severe distortion of the nanobeam shape, it is challenging to evaluate the precision of the hole position.

As a consequence, given the aspect of the patterned Si_xN_y determines the downstream diamond PCC geometry, the results shown in Figure 2.8 (b) would produce a completely unpredictable operation wavelength (if any) of the patterned cavity.

Implementing e-beam PEC and multipass to mitigate bias

The first hypothesis on the phenomenon causing both systematic bias and geometry-dependent bias has been a poor e-beam writing exposure, as in the previous transfer pattern etch tests no proximity effect correction (PEC) or lateral development (LD) calibration of

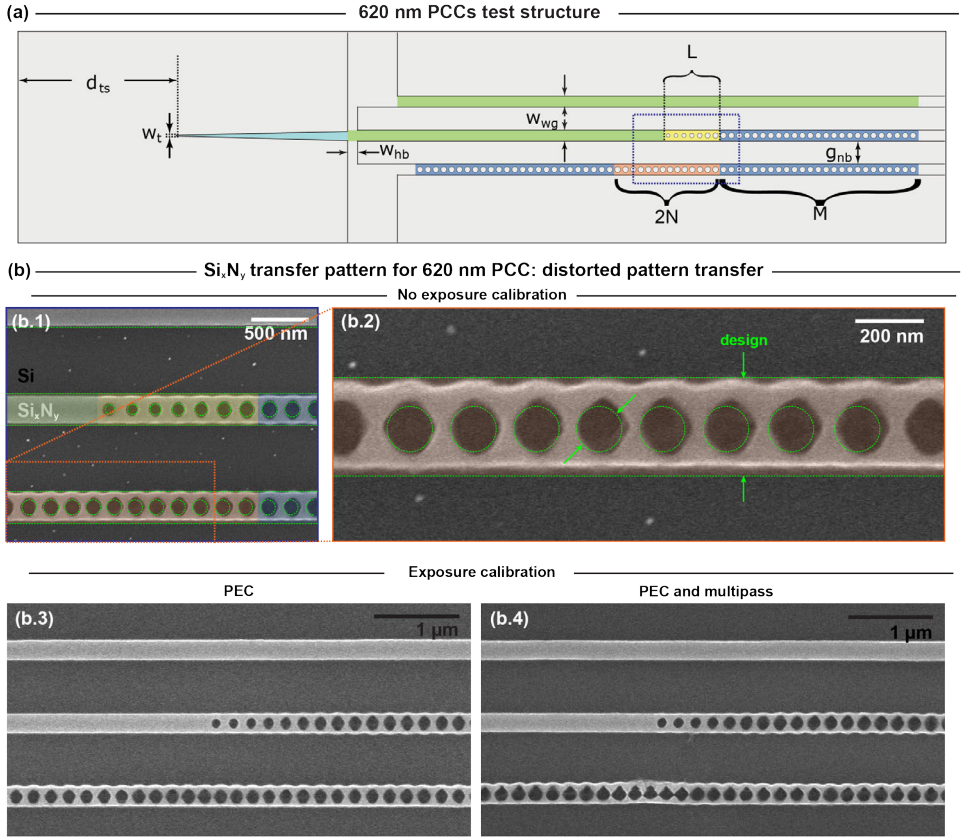


Figure 2.8: **High aspect ratio stack (400 nm CSAR / 200 nm PECVD Si_xN_y) pattern transfer bias** | (a) Schematic of triple structure chiplet design adapted to ZPL SnV center operating frequency, similar and adapted from 1550 nm triple structure chiplet [13]; | (b) PEC and multipass e-beam exposure do not improve the accuracy in the design transfer pattern: SEM (0° tilt view) pictograms of pattern transfer on Si / 200 nm Si_xN_y design structure in (a), respectively with no e-beam optimization (b.1) (overlaid in dashed-green the design dimensions, to scale), (b.2) zoom-in of the cavity region of (b.1); (b.3) PEC implemented, (b.4) combination of PEC and multipass implemented; This aspect ratio stack demonstrates high fidelity transfer pattern of 1550 nm triple structure chiplet and ZPL SnV center operating frequency nanophotonic waveguides, with minimal deviation in critical dimensions (systematic bias), for dense patterns characteristic of hole-based design nanophotonic cavities operating at SnV center ZPL frequency severely suffers of geometry dependent non-systematic bias, challenging to compensate in design phase.

the e-beam writing was implemented. Given that in the case of nanophotonic cavities, the pattern density is relatively high, the proximity effect leads to overexposure of the dense patterns in the circular holes layout region. Hence, a PEC may mitigate the distortions of the pattern due to unwanted exposure upon electron scattering and surplus exposure due to generated secondary electrons within the bulk target material. Next, considering that the exposed substrate is insulating and charging, an e-beam exposure in multipass would mitigate additional effects such as resist heating and charging effects.

Thus, as a starting strategy, to reliably compare fabrication results, within the same fabrication run, on identical Si / Si_xN_y test samples, same geometry and layout benchmark test designs with no calibration implemented, PEC implemented, PEC and multipass implemented, respectively, have been e-beam exposed.

Namely, first we implement a proximity effect correction (PEC): we simulate the PEC in the TRACER software with a Monte Carlo simulation over the system materials stack, combined with the electron beam parameters (beam acceleration energy and beam spot size). We determine the point spread function (PSF), based on which we then implement the PEC: this allows us to compensate for local backscatter energy due to e-beam exposure in the vicinity of the exposed feature, taking into account the pattern density (as well as shape and dimension). For the sake of rigor, in TRACER and BEAMER software, we have simulated the PEC for both a diamond substrate and a Si substrate, with minimal differences in the pattern-calibrated dose distribution.

Next, in addition to implemented PEC, we add a multi-pass exposure, specifically a two-pass, in order to further reduce the charging effects of the substrate: In a two-pass exposure, the exposure dose is reduced and the time delay between the two subsequent e-beam pass allows the accumulated charge in the substrate to dissipate. Although effects such as charging and resist heating, in principle, behave differently on a diamond substrate with respect to a Si substrate; here we conduct the above tests as a preliminary guideline on Si substrates, in order to first observe whether the pattern distortion is attributable to the aforementioned detrimental effects to start with.

We then proceed with SEM inspection (the same procedure as above) of the same chiplet layout device as in Figure 2.8 (a), here after a PEC is applied to the e-beam writing and after a combination of PEC and multipass are applied (Figure 2.8 (b.3) and Figure 2.8 (b.4), respectively). For the same e-beam parameters such as beam spot size, pattern fracture, writing order and respectively determined optimal exposure clearing dose, both (b.3) and (b.4) present a systematic bias of ~20 nm to 25 nm. Although this systematic bias has a lower value with respect to a lack of PEC and no multipass applied, still the improvement is not yet substantial. Next, the geometry-dependent bias does not present any substantial improvement with respect to no optimization applied.

For the sake of rigor, the same methods and tests (implementing the diamond / Si_xN_y PEC and adjusting the resist clearing exposure dose) have been carried out on diamond / Si_xN_y substrates, with no difference in outcome. Charging effects are more pronounced on insulating substrates with respect to the tested semiconducting silicon substrates, thus, if any difference due to charging effects in between the tests on the two types of substrates had been present, we would have suspected the diamond substrate case to be more affected. This has proven not to be the case, as charging effects are compensated on diamond substrates in the fabrication phase by the combination of e-beam writing parameters with the applied thin film of conductive polymer.

From these results, we conclude therefore that the overall bias in the transfer pattern is not largely a result of e-beam undesirable writing effects such as proximity effects or charging, and thus overall not due to non-optimal e-beam exposure. We shift our focus towards properties of the Si_xN_y hard mask material and the transfer pattern aspect ratio stack.

2.7.3 OPTIMIZING TRANSFER PATTERN: LOW ASPECT-RATIO AND ICP-CVD Si_xN_y

E-beam exposure tests (Section 2.7.2) have shown that the systematic and geometry-dependent bias in the transfer pattern of ZPL SnV center operating frequency tailored hole-based design cavities is not due to poor e-beam writing set of parameters, PEC and/or charging effects. Therefore, the next hypotheses considered on the origin of the pattern mismatch into the Si_xN_y hard mask material focus on the aspect ratio of the resist / Si_xN_y stack of materials. In order to obtain a higher reliability in the transfer pattern, minimizing the total bias, intuitively one should reduce the patterning aspect ratio and specifically the thickness of the e-beam resist. This consideration stems from the fact that the positive e-beam resist used in our process has a limited resolution (as per datasheet reported resolution best value of 6 nm). Next, when etching in CHF_3/O_2 highly inductively coupled plasma, local heating of the resist may occur, with the consequence of local deformation of the resist sidewalls during the ICP-RIE process itself.

However, considering the moderate selectivity of the e-beam resist to CHF_3/O_2 ICP-RIE plasma etch, reducing its thickness imposes the strong constraint of a shorter total etch time. In turn, this requires the Si_xN_y film thickness to be reduced, such that for the same total etch time, the mask is cleared out from the desired openings on the diamond substrate. Hence, for the requirements of the QIE-based fabrication process (Section 2.3), a lower Si_xN_y film thickness necessarily requires a higher etch resistance to the downstream O_2 and BCl_3/Cl_2 anisotropic as well as the QIE O_2 etch steps.

For the purpose of increasing the Si_xN_y etch resistance, we had first experimented with rapid thermal annealing (RTA) treatment of PECVD-deposited Si_xN_y (results not presented here): Literature study shows that treatment with RTA at 1000°C in LPCVD Si_xN_y has proven a densification of the film, indicative of a rearrangement to approach the film structure of a stoichiometric silicon nitride [37]. In turn, upon such treatment, we expect the etch resistivity of PECVD Si_xN_y to increase under plasmas of interest in the QIE-based fabrication process. From the series of tests conducted on Si / Si_xN_y test samples, RTA treated at 1000°C for a duration of 5 min in forming gas (mixture of hydrogen (H_2) and nitrogen (N_2)), we measure a reduction in Si_xN_y thickness of $\sim 11\%$, indicative of film densification. However, RTA treated Si_xN_y has shown no significant etch rate difference both to CHF_3/O_2 ICP-RIE and anisotropic O_2 ICP-RIE plasma etch. Hence, we concluded that high temperature thermal treatment was not efficient in increasing the etch resistivity of PECVD Si_xN_y .

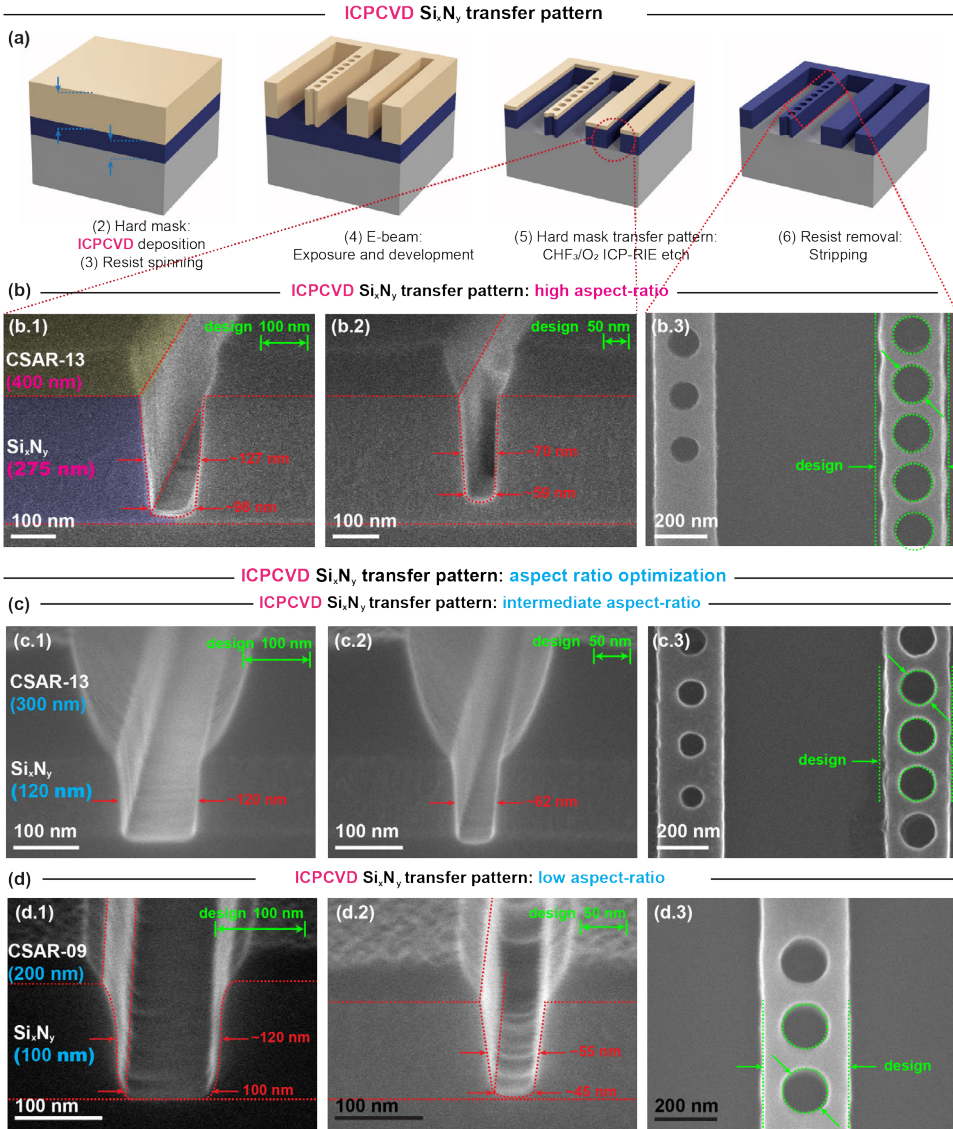


Figure 2.9: Minimizing transfer pattern bias: higher etch resistivity ICPCVD Si_xN_y allows for lower aspect ratio resist / mask stack. This minimizes both systematic and geometry dependent bias: high degree of fidelity between the intended design and the fabricated structures. | (a) Left to right: fabrication steps foreseen in the ICPCVD Si / Si_xN_y etch test; | (b) **High aspect-ratio:** 400 nm CSAR-13 / 275 nm Si_xN_y ; (b.1) and (b.2) SEM pictogram (85° tilt view angle) show the cross section of narrow width etch line trenches; (b.3) (underlying) SEM pictogram (0° tilt view angle) of patterned in Si_xN_y SnV center ZPL frequency operating nanophotonic structures design (overlying, in dashed-green, to scale); Systematic and geometry bias present, to a lower degree with respect to PECVD Si_xN_y ; | (c) **Intermediate aspect-ratio:** 300 nm CSAR-13 / 120 nm Si_xN_y ; (c.1) and (c.2) same benchmark etch test lines as in (b.1) and (b.2) respectively; (c.3) same as in (b.3): systematic bias ~20 nm, lower geometry bias pattern transfer; | (d) **Low aspect-ratio:** 200 nm CSAR-09 / 100 nm Si_xN_y ; minimal systematic bias, no geometry dependent bias.

Alternatively, we started investigating an alternative Si_xN_y deposition method and deposition recipe: we change the material deposition from PECVD to an inductively coupled plasma chemical vapor deposition (ICPCVD) method. ICPCVD deposition method is characterized by a plasma of higher density when compared to that of the PECVD counterpart, which allows for the deposition of high-quality denser dielectric films, with a lower hydrogen content (when compared to PECVD) at low temperature. Next, we shift from a 300 °C table temperature deposition to 400 °C: given a certain deposition recipe, a higher deposition temperature allows for a lower density of defects thin films and a closer material composition to the stoichiometric Si_3N_4 (stoichiometric Si_3N_4 can be obtained with the LPCVD deposition method). The ICPCVD Si_xN_y deposition recipe parameters are detailed in Appendix A.3 Table A.4.

Figure 2.9 shows the etch tests on Si / Si_xN_y samples process steps, where we start the investigation on the performance of ICPCVD deposited Si_xN_y with the new deposition recipe.

Following the etch test fabrication steps (described in Section 2.5.2, shown here in Figure 2.9 (a)), we start the investigation on the performance of ICPCVD deposited Si_xN_y with the new deposition recipe on Si / Si_xN_y test samples.

As baseline, on a non-patterned Si / Si_xN_y we determine the etch rate of ICPCVD Si_xN_y ~90 nm/min, through spectroscopic ellipsometry measurements.

Next, for the same e-beam exposure parameters as in previous Sections (beam spot size 2 nm, beam current 256pA, implemented PEC correction), same CSAR-13 resist parameters (400 nm thickness) and test patterns as in the PECVD deposited case, we evaluate the transfer pattern in the ICPCVD Si_xN_y . The optimal exposure clearing dose is determined within the same etch test rounds: here the presented results in Figure 2.9 (b), (c) and (d) illustrate the etch test results with the determined optimal exposure clearing dose for the respective stack of materials aspect-ratios.

After fabrication step (5), the Si / Si_xN_y samples are cleaved to allow SEM investigation (85° angle tilt view) of the vertical transfer pattern on (resist not cleared) benchmark etch test lines are patterned with variable width to test the highest resolution in the pattern transfer, while evaluation of transfer pattern bias on patterned nanophotonic structures (resist cleared out) is allowed with top-down SEM inspection (0° angle tilt view).

We start with a high aspect ratio of the stack materials 400 nm CSAR-13 on 275 nm Si_xN_y (Figure 2.9 (b)), similar thickness parameters to the PECVD stack tested previously. This bridging test allows us to assess the exposure dose of the e-beam writing and applied PEC to the newly ICPCVD material. Specifically, the ICPCVD Si_xN_y thin film may have a different stoichiometry and hydrogen content compared to the PECVD counterpart, therefore the charging of the material may be different.

In a 85° view angle SEM inspection on cross-section etch line trenches on 100 nm (Figure 2.9 (b.1)) and 50 nm (Figure 2.9 (b.2)), respectively, etched trench structures show a near to 90° vertical sidewalls, with a systematic lateral bias evaluated up to ~20 nm. From the cross-sectional evaluation, significant trench width dependent RIE lag can be observed. Figure 2.9 (b.3) shows the top-down (underlying) SEM inspection of the triple structure chiplet device (design illustrated in Figure 2.8 (a)) cavity region and coupling waveguide: the systematic bias is in agreement with the value determined from the cross section etch trench lines. The geometry dependent bias shows circular holes in good agreement with the

design dimensions (overlaid, in dash-green), whereas the nanobeam peripheral sidewall still show a corrugated profile (to a lesser extent) similar to the etch tests in Figure 2.8 (b).

The high aspect-ratio stack with the ICPCVD Si_xN_y , although to a lesser extent with respect to the PECVD Si_xN_y , still presents both systematic and geometry dependent bias. Nevertheless, the high aspect-ratio test with the new ICPCVD deposition material allows for a characterization of the Si_xN_y etch rate.

We thus now proceed with the optimization over the resist / ICPCVD Si_xN_y aspect ratio stack of materials, reducing the thickness values of both films, considering the minimum thickness value of Si_xN_y set by the selectivity of the former to all ICP-RIE steps downstream the QIE-based process steps.

The same analysis as in Figure 2.9 (b) of respectively intermediate and low aspect-ratio stack of materials is shown in Figure 2.9 (c) and Figure 2.9 (d) for 300 nm **CSAR** / 120 nm **ICPCVD Si_xN_y** and (d) for 200 nm **CSAR** / 100 nm **ICPCVD Si_xN_y** . In all test results, an overetch of 30 % in the CHF_3/O_2 ICP-RIE was implemented in order to compensate for RIE lag.

The intermediate aspect-ratio stack yields a systematic bias of ~10 nm to 20 nm (Figure 2.9 (c.1) and (c.2)), lower when compared to the respective (b.1) and (b.2) high aspect-ratio stack, with linear vertical sidewalls close to 90°. The geometry dependent bias is improved ((c.3), less corrugation with respect to (b.3)) with respect to high aspect-ratio stack stack, although not perfectly matching the design yet (overlaid to scale in (c.3), green-dashed).

Further decreasing the aspect-ratio to the lowest case limited by the determined resist / Si_xN_y to CHF_3/O_2 ICP-RIE selectivity, the SEM inspection is illustrated in Figure 2.9 (d). (d.1) and (d.2) display the etched trench lines, with a near to 90° vertical sidewalls and etched-through Si_xN_y layer. The evaluated systematic bias values are ~5 nm to 20 nm. An accurate evaluation of the systematic bias from the cross-section trench lines is challenging here, as the vertical sidewalls do not display a perfectly linear profile: the residual relatively shallow resist etches faster at resist / Si_xN_y interface, leading to locally etching the top side of the patterned Si_xN_y lines. Same SEM inspection as in (b.3) and (c.3) is shown in (d.3), where a high magnification of the nanophotonic cavity shows that the systematic bias in pattern transfer is accurate up to ~10 nm, whereas the geometry dependent bias is fully absent. The underlying patterned cavity in Si_xN_y matches closely the overlying design (to scale, green-dashed). Therefore, the lowest aspect-ratio stack ensures the transfer pattern of intended design preserving both the designed geometric shape aspect and critical dimensions of features.

Conclusions

Increasing the density of the hard mask material, hence the etch resistivity to anisotropic O_2 ICP-RIE, allows to lower the aspect-ratio of resist / hard mask, leading to minimization of the systematic bias and eliminating the geometry dependent bias. At the same time, given the considerably reduced total QIE undercut etch duration for a full suspension of nanophotonic devices, a lower Si_xN_y thickness is allowed by the **250 °C QIE-based variant** etch recipe. Therefore, an increased etch resistivity of the ICPCVD Si_xN_y here developed and presented (recipe parameters in Appendix A.3, Table A.4), combined with the newly established anisotropic O_2 QIE recipe discussed in Section 2.7.1 (parameters detailed in Table 2.3 and Appendix A.3, Table A.4) allow us to reduce the aspect ratio of the e-beam resist to hard mask material patterning stack.

From the etch tests conducted in this Section, we find that the lowest aspect-ratio of the resist / hard mask patterning stack renders the highest accuracy in transfer patterning SnV center ZPL operating frequency nanophotonic devices, with a systematic bias as low as ~ 5 nm to 20 nm and no geometry dependent bias. The systematic bias can be subsequently compensated in the nanophotonic design phase, or by implementing a LD in the e-beam exposure phase.

However, given the non-perfectly vertical linear aspect of the Si_xN_y sidewalls, we further experiment the optimization of the transfer pattern by choosing a middle scenario between the aspect-ratio stacks presented in Figure 2.9 (c) and Figure 2.9 (d). Thus the final aspect-ratio we choose is 220 nm CSAR-09 on 80 nm Si_xN_y , which should render vertical linear sidewalls while at the same time compatible with the overall several ICP-RIE steps foreseen by the **250 °C QIE-based variant** fabrication process.

Last but not least, the parameters space here optimized is tested on diamond substrates, as it will be presented in the following Section 2.8.

2.8 RESULTS: 250 °C QIE-BASED VARIANT | SnV CENTER INTEGRATED DIAMOND PCCs

In this Section we proceed showing and discussing the main results on the newly developed and optimized **250 °C QIE-based variant fabrication process** performance, for which the final optimized parameters are detailed in Appendix A.3, Table A.4.

Here we only highlight the main aspects of the process monitoring progress from the initial fabrication steps (phase **I. Transfer pattern**) and final fabrication steps (phase **III. Quasi-isotropic undercut etch**), as the fabrication steps between the initial and final phase did not undergo substantial development (calibrated the etch rates only) with respect to the **65 °C QIE-based variant** fabrication process, for which a detailed description can be found in Section 2.6.2. Again, SEM monitoring is performed at key fabrication stages, where interleaved imaging does not introduce cross-contamination or compromise the final result.

In order to evaluate the performance of the newly developed 250 °C QIE-based variant, we test the fabrication process in its entirety employing several diamond chiplet layout designs, i.e., the triple structure chiplet layout, double structure chiplet layout and single standing one-sided PCC chiplet layout, schematically illustrated in Figure 2.8 (a), Figure 2.3 (a), (b) and (c), respectively.

Specifically, the different geometry chiplet layout designs allow us to test the performance on the two majorly developed and modified optimized phases of the QIE-based variant of the process. First, as presented and discussed in Section 2.7.3, the revisited parameters of the fabrication steps (1) to (6) (see Figure 2.1) have been thoroughly tested on Si / Si_xN_y . However, in order to fully assert the e-beam exposure effects such as proximity effect and charging, testing the exposure parameters on the target substrate is strongly encouraged.

Second, experimenting with different geometry aspect device layouts allows us to evaluate the QIE undercut progress versus total etch time, and hence determine the device geometry-dependent total undercut etch rates.

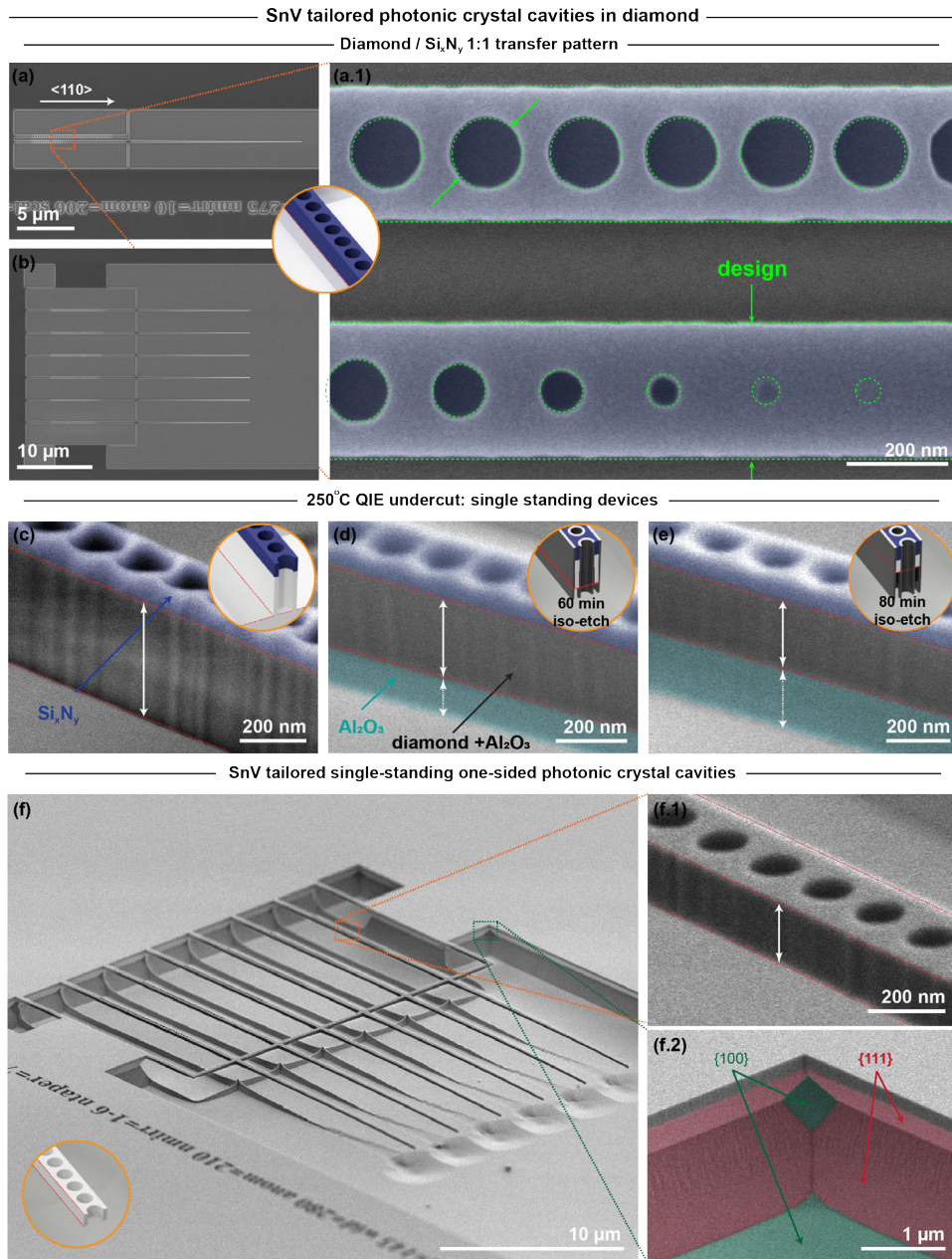


Figure 2.10: SnV center ZPL emission operating frequency tailored nanophotonic cavities: fabricated with the 250 °C QIE-based variant fabrication process | Top panel: bias-free transfer pattern on diamond / Si_xN_y (a) SEM pictogram (0° tilt view) of double structure chiplet design (schematic of layout in Figure 2.4.2 (b)); (a.1) zoom-in of the cavity region and tapered down radius circular holes region of coupling waveguide: accurate bias-free transfer pattern; (b) SEM pictogram (0° tilt view) of single standing one-sided PCCs chiplet design (schematic of layout in Figure 2.4.2 (c)) : hereafter inspected through the fabrication process; | Middle panel: QIE-based process progress monitoring, SEM inspection (65° tilt view); (c) Cavity region after fabrication step (7); (d) and (e) Same device at 60 min and 80 min of QIE undercut etch; | Bottom panel: ready devices, after step (11); (f) Same chiplet as in (b); (f.1) Same device as in (c, d, e); (f.2) Zoom-in showing the diamond crystallographic planes.

In the following, we present and discuss the results obtained implementing the final set of parameters **250 °C QIE-based variant** fabrication process final set of determined parameters (detailed in Appendix A.3, Table A.4). The substrates used throughout the entire fabrication process are 4 mm × 4 mm {100} oriented diamond plates from ElementSix, SnV centers generated following the protocol described in the Methods Section 3.4.4.

2.8.1 TRANSFER PATTERN

To assess the precision of the transfer pattern from the CAD design to the hard mask material, ICPCVD Si_xN_y , we perform the fabrication steps (1) to (6) (Figure 2.1), implementing the process parameters detailed in the Appendix A.3, Table A.4 on 4 mm × 4 mm × 500 μm , {100} oriented diamond substrate.

A higher magnification SEM inspection of the (top) cavity region and (bottom) coupling waveguide of the double structure device layout (Figure 2.10 (a.1)), by overlaying the design of the device (dashed-green, to scale) a systematic bias of ~5 nm and no geometry-dependent bias is observed, while the accuracy in the position of the circular holes is matching the design periodicity both in the tapered holes coupling waveguide and in the cavity region. However, while the cross section evaluation of the vertical transfer pattern of the etch trench lines of 50 nm width, the low aspect ratio stack (200 nm CSAR-09 on 100 nm Si_xN_y , Figure 2.9 (c.2)) shows RIE lag free full break through the mask, here, for higher resist thickness (here 220 nm CSAR-09 on 80 nm Si_xN_y), the circular holes of dimensions respectively 50 nm and 55 nm width are not etched through, even though in both cases the CHF_3/O_2 ICP-RIE overetch of 30% is implemented.

Additional investigation via atomic force microscopy (AFM) on fabricated dummy samples (same exposure parameters) topographic analysis of the developed resist (results not shown here) demonstrated that the respective pattern of the smallest holes is underexposed. As a result of underexposure, the pattern of the smallest holes (≤ 70 nm diameter) results in a developed resist thickness for an extent of only ~70 nm (radius dependent, out of the 220 nm total thickness) in depth with respect to the non-exposed thickness of 220 nm. This in turn translates into downstream result of shallowly etched Si_xN_y smallest holes, not clearing the Si_xN_y mask in correspondence of the ≤ 70 nm diameter holes.

In the results presented (Figure 2.10) the implemented exposure dose value is 250 $\mu\text{C}/\text{cm}^2$. However, a subsequent additional analysis of the exposure dose in diamond test samples indicated that the fully optimal clearing exposure dose is 300 $\mu\text{C}/\text{cm}^2$, higher than the 250 $\mu\text{C}/\text{cm}^2$ exposure dose used on the diamond sample shown in Figure 2.10. From this separate dose test round, we find that the exposure dose 300 $\mu\text{C}/\text{cm}^2$ generates a systematic bias of ~25 nm. Hence, after the results presented in the AFM analysis, an exposure dose of 300 $\mu\text{C}/\text{cm}^2$ combined with a LD~25 nm is implemented: This combination of parameters yields both reliable compensation of systematic bias and fully open ~25 nm radius smallest tapered holes.

After fabrication step (7), as demonstrated in Section 2.6.1 for the PECVD deposited Si_xN_y , the anisotropic O_2 ICP-RIE plasma causes enhanced mask erosion at the edges of the patterned geometric features. ICPCVD Si_xN_y demonstrates a relatively higher etch resistivity to anisotropic O_2 ICP-RIE. Thus, although to a lesser extent, enhanced mask erosion at the edges still affects the ICPCVD Si_xN_y as well, resulting in a rounded Si_xN_y mask at the diamond interface (blue false color in Figure 2.10 (c)). In order to limit erosion of

the hard mask material, we limit the extent of the O₂ anisotropic etch in diamond, etching a device thickness at this stage $\times 2.5$ to $\times 2.0$ (depending on the accuracy of the deposited Si_xN_y layer) the final value of the design device thickness.

Next, the surface roughness of the vertical sidewalls of the etched diamond structures, after the fabrication step (7), can be evaluated in Figure 2.8 (c): the surface roughness of the etched diamond can be resolved by SEM inspection, qualitatively showing moderate roughness. The vertical sidewall roughness has not been quantitatively characterized at this stage; nevertheless, we suspect the roughness at this scale to increase the optical losses of the nanophotonic devices.

At this stage, even though the suspected values are higher than the typical sub-nanometer (~ 0.3 nm) starting root mean square (RMS) roughness of the diamond substrates, our strategy is to focus on the full evaluation of the fabrication process performance. Subsequently, once the nanodevices are fully suspended, we evaluate the ultimate figures of merit quantifying the performance of the devices (Q quality factor for PCCs and, eventually, optical transmission losses for waveguides).

2.8.2 VERTICAL SIDEWALL PASSIVATION

After fabrication step (7), the vertical sidewalls of the top-down etched diamond structures are passivated via ~ 25 nm AlO_x ALD (step (8), same deposition parameters as in 65 °C QIE-based variant, higher thickness of the film here when compared to 65 °C QIE-based variant), followed by an anisotropic BCl₃/Cl₂ etch to clear the horizontal coverage (step (9), etching recipe adapted to Oxford PlasmaPro Cobra, parameters in Appendix A.3, Table A.4, implemented tolerance of 30%), opening access to the diamond substrate to downstream QIE O₂ plasma step (10).

2.8.3 QUASI-ISOTROPIC UNDERCUT

To evaluate the geometry-dependent QIE undercut etch rates of the newly developed 250 °C QIE-based etch recipe (parameters detailed in Table 2.3 and Appendix A.3, Table A.4 step (10)) discussed in Section 2.7.1, we proceed with the QIE undercut etch in sequential iterative steps.

The QIE step can be roughly divided into two main regimes. The first regime is the undercut phase where the $\langle 110 \rangle$ aligned devices are released from the substrate: In this etching phase, the $\{111\}$ crystallographic planes recede in the $\langle 100 \rangle$ direction downwards, converging underneath the hard mask protected nanobeams. As a result of further etch along the $\{111\}$ planes, these progress in the downwards $\langle 100 \rangle$ direction, leaving the patterned diamond nanobeams suspended. At this stage, the cross section of the suspended nanobeams is triangular. The second regime is the so-called 'upward-etch', where the nanobeams further etch upwards in the $\langle 100 \rangle$ direction from the backside exposed to the QIE plasma: in this regime, with advancement of the QIE etch, the triangular cross-section of the devices gradually changes, transitioning from triangular to a rectangular cross-section, flattening the bottom of the devices out.

The undercut process is geometry dependent, that is, the duration of the first and second phase of the QIE etch is dependent on the width of the patterned devices: for the same etch step duration, taking into account same $\langle 100 \rangle$ recession rate of $\{111\}$ planes,

for narrow width devices the $\{111\}$ planes converge earlier in the etch step session with respect to broader width devices.

For the sake of simplicity, here we present the QIE release and upward-etch behavior starting with the case of single standing one-sided PCCs (shown in Figure 2.10 (b)).

In order to systematically monitor the QIE etch release and upward-etch of the devices, we split the QIE etch steps into sequential etch steps of shorter duration. This allows interleaved SEM QIE progress monitoring, as well as measurement of the devices thickness.

In the presented example, the initial thickness of the diamond nanobeams ($\sim 2.5\times$ the final device thickness), determined by the O_2 anisotropic etch (step (7)) is measured ~ 372 nm (Figure 2.10 (c)). Next, at fabrication step (10), we start a first QIE step of continuous 60 min (Figure 2.10 (d)): the interleaved SEM inspection allows to determine the vertical extent of the AlO_x skirt (thanks to the contrast between protected underlying diamond / AlO_x and bare AlO_x), which in turn, allows to indirectly determine the thickness of the diamond nanobeam of ~ 263 nm. Here, after continuous 60 min QIE, the release of the devices with partial upward-etch can be observed. Following, a second QIE step of additional 20 min allows for further upward etch and flattening of the devices' bottom. The interleaved SEM inspection allows to estimate the etched extent of the diamond nanobeam (Figure 2.10 (e)), yielding a diamond beam thickness of ~ 180 nm. In retrospect, calculating the upward etch rate of this specific device design layout, assuming the upward etch rate constant, we hypothesize the release of the devices from the bulk diamond substrate converging $\{111\}$ planes underneath taking place after ~ 40 min QIE.

The estimation of the device thickness at this stage of the fabrication process is close to the designed device thickness of 200 nm, hence we proceed with fabrication step (11) (wet etch of mask materials). The typical example of fully suspended PCCs chiplet (Figure 2.10 (f)) is further inspected by SEM.

A direct measurement of the same device thickness after the fabrication step (11) yields a device thickness of ~ 177 nm (Figure 2.10 (f.1)), in good agreement with the indirect measurement in step (10). All listed values are summarized in Table 2.4. These are approximate values, taking into account the SEM measurement error, with the resolution dependent on the pixel size determined by the magnification.

Furthermore, in contrast to 65°C QIE etch recipe, here the newly tested 250°C QIE etch recipe yields remarkably smooth and uniform horizontal bottom plane of the chiplet (Figure 2.10 (f.2)), prevalently characterized by exposure of $\{100\}$ plane. This makes the overall post-nanophotonics 250°C QIE-based variant fabrication compatible with additional metallic routing patterning in the exposed etched bottom plane.

The reached device thickness is in line with the designed parameter. However, in our experience, the upward etch rate fluctuates around the mean value of ~ 4 nm/min. This makes upward etching a challenging step in the fabrication process, and hence targeting the exact design thickness of the devices is challenging. For this reason, we proceed with the upward-etch in several iterative steps, as well as compensate for this etch rate fluctuation in the design phase of devices by patterning different scalings of the same PCC design. This allows us to obtain devices with resonant wavelength within a window of frequencies, compatible with dynamic cavity resonance tuning, e.g. gas tuning.

| | O ₂ aniso-etched | O ₂ QIE etch steps | |
|------------------------|-----------------------------|-------------------------------|--------|
| Etch time [min] | 2 min 10 sec | 60 min | 20 min |
| Diamond thickness [nm] | ~372 | ~263 | ~180 |

Table 2.4: O₂ etch steps and measured diamond device thickness values measured from SEM (65° tilt angle view) inspection and corrected for tilt.

2.8.4 ASPECT-RATIO DEPENDENCY

We now evaluate the diamond devices aspect-ratio dependency of the 250 °C QIE recipe by SEM inspecting the cross-section of double structure device layout, where we vary the gap distance between the coupling waveguide and the nanophotonic cavity, respectively 100 nm and 300 nm (Figure 2.11 (a) and (b)), as well as 600 nm (Figure 2.11 (c)), triple structure device layout). All inspected devices have been fabricated within the same diamond substrate sample, within the exact same duration of QIE consecutive steps, for a total of 67 min etch.

In the presented example, the lattice constant a_n , hole radius r and nanobeam width w_{nb} are the same in all the considered cases of device layout design (triple / double and single standing layout) with the only varied design parameter being inter-nanobeam gap distance. By varying the inter-nanobeam gap, the effective aspect-ratio of the chiplet layout is dramatically changed. From a qualitative SEM inspection combined with simple trigonometry considerations, it can be promptly noticed that both cross-section and thickness of the presented chiplet layout devices are different.

Considering first the shorter inter-nanobeam gap of 100 nm (Figure 2.11 (a)), we measure the extent of vertical sidewall and the angled bottom of the coupling waveguide (~259 nm and ~243 nm respectively). Next, considering the opened circular holes on the tilted bottom plane, from simple geometric considerations we extrapolate an approximate angle of the $\langle 110 \rangle$ underlying devices bottom plane of ~48°. Therefore, we suspect the cross-section of the coupling waveguide / PCC system to be triangular, centered at the mid-gap of the double structure. This hypothesis is supported by two empirical observations. The first is the etched shape of the bottom plane diamond pedestal as a result of the peripheral to the double structure {111} planes convergence. The peripheral {111} planes perfectly converge underneath the double structure in a Λ -shape, showing no contribution of the quasi-isotropic etch from the area corresponding to the inter-device gap.

Second, from a twin diamond device (same design parameters), QIE etched for 13 minutes longer (inset in Figure 2.11 (a.1)), it can be noticed that the etched through circular holes shape is entirely visible and contained on the determined angled ~48° bottom. Next, considering the starting vertical sidewall extent of ~372 nm (defined at fabrication step (7), O₂ anisotropic etch), here we observe that the extent of the vertical sidewall is ~259 nm, indicating that the upward etch has started taking place and has advanced upwards for ~113 nm.

Thus, for a short gap of 100 nm, the double structure layout is effectively a single structure of total width 650 nm (waveguide width + gap width + photonic crystal cavity width).

Next, considering the intermediate inter-nanobeam gap of 300 nm (Figure 2.11 (b)), we measure the extent of vertical sidewall and the angled bottom of the coupling waveguide (~242 nm and ~158 nm respectively). In this case, from same considerations as previously, the extrapolated approximate angle of the $\langle 110 \rangle$ underlying devices bottom plane is of

$\sim 41^\circ$. The cross-section of the devices is triangular, this time centered in the middle of the nanobeams each. As in the previous case, this hypothesis is supported by the empirical observation of the shape of the bottom plane diamond pedestal as a result of the convergence of the $\{111\}$ planes. In this case, the 300 nm gap between the two adjacent nanobeams is wide enough, so that the etch along $\{111\}$ planes results in an efficient advancement along the $\langle 100 \rangle$ dimension. In fact, this time the pedestal underneath the suspended double structure presents an M-shape (pink), indicating convergence of the peripheral $\{111\}$ planes with the central (gap) $\{111\}$ planes.

Finally, considering the wide inter-nanobeam gap of 600 nm (Figure 2.11 (c)), the extent of vertical sidewall is (bottom, waveguide) ~ 201 nm, (central, coupling waveguide) ~ 286 nm and (top, photonic crystal cavity) ~ 244 nm respectively. Here the upward etch is completed in the case of the waveguide, with a measured thickness close to the design value. On the other hand, the thickness of the (central) coupling waveguide and adjacent (top) photonic crystal cavity is higher than the design value, once again confirming the aspect-ratio dependency of the QI etch. From a 65° tilt angle view SEM inspection, the bottom cross-section of the devices cannot be observed. Therefore, tilting the view angle to the maximum experimentally feasible (85° tilt angle view, Figure 2.11 (c.1)), we observe the bottom side of the devices to be near flat, with residual triangular cross-section of the devices at the substrate pinning points respectively.

2.8.5 CONCLUSIONS

From the presented results in this Section, the following conclusions can be drawn:

1. **Accuracy of pattern transfer:** 1:1 accuracy in transfer pattern can be achieved by implementing the optimized set of parameters optimized on Si / Si_xN_y test samples (Section 2.7.3), reproducible and transferable with minor adjustments on diamond substrates (Section 2.8), detailed in Table A.4.
2. **QIE undercut and upward etch for single-standing devices:** the established and optimized 250 °C QIE recipe yields full undercut and upward etch of nanophotonic devices in as short as 80 min total etch time (in contrast to 20 h total etch time of the 65 °C QIE recipe). Suspended nanophotonic waveguides and PCCs with target design thickness and rectangular cross-section can be achieved. However, the upward etch rate fluctuates around the mean value of ~4 nm/min. This renders the upward etch a relatively challenging step in the fabrication process. Hence, interleaved SEM inspection of the upward etch is necessary in order to monitor the progress of the upward etch. The established method of indirectly measuring the nanobeams thickness proved reliable and in good agreement with the direct measurement of devices thickness after the removal of hard mask materials.
3. **QIE undercut and upward etch design aspect-ratio dependency:** from the presented results, we conclude and confirm that the QIE undercut is indeed device aspect ratio dependent. This can be explained by the intrinsic difference in the etch rates along the {100} and {111} family of lattice planes, with {111} being the slowest between the two. When comparing the area defined by the inter-nanobeam gap, for the same etch rate along the {111} planes, the <001> direction advancement of the etch along the {111} planes is lowest (highest) for the smallest (biggest) inter-device gap. Therefore, by increasing the inter-device distance, e.g. to ~3 μm, or more, as presented in Figure 2.10 (middle and bottom panel), we find that a uniform thickness with a rectangular cross-section of the devices can be obtained. In such case, the aspect-ratio of the overall chiplet does not influence the undercut of individual nanobeams, yielding peripheral devices with same resulting thickness as centrally (within the chiplet) placed ones. Next, comparing different effective diamond devices aspect-ratio (single-standing to double-structure) we find that for the given prior QIE-based variant process parameters, the single-standing device layout yielded full undercut and upward etch, whereas higher effective aspect-ratio device layout e.g. double-structure, requires both a longer anisotropic O₂ step and longer QIE consecutive steps for full upward-etch completion. Therefore, for higher effective diamond devices layout aspect-ratio, the overall QIE-based fabrication process parameters require ad-hoc calibration and optimization.

Overall, the developed and optimized **250 °C QIE-based variant** fabrication process presented here, with a tolerance of ~25 % to 30 % over the deposition and etch duration process parameters, shows systematic and reproducible results across separate fabrication rounds. Nevertheless, the upward etch rate fluctuation around the mean value of ~4 nm/min requires calibration over the real-time etch duration and interleaved SEM monitoring in order to reach the target design device thickness.

Aspect-ratio dependent QIE undercut etch
Inter device gap distance sweep

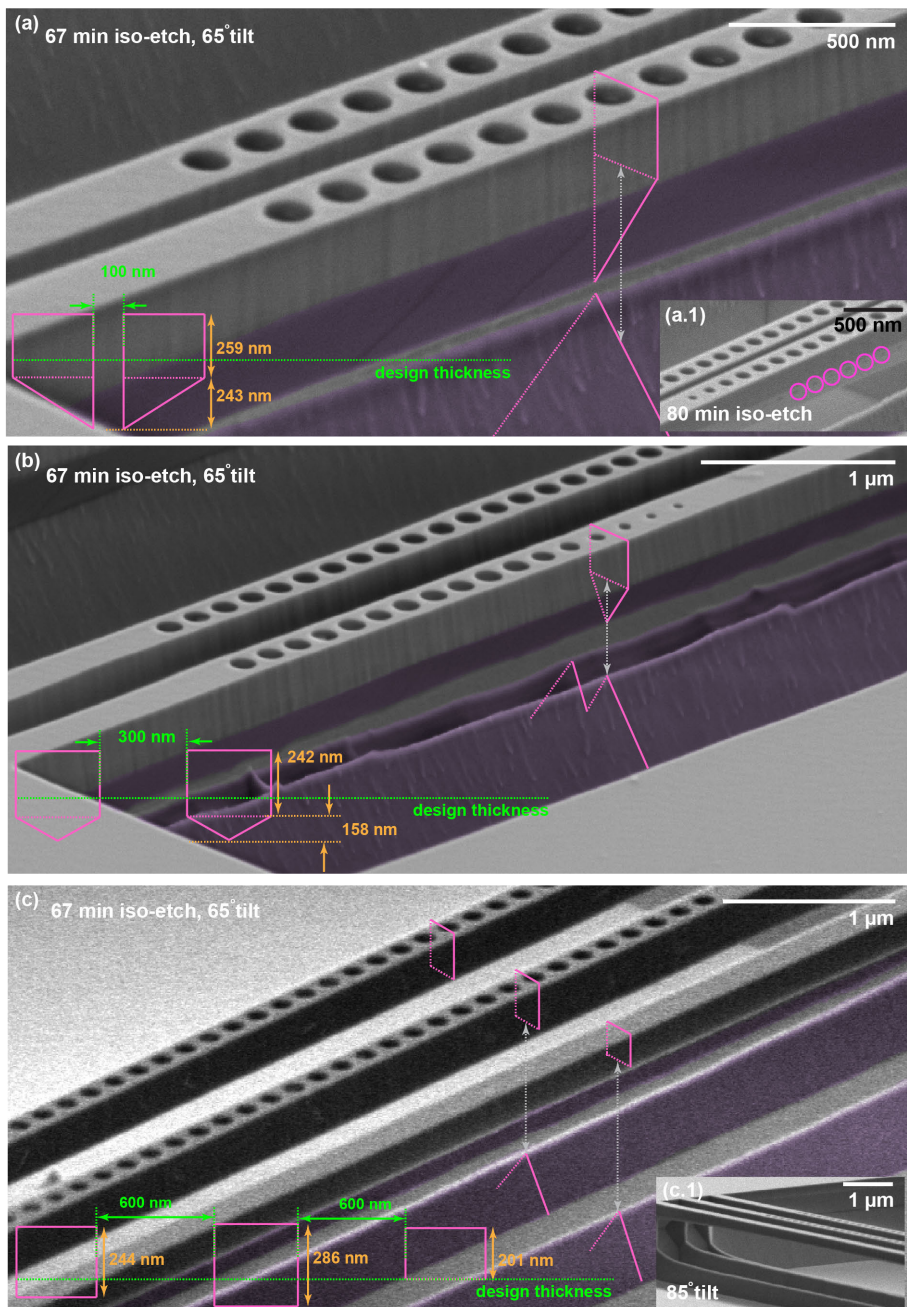


Figure 2.11: **250 °C QIE aspect-ratio undercut dependence** SEM inspection (65° tilt view) of respectively 100 nm (a), 300 nm (b) gap distance of the fabricated and undercut double structure and 600 nm (c) gap distance of the triple structure chiplet layouts after a total 67 min 250 °C QIE; (a.1) same parameters as (a), for a total of 80 min 250 °C QIE; (c.1) same parameters as (c), SEM inspection 85° tilt view; | Full undercut and removal of the triangular cross-section is strongly dependent on the design aspect-ratio.

ACKNOWLEDGMENTS

We thank the entire SnV-team for fruitful discussions that supported the scientific development presented in this chapter, C.E. Smulders and L.G.C. Wienhoven for fabrication assistance, helpful discussions and feedback on this manuscript.

We thank A. Wallucks, B. Hensen, N. Fiaschi, S. Gröblacher for helpful discussions, and for providing us with initial code of simulating an individual rectangular nanophotonic structure in Comsol via an interface to Matlab. We thank M. Ruf, C. van Egmond, B. Simon, Y. Li, T. van der Sar, R. Norte, N. Wan, P. Barclay, A. Rugar, S. Aghaeimeibodi, D. Riedel, E. Zohari, K. Kuruma, C. Chia, S. W. Ding, M. Haas and M. Loncar for helpful discussions, Z. Sadre Momtaz for help and fabrication assistance, and the entire staff of the Kavli Nanolab Delft for assistance and support, in particular M. Zuiddam, C. de Boer, H. Miro, A. van Langen-Suurling, A. van Run, L. Schriek, B. van Asten, E. Pot, P. Stevic, and E. Straver.

2.9 REFERENCES

1. Khanaliloo, B., Mitchell, M., Hryciw, A. C. & Barclay, P. E. High-Q/V Monolithic Diamond Microdisks Fabricated with Quasi-isotropic Etching. *Nano Letters* **15**, 5131–5136 (2015).
2. Shaw, K. A., Zhang, Z. L. & MacDonald, N. C. SCREAM I: a single mask, single-crystal silicon, reactive ion etching process for microelectromechanical structures. *Sensors and Actuators A: Physical* **40**, 63–70 (1994).
3. Rugar, A. E., Dory, C., Aghaeimeibodi, S., Lu, H., Sun, S., Mishra, S. D., Shen, Z.-X., Melosh, N. A. & Vučković, J. Narrow-Linewidth Tin-Vacancy Centers in a Diamond Waveguide. *ACS Photonics* **7**, 2356–2361 (2020).
4. Pasini, M., Codreanu, N., Turan, T., Riera Moral, A., Primavera, C. F., De Santis, L., Beukers, H. K., Brevoord, J. M., Waas, C., Borregaard, J., *et al.* Nonlinear quantum photonics with a tin-vacancy center coupled to a one-dimensional diamond waveguide. *Phys. Rev. Lett.* **133**, 023603 (2024).
5. Wan, N. H., Lu, T.-J., Chen, K. C., Walsh, M. P., Trusheim, M. E., De Santis, L., Bersin, E. A., Harris, I. B., Mouradian, S. L., Christen, I. R., Bielejec, E. S. & Englund, D. Large-Scale Integration of Artificial Atoms in Hybrid Photonic Circuits. *Nature* **583**, 226–231 (2020).
6. Rugar, A. E., Aghaeimeibodi, S., Riedel, D., Dory, C., Lu, H., McQuade, P. J., Shen, Z.-X., Melosh, N. A. & Vučković, J. Quantum Photonic Interface for Tin-Vacancy Centers in Diamond. *Physical Review X* **11**, 031021 (2021).
7. Mouradian, S., Wan, N. H., Schröder, T. & Englund, D. Rectangular Photonic Crystal Nanobeam Cavities in Bulk Diamond. *Applied Physics Letters* **111**, 021103 (2017).
8. Wan, N. H., Mouradian, S. & Englund, D. Two-dimensional photonic crystal slab nanocavities on bulk single-crystal diamond. *Applied Physics Letters* **112** (2018).
9. Joe, G., Haas, M., Kuruma, K., Jin, C., Kang, D. D., Ding, S., Chia, C., Warner, H., Pingault, B., Machielse, B., *et al.* Observation of the acoustic Purcell effect with a color-center and a nanomechanical resonator. *arXiv preprint arXiv:2503.09946* (2025).
10. Brevoord, J. M., Wienhoven, L. G., Codreanu, N., Ishiguro, T., van Leeuwen, E., Iuliano, M., De Santis, L., Waas, C., Beukers, H. K., Turan, T., *et al.* Large-Range Tuning and Stabilization of the Optical Transition of Diamond Tin-Vacancy Centers by In-Situ Strain Control. *Appl. Phys. Lett.* **126** (2025).
11. Itoi, J., Zohari, E., Sorensen, N. J., El-Sayed, W., Losby, J. E., Luiz, G. O., Flågan, S. & Barclay, P. E. Non-volatile photorefractive tuning and green light generation in a diamond cavity. *arXiv preprint arXiv:2507.19583* (2025).
12. Mitchell, M., Lake, D. P. & Barclay, P. E. Realizing $Q > 300\,000$ in diamond microdisks for optomechanics via etch optimization. *APL Photonics* **4**, 016101 (2019).
13. Ruf, M. *Cavity-enhanced quantum network nodes in diamond* PhD thesis (Delft University of Technology, 2021).
14. Xie, L., Zhou, T. X., Stöhr, R. J. & Yacoby, A. Crystallographic orientation dependent reactive ion etching in single crystal diamond. *Advanced Materials* **30**, 1705501 (2018).

15. Chia, C., Machielse, B., Shams-Ansari, A. & Lončar, M. Development of hard masks for reactive ion beam angled etching of diamond. *Optics Express* **30**, 14189–14201 (2022).
16. Chia, C. *Quantum Optomechanics with Color Centers in Diamond* PhD thesis (Harvard University, 2021).
17. Reiserer, A. & Rempe, G. Cavity-based quantum networks with single atoms and optical photons. *Reviews of Modern Physics* **87**, 1379–1418 (2015).
18. Pasini, M. *Nanophotonics with Diamond Color Centers: Quantum Optics and Entanglement Protocols* PhD thesis (Delft University of Technology, 2024).
19. Chan, J. *Laser cooling of an optomechanical crystal resonator to its quantum ground state of motion* (California Institute of Technology, 2012).
20. Primavera, C. *Coupling Tin-Vacancy Centres to Diamond Waveguides* Master's Thesis. MA thesis (Delft University of Technology, 2022).
21. Javadi, A., Söllner, I., Arcari, M., Hansen, S. L., Midolo, L., Mahmoodian, S., Kiršanskė, G., Pregolato, T., Lee, E., Song, J., *et al.* Single-photon non-linear optics with a quantum dot in a waveguide. *Nature communications* **6**, 8655 (2015).
22. Pregolato, T., Stucki, M. E., Bopp, J. M., Gokhale, A., Krüger, O., Schröder, T., *et al.* Fabrication of Sawfish photonic crystal cavities in bulk diamond. *APL Photonics* **9** (2024).
23. Sakoda, K. & Sakoda, K. *Optical properties of photonic crystals* (Springer, 2005).
24. John, D. J., Joannopoulos, D., Winn, J. N. & Meade, R. D. Photonic crystals: molding the flow of light. *In Princeton University of Press: Princeton, NJ, USA* (2008).
25. Meenehan, S. M. *Cavity optomechanics at Millikelvin temperatures* (California Institute of Technology, 2015).
26. Burek, M. J., Meuwly, C., Evans, R. E., Bhaskar, M. K., Sipahigil, A., Meesala, S., Machielse, B., Sukachev, D. D., Nguyen, C. T., Pacheco, J. L., *et al.* Fiber-coupled diamond quantum nanophotonic interface. *Phys. Rev. Appl.* **8**, 024026 (2017).
27. Burek, M. J., Meuwly, C., Evans, R. E., Bhaskar, M. K., Sipahigil, A., Meesala, S., Machielse, B., Sukachev, D. D., Nguyen, C. T., Pacheco, J. L., Bielejec, E., Lukin, M. D. & Lončar, M. Fiber-Coupled Diamond Quantum Nanophotonic Interface. *Phys. Rev. Appl.* **8**, 024026 (2017).
28. Zeng, B., De-Eknamkul, C., Assumpcao, D., Renaud, D., Wang, Z., Riedel, D., Ha, J., Robens, C., Levonian, D., Lukin, M., *et al.* Cryogenic packaging of nanophotonic devices with a low coupling loss < 1 dB. *Applied physics letters* **123** (2023).
29. Nguyen, C., Sukachev, D., Bhaskar, M., Machielse, B., Levonian, D., Knall, E., Stroganov, P., Chia, C., Burek, M., Riedinger, R., *et al.* An integrated nanophotonic quantum register based on silicon-vacancy spins in diamond. *Physical Review B* **100**, 165428 (2019).

30. Knall, E. N., Knaut, C. M., Bekenstein, R., Assumpcao, D. R., Stroganov, P. L., Gong, W., Huan, Y. Q., Stas, P.-J., Machielse, B., Chalupnik, M., *et al.* Efficient source of shaped single photons based on an integrated diamond nanophotonic system. *Phys. Rev. Lett.* **129**, 053603 (2022).
31. Kennedy, G., Taylor, S., Eccleston, W., Arnoldbik, W. & Habraken, F. Physical and electrical characterisation of oxynitride films produced by plasma oxidation of deposited silicon nitride layers. *Microelectronic Engineering* **28**, 141–144 (1995).
32. Luhmann, N., Jachimowicz, A., Schalko, J., Sadeghi, P., Sauer, M., Foelske-Schmitz, A. & Schmid, S. Effect of oxygen plasma on nanomechanical silicon nitride resonators. *Applied Physics Letters* **111** (2017).
33. Hill, J. T. *Nonlinear optics and wavelength translation via cavity-optomechanics* (California Institute of Technology, 2013).
34. Williams, K. R., Gupta, K. & Wasilik, M. Etch rates for micromachining processing-Part II. *Journal of microelectromechanical systems* **12**, 761–778 (2003).
35. Lai, S., Johnson, D. & Westerman, R. Aspect ratio dependent etching lag reduction in deep silicon etch processes. *Journal of Vacuum Science & Technology A* **24**, 1283–1288 (2006).
36. Dory, C., Vercruyssen, D., Yang, K. Y., Sapra, N. V., Rugar, A. E., Sun, S., Lukin, D. M., Piggott, A. Y., Zhang, J. L., Radulaski, M., *et al.* Inverse-designed diamond photonics. *Nature communications* **10**, 3309 (2019).
37. Jiang, W., Xu, D., Xiong, B. & Wang, Y. Effects of rapid thermal annealing on LPCVD silicon nitride. *Ceramics International* **42**, 1217–1224 (2016).

3

3

FABRICATION OF TIN-VACANCY CENTERS IN DIAMOND: SURFACE-PROTECTED ANNEALING METHOD AND GRAPHITIZATION ANALYSIS

Generation and activation of color centers in diamond is of great interest for quantum technologies. Ion implantation methods offer the advantage in terms of control over implantation depth, spatial accuracy, and nature of the implanted species. However, this comes at the cost of crystal damage, which upon high temperature annealing treatment can be alleviated, to some extent. Conventional high temperature annealing under high vacuum is challenging, as fluctuations in the oven pressure, as well as presence of residual gases promote surface graphitization of diamond substrates. The extent of the graphitization phenomenon is greatly dependent on several parameters of the process, which are often challenging to control and predict. In this study, we present the effects of this phenomenon with the conventional annealing process on nanophotonic devices. Next, we present an alternative surface-protected annealing method on bulk diamond substrates. We quantify the extent of the graphitization phenomenon with complementary topographic and chemical studies. Finally, we assess the efficacy of the alternative annealing method proposed.

3.1 INTRODUCTION

In this chapter, we will focus primarily on generation and activation of color centers in type II, electronic grade diamond substrates.

In Section 3.2 we briefly discuss the main methods aimed at the generation and activation of color centers in diamond, with a focus on the ion implantation method (briefly discussing the main ion implantation parameters), as this is of higher interest in the context of this work. Here, we briefly introduce the most relevant methods and techniques of generation and activation of color centers, up to the point of understanding the relevance of the method developed in this chapter. In Section 3.3 we proceed with a brief literature overview on the generation and activation of nitrogen-vacancy (NV) centers and group-IV color centers (SiV, SnV, GeV and PbV), while for an in-depth discussion on the various methods of color center generation methods, we refer the reader to more extensive review studies, e.g. Refs. [1, 2]. In Section 3.3.1 we discuss the main generation and activation methods developed for the SnV centers in diamond.

Next, in the context of ion implantation and high temperature annealing color center generation, in Section 3.3.2 we discuss the relevance of the high temperature low pressure method, while in Sections 3.3.3 and 3.3.4 we elaborate on the associated graphitization challenge.

In Section 3.4 we present the methods we developed, aimed at the successful generation and activation of SnV centers in diamond: After detailing the fabrication steps and ion implantation parameters aimed at high-control ion implantation, in Section 3.4.3 we detail the conventional high temperature low pressure annealing activation method fabrication process, while in Section 3.4.4 we present our alternative surface-protected high temperature low pressure annealing method.

In Section 3.5, we show the results of the conventional annealing treatment, discussing the challenges associated with the resulting graphitization at the sample surface. In Section 3.6 we present the results and assess the performance of the proposed alternative surface-protected high temperature low pressure annealing method.

Finally, in Section 3.7, we discuss the performance and advantages of the proposed alternative activation method for SnV centers in diamond.

We will refer to the negatively charged state of the group-IV and nitrogen-vacancy color centers, unless stated otherwise, as these are of most interest and have been extensively studied.

3.2 COLOR CENTERS IN DIAMOND: GENERATION METHODS

Typically, the generation of color centers in diamonds consists of the introduction of impurities into the carbon crystal lattice, the generation of lattice vacancies, and the combination of lattice vacancies with the impurities. Color centers in diamonds can be created primarily via two approaches. The bottom-up approach is doping during in-growth synthesis, while the top-down approach is post-growth ion implantation.

3.2.1 IN-GROWTH SYNTHESIS

In the case of in-growth synthesis of impurities incorporation, the fabrication methods foresee the incorporation of the non-native atomic species step, followed by the generation

of lattice vacancies step and concludes with the migration of the vacancies step (to combine with the incorporated impurities into vacancy-atom complexes).

In the case of specific color centers in diamonds, e.g. nitrogen vacancies (NV) and silicon vacancies (SiV), the atomic impurity incorporation step can be omitted, as both are widely present in chemical vapor deposition (CVD) growth reactor chambers. The most straightforward example is represented by the NV centers: CVD grown Type II diamond substrates have a nitrogen impurity concentration less than 5 ppb (typically between 0.1 and 1 ppb for Type IIa single-crystal electronic grades, used in this work) and a boron concentration < 1 ppb. Therefore, typically relatively low doping, or none at all, is required. Doping in-growth synthesis has been successfully realized and demonstrated for other atomic species, not commonly available in CVD reactor chambers, for which the incorporation via a source material is foreseen. In addition to the successful generation of NV centers during CVD synthesis of diamond, e.g. δ -doping [3], most recently some of group-IV color centers have also been successfully demonstrated.

In case of the in-growth incorporation of atomic species method, the diamond crystal lattice is characterized by a relatively low strain, a high substrate crystal purity, and a relatively low density of lattice vacancy sites. This implies that the generation of atom-vacancy complexes requires the generation of additional lattice vacancies in a separate fabrication step. For this, several methods have been developed and demonstrated (for example, in the case of NV centers generation), such as electron irradiation [4] and ion irradiation [5–7]. In order to combine the vacancies with the incorporated non-carbon atoms, the vacancies require mobilization such that atom-vacancy complexes may be formed. This can be achieved by a high temperature treatment step, e.g. high temperature annealing or laser activation.

The advantage of in-growth incorporation of impurities is that, in general, these have shown better optical and spin properties, compared to their implanted ion counterparts [2]. However, except for the nitrogen δ -doping method, in the growth synthesis of diamond defect centers, control over spatial positioning and density of impurities remains a challenge.

3.2.2 POST-GROWTH INCORPORATION: ION IMPLANTATION

The top-down approach foresees post-growth insertion of a foreign atomic species into the diamond crystal lattice, with the only viable up-to-date method being ion implantation. The advantage of the implantation process is that it allows the insertion of any impurity into any host material, regardless of the solubility and thermodynamic considerations [8]. Next, ion implantation allows full spatial control over the positioning of foreign atomic species, allowing precision placement to be as low as sub-50 nm implantation accuracy [9].

Pragmatically, this process relies on accelerating charged ions, with sufficiently high energy, towards the target substrate. Upon ion implantation, the accelerated ions penetrate the target substrate and are gradually slowed down. During this process, considering the atomic mass and kinetic energy of the accelerated ions, the accelerated ions lose energy via the Coulomb interaction between the charged ions and the electrons of the host material (electronic energy loss) and the interaction between the ions and the atoms of the host material (nuclear energy loss). This Coulomb interaction slows the charged ion, causing both ionization and cascaded displacement of the atoms of the host material, resulting in

crystal damage, the extent being dependent on the projectile ion energy and ion fluence [10, 11].

The crystal damage therefore may yield a noisier and more strained environment around the implanted atoms of interest, resulting in less narrow and spectrally less stable emitters. Therefore, in order to reduce the radiation damage and anneal the host material, energy must be supplied to the system to enable diffusion of interstitials and vacancies. This energy is typically provided by heating the host material.

From Ref. [11], in order to understand the important parameters that ultimately determine the optimal implantation density of ions in the diamond substrate, here we briefly describe the relevant implantation parameters.

Generally, the slowing down mechanism of an ion in a solid is divided into two dominant mechanisms that determine the energy loss of the incident ions:

1. Electronic energy loss: interaction of projectile ion with the electrons of the host material;
2. Nuclear energy loss: interaction of projectile ion with the atoms (considered as shielded point charges) of the host material. The ion-nucleus interaction is given by the Coulomb interaction between two positive charges, resulting in energy loss and trajectory deviation of the projectile ion. The trajectory deviation results in the lateral spread and depth distribution of the implanted ions. At the same time, host atoms may also be dislodged from the original lattice site positions, giving rise to lattice defects.

The slowing mechanism of projectile ions in a solid is generally described through the *stopping power* dE/dx , defined as the energy dE lost by the ion traversing a distance dx :

$$\frac{dE}{dx} = N \int T d\sigma, \quad (3.1)$$

where $d\sigma$ is the collision cross section, T is the lost energy in the course of the collision event, and N is the density of the scattering centers in the host material.

The total stopping power, due to electronic interaction processes and nuclear interaction processes, is thus given by:

$$\frac{dE}{dx} = \left(\frac{dE}{dx} \right)_e + \left(\frac{dE}{dx} \right)_n = N(\mathcal{E}_e + \mathcal{E}_n), \quad (3.2)$$

where \mathcal{E}_e and \mathcal{E}_n are the electronic and nuclear stopping cross sections, respectively, and the stopping cross section \mathcal{E} is given by:

$$\mathcal{E} = \frac{1}{N} \frac{dE}{dx} = \mathcal{E}_e + \mathcal{E}_n. \quad (3.3)$$

The energy of the projectile ion before (E_0) and after (E_1) the scattering event is related as:

$$E_1 = kE_0, \quad (3.4)$$

where k is the kinematic factor:

$$k = \left(\frac{M_1 \cos \theta \pm (M_2^2 - M_1^2 \sin^2 \theta)^{1/2}}{M_1 + M_2} \right)^2, \quad (3.5)$$

where M_1 is the mass of the projectile atom, M_2 is the mass of the target atom, and θ is the scattering angle of the projectile atom in the laboratory frame given by:

$$\cos \theta = \frac{1 - (1 + M_2/M_1)(T/2E_0)}{\sqrt{1 - T/E_0}}. \quad (3.6)$$

with $T = E_0 - E_1$ the energy transferred from the projectile to the target.

Next, the ion range can be calculated as follows:

$$R = \int \frac{dE}{dE/dx}, \quad (3.7)$$

with integration limits from the initial ion energy to zero. At low energies of the projectile ion, nuclear stopping is dominant due to the $\sim 1/E^2$ dependence of the Rutherford cross section, whereas electron stopping dominates at high energies. The host atoms are severely dislodged in the energy region where nuclear stopping dominates, whereas electronic stopping does not create extensive damage to the host crystal in this energy regime [12].

Generally, slowing processes of an ion moving into a solid is a statistical process; therefore, the locations at which the projectile ions stop are also statistical. Thus, the ion range R (Equation 3.7) is related to the mean trajectory length of the ion before coming to rest, while R_p represents the mean penetration depth of the ion relative to the surface of the host material. The implant density $n(x)$ is given by Equation 3.8:

$$n(x) = \frac{\phi}{\sigma_p \sqrt{2\pi}} \exp \left[-\frac{(x - R_p)^2}{2\sigma_p^2} \right] \quad (3.8)$$

where x is the distance measured along the implanting direction beam, ϕ is the ion fluence (or ion dose), σ_p is the standard deviation in the projected R_p , with ΔR_p the ion range straggling, which naively statistically quantifies the deviation of the implant position from the target implant position.

Equation 3.8 describes the Gaussian approximation of the implantation density $n(x)$, not taking into account diffusion effects, higher-order effects and ion channeling.

The two most relevant parameters for ion implantation are ion fluence ϕ (as it determines the density of implanted ions) and ion energy E_0 (as it defines the stopping range R_p of the ions inside the crystal lattice, hence determining the implantation depth). In order to take into account the effects of the ion channeling, a third implantation parameter of great importance is the ion implantation angle. Other implantation parameters to which one should pay attention are the dose rate (beam current) and implantation temperature: the first is to establish an optimal beam current so that the rate at which the ions are penetrating the host material is slow enough to allow for partial radiation damage recovery. Concerning the implantation temperature, one should keep in mind that a higher host

material temperature enables higher diffusion rates of both implanting ions and defects. Low temperature implantation is desirable to achieve more precise control over R_p [11].

As detailed in Section 3.3.0.2 and Methods Section 3.4.2 (Sn implantation), the Stopping Range of Ions in Matter (SRIM) and Transport of Ions in Matter (TRIM) simulations are powerful tools for tuning implantation parameters such as ion energy in order to obtain the designed R_p , bearing in mind that TRIM simulations do not take into account effects such as ion channeling.

In order to mitigate crystal damage, high temperature annealing methods have typically been developed with a twofold objective: on the one hand, to allow vacancies migration to combine into atom-vacancies complexes, for diamond temperatures typically well below 1000 °C; on the other hand, annealing temperatures higher than 1000 °C allow repair of additional defects (e.g. paramagnetic defects) created during implantation. This approach has been shown to be successful in activating both implanted NV centers [13, 14] and group-IV color centers [15–20]. Concerning the straggle of the implanted species, the higher is the atomic mass, the lower is the straggle, therefore allowing for precision placement dictated, again by the energy of the beam and the atomic mass.

In the past decades, significant effort has been focused towards the development of advanced methods for ion implantation, e.g. AFM nano-beam positioning, masked implantation and most recently focused ion beam implantation, for which we refer the reader to the excellent literature review [1, 2].

3.3 GROUP-IV COLOR CENTERS IN DIAMOND CREATION AND ACTIVATION

Group-IV color centers, comprising SiV, SnV, GeV, and PbV, have recently emerged as promising spin-photon candidates for quantum communications applications due to remarkable optical properties, long spin coherence times, and spin control.

SYMMETRY CONSIDERATIONS

The group-IV color centers are split vacancy defects, i.e. the group-IV atom is placed in an interstitial site, between two lattice vacancies, aligned on [111] equivalent crystallographic axes. This atomic spatial configuration renders unique optical and spin properties of this class of defects. The symmetry of this complex belongs to the D_{3d} point symmetry group: this is an extremely concise way to summarize and classify the symmetry properties of the defect, upon which, assuming perfect symmetry, the group theory further predicts selection rules on the optical transitions, predicts allowed transitions, and identifies symmetry based degeneracies (to name a few). Although we refer the reader to the comprehensive Doctoral thesis work of C. Hepp [21] for a thorough exploration, it is most important to note that one of the most relevant properties of this symmetry group is that it prohibits the presence of a permanent electric dipole.

The absence of a permanent electric dipole in the group-IV color centers renders this class of emitters insensitive to external electric field fluctuations to the first order, while the response to external electric fields remains only of 2nd order [15]. The latter property represents a welcomed advantage in the context of nanophotonic integration.

INCORPORATION OF GROUP-IV IN THE DIAMOND CRYSTAL LATTICE

Before exploiting the great properties of these emitters in the context of quantum communications, the natural question arises: How does such a split vacancy form?

In-growth synthesis incorporation of group-IV color centers has been achieved with SiV (HPHT synthesis [22]), GeV (CVD [23] and HPHT [24]) and SnV (HPHT synthesis [25]). Although these have shown remarkably high spectral coherence and transform-limited optical linewidths, the research community has focused efforts substantially on the ion implantation counterpart. The main reason for this shift is attributable to control over the spatial positioning of the color centers, which is of fundamental relevance in the context of nanophotonic integration.

Ion implantation methods have involved mainly efforts towards masked implantation and focused ion beam implantation in order to achieve 3-dimensional position accuracy. Focused ion beam implantation, in principle, holds the potential of highest position accuracy control.

Several methods of high temperature annealing have been developed, most common being high temperature high pressure annealing, high temperature low pressure annealing and high temperature under a gas atmosphere. All group-IV activation has been demonstrated with high temperature low pressure annealing, representing the method of choice. Laser writing of color centers within diamond nanophotonic devices has been demonstrated in diamond nanopillars, where the creation of color centers and the enhancement of NV centers has been successfully observed [26]. The work of Ref. [26] focuses on the creation of NV centers, the method presented can be applied to other color centers, e.g. group-IV. Recently, laser annealing of SnV centers in diamond has been demonstrated [27].

3.3.1 SnV CENTERS GENERATION METHODS

We shift the focus now towards SnV centers, which are of the highest interest in the context of this thesis.

The in-growth incorporation of Sn ions, this is a question of open research, as the high Sn atomic mass combined with the high atomic density and rigid cubic structure of the diamond host crystal renders in-growth incorporation challenging. In-growth HPHT synthesis of SnV centers has been demonstrated by Palyanov *et al.* [25], where the authors reported on a systematic study of high-pressure synthesis and the study of growth conditions favorable for the incorporation of Sn ions in crystallized diamonds. Synthesis has been shown to be successful for pressures ranging from 6.3 GPa to 7.5 GPa and temperatures in the range 1420 °C to 1900 °C. This work reports on the successful incorporation of Sn ions, leading to the formation of optically coherent SnV centers in single crystals of dimensions ranging from 50 μm to 1 mm. In general, the advantage of this method is the resulting high crystalline quality of the diamond substrate, with low imperfections density, thus yielding a virtually strain-free environment. However, in the context of group-IV defects, a strain free environment is not necessarily advantageous: strain enables orbital components mixing, thereby enabling efficient microwave spin control [28, 29]. In addition to HPHT in-growth synthesis, no other in-growth synthesis of Sn ions has been reported.

As discussed in the previous chapters, to successfully engineer photonic light-matter interfaces, the environment around the color centers has to be modified with high accuracy

over the relative position of the color center with respect to the optimal optical mode confinement of the emitted photons. Ion implantation represents the most viable solution for the incorporation of Sn ions and subsequent generation of SnV centers, offering generally high spatial precision and accuracy. The current available methods for Sn ion implantation are high-energy ion implantation followed by high-temperature thermal annealing [30] and low-energy ion implantation followed by CVD overgrowth of a diamond cap layer [31]. Both methods have reported a relatively low percentage of conversion yield from Sn to SnV center, as high as 4 % in the case of high-energy implantation and HPHT annealing [30]. The authors in Ref. [30] attribute a higher stability of the generated SnV centers, this being due to the high pressure high temperature thermal treatment. Tchernij *et al.* [32] report an estimate of the Sn to SnV center conversion yield of ~5% for high energy implanted Sn ions at 60 keV and 850 °C high temperature low pressure annealing, although requiring further empirical studies. Taking into account the relatively low conversion yield, one way to increase the overall density of created SnV centers would be to increase the ion fluence. However, the relatively high atomic mass number (higher than that of Si and Ge, both commonly studied) is suspected to produce a higher degree of crystal damage compared to the other two group-IV counterparts. Crystal damage in turn contributes to the local strain environment, therefore, causing each of the generated SnV centers to experience different environments with the result of having different optical transition frequencies. Moreover, a high degree of crystal damage contributes to the charge-state instability: a higher degree of dislodged carbon atoms leaves a higher density of lattice vacancies and surrounding unsaturated carbon bonds. Together, these may yield a noisier environment surrounding a potentially activated SnV center; hence, such a charge-rich surrounding environment may change the charge state of the SnV center from the negatively charged state to the neutral state, whereas the free spins create a surrounding environment characterized by higher magnetic noise. Together, these represent challenges for the reliable fabrication of SnV centers in diamond.

HIGH ENERGY ION IMPLANTATION OF SN IONS

High-energy ion implantation of Sn ions involves typical ion beam acceleration energies on the order of hundreds of keV. Such values, combined with the relatively high mass number of Sn, create significant crystal damage. This translates into a locally strained environment surrounding the implanted ion, to a different degree. As a result, this may lead to a relatively high inhomogeneous broadening of the generated SnV centers.

The three most important parameters to fix in order to successfully implant Sn ions at a specific designed depth are the acceleration energy, ion flux, and ion implantation angle:

Ion implantation angle: this parameter is relevant to prevent the effect of ion channeling. When the ion beam is aligned along a major crystallographic direction in a perfect crystal, the "channeled" ions will experience significantly less scattering events, resulting in deeper penetration inside the crystal [11]. This is a detrimental effect and is typically undesirable as it leads to uncertainty in the depth of implantation. This effect is mitigated (to some extent) by adopting an ion implantation angle of 7° for diamond and cubic crystals, for example, Si and Ge [33].

Acceleration energy: the combination of the ZPL emission of the SnV center at 619 nm (the emission line) with optimally engineered coupling to the nanophotonic

devices gives an indication and trade-off for the required implantation depth of the Sn ions. The typical thickness of nanophotonic devices is on the order of 200 nm in depth, or less. The required acceleration energy of the Sn ions is then calculated by Stopping Range of Ions in Matter (SRIM) simulations. SRIM and Transport of Ions in Matter (TRIM) simulations do not take into account effects such as ion channeling; therefore, the implantation angle in order to avoid such an effect should be decided in the previous step and inserted as input in the TRIM Montecarlo simulations. The first important aspect to be considered when deciding the acceleration energy is the implantation damage: the higher the acceleration energy of the ion beam, the higher is the number of defects created in the crystal. Next, straggle represents a challenge when considering accuracy in the position of the implanted ions. The straggle quantifies the broadening of the ion beam in the lateral and longitudinal directions. This increases with ion energy and decreases with atomic number. This effect has high relevance when considering typical dimensions of post-implantation nanofabrication devices such as waveguides, and more stringent for resonant cavities where the typical required accuracy and precision are up to a few nanometer. Therefore the acceleration energy should be carefully decided as a trade-off between implantation depth and spatial accuracy.

Ion fluence: this parameter is decided taking into account the empirical conversion yield in order to obtain an average density of resolvable SnV centers per unit area. Taking into account the relatively low conversion yield [32], crystal damage, spatial positioning accuracy, and density of resulting converted SnVs, the ion fluence should be decided as an optimal trade-off based on further types of integration in the nanofabrication phase.

3.3.2 IMPLANTATION DAMAGE AND HIGH TEMPERATURE LOW PRESSURE THERMAL ANNEALING

Ion implantation inevitably causes damage to the crystalline structure of the target material. As such, in the context of the spectral stability of the to-be-activated color centers in diamond, damage to the crystalline structure surrounding the generated SnV centers is considered detrimental.

Once Sn ions are implanted, migration of vacancies is required in order to combine and form the SnV center interstitial complex, as well as mitigate radiation damage as a consequence of the implantation process itself, as discussed in Section 3.2. High temperature low pressure thermal annealing is one of the most commonly available methods for activation of color centers in diamond and is considered the preferred choice in the field. The method requires relatively simple equipment, commonly commercially available. Alternatively, a vacuum thermal annealing oven assembly requires commonly accessible tools and equipment such that such a tool could be built in-house. As such, extensive efforts have been directed towards the development and optimization of annealing protocols, in particular in the context of generation of NV centers.

The diamond surface begins to oxidize around 600 °C [1, 34] and is attacked by oxygen, water vapor, and other gases. Therefore, diamond substrates must be annealed in an inert environment, and hence the quality of the vacuum of the thermal annealing oven is an

important parameter to monitor.

3.3.3 CHALLENGE: HIGH TEMPERATURE LOW PRESSURE ANNEALING SURFACE GRAPHITIZATION

Annealing is achieved by heating the diamond substrate at sufficiently high temperatures in order to allow both vacancies and interstitials to become mobile and recombine. In the case of diamond, annealing represents a major challenge as the damaged surface (upon e.g., RIE or radiation damage upon implantation) tends to graphitize [11].

The diamond crystal is constituted of hybridized carbon atoms sp^3 , where each carbon atom is surrounded by four nearest neighbors placed in a tetrahedral configuration. This represents a metastable bonding configuration. The transformation of diamond into graphite requires breaking sp^3 carbon-carbon bonds and form sp^2 bonds: due to strong orbital overlap and high dissociation energy per bond, the transformation of diamond into graphite under normal conditions takes place at very low rates.

However, studies report that this process can be enhanced if ion implantation damage changes the bond configuration. In fact, in the case of ion implantation at room temperature, the damage density threshold beyond which graphitization occurs is 10^{22} vacancies/cm², independent of ion species or implantation energy (Kalish *et al.*, in Ref. [8]). Taking into account the typical implantation energy of Sn ions of 350 keV, and the ion fluence of 10^{11} ions/cm², this creates ~ 2500 vacancies per implanted ion, a value comfortably below the graphitization threshold. Therefore, in principle, under typical high temperature annealing of 1100 °C and low pressure, i.e., oxygen-free, graphitization of diamond within the crystal should not take place.

Surface graphitization, on the other hand, is a common and well-known challenge to occur upon high temperature annealing, the extent of the graphitization being dependent on several factors such as temperature, pressure, the chemical nature of the environment and duration [35] (Evans *et al.*, 1961). The authors of Ref. [35] reported on surface graphitization of samples at temperatures as low as 900 °C at 1.3×10^{-6} mbar for 16 hours of heating. The authors reported that heating for 5 minutes at atmospheric pressure provided a much more appreciable black layer of graphite by visual inspection. The formation of graphite at the surface is attributed to the deposition of carbon on the diamond surface as a result of surface chemical reactions, concluding that the effect of a purely physical phase change is not evident. In addition, the authors report that the extent of graphitization is dependent on the chemical nature of the surrounding oven atmosphere, with the extent of graphite being the highest in the experiments performed under the air atmosphere, as opposed to the carbon dioxide case.

The author of Ref. [36] (Seal, 1963) investigated the effects of high temperature low pressure annealing on diamond graphitization, for pressures around 1.3×10^{-4} mbar, for duration from 10 to 30 minutes and for different ranges of temperature. For this purpose, the annealing is carried out in graphite crucibles packed with diamond dust: This is implemented to isolate the diamonds from the residual atmosphere in the chamber. For diamond samples heated below 1400 °C, the author concludes that the graphite coating has no orientation effects, while for temperatures higher than 1400 °C there is a clear indication that {001} diamond faces are the most resistant to thermal graphitization. The author specifies also that the partial pressure of residual oxygen from the chamber in the

vicinity of the diamond samples is lower than the measured 1.3×10^{-4} mbar in the chamber, concluding that "*Diamond dust acts as a "getter" for oxygen*".

Most recently, Naydenov *et al.* [13] reported on substantial graphitization of diamond substrates, covered by diamond powder under nitrogen gas atmosphere. The graphitization phenomenon extended to 70 nm, despite the best efforts to prevent surface damage.

3.3.4 WHY IS SURFACE GRAPHITIZATION A CHALLENGE?

Although surface graphitization is a well-known effect that takes place in high-temperature low-pressure annealing, it is equally challenging to quantify to what extent this effect is taking place.

This challenge is relatively easy to mitigate in the case of color centers in diamond that are located far from the surfaces, where a combination of wet inorganic etch of graphite and post-micromachining of devices (e.g. solid immersion lenses fabricated via focused ion beam milling) fully remove any traces of the graphitized surface layers. When placed far from interfaces, charge-noise effects are not a concern. However, in the case of relatively shallow implanted color centers, such as group-IV, graphitization represents a major challenge, hindering the successful incorporation and activation of the color centers to begin with. The complete removal of the graphitized layer results in a reduced color center depth with respect to the sample surface. Activated SnV centers closer to surfaces may experience charge-noise to a larger extent, thus potentially detrimental both to optical and spin properties.

The reason why graphitization represents such a major challenge relies on the extent of the graphitization process itself. First, the extent of the graphitized layer is unpredictable and uncontrollable. This depends on several parameters, briefly listed below:

Annealing oven vacuum quality and stability: the residual concentration of, e.g., oxygen atoms in the chamber promotes oxidation of the diamond surface, as well as etching effects, which results in uncontrolled etching of the diamond cap layer. This represents a challenge, as the implantation depth of the shallow Sn ions is reduced, bringing them closer to surfaces, which might compromise their optical and spin properties. In the extreme case of shallow implanted ions (for sensing applications), the extent of surface graphitization might reach the doped layer, compromising the generation of the color centers altogether. The lowest pressure in the chamber is desirable over the entire duration of the annealing sequence, avoiding pressure variations especially in the ramp-up steps, where pressure can increase in case of sudden temperature gradients;

Annealing temperature: it is beneficial to have a high annealing temperature in order to (at least to some extent) heal the crystal from radiation damage, at the same time keeping the temperature below the gross graphitization threshold (below $\sim 1600^\circ\text{C}$ [36]);

Duration of the annealing sequence: long duration of high temperature annealing is suspected to produce graphitization to a higher extent, therefore short annealing duration is desirable in order to limit the graphitization phenomenon;

Crystallographic orientation: studies have reported $\{100\}$ oriented diamond surfaces to be most resistant and $\{110\}$ least resistant to high temperature thermal graphitization [36] at temperatures $\sim 1700^\circ\text{C}$, while the graphitization below 1400°C stems from an etching effect [35]. This poses a challenge when considering post nano-fabrication annealing, as the fabricated devices will not maintain the original designed dimensions;

The second challenge associated with the graphitization phenomenon relies on the chemical stability of the "graphitized layer". The nature of the suspected "graphite" layer might be different from the one of pure graphite, as a result of the poor oven vacuum that contains other than oxygen residual gases. Such a layer might have high wet etch resistance to, e.g. tri-acid inorganic clean, posing a challenge for wet etching of the graphitized layer.

Considering typical implantation depths of group-IV color centers of the order of 30 nm to 100 nm, even in the optimistic scenario where the graphitization phenomenon extends to a few tens of nanometers at the surface, the latter represents a serious concern. The unpredictability of the graphitized cap layer extent renders the exact SnV center position with respect to the diamond surface unpredictable. As a result, in the context of nanophotonic integration, maximization of optical coupling of the SnV center ZPL emission to the guiding mode (waveguides) or to the resonating mode (photonic crystal cavities) as nanophotonic device tailoring (compensating for SnV center depth position mismatch) results challenging *a priori*.

Ideally, avoiding graphitization on the surface of the diamond is highly desirable. Thereby, the only solution is to prevent the graphitization of the diamond surface to start with, in a systematic and reproducible way.

3.4 METHODS: HIGH ENERGY SN IMPLANTATION AND HIGH TEMPERATURE THERMAL ANNEALING

In this section, we elaborate on the methods developed in order to implant and activate SnV centers in diamond with conventional annealing methods and with a surface-protected modified annealing process method.

This section is organized as follows: we start with describing the pre-implantation methods in Section 3.4.1, followed by considerations on the ion implantation parameters in Section 3.4.2. In Section 3.4.3 we proceed with elaborating on the conventional fabrication process for high temperature thermal annealing. Finally, in Section 3.4.4, we conclude by presenting the alternative fabrication process (surface-protected annealing method) developed to alleviate the challenges associated with the conventional process.

3.4.1 PRE-IMPLANTATION SUBSTRATE PREPARATION

As schematically illustrated in Figure 3.1 (a), before the ion implantation takes place, diamond substrates undergo a series of pre-implantation fabrication steps. For our experiments, we start with ElementSix $4\text{ mm} \times 4\text{ mm} \times 500\text{ }\mu\text{m}$ $\{100\}$ surface-oriented electronic grade diamond plates.

The first step in the preparation of the substrates is to completely remove the traces of the polishing grease compound from the surface of the diamond substrate. Upon optical microscope investigation and qualitative inspection of the traces, we choose to implement

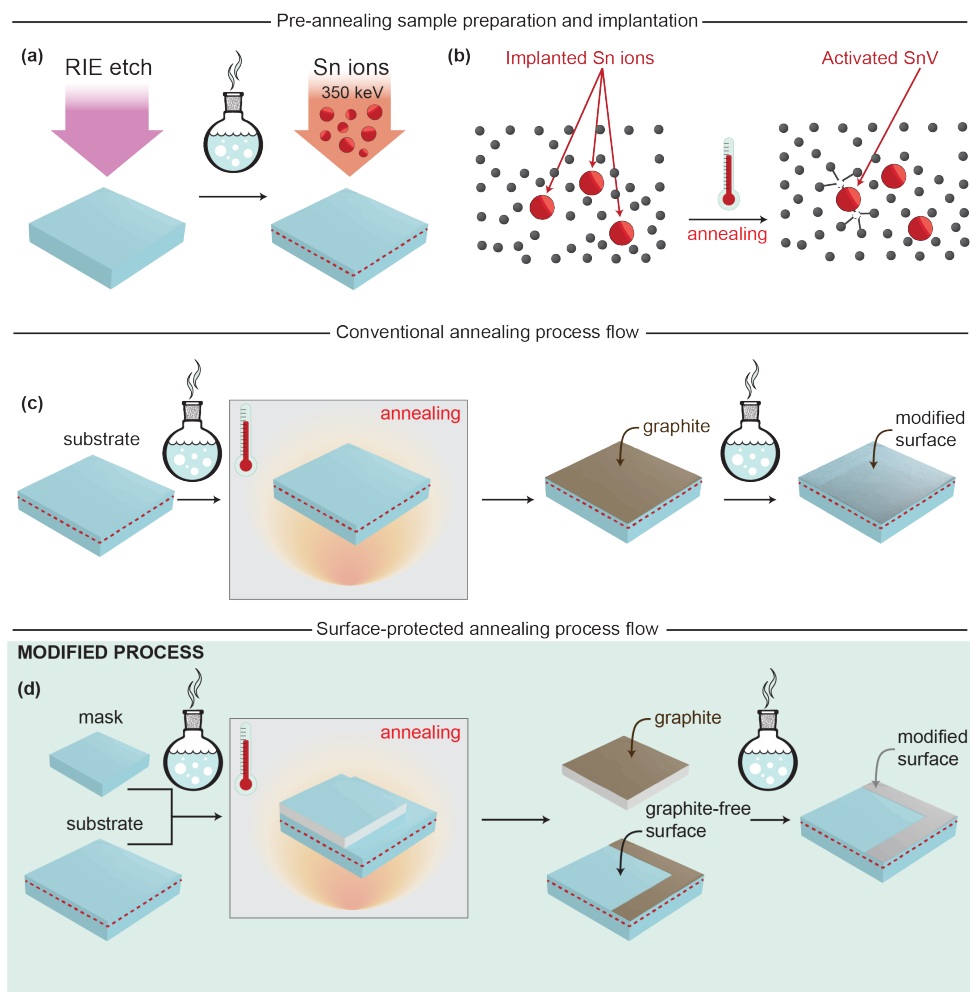


Figure 3.1: **Fabrication processes for high temperature annealing** | (a) **Incorporation of Sn ions into the diamond substrate:** Pre-implantation substrate preparation, including ICP-RIE with Ar/Cl_2 and O_2 strain relief etch is followed by inorganic acid Piranha clean; Next, implantation of Sn ions with an ion fluence comprised between $3 \times 10^{10} \text{ ions/cm}^2$ to $5 \times 10^{11} \text{ ions/cm}^2$ at an acceleration energy of 350 keV; | (b) **Schematic of the ion implantation process:** the trajectory of the Sn ions leaves damage to the crystal, which can be healed by high temperature thermal annealing; | (c) **Conventional fabrication process:** the implanted substrate is inorganic cleaned, followed by high temperature annealing; upon annealing, a thin layer of graphite is suspected to form, which upon tri-acid inorganic cleaning is wet etched. As a result, the surface of the diamond substrate is modified; | (d) **Surface-protected method for high temperature annealing:** in addition to the diamond substrate, a diamond cover sample is prepared, both undergo inorganic tri-acid clean, followed by the arrangement of the cover on top of the substrate in near complete surface contact; we then proceed with high temperature annealing, after which we obtain a surface-protected diamond region, suspected graphite-free non-modified surface and an exposed to annealing vacuum modified region of the diamond substrate; upon inorganic clean, the exposed region graphite layer is wet etched, leaving a modified surface of the substrate.

one of the variants of the following cleaning protocol. In case of a large amount of residual polishing grease compound on the sample surface, our cleaning protocol foresees the soak of diamond substrates in PRS-3000 (stripper solution and residue remover). Typical protocol parameters foresee a soak of 12 hours at room temperature, followed by a 80 °C ramp-up temperature over 30 minutes, followed by acetone and IPA rinse, N₂ blow dry. In case of a low amount of residual polishing grease compound on the sample surface, typically a 80 °C ramp-up temperature over 30 minutes is sufficient (followed by acetone and IPA rinse, N₂ blow-dry).

We then performe an inorganic cleaning protocol, where we start with a 20 minutes 40% HF inorganic cleaning at room temperature, directly followed by a double sequentially 20 minutes each Piranha mixture (ratio 3:1 of H₂SO₄ (95 %) : H₂O₂ (31 %)) at 80 °C. The diamond substrates are then thoroughly rinsed in 3x DI water and blown dry with N₂.

Next, we proceed with an inductively coupled plasma reactive ion etching (ICP-RIE) of ~5 μm etching in a recipe based on Ar/Cl₂ plasma chemistry to remove the residual polishing-induced strain from the substrate surface. Afterward, additional ~5 μm ICP / RIE O₂ chemistry-based plasma etch is performed in order to remove residual chlorine contamination from the previous etching step [4].

We then conclude the pre-implantation protocol with an inorganic cleaning in Piranha solution for 20 minutes at 80 °C.

The samples are then mounted on a 4'' × 1000 μm, {100} silicon carrier wafer and out-sourced for ion implantation. For this step, the depth localization of the implanted Sn ions is controlled in the [001] direction by deciding the implantation energy. In-plane spatial localization is random, which means a blanket implantation is performed.

In order to monitor both topography and chemical purity of the diamond substrates, we implement both quantitative topography characterization methods (e.g. atomic force microscopy (AFM) surface roughness analysis) and chemical component characterization methods (e.g. Raman spectroscopy) and qualitative characterization methods (e.g. scanning electron microscopy (SEM) inspection) before and after each of the subsequent fabrication steps on the diamond substrates. This allows us to monitor the quality of the substrates at each fabrication step and, if necessary, optimize the process parameters of each fabrication step. The goal of this routine is to maintain oversight on any possible detrimental source of organic cross-contamination, as well as to minimize the surface roughness of the substrates due to organic contamination causing micromasking in the RIE etch steps.

3.4.2 ION IMPLANTATION PARAMETERS

While the diamond substrates pre-implantation preparation fabrication methods and post-implantation treatment methods are developed and performed completely in house at Kavli Nanolab Delft cleanroom facility, the Sn ion implantation fabrication step is an outsourced and performed step by an external company.

In order to decide the implantation energy, since the desired optical position of the Sn ions in our nanophotonic devices is up to ~100 nm depth, we first perform SRIM and TRIM simulations to determine the implantation energy.

From TRIM simulations, we find that for an implantation energy of 350 keV, the average implantation depth is 86 nm ± 16 nm. TRIM and SRIM simulations do not take into account

the effect of ion channeling; therefore, based on the values reported in the literature, we adopt an implantation angle of 7° to avoid this effect [11, 21].

Given that typical implantation yields of SnV center creation reported in the literature are on the order of 4 % to 5 % [30, 32] and typical yield of 1 % to 5 % from previous studies in our group, we decided to sweep the ion fluence from low dose (3×10^{10} ions/cm²), intermediate dose (1×10^{11} ions/cm²) and high dose (5×10^{11} ions/cm²).

From TRIM simulations, each Sn implanted at this energy generates on average ~ 2500 vacancies. In order to activate the SnV center, we enable lattice vacancy migration and, at least to some extent, repair the crystal lattice damage by employing a long-duration high-temperature thermal annealing sequence.

3.4.3 CONVENTIONAL ANNEALING PROCESS

As schematically illustrated in Figure 3.1 (c), the conventional high temperature low pressure annealing process is rather straightforward. A complete description of the fabrication steps of the process, including the parameters of the annealing sequence, can be found in the Appendix, Table A.1.

Once the diamond substrates are ion-implanted, we implement a pre-annealing cleaning protocol. This protocol is crucial in order to ensure that no organic contamination is present on the substrates. The presence of organic contamination could be detrimental in the high temperature annealing step for mainly two reasons: first, the organic contamination might degas during the annealing step, increasing the pressure of the vacuum annealing chamber; second, diffusion of foreign atomic species in the substrate is detrimental, as well as diffusion on the surface that might promote the probability of localized graphitization. Thus, we start with a double 20 minutes Piranha inorganic cleaning, followed by a 1 hour tri-acid mixture (ratio 1:1:1 of HNO₃(65%) : HClO₄(70%) : H₂SO₄(> 99%)) in a reflux configuration setup at 120 °C.

Next, we start the high temperature low pressure annealing recipe, parameters described in Ref. [4, 37] and previously developed in the group. The typical annealing time is on the order of 10 hours at 1100 °C. Generally, when designing a thermal annealing recipe, the overarching conclusion is that the temperature gradient over time should be low enough so that the temperature gradient over time is low (to avoid sudden pressure variations) and the vacuum pressure is maintained low and constant at all times. Therefore, the gradient temperature typically is about $\leq 1^\circ\text{C}/\text{min}$ with typical vacuum pressures of $\leq 1 \times 10^{-6}$ mbar. Assuming that the surface of the diamond substrates is free of organic contaminants, as well as water residues, in an oxygen-free vacuum annealing chamber, it is typically hypothesized that the amount of graphite formed on the surface depends on the duration of annealing at temperatures higher than 580 °C (where the diamond surface is expected to start to oxidize [1]) and the quality of vacuum and pressure fluctuations.

Under such annealing conditions, a wet inorganic tri-acid inorganic clean is required to wet etch the formed graphite: we proceed with a 1 hour (or higher) tri-acid wet inorganic clean (ratio 1:1:1 of HNO₃(65%) : HClO₄(70%) : H₂SO₄(> 99%)) in a reflux configuration setup at 120 °C (schematic illustrated in Appendix, Figure A.1 (b)).

3.4.4 SURFACE-PROTECTED METHOD FOR HIGH TEMPERATURE ANNEALING

Figure 3.1 (d) shows a schematic illustration of the surface-protected annealing method. A complete description of the process, including the parameters of the annealing sequence, can be found in Appendix, Table A.2.

In this case, the surface-protected annealing method foresees the addition of a cover material with the goal of protecting the substrate surface from the residual gases in the high temperature annealing oven. Most importantly, it is desirable that the cover material satisfies the following requirements: surface roughness similar to that of the substrate diamond sample, such that close contact between the two surfaces is ensured. A non-near surface contact between the cover and the substrate would allow the diffusion of residual gas molecules in the interstitial residual volume between the cover and the substrate. As a result, diffusion of these can promote modification of the substrate surface, promoting the graphitization phenomenon. Next, the cover material must be chemically inert in order to prevent cross-contamination of the diamond substrate: This ensures that no other atomic species can diffuse into the diamond substrate during high-temperature annealing. Finally, the cover material has to have a high temperature melting point and chemical stability upon high temperature low pressure annealing itself.

The most straightforward optimal candidate for such a cover material is a cover material made out of diamond itself. By choosing a diamond cover, we ensure that the above criteria are met by definition. We chose therefore a pristine two-sided polished {100} diamond cover. We start with the pre-annealing wet inorganic Piranha cleaning, followed by the tri-acid inorganic cleaning protocol, executed on both the implanted diamond substrate and the diamond cover, after which we carefully position the cover material in contact on top of the implanted diamond substrate. The contacted cover + substrate system is carefully placed inside the annealing chamber crucible, evaluating the spatial positioning upon visual inspection. The covered implanted diamond substrate is then annealed at high temperature for 4 hours at 1100 °C, following the annealing sequence described in Appendix, Table A.2 (annealing recipe sequence adapted from [38]).

Once the annealing sequence is complete, the diamond substrate is inspected. First, a qualitative optical microscope inspection is carried out: as will be presented in Section 3.6, typically 100 % full coverage of the substrate surface is challenging to guarantee. This is because during the pumping down step of the annealing oven chamber, a sudden pressure drop can result in a small displacement of the cover along the surface of the substrate, leaving the edge of the substrate uncovered. Typically, the fully exposed edge amounts to ~200 µm to 300 µm length from the sample border. On the basis of the degree of contact between the cover and the substrate, the transition region from covered to non-covered region may be spatially net and sharp, or spatially extended and gradual. Both cases offer the possibility of investigating the nature of the suspected modified diamond surface of the substrate and comparing the properties with the non-modified covered region of the sample. At this stage, the substrate properties are investigated via Raman spectroscopy, SEM, and AFM analysis.

Surface termination of the substrate may have significant impacts on the optical properties performance of color centers, with oxygen termination being the preferred one. In fact,

oxygen termination through soft O₂ plasma treatment has been shown to improve spin-coherence times of near-surface NV centers [39]. In an X-ray photoelectron spectroscopy (XPS) investigation analysis of {100} diamond substrates, in various wet and dry treatment studies, the authors of Ref. [40] report a similar atomic percentage of O 1s between the wet Piranha treatment (5.19 ± 0.36) and the tri-acid treatment (4.84 ± 0.31). Oxygen surface termination might be beneficial for the optimal performance of activated SnV centers, although it has not yet been investigated in the literature. Although wet inorganic clean is no longer required for removing the graphitized layer (not identified on the covered diamond surface), it remains necessary to favor an oxygen surface termination. Thus, post-anneal surface treatments, such as a tri-acid clean, Piranha clean, or ozone surface treatment, are recommended.

Taking into account the considerations above, we proceed with a post-anneal wet inorganic clean, where we first proceed with a double Piranha treatment of 20 minutes each at 80 °C. Following an optical properties characterization of the SnV centers in cryogenic conditions, we proceed with a modified tri-acid cleaning protocol, namely di-acid (developed together with [41]).

In order to achieve efficient wet etching of the suspected graphitized layer on the exposed edges of the diamond substrates, and to favor an oxygen termination on the diamond surface, we follow the considerations of Ref. [42]: we proceed with a double Piranha cleaning at 80 °C, 20 minutes each (to remove organic residues), followed by direct di-acid mixture inorganic cleaning (ratio 1:1 of HClO₄(70%) : H₂SO₄(> 99%)) at 190 °C for 2 hours.

After post-annealing wet inorganic clean, we proceed with the post-annealing inspection of the sample, in a sequence analysis detailed in Section 3.4.5, with results presented in Section 3.6.

3.4.5 ANALYSIS METHODS

ORDER OF ANALYSIS

Pre-anneal, post tri-acid: The analysis starts with a quantitative Raman spectroscopy analysis within ~ 1 hour after the inorganic cleaning step, so the Raman spectra do not detect any organic contaminants. Next, we continue with AFM topography and surface roughness analysis.

Post-anneal, pre-diacid: To ensure that the diamond substrate is free of organic contaminants, we start with a Piranha cleaning for 20 minutes at 80 °C. The analysis starts with a quantitative Raman spectroscopy analysis within ~ 1 hour after the inorganic cleaning step. Next, we continue with qualitative SEM analysis. Afterward, we clean the sample with ethanol, acetone, and IPA, followed by blow-drying N₂ and conclude with an analysis of the surface roughness by AFM. The order of analysis performed here is not the conventional best order, as SEM inspection might introduce carbon contamination: Ideally, the sequence of analysis should be Raman spectroscopy, followed by AFM, and concluded with SEM.

Post-anneal, post-diacid: Within ~1 hour from the di-acid cleaning, we proceed with the same analysis sequence as in the post-anneal, pre-diacid phase.

RAMAN SPECTROSCOPY

We employ a Renishaw Invia Reflex Raman spectroscopy tool, in combination with a 488 nm laser source and a $3000 \text{ gr} \times \text{mm}^{-1}$ fine grating.

ATOMIC FORCE MICROSCOPY

AFM surface roughness analysis can be considered quantitative and comparable one-to-one in absolute values when analyzing different regions of the same diamond substrate. The previous statement is fully valid if the AFM scans are executed within the same AFM analysis session and using the same Atomic Force Microscopy (AFM) cantilever tip, without further assumptions on error introduced by the AFM scanning method. The AFM topographic analysis is executed on a Bruker AFM Dimension Fastscan in non-contact mode (SCANASYST-AIR-HPI, nominal tip radius 2 nm, maximum tip radius 12 nm).

The typical scan area dimension $500 \text{ nm} \times 500 \text{ nm}$: The spatial scan extent is chosen as a compromise between the duration of each scan combined with a representative scale of the dimensions of nanophotonic devices (nanophotonic waveguide width $\sim 275 \text{ nm}$, photonic crystal cavity devices lattice constant $\sim 206 \text{ nm}$).

Data analysis is performed using open source software Gwyddion [43]. The only data processing operation performed on the raw data, in line with the indications from open source user manual, is row alignment with the polynomial method: this method fits a polynomial of given degree and subtracts it from each line and allows one to compensate for the ubiquitous scan line defects. We apply an align row with a 1st degree polynomial, where 1st implies the removal of linear slopes [43]. For a complete overview of the surface topography, we first evaluate the following one-dimensional roughness parameters, defined here: roughness average R_a , root mean square roughness R_q , maximum roughness valley depth R_v . Next, we evaluate the following moment-based statistical quantities quantifying the height irregularities: mean roughness S_a , mean square roughness (RMS) S_q , maximum pit depth S_v , maximum peak height S_p .

SCANNING ELECTRON MICROSCOPY

SEM analysis is performed on a Hitachi Regulus system. Qualitative Scanning Electron Microscopy (SEM) analysis, the data is acquired from a combination of Secondary Electrons (SE, topographical surface information) and Low-Angle Backscattered Electrons (LA-BSE, mixture of compositional and topographical surface information). A contrast difference in the SEM pictograms might represent a difference in either topographical features between the two regions, a difference in compositional information, or a difference in the extent of charging between the two regions, which again might be attributable to presence of different materials of different chemical composition present on the substrate.

Taking into account that the diamond substrate is an insulating material, charging of the substrate represents a challenge, and therefore a low acceleration voltage of the primary electron beam is used. We do not coat the substrate with any conducting layers to mitigate the charging effect (a common method used to prevent the charging of insulating specimens) in order to avoid artifacts and ambiguity in the results obtained.

In order to prevent surface contamination from the SEM session, which might be detected in the Raman spectroscopy chemical analysis, we perform the SEM analysis after the Raman inspection. This gives the additional advantage of inspecting the properties of the exact Raman scanning map region. As will be presented in Section 3.6.2, this offers the

advantage of correlating the qualitative inspection of the SEM with the Raman spectroscopic analysis one-to-one at nanoscale. At the same time, we use a cold trap to mitigate carbon deposition as a result of the electron beam raster scan across the sample surface and we limit the SEM session in time to ~30 minutes.

3.5 RESULTS: CONVENTIONAL HIGH TEMPERATURE ANNEALING METHOD

The extent of the graphitization process during high temperature low pressure annealing depends on several parameters. Fluctuations in the process parameters are a variable prone to fluctuations, therefore, the extent of graphitization in different vacuum annealing oven environments may be extending to more or less graphitization of the surface. Authors in Ref. [44] report on typical 5 nm to 10 nm in similar pressure annealing conditions as presented in this study.

Typically, this phenomenon is suspected to be greatly dependent on the temporal extent of the high temperature annealing process: the longer the annealing time, the more extended is the graphitization phenomenon, with various degrees of spatial extent. Hence, graphitization represents a limiting factor in terms of annealing time and, therefore, a hindering factor both in successful activation of implanted color centers and efficient healing of the damage in the diamond crystal.

To date, to our knowledge, no method has been invented in order to prevent or at least alleviate the extent of the surface graphitization in diamond in a systematic and reproducible way that does not foresee etching (dry or wet) of the graphitized diamond cap layer. The objective of this study is to quantify the amount of graphitization post-annealing on our samples and propose a method to prevent or at least alleviate the extent of the surface graphitization in diamond.

For this purpose, we evaluate the effect of the high temperature low pressure thermal annealing, following the conventional fabrication process schematically illustrated in Figure 3.1(c) and described in Section 3.4.3.

To evaluate the spatial extent of the graphitization phenomenon under 1×10^{-6} mbar pressure and 1100 °C annealing treatment, we employ the conventional annealing recipe (described in Section 3.4.3 and detailed in Appendix, Table A.1), developed in Ref. [37] (extensively and successfully employed in the generation of narrow-linewidth NV centers in diamond) for a continuous annealing time of 10 hours.

NANOPHOTONIC DIAMOND DEVICES

In order to evaluate the spatial extent of the graphitization phenomenon, we dedicate a diamond substrate on which diamond photonic crystal cavity and 1D waveguide devices have been previously fabricated. Specifically, the fabrication of photonic crystal cavity designs is based on quasi-isotropic undercut etch process [45–47], described in Chapter 2. In this case, the diamond substrate first undergoes the fabrication process to obtain suspended nanophotonic devices, while activation of SnV centers by high temperature annealing follows post-nanofabrication with the conventional high temperature annealing fabrication process described in Section 3.4.3, as detailed in Appendix, Table A.1. Given

the nature of the quasi-isotropic undercut etch, all devices are aligned parallel to $\langle 110 \rangle$ crystallographic axis, to ensure a uniform longitudinal cross-section of devices.

Typical nanophotonic cavities chiplet devices are shown in Chapter 5, Figure 5.1 (b). We fabricate asymmetric one-sided photonic crystal cavities (design discussed in Section 2.4.2, schematically illustrated in Figure 2.3). The design of the equivalent symmetric mirrors device shows in Finite Element Method (FEM) COMSOL® simulations the cavity resonance at 620 nm and the quality factor $Q \sim 1 \times 10^6$. Given that the fabrication process implies uncertainty over several fabrication steps, we sweep the design parameters of the photonic crystal cavities to compensate for fabrication imperfections in the design phase, as detailed in Chapter 5. Therefore, a typical sweep of the device parameters has the objective of fabricating devices with an expected cavity resonance in the range 600 nm to 650 nm (as shown in Chapter 5, Section 5.3). Once the device fabrication has been completed, we characterize the devices in a room-temperature reflection setup (setup schematic in Section 5.6.2, Figure 5.7). Before the annealing step, we systematically find photonic crystal cavities with resonant wavelengths in the range of 619 nm to 680 nm and quality factors of $Q \sim 4500$ to $Q \sim 18000$ (values in-line with statistics presented in Section 5.3).

Resonant photonic crystal cavities are extremely sensitive to fabrication parameters, namely, assuming a constant refractive index of diamond over the following fabrication steps, any variation in the geometric parameters of the fabricated devices translates into a shift in the resonant wavelength, as well as a variation in the quality factor of the pre-annealed characterized devices. For this reason, photonic crystal cavities are excellent indicators of the extent of the surface graphitization phenomenon. As shown in Ref. [37], simulations show that even for extremely small deviations from the optimal design of devices, the quality factor is greatly affected and decreased.

Therefore, if post-nanofabrication high temperature annealing is characterized by surface graphitization phenomenon, we expect to measure a variation in the quality factors as well as a shift in the resonant wavelengths of the fabricated devices. Moreover, given the broad sweep of cavity parameters in the design phase, we can quantify a resonant wavelength shift up to ~ 60 nm in fabricated devices.

After annealing the diamond substrate containing the fabricated devices with the conventional annealing protocol described in Section 3.4.3, we perform 3 consecutive inorganic wet tri-acid cleaning steps at 120°C (temperature limited), each of 1 hour duration to wet etch the graphitized layer. Post-inorganic clean Raman spectroscopy analysis shows that when scanning on a flat area of the diamond substrate, no Raman graphite peak is detected. In contrast, when the laser source is focused on a nanocavity, although not prominent, a small graphite peak is detected at 1600 cm^{-1} , indicating residues of graphite on the fabricated devices. This indicates serious challenges in wet etching graphite residues on annealed substrates post-fabrication.

A room-temperature optical characterization of the nanophotonic cavities was performed with the same measurement conditions as in the pre-anneal optical characterization step. The optical characterization of the cavity devices, after the post-annealing and consecutive (3x) inorganic tri-acid clean steps, shows no resonance on any of the fabricated devices, thus unable to evaluate the quality factors of the devices. This result indicates two hypothetical scenarios: one is that the resonance of the fabricated devices falls out of our measurement window (in the range of 590 nm to 695 nm), or, second, the resonance of

the devices is destroyed altogether due to severe modification of the device geometry and increased surface roughness. In either of these hypotheses, the outcome of the nanocavity device optical characterization is a clear indication that the graphitization phenomenon is not shallow surface limited but rather extended to a range of tens of nanometers, indicating a severe modification of the diamond surface upon high temperature low pressure annealing.

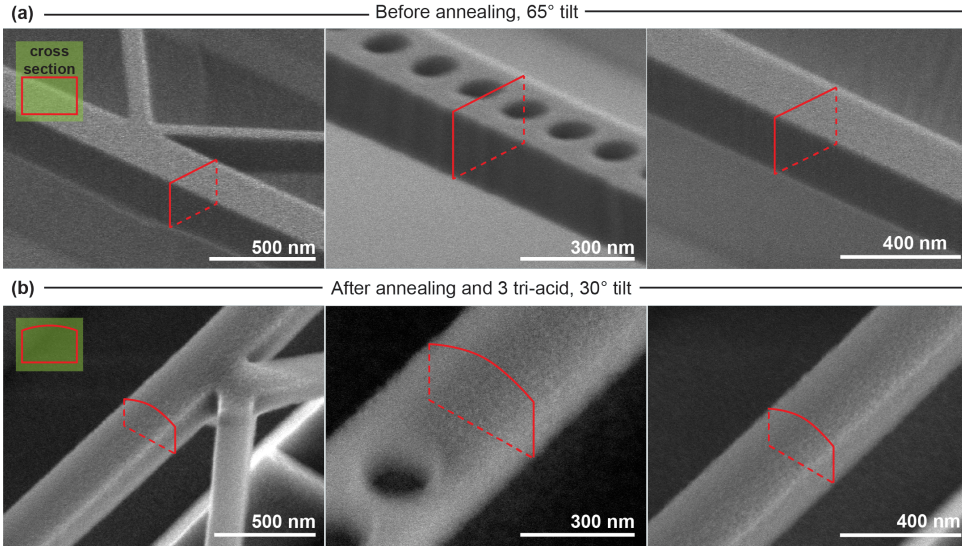


Figure 3.2: **Annealing with conventional process: SEM inspection** SEM pictograms of diamond nanophotonic devices: left - diamond waveguide with a cross holding bar, center - nanophotonic crystal cavity, right – simple nanophotonic waveguide; | **Before annealing (a)**: rectangular cross section fabricated devices via quasi-isotropic undercut fabrication process: prior to annealing, the cross section of the devices is rectangular; | **After annealing (b)**: rounded-top cross section, same devices after the conventional high temperature thermal annealing fabrication process flow (illustrated in Figure 3.1 (c)), followed by 3 consecutive inorganic tri-acid cleaning steps; the cross section of the devices is round on top side and visibly modified, indicating the graphitization process is not limited to the few nanometers surface layer: the edges at the intersection of top side with vertical sidewalls of the devices are affected eroded more than flat surfaces.

The absence of any resonant cavity signatures prompted us to start a systematic investigation of the graphitization phenomenon. Therefore, a qualitative SEM investigation of the fabricated devices has been performed first. Figure 3.2 presents a qualitative SEM comparison of the fabricated devices before and after the annealing process with the conventional fabrication process.

Specifically, we inspect the geometry of waveguides and photonic crystal cavities. Figure 3.2 (a) shows (left) waveguides with V-shaped holding bars, (center) holes region of photonic crystal cavity, and (right) nanophotonic waveguide before high temperature annealing is performed. The cross section of the presented devices is rectangular, with well-defined top-side flat horizontal and vertical surfaces on each device's sides. Figure 3.2 (b) shows the same devices as above, inspected after high temperature annealing and 3 consecutive inorganic tri-acid cleaning steps. In contrast to Figure 3.2 (a), here the devices display a rounded cross section on the top side, indicating a severe modification of the

devices' aspect. In addition, the vertical and horizontal device surfaces do not exhibit clear and net edges, e.g. rather blurred and rounded transitions from the top surface to the inspected vertical sidewalls. This indicates an enhanced graphitization rate at the intersection of the horizontal surface with the vertical sidewall of the devices.

From a qualitative inspection, the post-anneal surface roughness of the devices is visibly increased, with the graphitization phenomenon presenting no differences in between the differently oriented exposed crystallographic planes (when comparing exposed $\{100\}$, $\{110\}$ and $\{111\}$ planes exposed after the quasi-isotropic etch on the overall substrate) and shapes (when comparing V-shaped, straight waveguides and circular holes on nanofabricated devices presented here).

Taking into account the SEM resolution (pixel size between 1 nm to 2 nm for the scale bars here presented respectively examples in Figure 3.2) of 300 nm to 500 nm, a graphitization phenomenon limited to 1 nm or 2 nm on the surface of the devices, would be below the SEM detection limit and hence non-observable even in a qualitative SEM inspection. Thus, given the clearly detectable high surface roughness observed in the SEM inspection in Figure 3.2, we conclude that this phenomenon is hypothetically extended to a few tens of nanometers (to the least, potentially higher than reported in Ref. [44] under similar annealing conditions) and is not limited to the superficial layer of a few nanometers diamond cap.

The extent of graphitization to tens of nanometers poses a great challenge when considering the depth of implantation of the SnV centers (typically at ~ 86 nm depth from the surface in our diamond substrates), as graphitization in post-annealing and tri-acid cleaning on the scale of tens of nanometers results in a shallower depth of comparable order of magnitude with respect to the designed ion implantation depth. Given that the extent of the graphitization phenomenon is difficult to predict beforehand, this effect is challenging to compensate for in the design phase of devices by changing the dimensions of devices parameters. In turn, as shown in Ref. [17], non optimal positioning of color centers in diamond waveguides decreases the coupling of the ZPL photons to the waveguide mode. In addition to alteration of the device geometry parameters, a more serious issue associated with graphitization phenomenon on fabricated devices is the substantial surface roughness of the devices after inorganic wet etch of the formed graphite. The inorganic tri-acid clean efficiently wet etches the graphite layer from the devices surfaces, however, as will be shown in the next sections, the surface roughness of the devices is dramatically increased. The substantially increased surface roughness at the devices' surfaces dramatically increases scattering losses of e.g. diamond nanophotonic waveguides and destroys the cavity resonance in the case of nanophotonic crystal cavities.

Thus, it is highly desirable to avoid the graphitization of the diamond surface to begin with.

3.6 RESULTS: SURFACE-PROTECTED METHOD FOR HIGH TEMPERATURE ANNEALING

Surface modification resulting from high-temperature thermal annealing is a highly undesirable effect, as mentioned in the previous section. In order to avoid, or at least alleviate to some extent, this effect, we propose a modified annealing method, i.e. surface-protected

annealing method. This consists of fully covering the diamond substrate with a protective slab of material during high temperature treatment, thereby protecting the surface of the substrate from residual gases in the annealing oven chamber that promote the graphitization phenomenon.

In this section, we evaluate the performance of the alternative proposed surface-protected annealing method described in Section 3.4.4, schematically illustrated in Figure 3.1 (d), on a diamond substrate named **Sample A**. The surface-protected annealing method here proposed has two main advantages: first, as it will be presented following, it allows for obtaining non modified diamond surface upon high temperature annealing, and second, in case of limited exposed edges of the diamond substrate, it offers the possibility to reliably and quantitatively investigate the graphitization phenomenon.

This section is organized as follows: we start with a qualitative optical microscope inspection of the annealed substrate surface here. We then proceed with investigating the graphitization phenomenon in the transition region from surface-protected to exposed diamond region. Section 3.6.1 shows the qualitative SEM investigation. Next, Section 3.6.2 shows a quantitative Raman spectroscopy analysis of the aforementioned region. Section 3.6.3 shows the quantitative topographic analysis of the surface roughness and Section 3.6.4 concludes with a quantitative analysis of the graphitization phenomenon on a separate experiment aimed at providing a quantitative XPS analysis on similar fabricated diamond substrates. We conclude each section with a discussion of the respective analysis outcome and the benefits of the proposed surface-protected annealing method.

A preliminary optical microscope inspection of the diamond substrate, prior (Figure 3.3 (a)) and after (Figure 3.3 (b)) annealing with the surface protected method, is illustrated in Figure 3.3. The upper left corner and lower right corner in (b) have different optical-microscope contrasts, qualitatively indicating a difference in properties between the two regions of the substrate surface. Indeed, the top-left corner corresponds to the region of the diamond substrate which has been fully covered throughout the high temperature annealing process, while the bottom-right corner has been exposed to the annealing oven vacuum. We chose to investigate this region of the sample, which is indicative of the graphitization phenomenon on all the diamond substrates fabricated with this method so far.

Virtually, this exposed region of the sample has undergone the same graphitization phenomenon as in the annealing conditions with the conventional annealing fabrication method described in Section 3.4.3. Therefore, the chosen region of the sample represents an excellent candidate for investigating the nature of the supposedly graphitized diamond surface. At the same time, we take into account that the starting surface properties (both chemical and topographical) are the same on the diamond surface, by the design of the experiment. Therefore, this substrate offers the advantage of comparing chemical and topography properties on both the non-graphitized (covered) and graphitized (uncovered) regions one-to-one. This enables a comparison of the absolute values of both types of measurement. Prior to the high temperature treatment, the two regions of the substrate underwent exactly the same fabrication process treatment. Hence, even if any organic contaminants or unforeseen effects were present on the sample surface, these would be the same on both covered and uncovered diamond regions and would result in chemical

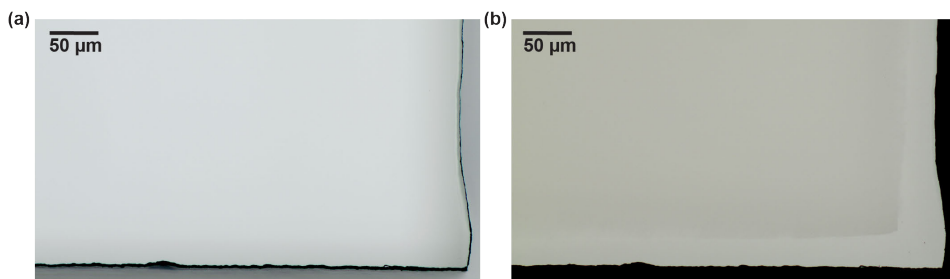


Figure 3.3: **Annealing with surface-protected annealing method: optical microscope inspection** | (a) Overview of the sample before high temperature annealing: the overall top surface of the sample has the same uniform contrast; | (b) Overview of the same area as in (a), after surface-protected high temperature annealing: top left corner corresponds to area of the diamond substrate fully covered during the annealing process, bottom right corner corresponds to the diamond surface edge exposed to the annealing oven vacuum throughout the high temperature treatment. A contrast between the two regions is identified, therefore, this edge of the sample is suspected graphitized.

analysis to the same extent.

The starting substrate surface properties are uniform across the entire surface, with comparable same order of magnitude surface roughness values. Therefore, an AFM surface roughness analysis can be considered quantitative and comparable one-to-one in absolute values when analyzing different regions. With the above considerations, a sample that presents both covered and exposed areas that have undergone the surface-protected annealing treatment offers the advantage of easier data analysis and interpretation of the results of both quantitative and qualitative results, enabling a clearer understanding of the phenomenon, while eliminating potential uncertainties related to substrate sample preparation.

3.6.1 SCANNING ELECTRON MICROSCOPY INVESTIGATION

In this analysis, we image the sample in a tilt-angle view of the sample stage 0° (a top-down image of the surface is obtained) such that the SEM contrast identified in the scan is exclusively attributable to the presence of different chemical composition materials (identified in the inspected region) or different degrees of surface roughness.

Figure 3.4 illustrates the SEM analysis of the diamond sample region, previously inspected under the optical microscope (Figure 3.3), with the substrate analysis after the annealing step (top panel (a) and (b)) and after the wet inorganic clean (bottom panel (c) and (d)).

POST-ANNEAL

Figure 3.4 (a) presents an overview of the edge of the diamond surface analyzed after annealing treatment. The upper right area (bright gray) corresponds to the area of the diamond substrate which has been fully covered during the annealing treatment and hence fully protected from the residual gases in the vacuum chamber of the oven. The bottom right edge (dark gray) corresponds to the surface of the diamond that has been fully exposed to the vacuum of the annealing oven during the annealing treatment (sequence described

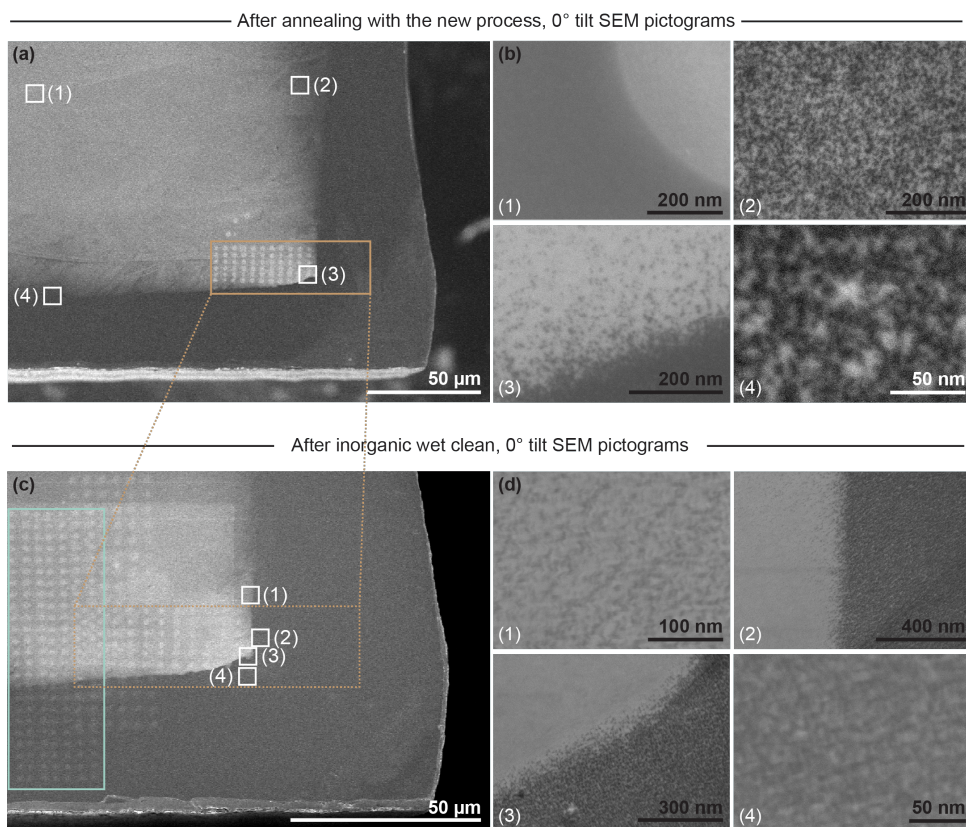


Figure 3.4: **Surface-protected annealing method: SEM inspection.** SEM inspection of a diamond substrate high temperature treated with the surface-protected annealing method: The covered region is not modified by the high temperature treatment, while the exposed region is irreversibly modified. **Top panel:** after annealing | **Bottom panel:** after annealing and inorganic wet clean and etch of graphitized region; | (a) Overview of the sample after high temperature annealing: the center sample is graphite-free, the edge is suspected graphitized; | (b) Zoom-in qualitative inspection: (b.1) covered surface graphite-free area; (b.2) spatially broad extended transition region graphite-free to graphitized region; (b.3) spatially abrupt and net transition region graphite-free to graphitized region; (b.4) fully graphitized region; | (c) Overview after inorganic wet Piranha clean + 2 h of inorganic di-acid clean: center sample is not affected, the graphite on the sample corner is suspected to be fully wet etched, but the surface is modified: (c.1) spatially broad and extended transition region; (c.2) and (c.3) net transition region; (c.4) corner edge of the sample: previously suspected graphitized. Scale bars shown respectively.

in detail in Appendix, Table A.2). In Figure 3.4 (b) we zoom in on 4 representative regions on the analyzed substrate.

Panel (b.1) shows the qualitative surface appearance of the fully covered region, where the contrast is uniform on the lower left region. The difference in contrast in (b.1) is fully attributable to a height difference in the analyzed region: we choose a diamond pit resulting from a localized micromasking (after the strain-relief etch) identified roughly in the center of the sample. This choice of region analysis is a compromise and purely practical: the high amount of charging in the micromasking hole during the inspection prevents us from

acquiring a sharp stable pictogram for fully flat uniform areas.

Panel (b.2) shows a spatially extended transition region from covered to non-covered diamond substrate: a clear contrast between small dark gray islands and light gray islands can be noticed in a dense random pattern. Taking into account the latitude coordinates centered on the inset of the illustrated figure, the gradual transition is spatially extended to $\sim 30\text{ }\mu\text{m}$ from the fully covered region to the fully exposed region. This extended transition region may be the result of non-perfect contact between the cover and substrate, which in turn allows for diffusion of residual gases between the two, promoting graphitization in this area but to a limited extent.

Panel (b.3) shows a sharp net transition region, where the density of dark gray islands on the top right side is less than in (b.1). In this case a sharp transition can be observed from the fully covered to fully exposed region, spatially extending on a scale of $\sim 300\text{ nm}$, roughly an order of magnitude lower than the (b.2) region. This is indicative of a better contact between the cover and the substrate, preventing more efficiently the diffusion of vacuum chamber residual gases, hence efficiently preventing the graphitization phenomenon.

Panel (b.4) shows a region of the diamond surface closer to the fully exposed surface region to the annealing oven chamber conditions, where the dark gray pattern distribution can be clearly evaluated, at the limit of the SEM resolution (here the pixel size is 0.20 nm). We chose to inspect the region closest to the fully exposed region of the sample, which is close to the representative fully exposed region. This is a compromise due to the challenging SEM imaging conditions at this scale.

Comparing panels (b.1), (b.2), (b.3), and (b.4), it can be seen that there is a clear modification of the surface between the covered diamond region and the fully exposed region.

POST-INORGANIC CLEAN

Figure 3.4 (c) presents an overview of the edge of the diamond surface analyzed after the inorganic cleaning and removal of the suspected graphitized layer in the exposed region. This is the same spatial region inspected in Figure 3.4 (a). For the same considerations as in the post-anneal SEM analysis, we perform the post-inorganic clean analysis of the sample after the chemical Raman spectroscopy. Qualitatively, the same considerations as in Figure 3.4 can be made: the non-covered region clearly shows a different contrast than the covered sample region. It is important to note that although the suspected grown graphite was fully wet etched, previously present on the exposed edge of the sample surface, the different contrast between the covered and uncovered regions still persists. As will be shown in Section 3.6.2, after the inorganic cleaning step, there is no presence of graphite material, therefore, the observed contrast can be fully attributed to different surface topography.

Panel (d.1) shows the closest bottom part of the extended covered to non-covered diamond region, clearly showing a non-uniform surface topography. Similarly as in Figure 3.4 (b.2), the contrast can be attributed to the effects of the surface topography.

Panels (d.2) and (d.3) are pictograms of the net transition region, with (d.3) located at the nanoscale the same as in (b.3). Both show a spatial extent region up to $\sim 300\text{ nm}$, indicative of good contact between the cover and the substrate. In this case, the upper right side of both subfigures show uniform contrast, indicative of a uniform surface topography. This indicates that optimal contact between the cover slab and the substrate potentially yields no graphitization at all on the covered side of the sample, with the transition region spatially limited to a few hundreds of nanometers.

Finally, Panel (d.4) shows a fully exposed region of the diamond substrate. Crucially, to note, is that despite full removal of the graphitized layer, the surface of the fully graphitized region presents significant surface topography features. This may be indicative of non-uniform surface graphitization phenomenon, leaving a higher surface roughness diamond after wet etching the graphitized layer.

DISCUSSION

Panels (c.3) and (d.3) present the SEM analysis of the transition from the covered to the non-covered region at the nanoscale. It should be noted that before wet inorganic clean (c.3) of the graphitized exposed layer the image contrast can be attributed to both chemical and topography effects differences between the two regions, while after wet inorganic clean (d.3) the difference in contrast is unequivocally attributed to surface topography effects only. This implies that exposing the diamond substrate surface of interest during annealing treatment to annealing oven chamber conditions results in an irreversible modification of the diamond surface properties.

As a final remark, the brown inset in Figure 3.4(a) and cyan inset in Figure 3.4(c) show in bright gray the grid of laser spots corresponding to the Raman analysis maps, performed after annealing and following after inorganic cleaning wet etch of graphitized layer, respectively.

3.6.2 RAMAN SPECTROSCOPY INVESTIGATION

Raman spectroscopy is a powerful non-destructive analysis tool, commonly used to probe a variety of properties of molecules and materials. Specifically, when applied to both amorphous and/or crystalline materials, this investigation method provides insights into properties of interest in semiconductor applications, e.g. crystal symmetry, chemical composition, stress and strain, disorder and defects, among others. In our case, specifically, Raman spectroscopy represents the go-to non-invasive diagnostic tool to inspect the quality of diamond films [48, 49], as well as to investigate the nature of graphite formation in diamond under different process parameters [50].

Typically, the Raman shift peak of the in electronic grade diamond substrates, in several distinct samples, is measured and located at 1332.47 cm^{-1} with a FWHM of $\sim 1.31\text{ cm}^{-1}$ to 1.46 cm^{-1} (similar to the values reported by the manufacturer). Although the diamond peak position is identified and located at the measured value above in all fabrication steps (up to the spectrometer calibration error), the FWHM may vary. Taking into account that there are no significant changes in the position of the diamond peak, with slight variations in the FWHM and given that we are interested in the spectral region where the graphite peak could present, in this study we focus and acquire the spectral region between $\sim 1350\text{ cm}^{-1}$ to 1950 cm^{-1} . By starting spectral acquisition at 1350 cm^{-1} , we are close enough to the diamond peak at 1332 cm^{-1} , but we avoid blinding the detector counts at 1332 cm^{-1} . With the combination of acquiring parameters (100% power 488 nm laser source, $3000\text{ gr} \times \text{mm}^{-1}$ fine grating, 10 second acquisition time per trace) we obtain a good signal-to-noise ratio (ratio of the peak value of the signal to the root mean square of the noise) between the graphite peak ($\sim 1600\text{ cm}^{-1}$) and the background noise.

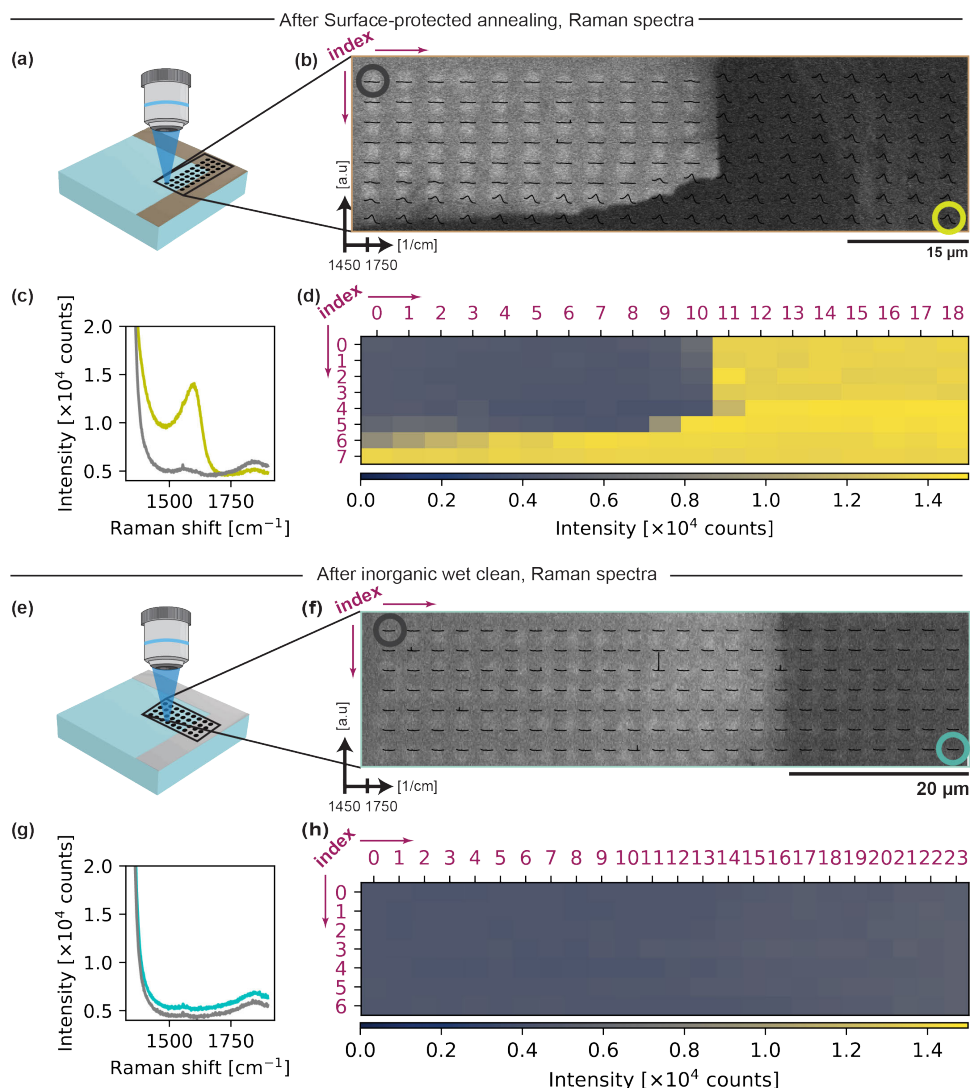


Figure 3.5: **Surface-protected annealing method: Raman spectroscopy investigation.** Top panel: after annealing and Bottom panel: after inorganic clean wet etch of graphite; | (a) Schematic of the scanned map region of the sample; | (b) Correlated (underlying) SEM pictogram of the analyzed graphite-free to graphitized transition region (overlying) Raman map (grid of acquisition spots): graphed spectra (from 1450 cm^{-1} to 1750 cm^{-1} (graphite vibrational peak around 1580 cm^{-1}) of laser spots grid; | (c) Full Raman spectra (from 1350 cm^{-1} (vicinity of the diamond peak at 1332 cm^{-1}) to 1900 cm^{-1}); | (d) Heat-map of the grid of evaluated points, peak height evaluated at maximum intensity counts at 1600 cm^{-1} ; | (e) Same as (a); | (f) Same analysis as in (b), here after di-acid inorganic wet etch clean of graphite; (underlying) correlated SEM map; | (g) Full Raman spectra (from 1350 cm^{-1} (vicinity of the diamond peak at 1332 cm^{-1}) to 2000 cm^{-1}): no graphite peaks visible in either regions; | (h) Heat-map of the grid of evaluated points, peak evaluated at maximum intensity counts at 1600 cm^{-1} . Index number (XY) of Raman laser spots same for (b) and (d), and for (f) and (h).

POST-ANNEAL

Figure 3.5 (a) shows a schematic of the Raman inspection analysis area after annealing (the correlated SEM inspection shown in the inset of 3.4 (a)). In order to cover a large area that would map both net and broad transition regions, we scan a map of 8×18 points, with a spatial resolution of $\Delta x = 4 \mu\text{m}$ and $\Delta y = 3 \mu\text{m}$.

Figure 3.5 (b) shows (underlying) the SEM nanoscale inspection of the (overlying) Raman map of acquired intensity spectra, spectra graphed from 1450 cm^{-1} to 1750 cm^{-1} (full spectra from 1350 cm^{-1} to 1900 cm^{-1} , 100% laser power, 10 second acquisition time per trace). By underlying the SEM pictogram, showing the array of laser spots, we can correlate the intensity of the Raman spectra with the analyzed surface location spots in the area of interest at nanoscale. In fact, inspecting the spectra in the region of 1450 cm^{-1} to 1750 cm^{-1} , it can be noticed that the spectra corresponding to the points in the previously fully covered region do not show prominent Raman peak within the same spectral window where the graphite peak is expected, with intensity counts at the noise level. Spectra corresponding to the laser spots points in the transition region and the fully exposed region of the diamond surface all present the typical broad Raman peak of disordered graphite [50].

On the other hand, taking into account the spatial resolution of $\Delta y = 3 \mu\text{m}$, one can roughly estimate to the micrometer scale the spatial extension of the broad transition regions amounting to $\sim 9 \mu\text{m}$ in the y direction, typical of samples prepared with this method. For spatially broad transition regions, this estimate is more accurate upon Raman analysis than upon SEM inspection. From this analysis, we conclude that the Raman analysis is suitable for measuring the spatial extent of broad transition regions at micrometer scale. The case of the net transition region (SEM zoom in Figure 3.4 (b.3)), shows an abrupt drop from the high graphite Raman peak to noise level; therefore, in the case of net abrupt transition regions, SEM inspection is a more suitable tool to estimate the spatial extension at nanoscale.

Figure 3.5 (c) shows the full acquired Raman spectra from 1350 cm^{-1} to 1900 cm^{-1} of the first (top left) acquisition point in the fully covered diamond region and last (bottom right) acquisition point in the fully uncovered and exposed diamond region. Figure 3.5 (d) shows the heat-map intensity evaluated in 1600 cm^{-1} , that is, the maximum of the typical disordered graphite Raman peak. It can be noticed that the intensity of the peak increases going from the fully covered to fully exposed diamond surface, with different spatial extents, matching the SEM qualitative analysis, once again confirming a good correlation between the two complementary diagnostic tools.

POST-INORGANIC CLEAN

Figure 3.5 (e) shows a schematic of the Raman inspection analysis area after inorganic cleaning (the correlated SEM inspection shown in the inset of 3.4 (d)). Again, in order to cover a large area that would map both net and broad transition regions from previously covered to non-covered regions of the diamond surface, we scan a map of 7×20 points, with a spatial resolution of $\Delta x = 3 \mu\text{m}$ and $\Delta y = 3 \mu\text{m}$. In this case the Raman map partially overlaps with the map presented in Figure 3.5 (b): the reason for this experiment decision is to determine whether the bright gray spots left by the Raman map scan before the wet inorganic clean have caused a modification of the diamond surface, while at the same

time acquiring a post inorganic cleaning Raman map on a laser-induced modification-free region of the sample. The overlap area is $\sim 6\ \mu\text{m} \times 21\ \mu\text{m}$, therefore large enough to consider similar graphitization phenomena occurring on both post-anneal and post-inorganic clean analyzed adjacent surface areas.

Figure 3.5 (f) shows (underlying) the SEM nanoscale inspection of the (overlying) Raman map of acquired intensity spectra, graphed from $1450\ \text{cm}^{-1}$ to $1750\ \text{cm}^{-1}$ (full spectrum from $1350\ \text{cm}^{-1}$ to $2000\ \text{cm}^{-1}$, laser power and acquisition time the same as in (c)). After the inorganic clean protocol described in Section 3.4.4, the expectation is that no organic matter is left on the surface of the diamond substrate. No substantial difference can be noted between the spectra acquired in the overlap region of the Raman grids with respect to the spatially separated ones (before and after the inorganic clean step), hence indicating that the laser-induced surface modification of the diamond substrate is not a chemical nature one.

Figure 3.5 (g) shows the full acquired Raman spectra from $1350\ \text{cm}^{-1}$ to $2000\ \text{cm}^{-1}$ of the first (top left) acquisition point in the fully covered diamond region and last (bottom right) acquisition point in the fully uncovered and exposed diamond region. The two spectra have a full qualitative overlap. Although the order of magnitude of the intensity counts is the same, the intensity counts in first (top left) show a higher number of counts compared to the acquisition point last (bottom right).

When evaluating the intensity counts in $1600\ \text{cm}^{-1}$, in Figure 3.6 (h) heat-map intensity a continuous transition from the covered to uncovered surface region can be observed with a non-significant gradient in intensity counts. Again, this shows that the graphite formed during the annealing treatment was efficiently etched upon wet inorganic treatment.

DISCUSSION

In the above Raman and SEM analysis, we have investigated the chemical nature of the surface modification upon high temperature annealing treatment, inspecting the degree of graphitization phenomenon at nanoscale.

Taking into account the Raman spectra in Figure 3.5 (b), after the high temperature treatment, the uncovered diamond region shows clear peaks located at $1600\ \text{cm}^{-1}$, indicative of graphite formation, while the Raman spectra in the covered region evaluated in the same spectral region show counts to the noise level, indicating no graphite formation at all. This result confirms the correlated SEM inspection of the Raman grid of points, where the contrast between covered and uncovered regions is different, respectively.

Considering the spatially broad transition region (bottom left) of Figure 3.5 (b) (equivalent SEM zoom in Figure 3.4 (b.2) and (b.4)), the non-graphitized to graphitized transition region shows that the intensity of the disordered graphite peak gradually decreases to the noise level when moving from fully uncovered to fully covered surface region. This indicates that even in the case of not perfect contact between the cover and the substrate, the formation of the graphite presents a gradient proportional to the degree of contact. This leans in favor of the hypothesis that the graphite formation mechanism is caused by diffusion of residual gases from the annealing oven, which might promote the graphitization phenomenon. Most importantly, analysis of the gradient of graphitization in the broad extended transition region clearly shows that Raman spectroscopy is extremely sensitive to the presence of disordered graphite on the diamond surface. From the Raman and SEM

analysis results presented here, we conclude that we can detect the presence of disordered graphite at nanoscale.

After wet inorganic clean, that is, wet graphite etching, taking into account the same Raman spectra in Figure 3.5 (f), it can be seen that the Raman intensity counts are at the noise level, indicating that there is no presence of graphite in both the covered and uncovered areas. This indicates that the new inorganic cleaning protocol presented in Section 3.4.4 is efficient in etching disordered graphite on the exposed surface of the substrate during high temperature treatment. However, by inspecting the underlying SEM pictogram, it can be clearly noticed that the diamond surface of the exposed area (right side) is clearly modified.

Despite fully wet etching the graphite, as shown by the correlated Raman spectra, the exposed area has a different SEM contrast from the fully covered area. At this fabrication step, this contrast can only be attributed to a topographic difference between the two regions, unequivocally demonstrating that the diamond surface exposed to the vacuum of the annealing oven, upon high temperature annealing treatment is modified irreversibly.

3.6.3 ATOMIC FORCE MICROSCOPY INVESTIGATION

Atomic Force Microscopy (AFM) is a high-resolution scanning probe technique capable of delivering nanometer-scale topographic insights into substrate properties, offering a powerful tool for investigating surface characteristics with exceptional precision. We specifically utilize this tool to investigate the surface roughness of diamond substrates, enabling us to track how this evolves throughout the annealing fabrication process, following the methods described in Section 3.4.5.

For this analysis, we use a new scanning tip at each scanning session in order to avoid any artifacts in our scans attributable to a worn-down tip, thus guaranteeing virtually the same tip resolution scans. We evaluated the area surface roughness parameters in the center (covered diamond region) and at the edge of the diamond substrate. This analysis is performed after the annealing fabrication step and after the wet inorganic clean step, scanning the areas representative of the covered and uncovered diamond surface in the high temperature treatment.

Figure 3.6 shows the typical analysis performed on the diamond sample annealed with the surface-covered annealing method (described in Section 3.4.4): same substrate investigated in this study, after annealing (left panel) and after wet inorganic clean (right panel). All topographic maps have a dimension of 500 nm × 500 nm, the scan dimension chosen according to the considerations detailed in Section 3.4.5. The AFM analysis is performed in the same region analyzed in Sections 3.6.1 and 3.6.2. However, a nanoscale AFM/SEM correlation one-to-one cannot be asserted due to the absence of a nano-positioning method, i.e. the optical microscope line of sight allows us to localize and position the AFM tip

For a complete overview of the surface topography, we first evaluate the following one-dimensional roughness parameters (roughness average R_a , root mean square roughness R_q , maximum roughness valley depth R_v), followed by moment based statistical quantities quantifying height irregularities (mean roughness S_a , mean square roughness (RMS) S_q , maximum pit depth S_v , maximum peak height S_p).

In the following section, we will consider the S_q values through the discussion of results.

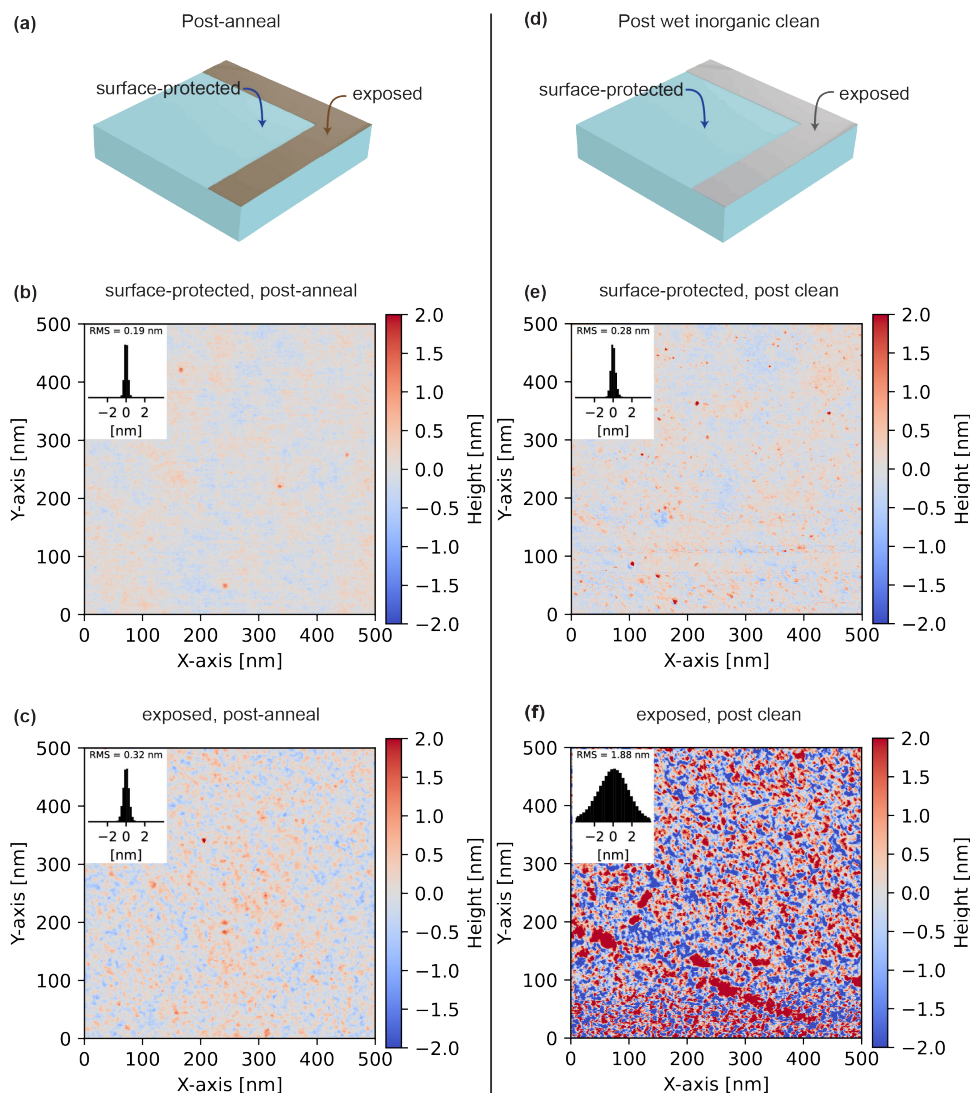


Figure 3.6: **Surface-protected annealing method: AFM topographic analysis** (a) and (d) Schematic illustrations of indicative position of the scanned areas; | **Left panel:** Post-anneal analysis: (b) surface-protected diamond area: surface roughness in the covered region of the substrate shows parameters values comparable with the same in the fabrication steps before annealing. (c) diamond surface area exposed to the annealing oven environment during high temperature treatment, S_q is ~ 1.68 fold increased, thus not significantly. | **Right panel:** Post-anneal and post inorganic clean analysis: (e) surface-protected region close to the center of the plate: surface roughness is qualitatively similar to (b), S_q ~ 1.47 fold increased, a value not significant to indicate a surface modification caused by the high temperature annealing treatment. (f) post inorganic clean (graphite wet etch), same area as in (c): surface roughness parameters values are significantly increased with respect to the the same evaluated in the surface-protected area, after the same fabrication step.

POST-ANNEAL

Figure 3.6 (a) shows a schematic illustration of the approximate regions analyzed with the AFM method. We position the AFM tip in the same region analyzed with SEM in Section 3.6.1, shown in Figure 3.4 (a): vicinity of the upper left corner and bottom right corner of the surface-protected region (here scan in Figure 3.6 (b)) and exposed region (here scan in Figure 3.6 (c)), respectively.

Figure 3.6 (b) shows the area inspected by AFM in the surface-protected region of the sample. The evaluated roughness $S_q = 0.19$ nm, a value comparable to typical S_q measured on diamond plates before and after the ion implantation fabrication step (described in Section 3.4.1 and Section 3.4.2). This indicates that the surface-protected annealing method does not produce any topographic surface modification upon high temperature annealing treatment.

Figure 3.6 (c) shows the area inspected by AFM at the edge of the sample of the diamond substrate, corresponding to the surface area exposed to the vacuum of the annealing oven during high temperature treatment. The evaluated $S_q = 0.32$ nm is ~ 1.68 times higher than the evaluated parameter in the surface-protected region, thus not significantly. To quantitatively assess the graphitization phenomenon, an AFM scan of the net covered to uncovered transition region (such as in the zoom-in SEM Figure 3.4 (b.3)) is required: a z cantilever height difference would be indicative of graphitization. However, the lack of AFM tip positioning at the nanoscale renders such a measurement an experimental challenge, which we did not pursue here. Qualitatively, the exposed surface presents topographic features similar to the texture observed in the SEM analysis in Figure 3.4 (b.4), with only a slight increase in the density of spots, quantified by the increased RMS surface roughness.

Table 3.1 summarizes the relevant topography parameters that characterize the surface topography of the diamond surface, measured on the sample post-anneal. All evaluated one-dimensional roughness parameters are higher in the exposed area of the diamond substrate when compared to the same values in the surface protected region. This results indicates already in the post-anneal stage that the exposed area of the diamond substrate is modified by the environment of the oven chamber during high temperature annealing.

| Parameter | Surface-protected [nm] | Exposed area [nm] | Parameter | Surface-protected [nm] | Exposed area [nm] |
|-----------|------------------------|-------------------|-----------|------------------------|-------------------|
| R_a | 0.119 | 0.255 | S_a | 0.148 | 0.251 |
| R_q | 0.150 | 0.321 | S_q | 0.188 | 0.321 |
| R_v | 0.392 | 0.786 | S_v | 0.870 | 1.270 |
| R_p | 0.498 | 0.957 | S_p | 1.650 | 2.960 |

Table 3.1: **Post-anneal AFM analysis:** evaluated surface roughness parameters on the sample post-anneal.

POST-INORGANIC CLEAN

Figure 3.6 (d) shows a schematic illustration of the approximate regions analyzed with the AFM method. In this case, we moved the AFM tip at the center of the diamond plate in the surface-protected region of the sample to evaluate whether the surface far on the millimeter scale from the transition regions has been subjected to topography modifications. This allows us to roughly compare the surface-protected area topography of the pre-inorganic clean and post-inorganic clean. At the same time, we analyze the post wet

etched graphitized region in the vicinity of the bottom right corner of the surface-protected region and analyzed with SEM in Section 3.6.1 shown in Figure 3.4 (a). This allows us to compare one-to-one the surface topography of the graphitized region before wet etching and after wet etching of the graphite.

Figure 3.6 (e) shows the area inspected by AFM in the surface-protected region of the sample after the inorganic clean. In this case, we evaluate the roughness parameters close to the center of the 4 mm×4 mm diamond plate. The evaluated roughness $S_q = 0.28$ nm is comparable to the same roughness parameter evaluated in the surface-protected region of the diamond surface after the annealing step in Figure 3.6 (b). Qualitatively, the topographic map of this region presents the same background pattern as in the previous fabrication step. However, nanoscale spot features can be noticed present. The values of S_q before and after wet inorganic clean in the surface-protected regions are quantitatively comparable: ~ 1.47 times increase after inorganic clean, this could be attributed to organic debris on the sample surface introduced in the wet cleaning step. In either case, the ~ 1.47 -fold increase is not indicative of a modification of the surface of the diamond substrate that is attributable to high temperature annealing treatment. The surface roughness in the covered region remains sub-nanometer level after the wet etching of the disordered graphite in the exposed area at the edge of the sample, clearly indicating that there is no modification of the surface in the covered region to start with.

Figure 3.6 (f) shows the same inspected area as in (c), here inspected after the inorganic wet etch of the graphite. As shown in the Raman spectroscopy analysis, the graphitized layer is fully and selectively wet-etched, with the spectra showing no sign of graphite residues. The evaluated root mean square area surface roughness is $S_q = 1.88$ nm. When comparing the post-clean exposed area with the surface-protected region, the value of S_q in the exposed region is 6.71 times higher: this clearly indicates that the diamond surface here has undergone significant topographic modification. When comparing the same exposed area before (Figure 3.6 (c)) and after (Figure 3.6 (d)) the wet inorganic etch of graphite, S_q increases 5.87 times. Thus, we can assert that when the formed graphite is fully wet etched, it leaves a diamond surface characterized by significant disorder and significantly higher surface roughness.

Table 3.2 summarizes the relevant topography parameters that characterize the surface topography of the diamond surface in this fabrication step (post-anneal and post-wet inorganic etching of the graphitized layer identified on the uncovered sample edge). All evaluated one-dimensional roughness parameters are higher in the exposed area of the diamond substrate when compared to the same values in the surface protected region, with exposed area values higher by one or even two orders of magnitude. The values of maximum roughness valley depth $R_v = 10.34$ nm and maximum pit depth $S_v = 13.94$ nm are respectively 19 and 9 times higher than the surface protected values of the same parameters. The most conservative estimate of the disordered graphite thickness is therefore at least ~ 14 nm, not making any assumptions on the further etched graphite thickness uniformly wet etched.

DISCUSSION

AFM analysis unambiguously confirms a substantial modification of the surface properties of diamond substrates upon high temperature low pressure annealing.

| Parameter | Surface-protected [nm] | Exposed area [nm] | Ratio | Parameter | Surface-protected [nm] | Exposed area [nm] | Ratio |
|-----------|------------------------|-------------------|-------|-----------|------------------------|-------------------|-------|
| R_a | 0.160 | 1.329 | ~8.3 | S_a | 0.211 | 1.429 | ~6.8 |
| R_q | 0.209 | 1.736 | ~8.3 | S_q | 0.285 | 1.875 | ~6.6 |
| R_v | 0.547 | 10.34 | ~18.9 | S_v | 1.530 | 13.94 | ~9.1 |
| R_p | 0.804 | 5.211 | ~6.5 | S_p | 3.760 | 9.39 | ~2.5 |

Table 3.2: **Post-anneal and post inorganic clean AFM analysis:** surface roughness evaluated parameters post-anneal and post-wet inorganic etch of graphitized layer (identified on the uncovered area on the sample edge).

3

When considering the evaluated surface roughness parameters (summarized in Table 3.1 and Table 3.2 after annealing and after wet inorganic treatment, respectively), all values corresponding to the exposed to annealing oven vacuum surface area are significantly higher when compared to the surface-protected region counterparts. The roughness parameter of the exposed surface region S_q , after the disordered graphite is fully wet etched, is ~ 6.71 times higher. While in the covered area, the surface presents sub-nanometer values of the roughness parameters, the roughness of the previously graphitized surface exposed area is significantly increased, clearly indicating a surface topography modification caused by high temperature annealing graphitization and subsequent inorganic wet etch.

These results indicate a dramatic change in the roughness of the exposed and graphitized region of the diamond surface, leaving no doubt on the severity of the graphitization phenomenon upon high temperature thermal annealing, under optimal vacuum conditions commonly reported in the literature.

The graphitization challenge therefore presents two equally critical major challenges associated with the conventional annealing process.

One is the depth extent of the graphite: for optimally monitored 1×10^{-6} mbar and limited to 4 hours of annealing time, the optimistic estimate of the thickness of the graphite, at least ~ 14 nm, considering the maximum pit depth $S_v = 13.94$ nm (Table 3.2) evaluated in the graphite post-wet etch area. As suspected, this is not limited to a few surface nanometers but is extended in the diamond substrate to the previous values to the least. This represents a serious challenge when considering the typical implantation depths of the SnV centers being ~ 100 nm, as post-wet etching of the graphite implies shallower color centers. The estimated graphite thickness extent presented here is obtained within 4 hours of annealing time. Keeping in mind that this phenomenon depends on the annealing duration time, namely, increasing with a longer duration annealing time, this results indicates that the annealing time should be significantly reduced under conventional annealing fabrication process (no surface protection) at the expense of not efficiently healing the ion implantation-induced crystal damage. At the same time, a higher vacuum is advisable.

The second is the increased surface roughness upon graphite wet etch: this challenge is impossible to prevent or alleviate in the conventional annealing fabrication process (no surface protection), as the surface roughness of the exposed area is irreversibly significantly increased. In turn, a higher surface roughness of the diamond might result in a higher density of trapped charges at the interface, thus potentially detrimental to the optical stability of color centers in the vicinity of such. Next, an increased surface roughness of the diamond substrate is detrimental to the optical properties of nanophotonic devices. The quality factor of resonant cavities is directly negatively impacted by increased surface

roughness, as well as increased optical absorption.

Finally, the results presented confirm the efficacy of the proposed surface-protected annealing method in fully preventing surface modification of diamond substrates and circumventing the challenges presented above. This implies first preserving a low surface roughness, thus minimizing the density of carbon dangling bonds, as well as the amount of trapped charges at the interface. Second, this method allows one to preserve the original thickness of the diamond substrate, which implies preserving the designed ion implantation depth in a systematic and reproducible way. This gives the advantage of reliably coupling SnV centers to designed and fabricated nanophotonic structures without the necessity of compensating for ion implantation depth mismatch.

3

3.6.4 X-RAY PHOTOELECTRON SPECTROSCOPY INVESTIGATION

Although Raman spectroscopy is a powerful diagnostic tool for determining the chemical nature and disorder of materials, this measurement lacks information on the ratio of sp^3 (diamond) to sp^2 (graphitic) carbon bonds, so other analytical tools such as X-ray photoelectron spectroscopy (XPS) are beneficial. This analysis tool has been extensively used in the study of properties of, e.g., diamond films [51], or diamond-like carbon films [52], among others, proving the efficacy of this method.

In order to reliably compensate for the charging effects in the XPS analysis and to understand the origin of atomic species within our fabrication process, we design the experiment as illustrated in Figure 3.7: we prepare 3 diamond samples with the fabrication process described in Section 3.4.1 (pre-implantation substrate preparation) and Section 3.4.4 (surface-protected annealing method) but we exclude ion implantation from the overall fabrication process. The objective of this study is to verify whether there is a difference in the graphitization phenomenon between samples that have undergone ion-implantation (diamond substrate investigated in the previous sections) and non-implanted diamond substrates that undergo the same fabrication process but do not undergo ion bombardment. We compare the non-implanted samples here prepared with implanted samples (results presented in Sections 3.6.1, 3.6.2 and 3.6.3) employing SEM and Raman spectroscopy, whereas in the XPS study we analyze non-implanted samples only. Thus, in this XPS study, **Sample 1**, **Sample 2** and **Sample 3** do not undergo the ion implantation fabrication step.

Figure 3.7 (a) shows the fabrication process used for the preparation of the sample in this study:

Sample 1: pristine diamond substrate, inorganically cleaned with the process described in Section 3.4.1;

Sample 2: diamond substrate inorganically cleaned with the process described in Section 3.4.1, followed by strain-relief etch and concluding with a double Piranha clean + 1 hour of tri-acid clean;

Sample 3: diamond substrate inorganically cleaned with the process described in Section 3.4.1, followed by strain-relief etch. Next, a double Piranha clean + 1 hour of tri-acid clean is performed. We conclude with high temperature annealing (recipe detailed in Appendix, Table A.2) with the surface-protected annealing method described in Section 3.4.4. Before XPS analysis, we perform an inorganic cleaning of 20 minutes HF 40% at room temperature, followed by (2x) 20 minute Piranha cleaning at 80 °C.

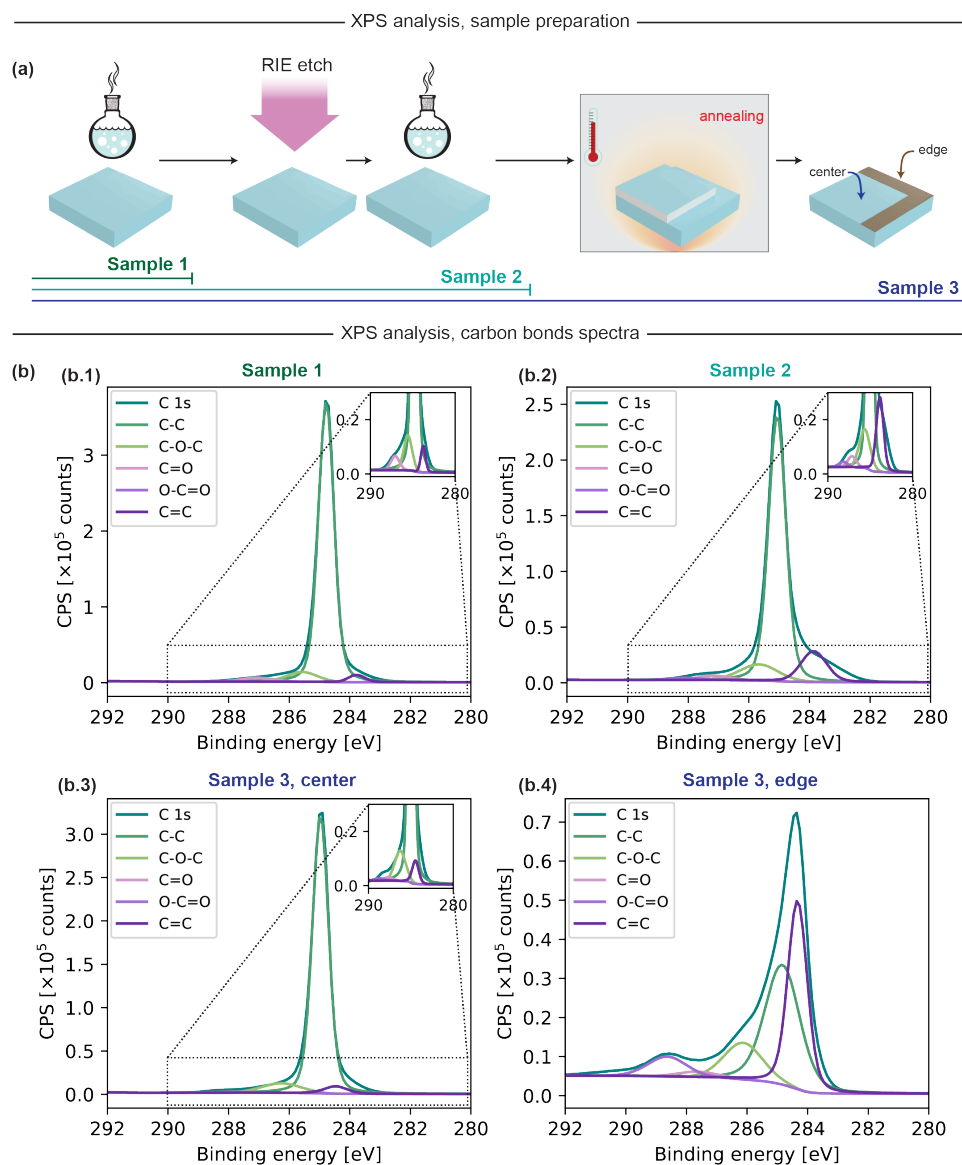


Figure 3.7: XPS analysis of the atomic species on the analyzed samples: (a) Schematic of sample preparation of the diamond substrates in this study. | (b) C 1s peak fits and carbon bonds peaks of respectively Sample 1 (b.1), Sample 2 (b.2), Sample 3 **surface-protected region** (b.3) and **exposed region** (b.4). C 1s peak fit shapes of respectively (b.1), (b.2) and (b.3) are qualitatively similar, with high counts of C-C (sp³ carbon) indicative of diamond analyzed surface, while (b.4) shows a C 1s peak fit as a result of prevalently high C=C bonds (sp² carbon) and relatively lower C-C (sp³ carbon) content when compared to (b.1), (b.2) and (b.3). C 1s peak fit of (b.4) thus strongly resembling that of typical graphite-oxide.

SEM and Raman investigation of **Sample 3 (non-implanted)** shows similar results to the diamond substrate **Sample A (ion-implanted)** investigated in the previous sections (SEM (Section 3.6.1), Raman (Section 3.6.2) and AFM (Section 3.6.3)). Thus, we did not identify significant differences in the graphitization phenomenon between implanted and non-implanted diamond substrates.

All C 1s peak fittings in this study are rough estimates based on literature values, with an uncertainty in peak position of 0.5 eV to 1.0 eV: this uncertainty is due to the charging of the substrate sample, which is difficult to resolve by charge correction. Generally, the charging effects in the XPS analysis of insulating substrates might be difficult to compensate for. An interpretation of XPS analysis peak fittings in this study has been carried out following indications in Ref. [53].

Figure 3.7 (b) shows the XPS analysis of the identified carbon bonds for, respectively, Sample 1 in (b.1), Sample 2 in (b.2), Sample 3 surface-protected region in (b.3), Sample 3 exposed region in (b.4).

C 1s envelope fitted peak shape of Sample 1 in (b.1), Sample 2 in (b.2), Sample 3 surface-protected region in (b.3) is typical of diamond and all qualitatively similar. All previous data show a C-C XPS peak centered around ~285 eV binding energy, strongly indicative of the analyzed diamond material substrate. Sample 2 (b.2) exhibits a slightly higher peak of C = C bonds compared to Sample 1 in (b.1) and Sample 3 covered region (b.3). The slight increase can be attributed to surface damage induced by the strain relief RIE performed on this sample.

Considering now the C 1s envelope peak shape of the exposed region of Sample 3 in (b.4), it can be seen that this is significantly different compared to the C 1s envelope peak shape of the covered region of Sample 3 in (b.3). In fact, in the region of the sample exposed to the annealing oven chamber conditions during annealing, it can be noticed that here the C 1s envelope peak shape is typical of a graphite oxide peak shape. Moreover, here the C=C (sp^2) is significantly higher compared to C = C (sp^2) in the same sample in the covered region (b.3).

Table 3.3 summarizes the carbon peak fits of the detected bond configurations, carbon-carbon and carbon-oxygen bonds. The main difference between Sample 1 and Sample 2 is that Sample 2 has undergone an ICP-RIE strain relief etch with Ar/ Cl_2 followed by O_2 plasma. In fact, Sample 2 presents a higher normalized sp^2 carbon and carbon-oxygen bonds compared to Sample 1, indicative of plasma treatment that induces surface damage. When comparing the same parameters in Sample 2 and Sample 3 surface-protected region, comparable normalized values are identified. This indicates that the annealing process does not produce additional surface damage in the surface protected region.

Taking into account now the Sample 3 exposed region, C=C, C-O-C and O-C=O (and C-C) normalized peak fits %, all values are significantly higher (lower) compared to the surface-protected region. Taking into account all normalized peak fits of Sample 1, Sample 2 and Sample 3 surface-protected region, all measured values are comparable, indicating that no graphitization phenomenon occurs in the surface-protected region of Sample 3 upon high temperature annealing. At the same time, comparing all previous values with the Sample 3, exposed region ones, the data indicate significantly higher C=C bonds, indicative of considerable diamond surface modification in the sample region not protected in the annealing fabrication step.

| Sample / C-bonds | C-C [%] | C=C [%] | C-O-C [%] | C=O [%] | O-C=O [%] |
|-----------------------------------|---------|---------|-----------|---------|-----------|
| Sample 1 | 90 | 3 | 6 | 2 | 0 |
| Sample 2 | 76 | 14 | 6 | 3 | 0 |
| Sample 3 surface-protected | 89 | 3 | 7 | 1 | 1 |
| Sample 3 surface-exposed | 42 | 36 | 13 | 2 | 7 |

Table 3.3: **XPS analysis of the carbon bonds peak fits:** summary of normalized carbon bond peaks % on each sample (and region) inspected in this study.

Table 3.4 summarizes the atomic species identified in the prepared samples. Sample 1 has a normalized C 1s peak of 97 %, with an O 1s peak of 2.82 %. The % concentration of other atomic species is below 1 %. This oxygen concentration can be attributed to the surface oxidation of the diamond substrate upon Piranha cleaning.

Sample 2 presents a lower concentration of C 1s, with minimal residues of Cl detected, most likely due to Ar/Cl₂ plasma etching. At the same time, a higher concentration of O 1s is detected, most likely due to the final O₂ plasma etch.

Next, considering Sample 3, which has undergone high temperature annealing with the surface-protected method, similar values of C 1s and O 1s are detected, indicating that, after high-temperature annealing treatment, the diamond surface has not undergone significant modification. On the other hand, in the exposed surface region, the value of O 1s is increased almost twice. When comparing the N 1s value in surface-protected values with the exposed region value, a significant increased normalized value is detected in the exposed region.

| Sample / Species | C 1s [%] | Cl [%] | F 1s [%] | N 1s [%] | O 1s [%] | S 2p [%] | Si 2p [%] |
|-----------------------------------|----------|--------|----------|----------|----------|----------|-----------|
| Sample 1 | 97.0 | < | < | 0.08 | 2.82 | < | < |
| Sample 2 | 92.1 | 0.08 | 0.09 | 0.21 | 7.41 | < | < |
| Sample 3 surface-protected | 94.2 | < | < | 0.39 | 5.35 | < | < |
| Sample 3 surface-exposed | 83.5 | < | < | 2.82 | 13.6 | 0.06 | 0.05 |

Table 3.4: **XPS analysis of the atomic species on the analyzed samples:** summary of normalized atomic % on each sample (and region) inspected in this study. (<) Content measured, value below detection limit.

DISCUSSION

In summary, from the XPS surface analysis, we conclude that the covered region of the annealed Sample 3 in this study, for which, prior to the annealing step with the surface-protected method, the fabrication process steps are identical to, respectively, Sample 2, shows a C 1s envelope fitted peak shape similar to Sample 1 and Sample 2. Therefore, we conclude that high-temperature annealing does not cause any surface modification that is measurable by XPS analysis in the covered region of the diamond substrate.

In contrast, the region of the diamond exposed to the annealing oven environment during the high temperature treatment is dramatically modified, showing a C 1s envelope fitted peak shape as a result of a combination between diamond and graphite oxide.

The identified top-most layer in this analysis is graphite oxide; however, we do not conclude that it is the case of pure graphite oxide: when considering C-O-C, C=O and O-C=O peaks, in the case of pure graphite oxide such peaks should present a relative higher number of counts, as well as a slight shift towards higher binding energies, which is not the case when examining these in Figure 3.7 (b.4). The observed C-O-C, C=O and O-C=O peaks in Figure 3.7 (b.4) in Sample 3 in the exposed area could be attributed to oxidation of

the top-most graphite layer upon the final double Piranha clean before the XPS analysis is carried out, as well as exposure of the substrate to ambient conditions.

In fact, considering the typical inelastic mean free path of electrons in XPS surface analysis corresponding to ~ 3 nm, the surface analysis performed is strongly sensitive to the structure of the top-most surface depth extent of the same magnitude as the inelastic mean free path. Thus, the apparent incongruence between the non-pure graphite oxide identified here and the pure graphite identified in the Raman analysis may be attributed to surface oxidation of the underlying graphite formed in the exposed area on the bulk diamond substrate.

Taking into account the normalized values of C-C and C=C in Table 3.3, we obtain a comparative value of C-C and C=C between non-annealed and annealed (covered) samples, while the C=C normalized bond peaks % is significantly higher in the case of annealed (uncovered) region. Thus, we can conclude with high confidence that the Sample 3 surface-protected region of the annealed diamond substrate that no graphite or graphite oxide is identified from the XPS surface analysis we conclude that the center of the Sample 3 in the covered region does not present any traces of graphite or graphite oxide formation after high temperature annealing.

3.7 CONCLUSIONS AND OUTLOOK

In this Chapter we have investigated the graphitization phenomenon occurring during high temperature annealing of diamond substrates: this high temperature treatment is of great importance, allowing for successful activation of implanted color centers in diamond while at the same time repairing the host material crystal lattice from implantation induced radiation damage.

We have presented conventional methods (Section 3.4.3) and challenges associated to high energy Sn implantation and high temperature low pressure thermal annealing activation of SnV centers in diamond (Section 3.3.4).

In this context, we investigated and presented the results of the conventional annealing method and qualitatively investigated the effects of the graphitization phenomenon on nanophotonic devices, such as waveguides and photonic crystal cavities, fabricated with the quasi-isotropic undercut etch based fabrication process (Section 3.5). Here, we identify quasi-isotropic undercut etch process to render diamond substrates containing exposed family of $\{100\}$, $\{110\}$, and $\{111\}$ planes, as well as non crystallographic oriented shapes, such as circular holes when patterning nanophotonic structures. Such a platform allows one to systematically and quantitatively investigate the graphitization phenomenon, comparing the rate of surface graphitization for several exposed diamond crystallographic orientations on the same diamond substrate, as well as arbitrarily shaped features. Future investigations are required in order to quantitatively assess the graphitization phenomenon upon different crystallographic orientations of diamond, under the conventional high temperature low pressure annealing fabrication process.

In Section 3.5 we showed that the conventional annealing process causes dramatic graphitization at the diamond surface, with irreversible effects on the geometry of fabricated devices, yielding photonic crystal cavities fully inoperable after annealing and wet-etch removing the graphitized layer.

Next, we presented the methods of the proposed surface-protected method for high temperature annealing (Section 3.4.4) that we developed to prevent graphitization of diamond surfaces upon high temperature annealing. In order to qualitatively and quantitatively assess both the efficacy of the developed method in preventing surface graphitization, as well as systematically quantifying the extent of graphitization at the diamond surface, we present the methods and the thorough analysis using complementary analysis methods, such as qualitative SEM analysis (Section 3.6.1), quantitative Raman analysis (Section 3.6.2), quantitative AFM analysis (Section 3.6.3) and quantitative XPS surface analysis (Section 3.6.4).

From the SEM-Raman analysis, we have shown that the proposed method prevents the graphitization of the diamond surface to occur in the surface protected region of the diamond sample and accurately and systematically map the spatial extent of graphitization at the edge of the covered region of the sample in Section 3.6.2. Despite fully wet etching the graphite, as shown by the correlated Raman spectra, the exposed area has a different SEM contrast from the fully covered area. This contrast can only be attributed to a topographic difference between the two regions, unequivocally demonstrating that the diamond surface exposed to the vacuum of the annealing oven, upon high temperature annealing treatment is modified irreversibly.

The above statement is confirmed by topographic quantitative AFM analysis in Section 3.6.3: comparative quantitative analysis of surface roughness demonstrates a significantly increased surface roughness as a result of wet etch of graphitized layer in the region exposed to annealing oven reactor chamber, while quantitative analysis of surface roughness in the covered region shows no difference when compared to non annealed corresponding area. Thus, AFM quantitative analysis of surface roughness of the diamond substrate with the proposed surface-protected method for high temperature annealing demonstrates two important outcomes: one is the efficacy in preventing graphitization to take place in the covered region of the diamond sample, and two is that exposure of the diamond surface to annealing oven environment causes graphitization, which even upon successful full wet etch, yields an irreversibly higher surface roughness diamond surface.

Finally, we show quantitative XPS surface analysis of a diamond substrate annealed with the proposed surface-protected method for high temperature annealing (Section 3.6.4): this analysis demonstrates that high-temperature annealing does not cause any measurable surface modification in the covered region of the diamond substrate, with no quantifiable formation of graphite or graphite oxide.

In conclusion, the proposed method has proven to be efficient in fully preventing diamond graphitization upon high temperature annealing, within the tested parameters regime, while at the same time offering a powerful systematic investigation method of the graphitization phenomenon.

ACKNOWLEDGMENTS

We thank the entire SnV-team for fruitful discussions that supported the scientific development presented in this chapter, C.E. Smulders, L.G.C. Wienhoven and Z. Sadre Montaz for fabrication assistance and helpful discussions, C. Waas, A.M. Stramma and L.G.C. Wienhoven for feedback on this manuscript.

We thank M. Markham, T. Graziosi, S. Ruffieux for helpful discussions, F. Hashemi for help and data analysis assistance, Y. Li and G. Welker for helpful discussions and fabrication assistance, and the entire staff of the Kavli Nanolab Delft for assistance and support, in particular H. Miro, L. Schriek, B. van den Bulk, E. Pot, and E. Straver.

3.8 REFERENCES

1. Smith, J. M., Meynell, S. A., Bleszynski Jayich, A. C. & Meijer, J. Colour centre generation in diamond for quantum technologies. *Nanophotonics* **8**, 1889–1906 (2019).
2. Bradac, C., Gao, W., Forneris, J., Trusheim, M. E. & Aharonovich, I. Quantum nanophotonics with group IV defects in diamond. *Nature communications* **10**, 5625 (2019).
3. Ohno, K., Joseph Heremans, F., Bassett, L. C., Myers, B. A., Toyli, D. M., Bleszynski Jayich, A. C., Palmstrøm, C. J. & Awschalom, D. D. Engineering shallow spins in diamond with nitrogen delta-doping. *Applied Physics Letters* **101** (2012).
4. Ruf, M., Ijspeert, M., Van Dam, S., De Jong, N., Van Den Berg, H., Evers, G. & Hanson, R. Optically coherent nitrogen-vacancy centers in micrometer-thin etched diamond membranes. *Nano letters* **19**, 3987–3992 (2019).
5. Waldermann, F., Olivero, P., Nunn, J., Surmacz, K., Wang, Z., Jaksch, D., Taylor, R., Walmsley, I., Draganski, M., Reichart, P., *et al.* Creating diamond color centers for quantum optical applications. *Diamond and Related Materials* **16**, 1887–1895 (2007).
6. Ngambou, M. W. N., Perrin, P., Balasa, I., Brinza, O., Valentin, A., Mille, V., Bénédic, F., Goldner, P., Tallaire, A. & Achard, J. Optimizing ion implantation to create shallow NV centre ensembles in high-quality CVD diamond. *Materials for Quantum Technology* **2**, 045001 (2022).
7. Naydenov, B., Richter, V., Beck, J., Steiner, M., Neumann, P., Balasubramanian, G., Achard, J., Jelezko, F., Wrachtrup, J. & Kalish, R. Enhanced generation of single optically active spins in diamond by ion implantation. *Applied Physics Letters* **96** (2010).
8. Paoletti, A. & Tucciarone, A. *The physics of diamond* (Ios Press, 1997).
9. Pacheco, J., Singh, M., Perry, D., Wendt, J., Ten Eyck, G., Manginell, R., Pluym, T., Luhman, D., Lilly, M., Carroll, M., *et al.* Ion implantation for deterministic single atom devices. *Review of Scientific Instruments* **88** (2017).
10. Segre, E. *Nuclei and Particles* 2nd. ISBN: 0-8053-8601-7 (W.A. Benjamin, Inc., Reading, Massachusetts, 1977).
11. Dresselhaus, M. S. & Kalish, R. *Ion implantation in diamond, graphite and related materials* ISBN: 978-3-642-77173-6 (Springer Science & Business Media, 2013).
12. Dresselhaus, M. S. & Kalish, R. *Ion Implantation in Diamond, Graphite and Related Materials* (eds Gonser, U., Mooradian, A., Osgood, R. M., Panish, M. B., Sakaki, H. & Lotsch, H. K. V.) ISBN: 978-3-642-77173-6 978-3-642-77171-2 (Springer Berlin Heidelberg, Berlin, Heidelberg, 1992).
13. Naydenov, B., Reinhard, F., Lämmle, A., Richter, V., Kalish, R., D’Haenens-Johansson, U. F., Newton, M., Jelezko, F. & Wrachtrup, J. Increasing the coherence time of single electron spins in diamond by high temperature annealing. *Applied Physics Letters* **97** (2010).
14. Yamamoto, T., Umeda, T., Watanabe, K., Onoda, S., Markham, M., Twitchen, D., Naydenov, B., McGuinness, L., Teraji, T., Koizumi, S., *et al.* Extending spin coherence times of diamond qubits by high-temperature annealing. *Phys. Rev. B Condens.* **88**, 075206 (2013).

15. De Santis, L., Trusheim, M. E., Chen, K. C. & Englund, D. R. Investigation of the stark effect on a centrosymmetric quantum emitter in diamond. *Phys. Rev. Lett.* **127**, 147402 (2021).
16. Brevoord, J. M., Wienhoven, L. G., Codreanu, N., Ishiguro, T., van Leeuwen, E., Iuliano, M., De Santis, L., Waas, C., Beukers, H. K., Turan, T., *et al.* Large-Range Tuning and Stabilization of the Optical Transition of Diamond Tin-Vacancy Centers by In-Situ Strain Control. *Appl. Phys. Lett.* **126** (2025).
17. Pasini, M., Codreanu, N., Turan, T., Riera Moral, A., Primavera, C. F., De Santis, L., Beukers, H. K., Brevoord, J. M., Waas, C., Borregaard, J., *et al.* Nonlinear quantum photonics with a tin-vacancy center coupled to a one-dimensional diamond waveguide. *Phys. Rev. Lett.* **133**, 023603 (2024).
18. Wan, N. H., Lu, T.-J., Chen, K. C., Walsh, M. P., Trusheim, M. E., De Santis, L., Bersin, E. A., Harris, I. B., Mouradian, S. L., Christen, I. R., Bielejec, E. S. & Englund, D. Large-Scale Integration of Artificial Atoms in Hybrid Photonic Circuits. *Nature* **583**, 226–231 (2020).
19. Knall, E. N., Knaut, C. M., Bekenstein, R., Assumpcao, D. R., Stroganov, P. L., Gong, W., Huan, Y. Q., Stas, P.-J., Machielse, B., Chalupnik, M., *et al.* Efficient source of shaped single photons based on an integrated diamond nanophotonic system. *Phys. Rev. Lett.* **129**, 053603 (2022).
20. Sipahigil, A., Evans, R. E., Sukachev, D. D., Burek, M. J., Borregaard, J., Bhaskar, M. K., Nguyen, C. T., Pacheco, J. L., Atikian, H. A., Meuwly, C., *et al.* An integrated diamond nanophotonics platform for quantum-optical networks. *Science* **354**, 847–850 (2016).
21. Hepp, C. *Electronic structure of the silicon vacancy color center in diamond* PhD thesis (Universität des Saarlandes, 2014).
22. Crane, M. J., Petrone, A., Beck, R. A., Lim, M. B., Zhou, X., Li, X., Stroud, R. M. & Pauzauskie, P. J. High-pressure, high-temperature molecular doping of nanodiamond. *Science advances* **5**, eaau6073 (2019).
23. Sedov, V., Martyanov, A., Savin, S., Bolshakov, A., Bushuev, E., Khomich, A., Kudryavtsev, O., Krivobok, V., Nikolaev, S. & Ralchenko, V. Growth of polycrystalline and single-crystal CVD diamonds with bright photoluminescence of Ge-V color centers using germane GeH₄ as the dopant source. *Diamond and Related Materials* **90**, 47–53 (2018).
24. Palyanov, Y. N., Kupriyanov, I. N., Borzdov, Y. M., Khokhryakov, A. F. & Surovtsev, N. V. High-pressure synthesis and characterization of Ge-doped single crystal diamond. *Crystal Growth & Design* **16**, 3510–3518 (2016).
25. Palyanov, Y. N., Kupriyanov, I. N. & Borzdov, Y. M. High-pressure synthesis and characterization of Sn-doped single crystal diamond. *Carbon* **143**, 769–775 (2019).
26. Addhya, A., Tyne, V., Guo, X., Hammock, I. N., Li, Z., Leung, M., DeVault, C. T., Awschalom, D. D., Deegan, N., Heremans, F. J., *et al.* Photonic-Cavity-Enhanced Laser Writing of Color Centers in Diamond. *Nano Letters* **24**, 11224–11231 (2024).

27. Cheng, X., Thurn, A., Chen, G., Jones, G. S., Bennett, J. E., Coke, M., Adshead, M., Michaels, C. P., Balci, O., Ferrari, A. C., *et al.* Laser activation of single group-IV colour centres in diamond. *Nature Communications* **16**, 5124 (2025).
28. Guo, X., Stramma, A. M., Li, Z., Roth, W. G., Huang, B., Jin, Y., Parker, R. A., Arjona Martínez, J., Shofer, N., Michaels, C. P., *et al.* Microwave-based quantum control and coherence protection of tin-vacancy spin qubits in a strain-tuned diamond-membrane heterostructure. *Physical Review X* **13**, 041037 (2023).
29. Beukers, H. K., Waas, C., Pasini, M., Van Ommen, H. B., Ademi, Z., Iuliano, M., Codreanu, N., Brevoord, J. M., Turan, T., Taminiau, T. H., *et al.* Control of solid-state nuclear spin qubits using an electron spin-1/2. *Physical Review X* **15**, 021011 (2025).
30. Iwasaki, T., Miyamoto, Y., Taniguchi, T., Siyushev, P., Metsch, M. H., Jelezko, F. & Hatano, M. Tin-Vacancy Quantum Emitters in Diamond. *Phys. Rev. Lett.* **119**, 253601 (2017).
31. Rugar, A. E., Lu, H., Dory, C., Sun, S., McQuade, P. J., Shen, Z.-X., Melosh, N. A. & Vuckovic, J. Generation of tin-vacancy centers in diamond via shallow ion implantation and subsequent diamond overgrowth. *Nano letters* **20**, 1614–1619 (2020).
32. Tchernij, S. D., Herzig, T., Forneris, J., Küpper, J., Pezzagna, S., Traina, P., Moreva, E., Degiovanni, I. P., Brida, G., Skukan, N., Genovese, M., Jakšić, M., Meijer, J. & Olivero, P. Single-Photon-Emitting Optical Centers in Diamond Fabricated upon Sn Implantation. *ACS Photonics* **4**, 2580–2586 (2017).
33. Pezzagna, S., Rogalla, D., Wildanger, D., Meijer, J. & Zaitsev, A. Creation and nature of optical centres in diamond for single-photon emission—overview and critical remarks. *New Journal of Physics* **13**, 035024 (2011).
34. Davies, G. & Evans, T. Graphitization of diamond at zero pressure and at a high pressure. *Proc. R. Soc. Lond. A Math Phys Sci* **328**, 413–427 (1972).
35. Evans, T. & Sauter, D. H. Etching of diamond surfaces with gases. *Philosophical Magazine* **6**, 429–440 (1961).
36. Seal, M. The Effect of Surface Orientation on the Graphitization of Diamond. *physica status solidi (b)* **3**, 658–664 (1963).
37. Ruf, M. *Cavity-enhanced quantum network nodes in diamond* PhD thesis (Delft University of Technology, 2021).
38. Sangtawesin, S., Dwyer, B. L., Srinivasan, S., Allred, J. J., Rodgers, L. V., De Greve, K., Stacey, A., Dontschuk, N., O'Donnell, K. M., Hu, D., *et al.* Origins of diamond surface noise probed by correlating single-spin measurements with surface spectroscopy. *Physical Review X* **9**, 031052 (2019).
39. Fávaro de Oliveira, F., Momenzadeh, S. A., Wang, Y., Konuma, M., Markham, M., Edmonds, A. M., Denisenko, A. & Wrachtrup, J. Effect of low-damage inductively coupled plasma on shallow nitrogen-vacancy centers in diamond. *Applied Physics Letters* **107** (2015).

40. Vidrio, R., Vincent, D., Bachman, B., Saucedo, C., Zahedian, M., Xu, Z., Lai, J., Grotjohn, T. A., Kolkowitz, S., Seo, J.-H., *et al.* XPS analysis of molecular contamination and sp² amorphous carbon on oxidized (100) diamond. *Materials for Quantum Technology* (2024).
41. Li, Y. *Fiber-based scanning-probe magnetometry with nitrogen-vacancy spins in diamond nanobeams* Dissertation (TU Delft) (Delft University of Technology, 2025).
42. Brown, K. J., Chartier, E., Sweet, E. M., Hopper, D. A. & Bassett, L. C. Cleaning diamond surfaces using boiling acid treatment in a standard laboratory chemical hood. *Journal of Chemical Health & Safety* **26**, 40–44 (2019).
43. Nečas, D. & Klapetek, P. Gwyddion: an open-source software for SPM data analysis. *Central European Journal of Physics* **10**, 181–188 (1 2012).
44. Khmelnskiy, R. A. & Gippius, A. A. Transformation of diamond to graphite under heat treatment at low pressure. *Phase Transitions* **87**, 175–192 (2014).
45. Khanaliloo, B., Mitchell, M., Hryciw, A. C. & Barclay, P. E. High-Q/V Monolithic Diamond Microdisks Fabricated with Quasi-isotropic Etching. *Nano Letters* **15**, 5131–5136 (2015).
46. Mouradian, S., Wan, N. H., Schröder, T. & Englund, D. Rectangular Photonic Crystal Nanobeam Cavities in Bulk Diamond. *Applied Physics Letters* **111**, 021103 (2017).
47. Rugar, A. E., Aghaeimeibodi, S., Riedel, D., Dory, C., Lu, H., McQuade, P. J., Shen, Z.-X., Melosh, N. A. & Vučković, J. Quantum Photonic Interface for Tin-Vacancy Centers in Diamond. *Physical Review X* **11**, 031021 (2021).
48. Knight, D. S. & White, W. B. Characterization of diamond films by Raman spectroscopy. *Journal of Materials Research* **4**, 385–393 (1989).
49. Guo, X., Deegan, N., Karsch, J. C., Li, Z., Liu, T., Shreiner, R., Butcher, A., Awschalom, D. D., Heremans, F. J. & High, A. A. Tunable and transferable diamond membranes for integrated quantum technologies. *Nano Letters* **21**, 10392–10399 (2021).
50. Gogotsi, Y. G., Kailer, A. & Nickel, K. G. Transformation of diamond to graphite. *Nature* **401**, 663–664 (1999).
51. Wilson, J. I. B., Walton, J. & Beamson, G. Analysis of chemical vapour deposited diamond films by X-ray photoelectron spectroscopy. *J. Electron Spectros. Relat. Phenomena* **121**, 183–201 (2001).
52. Mößner, C., Grant, P., Tran, H., Clarke, G., Lockwood, D., Labbe, H., Mason, B. & Sproule, I. Characterization of diamond-like carbon by Raman spectroscopy, XPS and optical constants. *Thin solid films* **317**, 397–401 (1998).
53. Morgan, D. J. Comments on the XPS analysis of carbon materials. *C* **7**, 51 (2021).

4

4

NONLINEAR QUANTUM PHOTONICS WITH A TIN-VACANCY CENTER COUPLED TO A ONE-DIMENSIONAL DIAMOND WAVEGUIDE

Color-centers integrated with nanophotonic devices have emerged as a compelling platform for quantum science and technology. Here we integrate tin-vacancy centers in a diamond waveguide and investigate the interaction with light at the single-photon level both in reflection and transmission. We observe single-emitter induced extinction of the transmitted light up to 25% and measure the nonlinear effect on the photon statistics. Furthermore, we demonstrate fully tunable interference between the reflected single-photon field and laser light back-scattered at the fiber end and show the corresponding controlled change between bunched and anti-bunched photon statistics in the reflected field.

This chapter has been published as

– M. Pasini, N. Codreanu, T. Turan, et al., "Nonlinear quantum photonics with a tin-vacancy center coupled to a one-dimensional diamond waveguide", *Physical Review Letters*, **133**, 023603, (2024)

– M.P. and T.T. performed the experiments and analyzed the data. N.C. designed and fabricated the device. N.C. and M.P. fabricated the tapered fibers. M.P. designed the setup and built it with C.P. . A.R.M., T.T., C.P. and M.P. characterized the device. M.P. developed the theoretical model and simulations with input from J.B., L.D.S., H.K.C.B., J.M.B. and C.W. contributed to the development of the measurement infrastructure. M.P., T.T. and R.H. wrote the manuscript with input from N.C.. All authors commented on the manuscript. R.H. supervised the experiment.

4.1 INTRODUCTION

Nonlinear interactions between single photons and solid-state color centers are at the heart of many applications in quantum science [1, 2] such as the realization of a quantum internet [3, 4]. In particular, color centers in diamond have enabled advanced demonstrations in this direction showing multinode quantum network operation [5, 6], memory-enhanced communication [7] and scalable on-chip hybrid integration [8]. Among the diamond color centers, the tin-vacancy center (SnV) has recently emerged as a promising qubit platform as it combines the inversion symmetry of group-IV color centers [9, 10], allowing for integration in nanophotonic structures, with good optical properties [11–14] and above-millisecond spin coherence at temperatures above 1 K [15, 16]. Devices combining photonic integration with spin and optical control could serve as a future scalable building block for realizing spin-photon gates [17]. On the path towards such scalable on-chip integration, incorporation of emitters into nanophotonic waveguides [12, 18] enables exploration of the coherent emitter-photon interaction typical of waveguide-coupled systems [19, 20]. Compared to nanophotonic cavities [21], waveguides have the advantages of being broadband, eliminating the challenge of cavity tuning, and of having significantly higher error tolerance in fabrication.

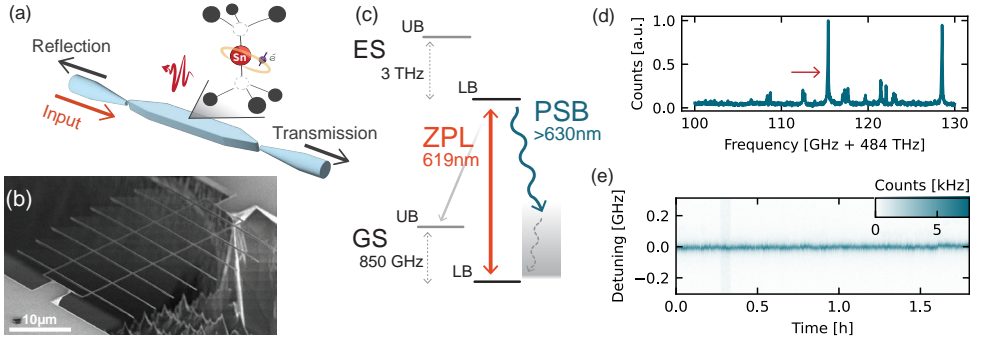


Figure 4.1: Device and optical transition properties. (a) Schematic of the device and the fiber coupling. (b) SEM image of one entire diamond device chip. (c) Energy level scheme of the SnV. At 5 K the SnV spectrum shows two ZPL transitions between the Lower Branch (LB) of the Excited State (ES) to the Lower (Upper) branches (LB, UB) of the Ground State (GS). Here we focus on the ZPL transition between LB of ES and LB of GS at 619 nm, and we filter the other ZPL out. Phonon assisted decay from the excited state gives rise to a phonon sideband (PSB) with a broad optical spectrum above 630 nm. (d) Consecutive photoluminescence excitation (PLE) scans conditioned on the SnV being in the right charge and frequency state. The scanning speed of each PLE is ~ 300 MHz/s.

In this work, we present a device consisting of a SnV center coupled to a nanophotonic diamond waveguide with tapered-fiber access, depicted in Fig.4.1(a). Thanks to efficient coupling, double-sided access, and real-time charge-resonance checks, we are able to perform a comprehensive investigation of the nonlinear interaction of the color center with the waveguide mode both in transmission and reflection. We observe the extinction of transmitted light which arises from interference between the photons interacting with the emitter and the single optical mode of the waveguide [22, 23], from which we quantify the coupling strength of the SnV to the waveguide. In the reflected signal we observe interference between single photons scattered by the emitter and a classical reflection of the probe laser. The tunability of our device enables us to map out the various regimes of

interference and their corresponding photon statistics.

4.2 DEVICE AND EXPERIMENT

Our device is fabricated in two main phases. First, SnV centers are generated by implantation on an electronic-grade diamond of ^{120}Sn ions at a target depth of $\sim 88\text{ nm}$, followed by an annealing step to create SnV centers. On the sample, we then fabricate suspended waveguides that support a single TE mode for SnV emission. The fabrication is based on the crystal-dependent quasi-isotropic-etch undercut method [8, 13, 24–27]. We first pattern a hard mask material Si_3N_4 , followed by the transfer pattern into the diamond substrate and vertical coverage with Al_2O_3 of the structures sidewalls. Next, the quasi-isotropic etch undercuts the devices, followed by an upward etch to thin the devices down to a thickness of $\approx 250\text{ nm}$. The fabrication concludes with an inorganic removal of the hard mask materials. The details of the fabrication can be found in Methods Section 4.8.

Our fabrication differs from earlier work [8, 13, 24–26] in one main aspect: we demonstrate successful quasi-isotropic undercut of the waveguides at a considerably lower temperature of the reactor wafer table of only 65°C . We show that the quasi-isotropic crystal-dependent reactive-ion etch in this temperature regime is successfully undercutting the waveguide structures without the need of an optional O_2 anisotropic etch step following the vertical sidewalls coverage with Al_2O_3 . This has the key benefit of preserving the hard mask aspect ratio, without further edge mask rounding stemming from the O_2 etch.

The fabricated devices consist of arrays of double-sided tapered waveguides, anchored to the surrounding bulk substrate by a square support structure, as seen in Fig.4.1(b). To couple light in and out of the waveguide we use optical fibers that are etched into conical tapers in hydrofluoric acid [28]. We position the fibers in front of the waveguide and exploit the lensing effect of the taper, as illustrated in Fig. 4.1(a). We choose this method as it allows easy variation of the distance between fiber and waveguide. This will later be used to tune the phase of the reflected signal. All experiments are performed at 5 K in a closed-cycle cryostat, with no external magnetic field. Within the SnV level structure (Fig. 4.1(c)), we focus on the optical zero-phonon line (ZPL) transition between the lower branches of the ground and excited states, of wavelength around 619 nm. Spontaneous emission from the excited state can also happen with a phonon assisted process, giving rise to a phonon sideband (PSB).

4.3 OPTICAL TRANSITION STABILITY

We investigate the optical stability of one emitter (red arrow in Fig.4.1(d)) by performing consecutive photoluminescence excitation (PLE) scans. The scans are pre-conditioned on a successful charge-resonance check [14]: Before each scan we turn on the probe laser at a set frequency and count how many PSB photons are detected. A threshold number of counts is chosen to make sure that the SnV is in the desired charge state and on resonance with the emitter (see Section 4.8). This heralding technique mitigates the effects of emitter ionization and of spectral diffusion [14].

Summing data from 1.8 hours of continuous measurement (Fig.4.1(e)), we observe an integrated linewidth of $(38.0 \pm 0.3)\text{ MHz}$, very close to the average linewidth of the single scans of $(32.1 \pm 0.1)\text{ MHz}$, indicating that there is very little effective spectral diffusion in our

measurements. This can in principle be further improved by increasing the conditioning threshold at the expense of experiment speed. All the measurements reported below are conditioned on a charge-resonant check with similar threshold. By measuring second-order photon correlations using different resonant laser powers (see Section 4.8), we extract the excited state lifetime of the emitter to be (5.91 ± 0.08) ns, corresponding to a transform-limited transition linewidth of (26.7 ± 0.3) MHz. This value is close to the average single scan linewidth, indicating that there is little residual broadening of the transition.

4.4 SPECTROSCOPY OF THE WAVEGUIDE-SnV SYSTEM

To probe the coupling of the SnV center to the waveguide, we scan the probe laser across the transition frequency, while simultaneously collecting both the transmitted and reflected signals. We spectrally filter the signals and record both ZPL and PSB (separately) in the reflected output port, and the ZPL in the transmission output port (see SI for details). This simultaneous measurement allows us to monitor the SnV behavior through the PSB emission while observing its coherent interaction with the input probe through the ZPL signal (Fig. 4.2(a)).

We observe a significant extinction of the transmission signal on resonance, indicating a coherent light-matter interaction in our waveguide-QED system [23]: destructive interference between scattered photons and the transmitted field causes the emitter-induced reflection of single photons. The magnitude of the transmission dip contrast on resonance is determined by the emitter-waveguide coupling factor $\beta = \gamma_{wg}/\gamma_{tot}$, where γ_{wg} (γ_{tot}) is the decay rate into the waveguide (the total decay rate of the excited state). In particular, in the absence of dephasing of the optical transition, the transmission behavior is described by [19]

$$T(\omega) = \left| 1 - \frac{\beta}{(1 + \frac{\langle n \rangle}{n_c})(1 + \frac{2i\omega}{\gamma_{tot}})} \right|^2, \quad (4.1)$$

where ω is the detuning of the probe laser from the emitter, $\langle n \rangle$ is the average photon number per lifetime in the input state and $n_c = \frac{1}{4\beta^2}$ is the critical photon number, which indicates saturation of the photon-emitter interaction. In the limit of low excitation ($\langle n \rangle \ll n_c$), the transmission contrast on resonance $\Delta T = 1 - T(\omega = 0)$ is thus related to the coupling factor β as $\Delta T = \beta(2 - \beta)$. Note that in this analysis, we ignore the small additional broadening of the optical transition due to dephasing, making our estimates for β a strict lower bound.

Experimentally, the value of the coupling factor β can be reliably extracted by measuring the transmission contrast as a function of input laser power, given that $\langle n \rangle/n_c = P/P_c$ with P_c the input power that saturates the interaction. To ensure that we are optimally coupling the probe field with the linear dipole of the optical transition, we sweep the polarization of the input field to find the maximal transmission contrast (Fig. 4.2(b)). Fitting Eq. (4.1) to the measured transmission contrast as a function of input power (Fig. 4.2(c)) we obtain $\beta = 0.143 \pm 0.005$. This value is in good agreement with numerical simulations for our waveguide geometry (see Ref. [29]) taking into account the emitter depth resulting from the implantation, a small lateral offset (≈ 50 nm) from the waveguide center, and the total efficiency of the transition of interest of 0.37 [30], obtained combining quantum

efficiency (0.8) [31], Debye-Waller factor (0.57) [32] and branching ratio between the two ZPL transitions (0.8) [13].

The critical laser power at the fiber input, P_c , corresponds to the critical photon number n_c at the SnV center: $P_c = \eta^{-1} h \nu n_c \gamma$, where η is the fiber-waveguide coupling efficiency, ν is the probe laser frequency and γ is the decay rate related to the excited state lifetime. From the fit value $P_c = (0.32 \pm 0.02)$ nW and knowing $n_c \sim 12$ photons from the value of β , we determine the fiber-waveguide coupling efficiency to be $\eta = 0.33 \pm 0.02$.

The reflection signal contains the single photons coherently reflected by the SnV center, interfering with classical reflection of the probe laser at the tapered fiber end. In a simplified picture, considering a Lorentzian response of the SnV, the reflection signal can be modelled as [18, 33]

$$R(\omega) = \left| 1 + \xi \frac{1}{1 - 2i\omega/\gamma_{tot}} e^{i\phi} \right|^2, \quad (4.2)$$

where ξ is the ratio between the reflected single photons and the coherent state amplitude, which gives the average number of photons per lifetime in the input field, and ϕ is the phase difference between the coherent and single photon components.

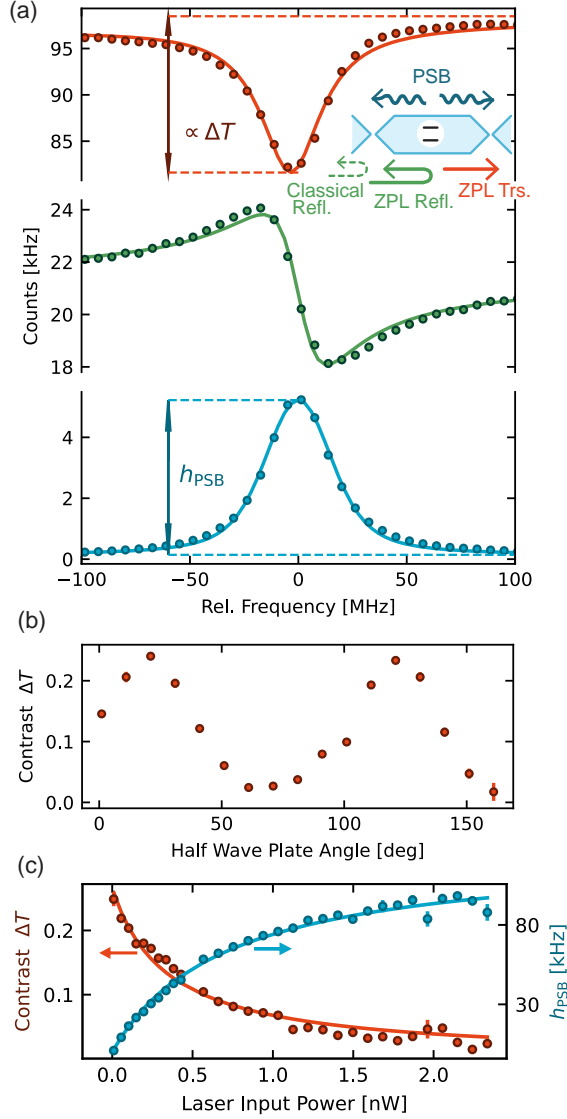


Figure 4.2: Spectroscopy of the waveguide-SnV system. (a) Simultaneous measurement of transmitted ZPL light through the system (top), reflected ZPL light (center) and PSB emission (bottom) while scanning the probe laser. The inset shows a schematic of the system, the colors represent the different channels measured. We highlight the transmission contrast ΔT and the peak height of the PSB emission scan h_{PSB} . (b) Contrast of the transmission extinction when varying the input fiber polarization using a half wave plate (HWP). (c) Transmission contrast and PSB peak height as a function of the power in the input fiber showing saturation of the SnV response when the average photon number increases. In the low power range, we observe a maximum transmission extinction of 0.25 ± 0.01 .

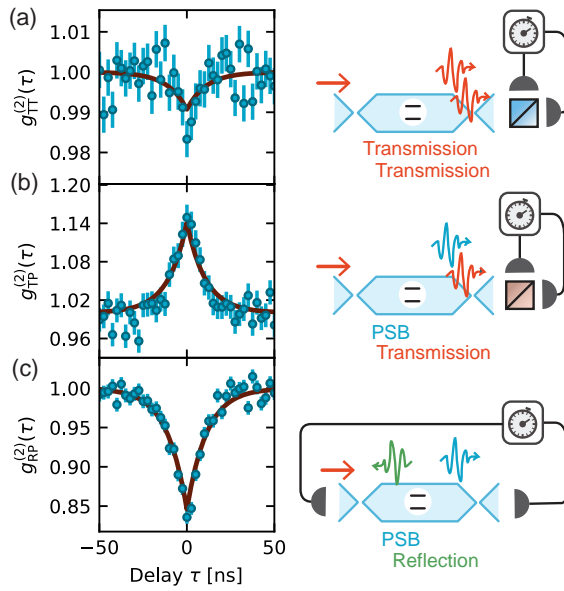


Figure 4.3: Second order correlation between (a) two transmitted photons, (b) a PSB and a transmitted photon, (c) a PSB and a reflected photon in the constructive interference regime (see main text and Fig. 4.4 for details). The blue dots are experimental data and the red line is the theoretical model, where the relevant parameters are extracted by fitting corresponding reflection and transmission spectra.

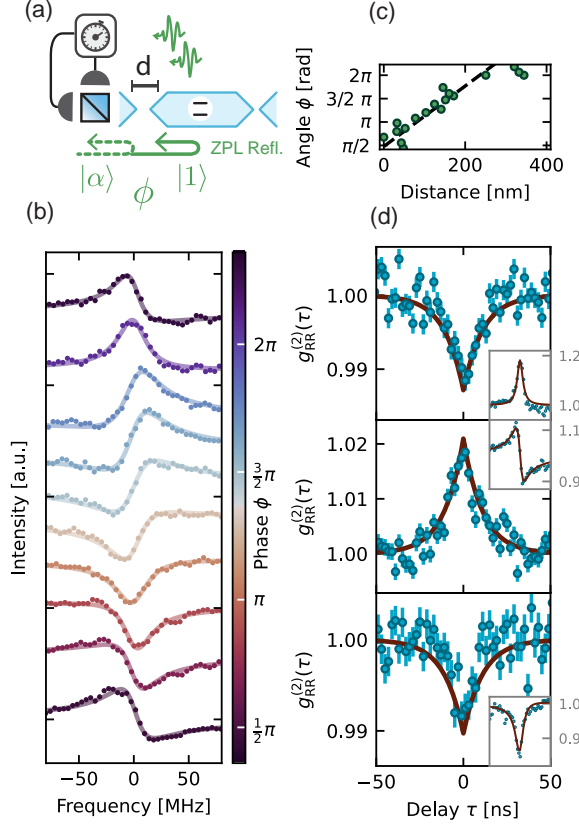


Figure 4.4: Reflection measurements. (b) Reflection spectra at different fiber distance d , corresponding to different relative phase between the single photon and coherent state components. The solid line is a fit with the simplified model of Equation 4.2, from this we extract the phase ϕ which is indicated by the colorbar. (b) Schematic of the measurement setting. (c) Second-order correlation of reflected photons in the constructive (top), dispersive (center) and destructive (bottom) interference regimes. The inset shows the reflection spectrum. We fit the reflection spectrum using Eq. (4.2) to extract ϕ and ξ , which we use as an input to the theoretical model. The red lines, both in the inset and the main figure, are the results of the theoretical model with the supplied parameters. The x axis in the inset is frequency, ranging from -80 MHz to 80 MHz.

4.5 PHOTON STATISTICS OF TRANSMITTED FIELD

The emitter-induced single-photon nonlinear reflection alters the photon statistics of the transmitted and reflected fields, as we expose below by measuring the second-order correlation for different combination of signals.

We start by correlating the transmitted signal with itself. The emitter can only reflect one photon per its optical lifetime. When two indistinguishable photons coherently scatter on the emitter within the timescale of its optical lifetime, the nonlinear interaction results in a strongly correlated two-photon bound-state that is perfectly transmitted [34]. In the case of $\beta \rightarrow 1$ the wavefunction of the scattered light is dominated by this bound-state component, resulting in strong bunching of the transmitted light [22]. In our case, however, the bound-state contribution is suppressed compared to the uncorrelated scattering of the two photons involving other channels. In other words, the probability that one of the two photons is incoherently scattered is higher than the probability of emitting the two-photon bound state in the waveguide. In this regime, upon detection of a photon in the transmission signal the conditional probability of a second ZPL photon detection within the lifetime is suppressed compared to the steady state value. In full agreement with the predictions in Ref. [22], we find that this results in anti-bunching in the photon statistics for the transmission $g_{TT}^{(2)}$ (Fig. 4.3(a)).

Since we have access to one of the incoherent decay channels, namely the photons emitted in the PSB, we can verify that the effect on the photon statistics is induced by the coherent interaction of light with the emitter. We measure the probability of detecting a transmitted (Fig. 4.3(b)) or reflected photon (Fig. 4.3(c)) conditioned on the emission of a PSB photon. Detecting a PSB photon heralds an incoherent interaction which results in a higher probability of detecting a ZPL photon in the transmission port and a lower probability of detecting a ZPL photon in the reflected port, leading to the observed bunching and anti-bunching, respectively.

We compare the results in Fig. 4.3 with numerical simulations (the red lines in the figures), where the system is modeled as a lossy cavity coupled to an emitter (see Supplementary [29] for details). Using values for the model parameters extracted from fits to the corresponding transmission and reflection spectra (similar to Fig. 4.2), we find that the simulations accurately reproduce the behavior of the $g^{(2)}$ measurements.

4.6 REFLECTED SIGNAL AND PHOTON STATISTICS

Finally, we investigate the interference between the coherently scattered single photons and the reflected laser light in more detail. By adjusting the fiber position relative to the waveguide, we can change the difference between the paths that the classical light and single photon components travel, and thereby controllably tune their relative phase ϕ . Figure 4.4(a) shows the variation in the reflection interference spectrum as we sweep the fiber distance, realized by applying a voltage on the piezo positioner.

The photon statistics of the reflected signal depend on the relative phase ϕ (Fig. 4.4(b)). We consider the three limit cases of constructive ($\phi = 6.28 \sim 2\pi$), dispersive ($\phi = 1.57 \sim \pi/2$) and destructive ($\phi = 3.41 \sim \pi$) interference. In the constructive interference case, single photons are added to the coherent state, resulting in sub-poissonian photon statistics as evidenced by the measured anti-bunching in $g_{RR}^{(2)}$ in Fig. 4.4(c, top). In the dispersive and

destructive interference cases, the presence of a non-zero phase makes the behavior of the photon statistics non-trivial as the relative phase is different for the one- and multi-photon components of the coherent state. Depending on the exact phase and the relative amplitudes of the single photons and the reflected coherent state, the relative weight of the one and two-photon components vary, resulting in either bunching or anti-bunching. In our regime we observe bunching for the dispersive interference Fig. 4.4(c, middle) and weak antibunching for destructive interference Fig. 4.4(c, bottom). Numerical simulations (red lines) using our theoretical model show excellent agreement with the data (see Supplementary [29] for details).

4.7 CONCLUSIONS

In summary, we have presented a detailed investigation of a diamond SnV center coupled to a waveguide, showing significant transmission extinction, tunable interference between single photons and the reflected laser field, as well as providing insights into the nature of the emitter-induced changes in transmitted and reflected fields through photon correlation measurements. These results highlight diamond SnV centers integrated in waveguides as a promising platform for realizing efficient integrated spin-photon interfaces.

Whereas nanophotonic cavities can provide overall much stronger interaction, the use of waveguides can alleviate significant fabrication overhead and by their broadband nature provide a more flexible platform, since they do not need to be tuned to the emitter frequency and readily allow for more centers to be used in the same device. We investigated four waveguides in this device and all contained suitably coupled SnV centers, with measured ΔT ranging between 15 – 34%.

While our work shows couplings that are in line with the state of the art for color center-waveguide systems [8, 18, 35], further improvement can be obtained by optimizing the emitter overlap with the optical mode: the waveguide thickness and the implantation depth can be matched to get the SnV closer to the center, while localized ion implantation could improve the lateral position. Already at the established coupling, these devices, when combined with coherent spin control [15, 16], may allow for remote entanglement significantly surpassing the generation rates obtained the diamond NV center [36, 37], opening up new avenues for scaling quantum networks.

4.8 METHODS

4.8.1 SAMPLE AND DEVICE FABRICATION

The sample fabrication process starts with pre-implantation surface treatment of a <100> surface oriented electronic grade diamond substrate (Element 6). The sample substrate is first cleaned in a wet Piranha (ratio 3:1 of H_2SO_4 (95 %) : H_2O_2 (31 %)) inorganic solution for 20 min at 80 °C, followed by the superficial $\sim 5 \mu\text{m}$ etching via inductively-coupled-plasma reactive-ion-etching (ICP-RIE) Ar/ Cl_2 plasma chemistry based recipe in order to remove the residual polishing induced strain from the surface of the substrate. An additional $\sim 5 \mu\text{m}$ ICP-RIE O_2 chemistry based plasma etch is performed in order to remove residual chlorine contamination from the previous etching step [27]. Following, the sample is inorganically cleaned in a Piranha solution (20 min at 80 °C) and implanted with Sn ions (dose $1\text{e}11 \text{ ions/cm}^2$ with an energy of 350 keV). Prior to the activation of the SnV centers by vacuum

annealing (1200 °C), a triacid cleaning (ratio 1:1:1 of HClO_4 (70%) : HNO_3 (70%) : H_2SO_4 (> 99%)) is performed for 1.5 hours in order to remove any residual organic contamination, followed by the same wet inorganic cleaning procedure after the annealing step in order to remove any superficial graphite thin film layer formed during the annealing step of the diamond substrate. In order to assess the successful activation of the SnV centers, the sample is characterized prior to the nanofabrication of the suspended structures.

The nanofabrication of waveguiding structures follows the process based on the crystal-dependent quasi-isotropic-etch undercut method developed in references [8, 13, 24–26] and [27]. A schematic of this is illustrated in Chapter 2 Fig. 2.1.

Specifically, we start with a pre-fabrication process extensive inorganic clean for 20 min in HF (40%) at room temperature (Fig. 2.1, step 1), followed by deposition and patterning of a hard mask material thin film layer of ~ 221 nm Si_3N_4 via plasma-enhanced-chemical-vapour-deposition (PECVD) (Fig. 2.1, step 2). The waveguide structures design is longitudinally aligned with the $\langle 110 \rangle$ diamond crystallographic orientation and exposed via e-beam lithography of ~ 450 nm of AR-P-6200.13 positive tone resist (Fig. 2.1, step 3). In order to avoid charging effects of the diamond substrate during the e-beam exposure, the surface of the e-beam resist is coated with ~ 40 nm Electra 92 (AR-PC 5090) conductive polymer. Next, this is developed by immersing the sample in 60 s gentle stirring in H_2O and N_2 blow-dry (to dissolve Electra 92), followed by 60 s DI water, 60 s pentyl acetate, 5 s ortho-xylene, 60 s isopropyl alcohol (IPA) (Fig. 2.1, step 4). The process proceeds with the transfer pattern into the Si_3N_4 hard mask material by means of ICP-RIE etch in a CHF_3/O_2 based plasma chemistry (Fig. 2.1, step 5) and complete removal of residual e-beam resist in a two-fold wet step: we first proceed with a resist removal in a PRS 3000 positive resist stripper solution, followed by extensive Piranha clean inorganic treatment for complete removal of organic material residues (Fig. 2.1, step 6). Such considerable inorganic cleaning is employed in order to prevent micro-masking within next dry etch steps that can potentially be caused by organic residues on the sample.

The transfer pattern from the Si_3N_4 hard mask material is transferred by etching top-down in a dry ICP-RIE O_2 plasma chemistry etch in the diamond substrate for an extent of $\sim 2.4\times$ the designed thickness of the devices (Fig. 2.1, step 7). It is crucial to note that the O_2 dry etch heavily affects the aspect ratio of the patterned Si_3N_4 hard mask: we observe the etch rate of Si_3N_4 to be higher at the edges of the patterned structures compared to the determined etch rate of Si_3N_4 on flat area test samples, leading to enhanced erosion of the Si_3N_4 at the edges of the nanostructures. This yields rounded vertical sidewalls with few nanometers of hard mask material at the diamond to Si_3N_4 interface [27]. This leads to weak points across the top surface of the hard mask that can compromise the integrity of the hard mask through the following fabrication steps. We circumvent this challenge by carefully tuning the trade-off between sufficient anisotropic diamond etch and Si_3N_4 mask integrity such that the last withstands the following O_2 based dry etch steps foreseen by the overall fabrication process.

Next, conformal atomic layer deposition (ALD) of ~ 26 nm of Al_2O_3 for hard mask coverage of devices vertical sidewalls (Fig. 2.1, step 8) and the horizontal coverage of Al_2O_3 is fully removed by ICP-RIE etch in a BCl_3/Cl_2 plasma chemistry etch (Fig. 2.1, step 9). This opens access to the diamond substrate: we directly follow with a two-step quasi-isotropic etch. For this, we employ the recipe developed in reference [27]. In contrast to

Ref. [8, 13, 24–26], here the quasi-isotropic etch plasma reactor wafer table temperature is only 65 °C, therefore completing the full undercut and upward etch of the devices to the target thickness in 2 steps of 9 hours etch each (Fig. 2.1, step 10). The full release and upward quasi-isotropic total etch time is considerably long when compared to high temperature plasma regimes. On the other hand, here we demonstrate that this method successfully undercuts diamond waveguides in a low temperature regime. Finally, the hard mask materials are removed in an extensive inorganic treatment for 20 min in HF (40%) at room temperature (Fig. 2.1, step 11).

The overall qualitative characterization of the fabrication steps presented in this work has been executed on a scanning electron microscope Hitachi SEM Regulus system. The etch rates concerning the fabrication steps 5, 7 and 9 (Fig. 2.1) have been pre-characterized on additional test samples, in parallel to the fabrication of the diamond sample employed in this work following similar methodology. Such etch tests have been conducted employing silicon substrate samples, with the thin films of interest deposited in parallel to the diamond substrate. Optical parameters and thickness of the employed materials have been determined via spectroscopic ellipsometry method on a Woollam M-2000 (XI-210) tool. The quasi-isotropic etch rate has been characterized employing supplementary diamond test samples (fabrication parallel to the sample in this work) and analyzed via SEM inspection.

4.8.2 INHOMOGENEOUS DISTRIBUTION IN THE WAVEGUIDE DEVICES

To measure the inhomogeneous distribution of the spectral lines of different SnVs in our sample, we combine 82 photoluminescence spectra taken in different waveguides and fit the averaged spectrum using a Voigt curve. From the fit, we estimate that the 619 nm transition has an inhomogeneous full-width at half-maximum of (144 ± 2) GHz. The average ground state splitting in the sample is (822 ± 2) GHz.

4.8.3 EXPERIMENTAL SETUP

Figure 4.5 shows a schematic of our experimental setup. The sample is cooled to 5 K in a closed cycle cryostat (Montana Instruments s50), together with two XYZ piezopositioner stacks (Attocube Systems ANPx51, ANPz51) which allow to control the position of the optical fibers. We image the sample through an optical window in the cryostat using a long working distance objective (Mitutoyo 50X Plan Apochromat, NA: 0.55, WD: 13 mm), which combined with an LED at ~ 470 nm provides enough resolution to image the waveguides and the fiber tip. Through the same objective we deliver the repump laser pulses (Cobolt MLD-06 515 nm). The resonant excitation and the photon collection is all via fiber. A tunable 1240 nm laser (Toptica DL Pro - TA) pumps a second harmonic generation fiber-coupled crystal (AdvR) to generate tunable laser light around 620 nm. Part of the red output is sent to a wavemeter (High Finesse WS8) for frequency stabilization through a PID loop running in background and feeding back on the DL Pro controller to tune the IR frequency. The light used for resonant excitation goes through a manual Variable Optical Attenuator (VOA) and an Acousto Optical Modulator (AOM) used to generate the pulses. A short fiber-freespace-fiber module (Thorlabs FiberBench) with polarization control is used to bridge between polarization maintaining fiber of the laser control and the single mode fiber used in the rest of the experiment. A 99:1 beam splitter is used to send 1% of the laser light to the input fiber, where we use motorized polarization paddles to control the

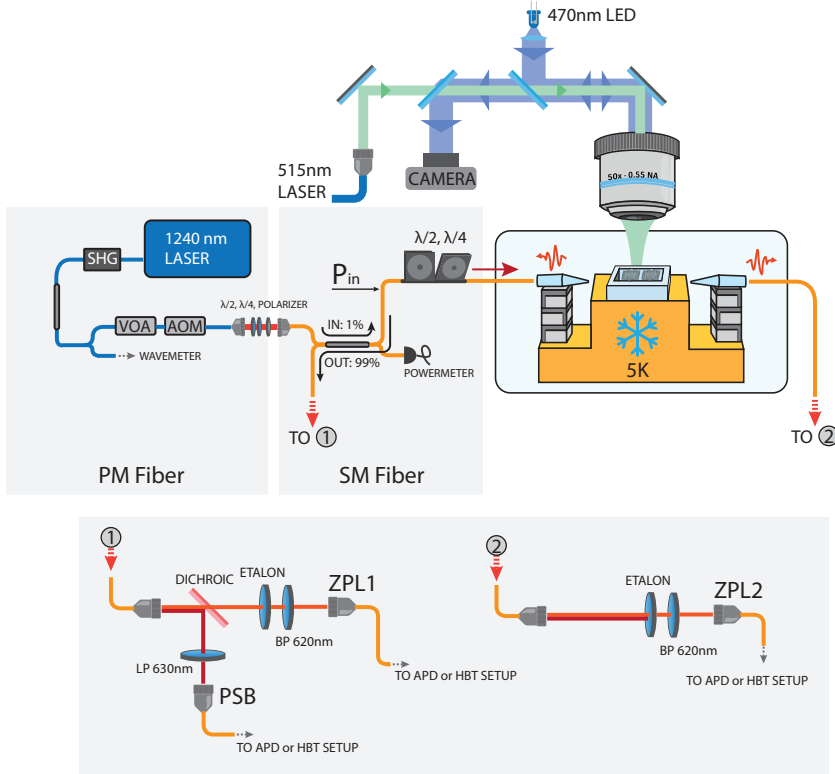


Figure 4.5: Experimental Setup. See text for explanation and abbreviations.

input polarization. The remaining 99% is used for calibration and monitoring. The reflected light goes through the beam splitter and is collected in the 99% return port. We have two free-space setups for filtering and detection of the light. In the first, usually connected to the reflection port, a dichroic filter (Semrock FF625, short pass ~ 620 nm) separates the PSB and ZPL light. The PSB is further filtered by a Band Pass filter (620 ± 5 nm) and a tunable narrow etalon filter (LightMachinery, ~ 45 GHz FWHM) to get rid of the second ZPL transition. In the PSB path we further filter the excitation laser with two Long Pass tunable filters set approximately at 630 nm. The second free-space stage only has the 620 nm band pass and the etalon to filter around the ZPL. The collected photons are fiber coupled and sent to avalanche photodiode (APD) single photon detectors (Lasercomponents COUNT) or to a Hanbury-Brown-Twiss (HBT) setup realized with a 50:50 fiber beam splitter and two APDs for correlation measurements. We run the experiment using custom software based on the QMI [38] package (version 0.41.0).

Our experiments use a lensed-fiber-like approach for coupling the waveguide to the tapered fiber. By optimizing the position, we consistently measure a fiber-waveguide-fiber transmission efficiency up to $\sim 4\%$, which translates to $\sim 20\%$ efficiency per side. Taking

into account the potential losses at the crossing between the waveguide and the square support structure, this is in good agreement with our estimation of the excitation efficiency of the emitter of $\sim 33\%$ (see main text) and hints to the fact that the emitter is located between the fiber taper and the support structure.

Phase dependence on the fiber Position

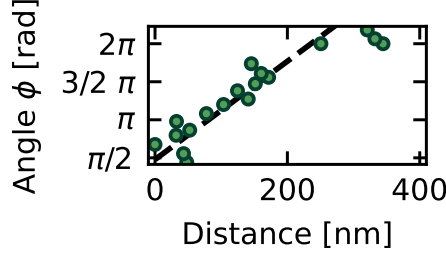


Figure 4.6: Interference phase ϕ between the single photon and coherent state components, extracted by fitting the reflection spectrum, as a function of the fiber displacement d , measured by a position sensor in the piezo positioner. The black dashed line is a guide to the eye indicating a 2π phase change in the distance of half a wavelength.

We control the interference phase of the measurements in Fig. 4 of the main text by moving the fiber compared to the waveguide. The phase dependence on the fiber displacement, which we extract from the piezo positioner sensor, is approximately linear and a full period is obtained in around half wavelength distance.

4.8.4 MEASUREMENT SEQUENCES

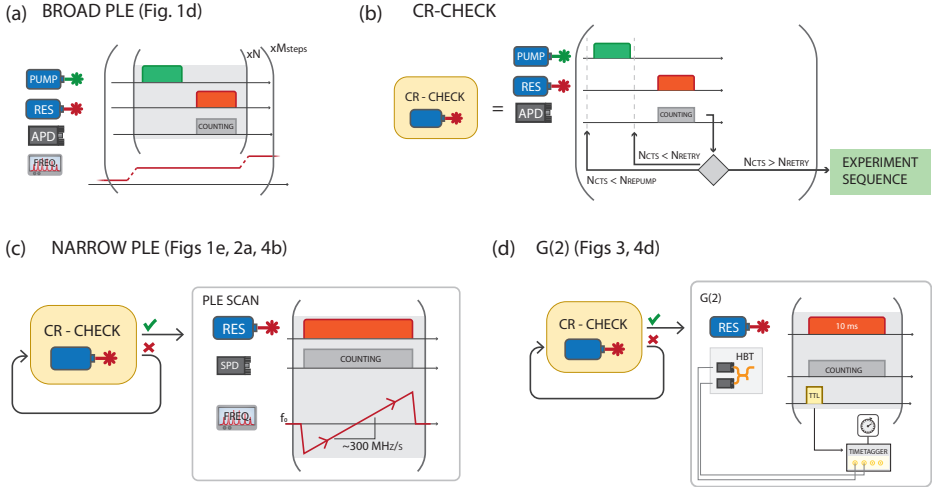


Figure 4.7: Measurement sequences. See text for details.

Figure 4.7 shows the measurement sequence for the experiments we realised. The control of the AOM pulses, laser frequency sweeps, APD counting, triggering of the time tagging hardware and logic operations are done by a Adwin Pro II microprocessor.

The broad photoluminescence excitation (PLE) measurement in Fig. 1(d) of the main text is done with the sequence in 4.7(a). We step the laser frequency and for each point we repeat a sequence consisting of a repump and a resonant pulse, during which we count the emitted photons.

To ensure that the SnV is in the correct charge and frequency state, we condition the measurements on a successful Charge-Resonance Check (CR-Check, Fig. 4.7(b)). A resonant laser probe pulse excites the SnV at a set frequency and the number of photon counts during the pulse (N_{CTS}) is recorded. This value is compared to two thresholds, N_{RETRY} and N_{REPUMP} chosen such that $N_{RETRY} > N_{REPUMP}$. If $N_{CTS} < N_{REPUMP}$ an off-resonant pulse is sent to probabilistically initialize the charge state before probing again with the resonant pulse. If $N_{REPUMP} < N_{CTS} < N_{RETRY}$ the probe pulse is repeated. If $N_{CTS} > N_{RETRY}$ the CR-check is considered successful and the experiment begins. More details on the procedure can be found in Ref [14].

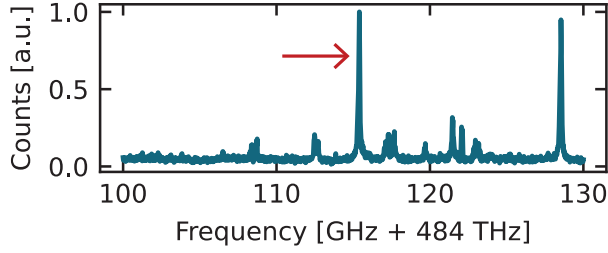
We use CR-conditioned repeated narrow PLE scans (Fig. 4.7(c)) to measure the PSB, transmission and reflection spectra in order to extract ΔT and the reflection parameters ξ and ϕ . We apply an analog voltage to scan the laser frequency around a set point in a step-wise way. In each step we integrate the counts of the APDs for 20 ms. The single scan speed is ~ 300 MHz/s.

We perform the $g^{(2)}$ measurements with the sequence in Fig 4.7(d), by repeatedly sending 10 ms resonant pulses, preceded by a trigger TTL pulse that serves as a sync signal for the timetagger. The pulses are conditioned on a CR Check to ensure that the SnV is resonant with the probe.

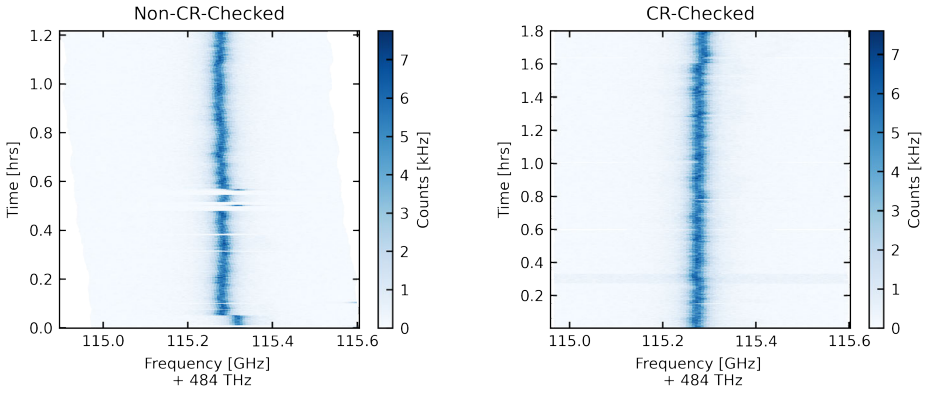
4.8.5 PLE AND CR-CHECKED LINESCANS

A photoluminescence excitation spectrum (PLE) (Fig. 4.8(a)) reveals several SnV centers in the waveguide, which are spectrally resolvable owing to local variations of the strain environment.

We compare the PLE conditioned on Charge-Resonance (CR) check [14] (sequence in Fig. 4.7(c), result on the right in Fig. 4.8) with a PLE done with a less strict "brightness check" condition (left in Fig. 4.8). In the latter, after each scan we check the maximum intensity of the PLE peak and compare it to the average countrate in the trace. If a threshold in the countrate is surpassed, indicating that there is a peak, we consider the emitter "bright" and we continue with the next scan. If the threshold is not met, we apply an off-resonant charge repump pulse (515 nm) before the next scan. In the trace on the left in Fig. 4.8 one can notice some frequency jumps and empty scans. The "brightness check" only probabilistically brings the emitter in the right charge state, but that can also be at a different frequency since the off-resonant pulse can modify the charge environment around the SnV. As long as the emitter is bright, in this case, it does not show significant spectral diffusion. Note that the condition only acts on the following scan. The CR-Check, instead, is a pre-condition. The scan only starts once we know that the emitter is in the right charge and resonance state. Therefore, each trace shows a peak at the target frequency. Conditioning the experiments with this technique prevents the recording of data when the emitter is detuned due to a



(a)



(b)

Figure 4.8: (a) Broad PLE scan in the waveguide. (b) PLE measurement comparison. On the left, PLE scan where the presence or absence of a peak (at any frequency) in each scan conditions an off-resonant repump on the next scan. On the right, PLE scans that are pre-conditioned on a successful charge-resonance check.

frequency jump or absent due to ionization. For the Non-CR-Checked linescans we did not lock the laser frequency after every scan. In contrast to the CR-Check linescans, the frequency of the probe Laser drifts over time. This is visible as a drift of the center frequency of the scan-range. The frequency reported in the scan is measured at the wavemeter, that we constantly monitor, showing that the emitter frequency is stable.

4.9 REFERENCES

1. Awschalom, D. D., Hanson, R., Wrachtrup, J. & Zhou, B. B. Quantum Technologies with Optically Interfaced Solid-State Spins. *Nature Photonics* **12**, 516–527 (2018).
2. Atatüre, M., Englund, D., Vamivakas, N., Lee, S.-Y. & Wrachtrup, J. Material Platforms for Spin-Based Photonic Quantum Technologies. *Nature Reviews Materials* **3**, 38–51 (2018).
3. Kimble, H. J. The Quantum Internet. *Nature* **453**, 1023–1030 (2008).
4. Wehner, S., Elkouss, D. & Hanson, R. Quantum Internet: A Vision for the Road Ahead. *Science* **362**, eaam9288 (2018).
5. Pompili, M., Hermans, S. L. N., Baier, S., Beukers, H. K. C., Humphreys, P. C., Schouten, R. N., Vermeulen, R. F. L., Tiggelman, M. J., Dos Santos Martins, L., Dirkse, B., Wehner, S. & Hanson, R. Realization of a Multinode Quantum Network of Remote Solid-State Qubits. *Science* **372**, 259–264 (2021).
6. Hermans, S. L. N., Pompili, M., Beukers, H. K. C., Baier, S., Borregaard, J. & Hanson, R. Qubit Teleportation between Non-Neighbouring Nodes in a Quantum Network. *Nature* **605**, 663–668 (2022).
7. Bhaskar, M. K., Riedinger, R., Machielse, B., Levonian, D. S., Nguyen, C. T., Knall, E. N., Park, H., Englund, D., Lončar, M., Sukachev, D. D. & Lukin, M. D. Experimental Demonstration of Memory-Enhanced Quantum Communication. *Nature* **580**, 60–64 (2020).
8. Wan, N. H., Lu, T.-J., Chen, K. C., Walsh, M. P., Trusheim, M. E., De Santis, L., Bersin, E. A., Harris, I. B., Mouradian, S. L., Christen, I. R., Bielejec, E. S. & Englund, D. Large-Scale Integration of Artificial Atoms in Hybrid Photonic Circuits. *Nature* **583**, 226–231 (2020).
9. Bradac, C., Gao, W., Forneris, J., Trusheim, M. E. & Aharonovich, I. Quantum Nanophotonics with Group IV Defects in Diamond. *Nature Communications* **10**, 5625 (2019).
10. Ruf, M., Wan, N. H., Choi, H., Englund, D. & Hanson, R. Quantum Networks Based on Color Centers in Diamond. *Journal of Applied Physics* **130**, 070901 (2021).
11. Trusheim, M. E. *et al.* Transform-Limited Photons From a Coherent Tin-Vacancy Spin in Diamond. *Phys. Rev. Lett.* **124**, 023602 (2020).
12. Arjona Martínez, J., Parker, R. A., Chen, K. C., Purser, C. M., Li, L., Michaels, C. P., Stramma, A. M., Debroux, R., Harris, I. B., Hayhurst Appel, M., Nichols, E. C., Trusheim, M. E., Gangloff, D. A., Englund, D. & Atatüre, M. Photonic Indistinguishability of the Tin-Vacancy Center in Nanostructured Diamond. *Phys. Rev. Lett.* **129**, 173603 (2022).
13. Rugar, A. E., Aghaeimeibodi, S., Riedel, D., Dory, C., Lu, H., McQuade, P. J., Shen, Z.-X., Melosh, N. A. & Vučković, J. Quantum Photonic Interface for Tin-Vacancy Centers in Diamond. *Physical Review X* **11**, 031021 (2021).

14. Brevoord, J. M., De Santis, L., Yamamoto, T., Pasini, M., Codreanu, N., Turan, T., Beukers, H. K., Waas, C. & Hanson, R. Heralded initialization of charge state and optical-transition frequency of diamond tin-vacancy centers. *Phys. Rev. Appl.* **21**, 054047 (2024).
15. Rosenthal, E. I., Anderson, C. P., Kleidermacher, H. C., Stein, A. J., Lee, H., Grzesik, J., Scuri, G., Rugar, A. E., Riedel, D., Aghaeimeibodi, S., *et al.* Microwave spin control of a tin-vacancy qubit in diamond. *Physical Review X* **13**, 031022 (2023).
16. Guo, X., Stramma, A. M., Li, Z., Roth, W. G., Huang, B., Jin, Y., Parker, R. A., Arjona Martínez, J., Shofer, N., Michaels, C. P., *et al.* Microwave-based quantum control and coherence protection of tin-vacancy spin qubits in a strain-tuned diamond-membrane heterostructure. *Physical Review X* **13**, 041037 (2023).
17. Beukers, H. K., Pasini, M., Choi, H., Englund, D., Hanson, R. & Borregaard, J. Remote-entanglement protocols for stationary qubits with photonic interfaces. *PRX Quantum* **5**, 010202 (2024).
18. Bhaskar, M. K., Sukachev, D. D., Sipahigil, A., Evans, R. E., Burek, M. J., Nguyen, C. T., Rogers, L. J., Siyushev, P., Metsch, M. H., Park, H., Jelezko, F., Lončar, M. & Lukin, M. D. Quantum Nonlinear Optics with a Germanium-Vacancy Color Center in a Nanoscale Diamond Waveguide. *Phys. Rev. Lett.* **118**, 223603 (2017).
19. Thyrrrestrup, H., Kiršanskė, G., Le Jeannic, H., Pregnotato, T., Zhai, L., Raahauge, L., Midolo, L., Rotenberg, N., Javadi, A., Schott, R., Wieck, A. D., Ludwig, A., Löbl, M. C., Söllner, I., Warburton, R. J. & Lodahl, P. Quantum Optics with Near-Lifetime-Limited Quantum-Dot Transitions in a Nanophotonic Waveguide. *Nano Letters* **18**, 1801–1806 (2018).
20. Faez, S., Türschmann, P., Haakh, H. R., Götzinger, S. & Sandoghdar, V. Coherent Interaction of Light and Single Molecules in a Dielectric Nanoguide. *Phys. Rev. Lett.* **113**. Publisher: American Physical Society, 213601 (2014).
21. Sipahigil, A., Evans, R. E., Sukachev, D. D., Burek, M. J., Borregaard, J., Bhaskar, M. K., Nguyen, C. T., Pacheco, J. L., Atikian, H. A., Meuwly, C., Camacho, R. M., Jelezko, F., Bielejec, E., Park, H., Lončar, M. & Lukin, M. D. An Integrated Diamond Nanophotonics Platform for Quantum-Optical Networks. *Science* **354**, 847–850 (2016).
22. Chang, D. E., Sørensen, A. S., Demler, E. A. & Lukin, M. D. A Single-Photon Transistor Using Nanoscale Surface Plasmons. *Nature Physics* **3**, 807–812 (2007).
23. Shen, J. T. & Fan, S. Coherent Photon Transport from Spontaneous Emission in One-Dimensional Waveguides. *Optics Letters* **30**, 2001–2003 (2005).
24. Khanaliloo, B., Mitchell, M., Hryciw, A. C. & Barclay, P. E. High-Q/V Monolithic Diamond Microdisks Fabricated with Quasi-isotropic Etching. *Nano Letters* **15**, 5131–5136 (2015).
25. Mitchell, M., Lake, D. P. & Barclay, P. E. Realizing $Q > 300\,000$ in diamond microdisks for optomechanics via etch optimization. *APL Photonics* **4**, 016101 (2019).
26. Mouradian, S., Wan, N. H., Schröder, T. & Englund, D. Rectangular Photonic Crystal Nanobeam Cavities in Bulk Diamond. *Applied Physics Letters* **111**, 021103 (2017).

27. Ruf, M. *Cavity-enhanced quantum network nodes in diamond* PhD thesis (Delft University of Technology, 2021).
28. Burek, M. J., Meuwly, C., Evans, R. E., Bhaskar, M. K., Sipahigil, A., Meesala, S., Machiels, B., Sukachev, D. D., Nguyen, C. T., Pacheco, J. L., Bielejec, E., Lukin, M. D. & Lončar, M. Fiber-Coupled Diamond Quantum Nanophotonic Interface. *Phys. Rev. Appl.* **8**, 024026 (2017).
29. Pasini, M., Codreanu, N., Turan, T., Riera Moral, A., Primavera, C. F., De Santis, L., Beukers, H. K., Brevoord, J. M., Waas, C., Borregaard, J., *et al.* Nonlinear quantum photonics with a tin-vacancy center coupled to a one-dimensional diamond waveguide. *Phys. Rev. Lett.* **133**, 023603 (2024).
30. Herrmann, Y., Fischer, J., Brevoord, J. M., Sauerzapf, C., Wienhoven, L. G., Feije, L. J., Pasini, M., Eschen, M., Ruf, M., Weaver, M. J., *et al.* Coherent coupling of a diamond tin-vacancy center to a tunable open microcavity. *Physical Review X* **14**, 041013 (2024).
31. Iwasaki, T., Miyamoto, Y., Taniguchi, T., Siyushev, P., Metsch, M. H., Jelezko, F. & Hatano, M. Tin-Vacancy Quantum Emitters in Diamond. *Phys. Rev. Lett.* **119**, 253601 (2017).
32. Görlitz, J., Herrmann, D., Thiering, G., Fuchs, P., Gandil, M., Iwasaki, T., Taniguchi, T., Kieschnick, M., Meijer, J., Hatano, M., Gali, A. & Becher, C. Spectroscopic Investigations of Negatively Charged Tin-Vacancy Centres in Diamond. *New Journal of Physics* **22**, 013048 (2020).
33. Koch, M. K., Hoese, M., Bharadwaj, V., Lang, J., Hadden, J. P., Ramponi, R., Jelezko, F., Eaton, S. M. & Kubanek, A. Super-Poissonian Light Statistics from Individual Silicon Vacancy Centers Coupled to a Laser-Written Diamond Waveguide. *ACS Photonics* **9**, 3366–3373 (2022).
34. Shen, J.-T. & Fan, S. Strongly Correlated Two-Photon Transport in a One-Dimensional Waveguide Coupled to a Two-Level System. *Phys. Rev. Lett.* **98**, 153003 (2007).
35. Parker, R. A., Arjona Martínez, J., Chen, K. C., Stramma, A. M., Harris, I. B., Michaels, C. P., Trusheim, M. E., Hayhurst Appel, M., Purser, C. M., Roth, W. G., *et al.* A diamond nanophotonic interface with an optically accessible deterministic electronuclear spin register. *Nature Photonics* **18**, 156–161 (2024).
36. Bernien, H., Hensen, B., Pfaff, W., Koolstra, G., Blok, M. S., Robledo, L., Taminiau, T. H., Markham, M., Twitchen, D. J., Childress, L. & Hanson, R. Heralded Entanglement between Solid-State Qubits Separated by Three Metres. *Nature* **497**, 86–90 (2013).
37. Hermans, S. *Quantum Networks Using Spins in Diamond* PhD thesis (Delft University of Technology, 2022).
38. Raa, I. T., Ervasti, H. K., Botma, P. J., Visser, L. C., Budhrani, R., van Rantwijk, J. F., Cadot, S. P., Vermeltfoort, J., Pompili, M., Stolk, A. J., Weaver, M. J., van der Enden, K. L., de Leeuw Duarte, D., Teng, M., van Zwieten, J. & Grooteman, F. *QMI - Quantum Measurement Infrastructure, a Python 3 Framework for Controlling Laboratory Equipment* 4TU.ResearchData. 2023.

5

TIN-VACANCY EMBEDDED ALL-DIAMOND PHOTONIC CRYSTAL CAVITIES

5

Quantum networks will require entanglement distribution to processing qubits on its end nodes via optical channels. Optically active spin qubits, such as tin-vacancy (SnV) centers in diamond, have emerged as one of the leading candidates to implement quantum networking hardware due to their favorable optical and spin properties. Their first order insensitivity to charge noise renders SnV centers excellent for integration into nanophotonic devices. Here we show our results on fabricated free-hanging SnV-embedded photonic crystal cavity devices in diamond. We present an empirical analysis and evaluation of the geometry of the obtained fabricated devices, followed by extensive optical characterization at room temperature, showing the dependence of the optical performance of the cavity on fabrication tolerances. Finally, we describe and show in situ cavity resonance tuning, as well as preliminary spectroscopy on device-embedded SnV centers. Coherent coupling of quantum emitters to photonic crystal cavities represents a key step towards realization of multinode quantum networks.

5.1 INTRODUCTION

The entanglement generation rate represents a major challenge in the demonstrations of modern quantum networks [1–4]. Due to their small mode volumes, photonic crystal cavities can significantly enhance the interaction with solid-state spins. Engineering and fabricating such light-matter interfaces is of great interest due to their high potential in addressing such a challenge.

In this chapter, we present successful integration and coupling of SnV centers in diamond photonic crystal cavities.

We start by introducing our cavity design and fabrication process in Section 5.2. We evaluate the performance of the **250 °C QIE-based variant** fabrication process (extensively discussed in Chapter 2) by characterizing the devices geometry via Scanning Electron Microscopy (SEM) and Atomic Force Microscopy (AFM) measurements.

In Section 5.3, we then characterize the optical properties of the devices at room temperature, presenting the cavity resonance and quality factor statistics of the fabricated PCC devices. We then conclude in Section 5.4 with showing in situ cavity resonance tuning, as well as preliminary spectroscopy on device-embedded SnV centers.

5

5.2 NANOPHOTONIC CAVITY DEVICES

The realization of SnV center integrated devices is described in two main steps: first, SnV centers are fabricated and activated via ion implantation and annealing; second, photonic crystal cavity devices are fabricated via **250 °C QIE-base variant** fabrication process.

Fabrication of SnV centers in bulk diamond substrates follows the methods described in Chapter 3, with process parameters detailed in Table 5.3. Specifically, we incorporate ^{120}Sn ions in the diamond crystal via high energy ion implantation (350 keV, 7° implantation angle) and activate the SnV centers via high temperature low pressure annealing treatment (1100 °C over a duration of 4 hours via the surface-protected annealing method presented in Chapter 3).

Fabrication of suspended cavity devices with resonant wavelength compatible with tuning strategies to optical SnV center zero-phonon line (ZPL) emission follows the methods described in Chapter 2, with device design parameters detailed in Table 5.1 and schematic illustrated in Figure 5.1 (a). The nano-fabrication process of the devices is based on the crystal-dependent quasi-isotropic-etch undercut method [5–10]. Specifically, device fabrication begins with patterning the Si_xN_y hard mask material, followed by the transfer pattern into the diamond substrate and vertical coverage with AlO_x of the structures sidewalls. Next, the quasi-isotropic etch (QIE) undercuts the devices, followed by an upward etch to thin the devices to a thickness of ~ 200 nm (Figure 5.1 (d)). Fabrication concludes with an inorganic removal of the hard mask materials. This allows for a thorough investigation of the geometry of the fabricated devices, as shown in Figure 5.1 (e) and Figure 5.2. The details of the fabrication of SnV centers and subsequent nanophotonic devices can be found in Section 5.6, with extensive development of the **250 °C QIE-based variant** fabrication process methods described in Section 2.8 (parameters detailed in Appendix, Table A.4).

5.2.1 CAVITY DESIGN AND LAYOUT

The devices are single-sided photonic crystal cavities (schematically illustrated in Figure 5.1 (a)), consisting of a strong mirror (over M_s mirror unit cells, blue-shaded), central cavity region (over $2N$ unit cells, red-shaded, defect introduced with a functional introduced by Ref. [11]) and a weak mirror (over M_w variable mirror holes, blue shaded). The design of the devices is inspired by Ref. [12], where we maintain a constant value of the lattice constant a_n , equal for both the strong and weak mirror. Effectively, in the presented design the two mirrors have the same stop-band, with the weak mirror characterized by a reflectance dependent on the number of mirror unit cells M_w . The directionality in the out-coupling from the cavity to the waveguide is realized by reducing the number of mirror unit cells. Next to the weak in-coupling mirror, the latter is adiabatically tapered to the waveguide region (green shaded, width w_{wg} same as the cavity width) by appending additional L mirror unit cells (yellow shaded), linearly decreasing the circular hole radius from optimal r to $r_{min, wg}$ (~ 50 nm feasible with the QIE-based fabrication process parameters), while the lattice constant a_n is kept constant. Next, the width of the waveguide is reduced from w_{wg} to end-taper width w_t , over the taper length L_t (cyan).

In order to guarantee structural stability, a careful trade-off between the overall length of free-hanging structure is considered, sweeping the coupling taper length. Optionally, for $L_t > 15 \mu\text{m}$, a support holding bar of width $w_{hb} \approx 200$ nm is implemented, to guarantee structural stability of the overall free-hanging device. Finally, in order to allow for efficient both in-contact and lensed-fiber configuration coupling to the devices, the taper-end to diamond substrate distance d_{ts} is fixed. The parameter values are detailed in Table 5.1. On the overall diamond substrate, we sweep the cavity design by varying the scaling factor on the lattice constant a_n , waveguide width w_{wg} and circular hole radius r incrementally by $\Delta=1\%$, with respect to the nominal values (scaling factor 100%) determined via finite element method optical simulations in COMSOL®. Thus we vary the scaling factor from 95% to 110% with respect to nominal 100% device parameters. This strategy is adopted in order to preventively compensate cavity resonance shifts from introduced fabrication process variability and yield cavity devices with resonances ≤ 619 nm (SnV center emission), thus allowing for dynamic in situ cavity resonance tuning to the embedded SnV centers emission lines.

The chiplet device consists of an array of single-sided cavity devices with varying $M_w=1$ to 6, inter-device gap distance g_n (center-to-center: $3 \mu\text{m}$) is decided as a trade-off between substrate space optimization as well as compatibility with the QIE undercut and upward etch, guaranteeing uniform device thickness across the chiplet. The devices are fixed to the diamond substrate via the end waveguide region distanced from the strong mirror ~ 850 nm and are fully free-hanging (finalized fabricated devices shown in Figure 5.1 (b) and (c)), with chiplet design optionally implementing the holding bars (holding bar width $w_{hb}=200$ nm).

High magnification SEM inspection (Figure 5.1 (d), 65° angle tilt view)) allows to quantify the device thickness and device geometry bias (a_n , w_{wg} and r respectively, Figure 5.1 (e), top-down (0° angle tilt view)), whereas atomic force microscopy (AFM) topographic analysis allows to estimate device transversal cross-section (Figure 5.2 (a)) and bottom surface roughness (Figure 5.2 (b)). The combination of the two inspection methods allows to fully determine the geometry of fabricated devices (Figure 5.2 (c)), for which design

compensation is implemented a priori and allows to calibrate the scaling factor range, as well as the device thickness within the QIE upward etch fabrication step.

| Rectangular hole-based PCC | | | | | Design parameters | | | | | | | |
|----------------------------|--------|----------|--------|--------|-------------------|-----|--------|-----|-------------------------------------|-------|------------------|-----------------|
| Parameter | a_n | w_{wg} | r | t_n | M_s | N | M_w | L | L_t | w_t | d_{fs} | g_n |
| Value | 206 nm | 275 nm | 142 nm | 200 nm | 13 | 7 | 1 to 6 | 7 | 7 μm to 16 μm | 50 nm | 60 μm | 3 μm |

Table 5.1: **SnV center integrated photonic crystal cavities** | Left: Unit cell parameter values used, defect introduced with functional form from Refs. [10, 11]; green-shaded: device parameters swept by varying the scaling factor | Right: integral structure device parameters (schematic illustrated in Figure 5.1 (a)).

5.2.2 FABRICATED DEVICES GEOMETRY EVALUATION

The optimal cavity design parameters listed in Table 5.1, implemented for a symmetric cavity (where $M_w = M_s$) [10], in Finite Element Method (FEM) COMSOL® simulations yield a cavity resonance ~ 619 nm and quality factor Q as high as $\sim 1 \times 10^6$. As shown in Ref. [10], any deviations from the simulated design, for example, lattice constant a_n , hole radius r , device width w_{wg} , and device cross section, can change the cavity resonance as well as lower the quality factor Q .

QIE-based fabrication process unavoidably introduces inaccuracy in the geometry of the fabricated devices, deviating from the simulated rectangular unit cell. These prevalently affect the hole radius r , the width of the device w_{wg} (as shown in Figure 5.1) and the cross section of the device (as shown in Figure 5.2), reducing the quality factor and changing the resonance of the cavity relative to the design one. In the following, we present the quantitative analysis of typical consistent geometry bias and transverse cross section, by combining high-magnification SEM inspection and AFM topography analysis. Here we present the device geometry analysis, performed on two twin diamond samples (SEM geometry analysis on Sample 1, AFM topography analysis on Sample 2), fabricated within the same fabrication run and same **250 °C QIE-based** fabrication process parameters as the optically characterized sample in Section 5.3 (Sample 3).

The transfer pattern accuracy (a_n , r and w_{wg}) yields differences on the order of a few nanometers (not quantifiable by SEM analysis), while the device thickness variability is ~ 10 nm between the analyzed samples (Sample 1 and Sample 2 have a device thickness ~ 10 nm lower than Sample 3). The transversal device cross section estimated in the following section (namely vertical sidewall angle deviation and bottom facet topography) is the same between the three fabricated diamond substrates.

Geometry estimation: SEM analysis

High magnification SEM analysis of Sample 1 (0° tilt angle view, pixel size ~ 0.52 nm) enables inspection of fabricated devices top facet, allowing for accurate estimation of lattice constant a_n , hole radius r and device width w_{wg} . In the presented example, we show the analysis carried out on a PCC device with scaling 95 % ($a_n = 0.95 \times 206$ nm = 195.7 nm, $r = 0.95 \times 71$ nm = 67.45 nm, $w_{wg} = 0.95 \times 275$ nm = 261.25 nm), that is the smallest device dimensions we pattern in our typical parameters scaling factor sweep.

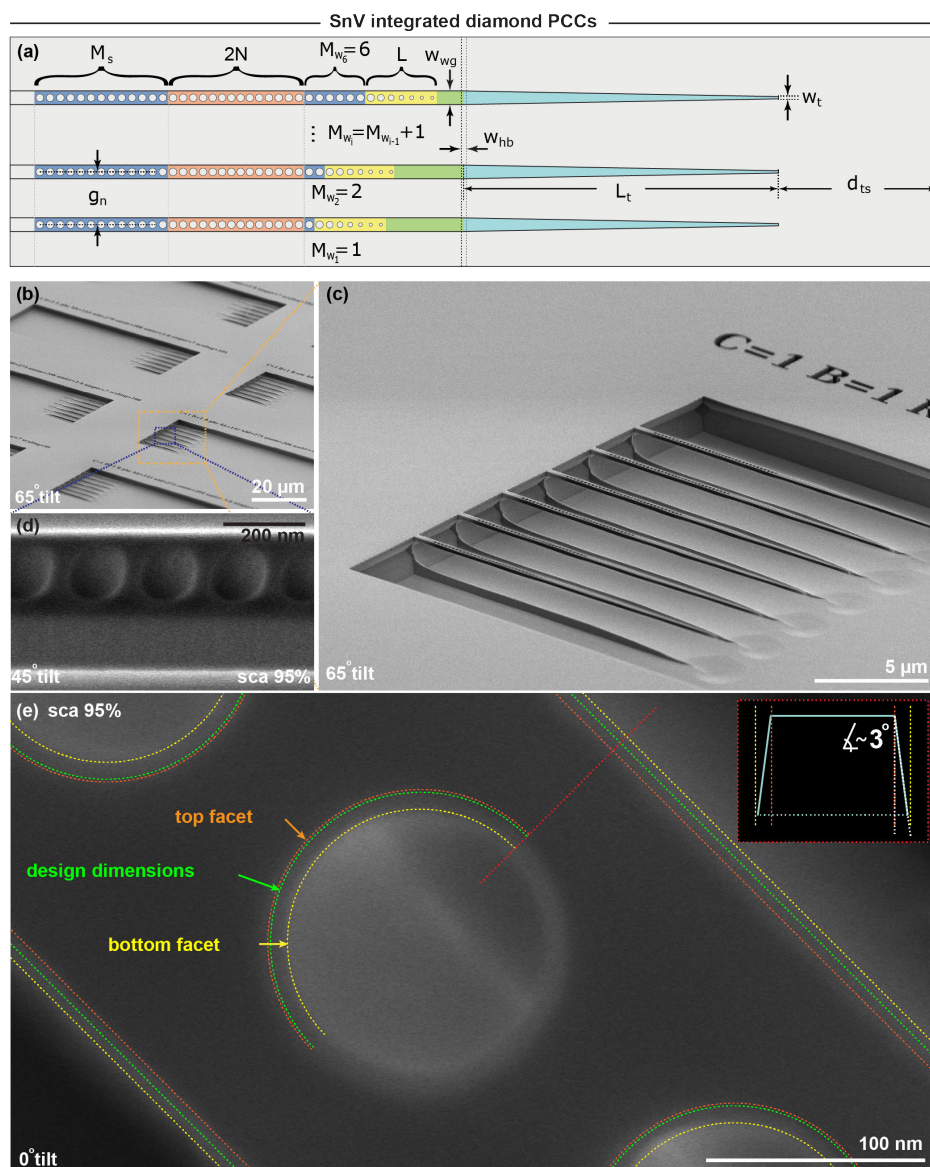


Figure 5.1: **SnV center integrated diamond photonic crystal cavities:** | **(a)** Schematic illustration of free-hanging single-sided photonic crystal cavity design (inspired from Ref. [12]), in an array chiplet configuration; | **(b)** SEM pictogram (65° view tilt angle): typical diamond chiplet array (two chiplet per scaling factor, arranged in three columns each, replicated in four sample quadrant areas); **(c)** Zoom-in SEM pictogram (65° view tilt angle) of a single chiplet: array of cavity devices with design in (a); **(d)** Zoom-in SEM pictogram (45° view tilt angle) of the cavity region of a single PCC, scaling factor 95%: tilted view enables evaluation of device thickness; **(e)** High magnification (underlying) SEM pictogram (0° view tilt angle) of the cavity region, with (overlaid, dashed yellow) evaluation of bottom facet circular hole and device sidewall, (overlaid, dashed orange) top facet aperture circular hole and device sidewall; (overlaid, to scale, dashed green) device design; | **inset:** evaluating the mismatch extent between top facet and bottom facet allows quantification of device sidewall angle.

Overlaying the CAD design (Figure 5.1 (e), dashed green) to the underlying corresponding scaling factor 95% fabricated device SEM pictogram (pixel size 0.53 nm), no significant deviation from the optimal a_n can be observed, confirming a high accuracy of a_n in 250 °C QIE-based process transfer pattern. When comparing the circular hole diameter and device width on the top facet (dashed orange) with the design parameters (r and w_{wg}), an r systematic bias of ~ 4 nm (radius larger than design) and a w_{wg} systematic bias ~ 20 nm (width smaller than design) can be identified. The parameter values evaluated from the top-down SEM inspection of diamond devices are in-line with the previously estimated systematic bias after transfer pattern into the Si_xN_y (in Chapter 2, Section 2.7.2).

At the same time, high magnification top-down SEM inspection allows for an accurate estimation of the vertical sidewall angle. That is, in the case of design sidewall angle of 90° , the top facet contour (Figure 5.1 (e), dashed orange) of the etched devices should perfectly align with the bottom facet contour (dashed yellow). Measurement of the horizontal extent between the top facet contours and the bottom facet contour allows to identify on average an extent of ~ 10 nm, indicating that the sidewall angle is $\leq 90^\circ$. When measuring the same quantity on a PCC device scaling 100% ($a_n=206$ nm, $r=71$ nm, $w_{wg}=275$ nm) PCC device, we find similar values within the SEM pixel size resolution error, thus independent of the absolute parameter values, given a certain device scaling factor. A measurement of (same scaling 95%) device thickness from SEM inspection (45° tilt angle view, pixel size 1.98 nm, Figure 5.1 (d)), yields a vertical extent from top facet to bottom facet of ~ 188 nm. Assuming the bottom facet of the device characterized by a flat planar surface, the estimated sidewall angle deviation from the designed $\sim 90^\circ$ is of ~ 3 nm.

While this sidewall angle estimation does not take into account the cross-section bottom facet topography of the device (for which an AFM topography analysis is required), it does nevertheless offer a rough estimation of the sidewall angle within assumption of roughly planar bottom surface facet. The estimation obtained from SEM analysis results in good agreement with the AFM topography analysis taking into account the full bottom facet topography of the device, with a discrepancy of $\approx 0.3^\circ$, as will be detailed in the next section.

Nevertheless, high magnification SEM analysis enables an accurate estimation of the devices sidewall tapering angle by identifying the distance mismatch between device top facet contours and bottom facet contours.

Geometry estimation: AFM topography analysis

Before proceeding with the atomic force microscopy (AFM) topography analysis, below we briefly list the relevant fabrication parameters differences between Sample 1 (SEM analyzed above) and Sample 2 (analyzed below with AFM).

In the Sample 2 case, instead of 67% over-etch, we implemented a over-etch of 79% in the CHF_3/O_2 ICP-RIE step the transfer pattern into of Si_xN_y mask step to ensure full clearance of the hard mask in correspondence of the dense patterns (i.e. circular holes). While ensuring full opening of circular holes in the intended design (as well as accurate transfer pattern with systematic geometry bias similar to Sample 1 and Sample 3, within ~ 5 nm), the 67% overshoot in the pattern transfer step led to mask breaking in the correspondence of circular holes in the downstream QIE undercut steps, where the plasma has locally etched and broken the suspended nanophotonic cavities, as shown in the inset of Figure 5.2 (a). The observed effect exhibited random variability throughout the sample. Although

mask breaking generally is an undesired effect as it compromises the process outcome, at the same time, it offered the possibility of identifying (post-fabrication) and locating locally etched (and cut-through) devices, repositioned to expose the device bottom facet.

This enabled SEM qualitative analysis (used to identify and correlate PCC device parameters) combined with AFM topography analysis of the bottom facet of PCC devices. In this analysis, we first qualitatively SEM inspect the sample in order to identify PCC devices detached from the bulk support and identify the device design parameters. Among the identified detached devices from the bulk diamond substrate, we identify the PCC devices rotated 180° along the longitudinal axis, facing the bottom facet up and compatible with the AFM topography scan. Typical SEM qualitative analysis is shown in Figure 5.2. In typical chiplet layout (schematic in Figure 5.1 (a)), free-hanging devices (Figure 5.2 (a)) are attached to the bulk diamond substrate from the end side of the strong mirror region of the device. On the same diamond substrate sample, devices for which the breaking effect randomly takes place (as detailed above), by qualitatively SEM inspecting the broken PCC structure, we are able to identify the parent chiplet. For devices repositioned to expose bottom facet, qualitative SEM inspection of the cavity region and waveguide region (Figure 5.2 (a.1) and (a.2) respectively, on three separate broken devices from different parent chiplets across the sample) allows to SEM resolve a triangular cross section and rectangular cross section in the taper-end region (Figure 5.2 (a.3)). At the same time, SEM resolved surface roughness can be identified, thus taking into account the pixel size ((a.1) 3.17 nm, (a.2) 1.44 nm and (a.3) 1.44 nm pixel size respectively) in the shown pictograms, we suspect the surface roughness of the bottom facet to be of the same order of magnitude, to the least.

First, an AFM topography scan of a PCC device (scaling factor 98%) exposing the topside facet enables a quantitative evaluation of the diameter of the circular hole and the width of the waveguide. This allows us to quantify the discrepancy between top-facet and design parameter values from topographic measurements.

Next, a consecutive AFM topography scan of a PCC device (scaling 97%), exposing the bottom facet, enables both a quantitative evaluation of bottom topography cross-section and surface roughness evaluation, as shown in Figure 5.2 (b).

By comparing the values evaluated for the top- and bottom-side facet of hole radius r and waveguide width w_{wg} , the AFM analysis confirms the accuracy of the high magnification SEM analysis presented above, here measuring a lower device facet w_{wg} extent ~ 20 nm higher and a r extent ~ 10 nm lower compared to the same parameters measured on the device top facet. Next, the topography maps of the cavity region and waveguide region show a triangular V-shaped bottom facet, with a height of ~ 16 nm, whereas the topography map of the taper-end displays a rectangular cross section.

Combining the evaluated experimentally measured device parameters allows us to infer the PCC device cavity and waveguide regions cross section, where we estimate the vertical sidewall angle $\sim 3^\circ$ and the bottom facet V-shaped with an angle $\sim 6^\circ$, schematically illustrated in Figure 5.2 (c). The total thickness difference between the cavity and waveguide regions is ~ 10 nm in the specific evaluated 97% device scaling factor here presented. The observed device geometry reflects the nature of the QIE aspect ratio undercut dependency, for which the complete upward etch flattening of narrow devices (i.e. design taper-end width of $w_t=50$ nm) takes place earlier in the etch process, when compared to wider devices (i.e., design cavity and waveguide region width of $w_t=275$ nm).

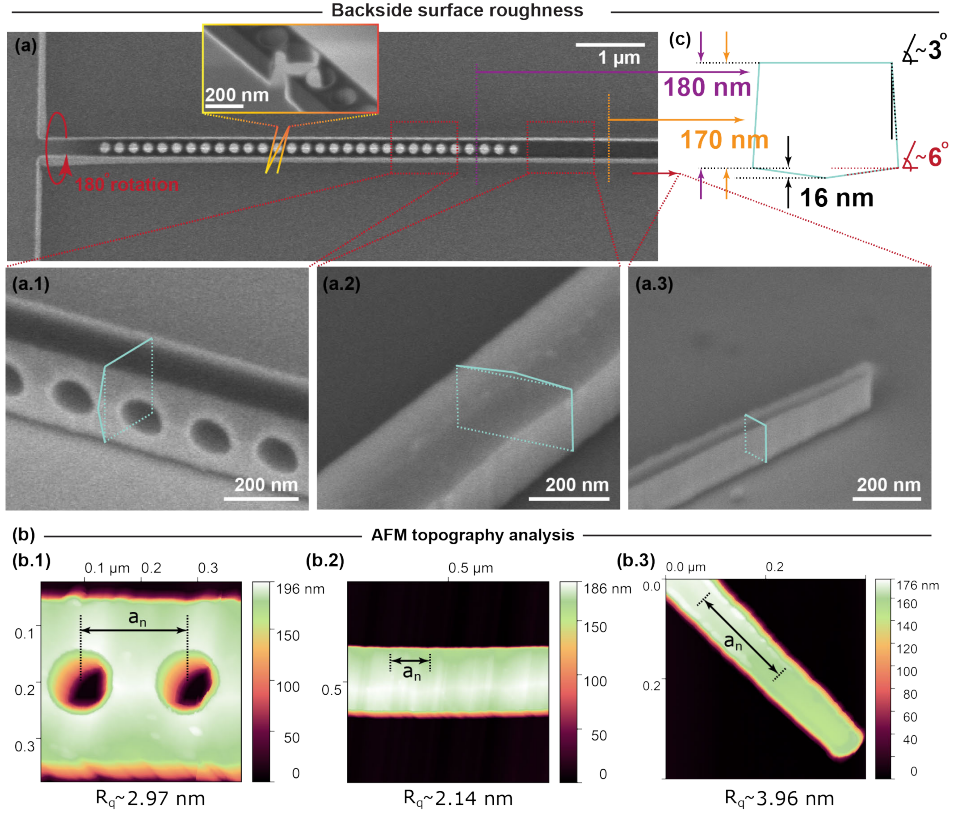


Figure 5.2: **SnV center integrated diamond photonic crystal cavities:** AFM topography analysis and device cross-section estimation | (Top panel) SEM, (Bottom panel) AFM analysis, respectively | (a) SEM pictogram (0° view tilt angle): free-hanging one-sided PCC; inset: breaking mechanism of PCC devices; | Broken and rotated by 90° and 180° around longitudinal axis devices allow for qualitative SEM inspection of the bottom surface of devices: qualitative SEM inspection (45° tilt view angle) of (a.1) rotated 90° PCC: bottom facet surface of cavity region, (a.2) rotated 180° PCC: bottom facet surface of waveguide region and (a.3) rotated 180° PCC: bottom facet surface of taper-end region; (overlaid, cyan) qualitative cross-section; | (b) AFM topography analysis of device bottom facet: cross-section and surface roughness R_q (evaluated over $a_n = 196$ nm) of (b.1) cavity region, V-shaped triangular cross-section and $R_q = 2.97$ nm, (b.2) waveguide region, V-shaped triangular cross-section and $R_q = 2.14$ nm, (b.3) taper-end region, rectangular cross-section and $R_q = 3.96$ nm; | (c) Estimated full cross-section of the device in cavity region from a combination of AFM topography and top-down high magnification SEM (Figure 5.1).

5.3 CAVITY OPTICAL PERFORMANCE: DEVICES STATISTICS

In order to evaluate the optical properties of the fabricated devices, we first proceed with a room-temperature optical characterization.

The optical properties of the devices are first characterized at room temperature (methods and setup described in Section 5.6.2) by positioning the fiber in contact with the device taper (of length L_t and taper end width w_t) and adiabatically transferring the incoupling probing light source. The in and out light coupling of the devices is delivered via optical fibers, etched into conical tapers in 40 % hydrofluoric acid (HF) [13]. The typical array of

devices (Figure 5.1 (c)) is aligned in the plane (XY direction) positioning the device to taper underneath the Z-controlled hovering tapered optical fiber. The coupling is maximized by optimizing first the optical fiber position in the XY direction on top of device taper, varying the longitudinal overlap between the optical fiber tip-end and the device coupling waveguide taper to ensure adiabatic mode transfer. Second, the white light probing source polarization is varied to match the polarization of the cavity device.

Here we present the cavity resonance and quality factor statistics of fabricated PCC devices on Sample 3, for which the final optimized **250 °C QIE-based** fabrication process parameters are detailed in Table A.4. Additionally to process parameters detailed in Table A.4, on this sample substrate, we specifically experiment with a sweep of e-beam exposure dose, i.e. $265 \mu\text{C}/\text{cm}^2$ (quadrants Q1 and Q3) and $275 \mu\text{C}/\text{cm}^2$ (quadrants Q2 and Q4) (on Sample 2 the e-beam exposure dose is $250 \mu\text{C}/\text{cm}^2$), whereas the transfer pattern CHF_3/O_2 ICP-RIE over-etch is limited to 67% (Sample 2: 79%) in order to preserve Si_xN_y mask robustness over the entire QIE-based process.

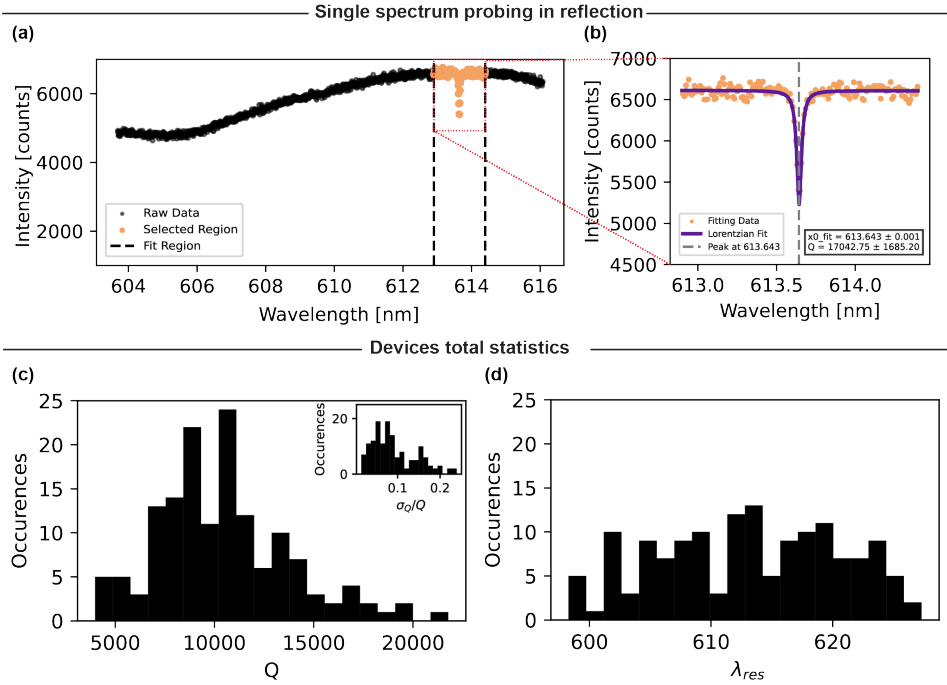


Figure 5.3: **Room-temperature optical characterization of PCC devices:** | (a) Example of single spectrum cavity Lorentzian dip of a device probed in reflection by positioning the coupling optical fiber on top of the device taper, in contact mode; all devices are probed with the same method, where the cavity dip is fit within a fit window centered on the identified cavity dip minimum, of width ± 0.75 nm; (b) Zoom-in the fit window: raw data is fit with a Lorentzian functional form with a bootstrap approach (allowing estimation of the fit error, hence propagated fit error on the estimated quality factor); The analysis is performed on a measured device subset: ~ 169 devices measured, analysis performed here on 146 devices, discarding entries with error on fit higher than 25%, 864 total fabricated devices with scaling from 95% to 100% of interest; estimated quality factor statistics in (c) and cavity resonant wavelength statistics in (d).

An SEM overview of the layout of the sample is shown in Figures 5.1 (b) and (c). We pattern PCC devices with a variable number of mirror unit cells in the in-coupling weak mirror region ($M_w = 1$ to 6) within the chiplet layout. Next, we sweep the devices scaling factor from 95% to 110% and replicate the same designs three times per each of the four quadrants across the diamond substrate as detailed in Table 5.2.

Total sample device statistics

Typical cavity spectra are acquired on a fine grating spectrometer, for which an example is shown in Figure 5.3 (a). When probed in reflection, the cavity spectrum displays a dip centered around the cavity resonant wavelength. We use non-linear least squares fitting with Lorentzian function with a linear background (standard *curve_fit* from the *scipy.optimize* package) to estimate the dip parameters and implement a bootstrapping approach to estimate the uncertainty of the fit parameters. The fit is performed in the spectral window centered on the determined cavity dip wavelength, of width ± 0.75 nm (Figure 5.3 (b)), from which the quality factor Q is estimated, together with the propagated fit error.

The analysis is performed on a subset of the total number of fabricated devices: ~ 169 devices are measured, the analysis here is performed on 146 devices, discarding entries with fit error greater than 25%, and 864 total fabricated devices with scaling from 95% to 100% of interest. The quality factor statistics are shown in Figure 5.3 (c) and the cavity resonant wavelength statistics is shown in Figure 5.3 (d). The total number of measured devices, with scaling from 95% to 100%, show a cavity resonant wavelength in the range from ~ 600 nm to 625 nm and quality factors ~ 10000 on average, with values as high as $Q \sim 21000$. The dataset comprises devices mainly with $M_w = 1$ to 4, as patterned devices with $M_w = 5$ to 6 are challenging to measure in reflection and analyze due to the poor contrast of the cavity resonance dip, often resulting in a fit error $> 25\%$, and thus are discarded.

Device statistics vs. device position on sample

The devices statistics in Figure 5.3 displays the total devices statistics for all different geometry devices with a scaling factor of 95% to 100% across the overall Sample 3 area. Extensive characterization of devices with scaling factors from 101% to 110% patterned on the substrate has not been performed, as the preliminary characterization of devices within this scaling factor range exhibited cavity resonance above the spectral range of interest.

In order to gain insight on the device cavity resonance spectral distribution, we first evaluate the cavity optical parameters in relation to the device spatial location on the sample. The diamond substrate area is divided into four regions of equal area (quadrants Q1, Q2, Q3, and Q4, respectively). Each quadrant has an effective area of $\sim 800 \mu\text{m} \times 800 \mu\text{m}$, on each of which we vary, respectively, the Sn implantation dose, e-beam exposure dose, and chiplet layout, as detailed in Table 5.2. Therefore, devices with the same scaling factor and weak mirror unit cells M_w , within the same quadrant, are spatially distant $\sim 30 \mu\text{m}$ (same column, column index 1), $\sim 260 \mu\text{m}$ and $\sim 530 \mu\text{m}$ (adjacent columns, column indices 2 and 3 respectively). Same column indices located in adjacent quadrants: devices with same scaling factor and weak mirror unit cells M_w are distanced $\sim 872 \mu\text{m}$ (x direction) and $\sim 900 \mu\text{m}$ (y direction).

| Quadrant | Q1 | Q2 |
|--|----------------------|----------------------|
| Sn Implantation Dose [ions/cm ²] | 1×10^{11} | 3×10^{10} |
| E-beam exposure dose [$\mu\text{C}/\text{cm}^2$] | 265 | 275 |
| Chiplet layout | no holding bar frame | no holding bar frame |
| Quadrant | Q3 | Q4 |
| Sn Implantation Dose [ions/cm ²] | 1×10^{11} | 3×10^{10} |
| E-beam exposure dose [$\mu\text{C}/\text{cm}^2$] | 265 | 275 |
| Chiplet layout | holding bar frame | holding bar frame |

Table 5.2: **Sample 3 chip layout**: implantation dose, e-beam exposure dose and chiplet support frame layout. Green colored: devices hole size and device width vary upon e-beam exposure dose sweep

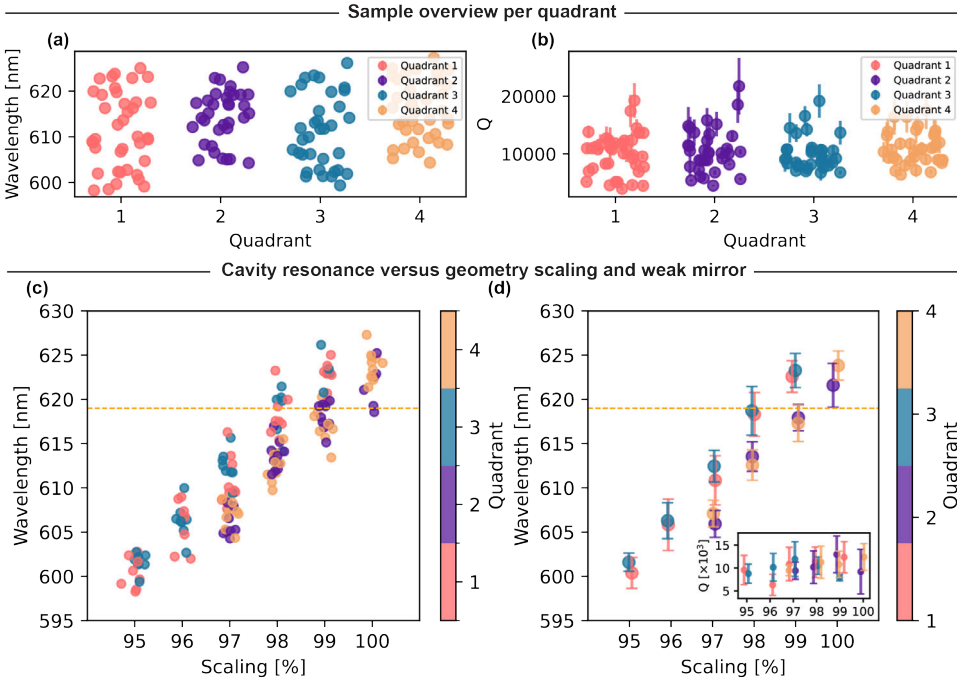


Figure 5.4: **Cavity devices statistics vs. scaling factor sweep and spatial location on substrate**: cavity resonance and quality factor distribution per quadrant on effective sample area; (a) All measured devices cavity resonance and (b) quality factor with scaling factor comprised between 95% and 100%; (c) Distribution of cavity resonance per scaling factor comprised between 95% and 100% (same data as in (a)); (d) Average cavity resonance (calculated from data in (c)) and (inset) average quality factor per scaling factor per quadrant.

When graphing the total statistics of the analyzed data versus the quadrant position (Figure 5.4), the distribution of cavity resonance (resonances between ~ 600 nm to 625 nm, Figure 5.4 (a)) and quality factor (quality factors between $Q \sim 5000$ and $Q \sim 21000$, Figure 5.4 (b)) is roughly uniform over the four quadrant areas on the substrate, showing no clear dependence between measured cavity optical parameters and the spatial location of the fabricated cavities on the diamond substrate.

Next, graphing the same data points, sorted by the device scaling factor (Figure 5.4 (c)), we see a discrete increase in cavity resonance with an increase in $\Delta = 1\%$ steps (1% step increase variation over the lattice constant a_n , waveguide width w_{wg} and hole radius r),

while at the same time the cavity resonance variability within the same scaling factor is relatively high.

We then compute the average cavity resonance per device scaling factor, per quadrant (Figure 5.4 (d)). The standard distribution of cavity resonance per quadrant per scaling factor is comprised 1.02 nm to 2.88 nm: this indicates a relatively low spread in the cavity resonant wavelength when both number of weak mirror unit cells ($M_w = 1$ to 4) and inter-device distance are varied (devices are spatially distanced $\sim 30 \mu\text{m}$ (same column, column index 1), $\sim 260 \mu\text{m}$ and $\sim 530 \mu\text{m}$ (adjacent columns, column indices 2 and 3 respectively)). Next, within same quadrant, when sweeping the device scaling factor, a linear increase of the average cavity resonant wavelength $\Delta\lambda_c \approx 4.5 \text{ nm}$ for a $\Delta_{sca}=1\%$ step increase. Therefore, taking into account the standard distribution of cavity resonances within the same scaling factor, by increasing the scaling factor of $\Delta_{sca}=1\%$, devices with cavity resonance between $\sim 600 \text{ nm}$ to 625 nm are achieved for scaling factors 95% to 100% in fabrication.

When comparing quadrants containing devices with the same e-beam exposure dose (comparing Q1 with Q3, or comparing Q2 with Q4), on average no significant cavity resonance mismatch can be identified, indicating that devices distanced $\sim 900 \mu\text{m}$ (y direction) exhibit the same optical cavity performance. This clearly indicates that no significant variability in the device geometry is present across large diamond substrate areas, up to standard distribution variability of cavity resonance within the same quadrant. Finally, when comparing same e-beam exposure dose but different chiplet layout (Q1 no holding bar with Q3 holding bar of width $W_{hb}=200 \text{ nm}$), no significant differences in the average cavity resonance can be identified, indicating that small modifications to the chiplet layout design do not introduce any cavity geometry distortion as a potential result of proximity effects upon e-beam exposure.

Thus, devices in distant quadrants (edge of the diamond substrate and center of the substrate) and slightly different chiplet layout (no holding bar vs. holding bar) show the same patterned cavity geometry (no variability in the geometry systematic bias) and the same devices thickness (QIE undercut and upward etch is uniform across the sample and across the two chiplet layout variants).

Comparing now devices in quadrants where the e-beam exposure dose is varied, namely comparing Q1 and Q3 (both e-beam exposed with $265 \mu\text{C}/\text{cm}^2$) with Q2 and Q4 (both e-beam exposed with $275 \mu\text{C}/\text{cm}^2$): evaluating the accuracy of the transfer pattern into the Si_3N_4 hard mask (**250 °C QIE-based variant** fabrication process, step (5) detailed in Appendix, Table A.4), a systematic bias of $\sim 5 \text{ nm}$ for both $265 \mu\text{C}/\text{cm}^2$ and $275 \mu\text{C}/\text{cm}^2$ e-beam exposure doses, respectively, can be estimated from SEM inspection (results not shown here). No systematic difference in the design transfer pattern geometry bias can be quantified from SEM inspection at this fabrication process stage.

However, optical characterization of the finalized diamond devices shows a significant difference in the average cavity resonance per quadrant. Comparing respectively scaling factors 98% and 99% here presented, same chiplet layout, different e-beam exposure doses (no holding bar frame chiplet layout: Q1 with Q2, holding bar frame chiplet layout: Q3 with Q4), the same cavity designs show a difference in the average cavity resonance of $\sim 5 \text{ nm}$, with a standard distribution $\sim 1.02 \text{ nm}$ to 2.88 nm in both cases.

Thus, devices exposed with a higher e-beam exposure dose (Q2 and Q4, $275 \mu\text{C}/\text{cm}^2$) show on average a $\sim 5 \text{ nm}$ lower cavity resonance than the devices exposed with a lower

e-beam exposure dose (Q1 and Q3, $265 \mu\text{C}/\text{cm}^2$), all other QIE-based fabrication process equal. This proves a high sensitivity of the cavity resonance upon fabrication process parameters, indicating that an extremely high degree of control over the entire process parameters during the fabrication is necessary to ensure high accuracy over the target cavity resonance. Next, systematic geometry bias in the design transfer pattern, with values below $\sim 5 \text{ nm}$ is challenging to systematically quantify with SEM inspection, which, nevertheless, directly affects the cavity resonance.

On the other hand, on average no significant dependency of cavity quality factors can be identified across the entire diamond substrate (inset of Figure 5.4 (d)), indicating that there is no significant correlation between cavity quality factors and the scaling factor, nor device position on the diamond substrate (edge or center of the substrate). Thus, we attribute the variability in the determined cavity quality factors to local random fabrication imperfections in both transfer pattern and bottom surface roughness as a result of the QIE upward etch.

Devices statistics vs. nr. mirror unit cells M_w

In modern 1D nanophotonic cavities, typically the cavity is composed of three distinct regions, namely cavity defect region, mirror regions and mirror-waveguide regions. Most cavity designs foresee a mirror to cavity region transition that is smoothly introduced (by deforming the mirror region to create a defect [14] or by adiabatically changing the lattice constant [7, 10, 11]) in order to minimize scattering losses and increase quality factor. Next, in order to further decrease scattering losses, the mirror to waveguide transition is again introduced smoothly, by tapering the mirror region into fully dielectric region.

In order to enable directional coupling, such that overcoupling (or undercoupling) is achieved, the number of mirror unit cells is reduced (increased), thus a single-sided cavity is obtained as a result. This is the design approach taken in this work, where we sweep the number of in-coupling mirror unit cells ($M_w=1$ to 6), thereby changing the coupling to the cavity, while the number of mirror unit cells on the opposite side of the cavity is kept constant ($M_s=13$). Notably, in our case, the lattice constant of the mirror unit cells is the same for both strong mirror and weak mirror, both mirrors thus characterized by the same strength, whereas directional coupling is achieved by leaking input light through the less reflective input mirror. The design of the nanophotonic cavity is inspired from Ref. [12].

We sweep the number of mirror unit cells in the weak mirror region from $M_w=1$ to 6 and append the mirror region to waveguide region over 7 additional unit cells with hole radius linearly tapered down from optimal $r = 71 \text{ nm}$ to 25 nm (smallest size compatible with our fabrication process).

In the optical characterization at room temperature presented in this Section, when probing the devices in reflection, we typically experience a clear resonance dip in correspondence to the cavity resonance, with a decreasing contrast dip for an increase in mirror unit cells for $M_w=1$ to 6.

By varying M_w mirror unit cells, no significant shift in cavity resonance is observed (Figure 5.5 (a) and (b)), as well as no significant impact on the quality factor Q (Figure 5.5 (c) and (d)). Graphing the total distribution of cavity resonance in the sample, categorized by device scaling factor, a linear trend increase in the average resonant wavelength of the cavity per scaling increase $\Delta_{scaling} = 1\%$ in the device geometry parameters is observed,

while there is no clear correlation between cavity resonance on the number of mirror unit cells M_w .

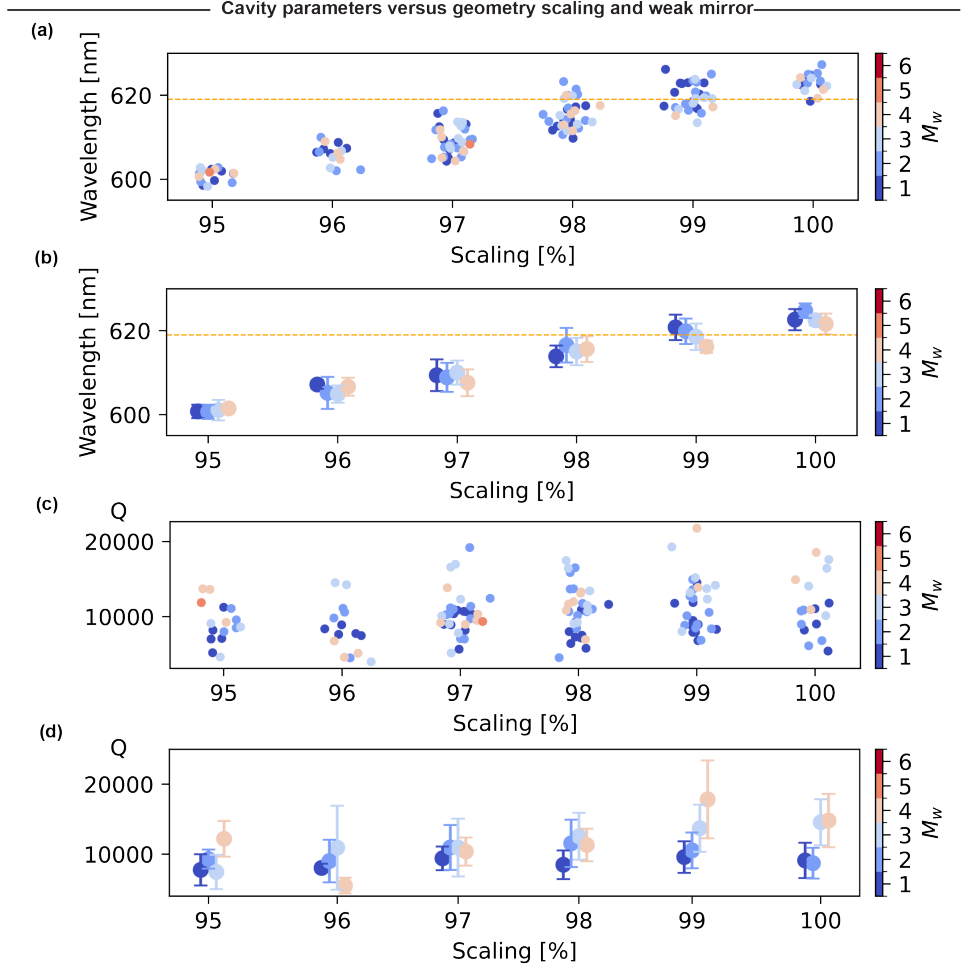


Figure 5.5: **Cavity devices statistics vs. M_w and scaling factor variation** | (a) Cavity resonant wavelength distribution dependency over variable scaling factor; dashed-orange line indicates 619 nm, close to SnV center ZPL emission, for which the devices with $M_w \leq 5$ a cavity resonance dip is measured; (b) Average cavity resonance per device scaling factor, per number of mirror unit cells M_w : average cavity resonance increases $\Delta\lambda_c \approx 4.5$ nm for a $\Delta_{scaling} = 1\%$ scaling increase in device geometry parameters, whereas no clear trend can be identified for increasing $M_w = 1$ to 5; | (c) Total distribution of cavity quality factors per device scaling factor; (d) Average cavity quality factor per device scaling factor, per number of mirror unit cells M_w : no obvious correlation between M_w and Q can be identified.

Graphing the total distribution of cavity quality factor across the sample, categorized by device scaling factor, no dependency between devices parameters and measured quality factors can be identified either. Thus, on average, by decreasing the number of mirror unit cells M_w so that both in-coupling and outcoupling is increased, no clear effect on the

cavity quality factor emerges. At the same time, the tapering from weak mirror M_w to the waveguide region over L unit cells, effectively adds additional ~ 3 mirror unit cells where the tapered radius is close to optimal r , thus we suspect that the fabricated devices to be in the undercoupled regime, although no further speculations on the coupling efficiency to the device can be made here.

Nevertheless, an increase of quality factor with increasing number of mirror unit cells M_w is expected. However, this is not captured in the global statistics of fabricated devices here presented, as the variability of quality factor of the measured devices (within the same scaling factor device distribution) is relatively high.

5.4 TOWARDS CAVITY-SnV CENTERS COUPLING

Once the cavity devices room-temperature characterization is completed, we proceed with SnV center spectroscopy characterization and experiments, performed at 5 K in a closed-cycle cryostat (methods and setup described in Section 5.6.4). Within the SnV center level structure, we focus on the optical ZPL transition between the lower branches of the ground and excited states, of wavelength around 619 nm. Spontaneous emission from the excited state can also occur with a phonon-assisted process, giving rise to a phonon sideband (PSB).

Here, the optical fiber tip-end is positioned in front of the device end-taper at a few micrometer distance, where the lensing effect of the optical fiber end-tip is leveraged in a lensed fiber configuration coupling mode. This method is chosen as it allows easy variation of the distance between fiber tip-end and device end-taper. Although this coupling method is less efficient than the adiabatic optical mode transfer with the fiber contact mode (extensively used in the room-temperature devices characterization), the lensed configuration is chosen to prevent any thermal contact between the fiber and the devices.

In the previous Section 5.3 we have shown that by varying a subset of cavity parameters in the design stage, i.e. varying the scaling factor (lattice constant a_n , circular hole radius r and beam width w_{wg}) we achieve nanocavities with resonant wavelength within the spectral region of interest, that is close to the SnV center emission. While this approach allowed us to obtain devices with resonant wavelength close to ~ 619 nm, around the SnV center ZPL emission, the precise matching of the cavity resonance with the exact SnV center emission line is quite challenging.

Even in the optimistic case of cavities with a resonant wavelength close to ~ 619 nm, the added challenge here relies in the typical inhomogeneous distribution of SnV center emission frequencies: typically, for SnV centers generated with conventional ion implantation and annealing methods, similar to presented in Chapter 3, the inhomogeneous distribution is relatively broad, with a FWHM C-transition of ~ 144 GHz [15]. This distribution in the SnV center frequency is due to surrounding local crystal strain environment, thus each of the activated SnV centers in the fabricated diamond nanostructures will experience a slightly different strain, resulting in a different transition frequency. Thus, the SnV center emission is precise, up to the frequency shift caused by local surrounding crystal strain.

Taking into account the above, the cavity resonance should be close to the typical coarse range ~ 619 nm of SnV center emission, with a margin of error at most equal to the inhomogeneous distribution FWHM. This imposes a stringent constraint on the precision of the cavity resonance spectral position, and although the probability to obtain nanocavities

with a resonance close to the target wavelength is not zero, the success is of probabilistic nature due to fabrication imperfections and non-predictable *a priori*.

Therefore, a dynamic in situ cavity resonance tuning is highly desirable. One relatively straightforward cavity resonance tuning method is gas tuning: deliberate introduction of a controlled amount of an inert gas into the cryostat chamber allows the gas to condense on the sample. The thin layer of solidified and deposited gas consequently changes the effective refractive index of the overall device [16], thus red-shifting device cavity resonances covered by the solidified gas. This dynamic in situ cavity frequency tuning has proven successful for group-IV color centers in diamond, e.g., SiV centers [17, 18], as well as SnV centers [9, 19], typically employing N₂ as tuning gas source. Next, by locally heating single device areas, for example, delivering intense localized laser light in the cavity region, controlled in situ reverse tuning can be achieved by sublimating the deposited N₂. The entire sample can be fully reversed tuned, thus restoring the initial post-fabrication cavity resonances by heating up the cryostat chamber.

Before proceeding with cavity resonance tuning, in order to assess the cavity resonance and evaluate the quality factor at low temperature, we typically probe single devices in two configurations (Setup schematically illustrated in Figure 5.8, Methods Section 5.6.4) with a white light supercontinuum source: devices are probed in reflection by in-coupling and collecting the reflected light from the lensed configuration optical fiber, or in transmission by sending the probing light free space through the optical microscope objective and collecting the cavity transmitted signal through the optical fiber.

We perform a non-exhaustive characterization of a subset of the same devices collection previously characterized at room temperature. The probed cavity devices (both in reflection and transmission) generally show cavity resonant wavelengths and quality factors in line with the determined values at room temperature. Occasionally, however, depending on the vacuum quality of the cryostat chamber, condensation of residual gas in the cryostat chamber introduces non reproducible cavity resonance red-shift.

Next, we probe the spectral properties of the activated SnV center within the fabricated nanostructures, by sending through the optical microscope objective free-space a green laser light source and / or a resonant tunable red laser light source in transmission configuration. In transmission configuration the in-coupling is free-space from top whereas collection of the signal through the lensed configuration fiber. Off-resonant photoluminescence (PL) spectroscopy, combined with off-resonant (detuned from the SnV center emission) cavity is performed (same setup as in Ref. [20] and Chapter 4). Typically, photoluminescence (PL, off-resonant excitation at 515 nm) spectra are acquired by illuminating the device from top, probing all SnV centers within the projected spot size on the cavity region of the device, and resolving the C and D transitions of the probed SnV centers ensemble. This allows us to determine target cavity resonance position for the coarse forward cavity resonance tuning, as well as fine reverse tuning, to match candidate SnV centers positioned within the device cavity region.

Next, off-resonant cavity (detuned from SnV center emission) photoluminescence excitation (PLE), in principle, should allow the optical transition stability of the identified SnV centers to be assessed. Preliminary pre-conditioned on charge-resonance (CR) check [21] heralding method (mitigating emitter ionization or spectral diffusion effects) PLE scans show a linewidth of ~337.9 MHz, higher than typical SnV center PLE scans in the (same)

bulk diamond device (~ 30 MHz, non CR-checked bulk diamond SnV center). Although this experiment in principle is possible, phonon-sideband (PSB) collection via lensed fiber configuration coupled to detuned from SnV center emission cavity results challenging.

CAVITY RESONANCE TUNING

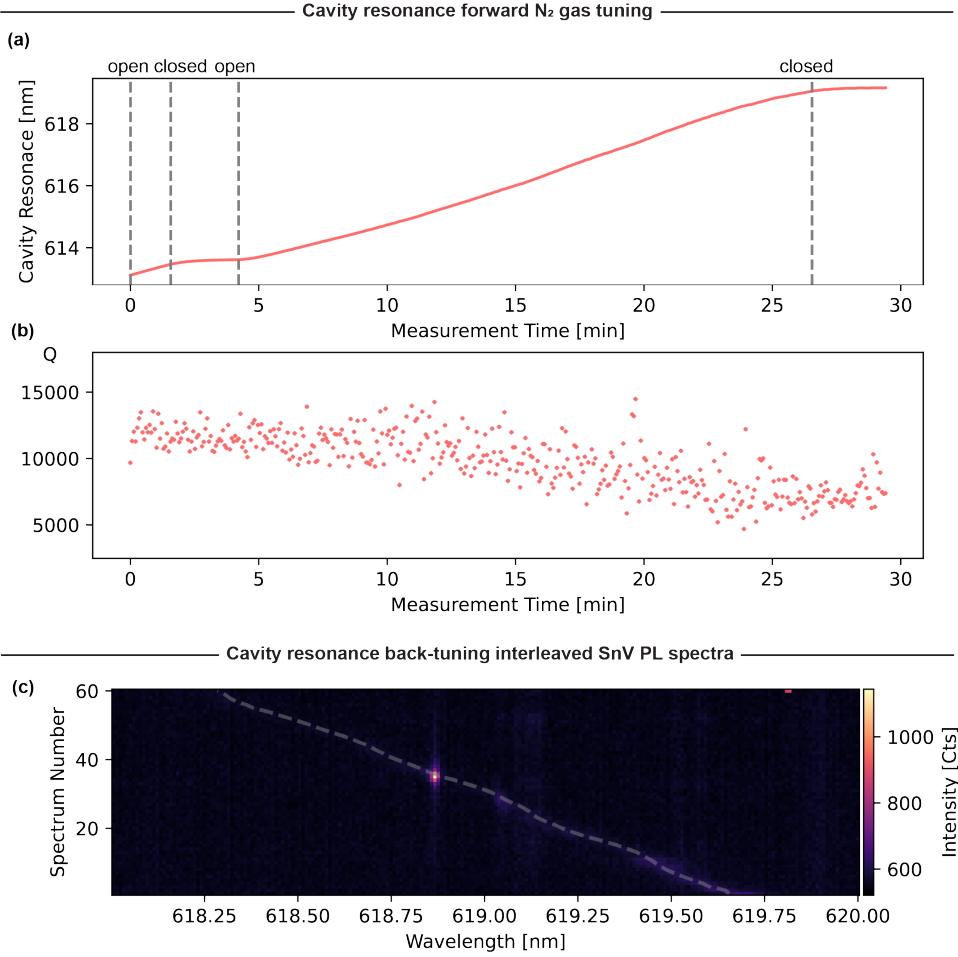


Figure 5.6: **Cavity devices resonance N_2 gas tuning** | (a) Forward coarse N_2 gas tuning cavity resonance; (b) Correlated to (a), fit quality factor; (c) Correlated reverse fine cavity resonance tuning with SnV center photoluminescence sequential spectra.

The non-exhaustive device characterization at cryogenic temperatures shows that the cavity resonance does not significantly shift when lowering the sample temperature from room temperature to 9K.

In order to tune the cavity frequency, before releasing the inert gas in the vacuum chamber, we first probe the cavity resonance, to evaluate the resonant wavelength and

quality factor and compare with the characterized values at room temperature. For the specific example shown in Figure 5.6 (a), at room temperature we determine a cavity resonance $\lambda_c \approx 609$ nm and $Q \approx 10852 \pm 1270$, while at cryogenic temperatures we measure $\lambda_c \approx 612$ nm and $Q \approx 11700 \pm 642$. We attribute the observed cavity resonance red-shift to residual chamber gas condensed on the sample substrate. Generally, this cavity resonance red-shift depends on the vacuum of the cryostat chamber, where, in highest quality vacuum quality, we observe no cavity resonance red-shift when decreasing the sample temperature from room temperature to 9K. Thus, room-temperature characterization provides us with a look-up table overview of blue-detuned cavity resonance devices compatible with the dynamic in situ gas tuning method. Specifically, all fabricated nanophotonic cavities with a scaling factor comprised between 95% and 98% post-fabrication resulted with a cavity resonance blue-detuned with respect to the SnV center ZPL emission, thus compatible with the gas tuning method.

In the following, we employ a gas source N_2 that we controllably release in the vacuum cryostat chamber through a gas inlet (regulating the inlet valve) and we monitor the cavity resonance dynamics by probing the device in transmission (probing the device with supercontinuum white light free space from top), collecting the signal through the lensed configuration mode tapered optical fiber. The collected signal is routed to and analyzed with the spectrometer. We then fit the cavity peak, determining the cavity resonance spectral position and quality factor throughout the entire cavity forward tuning process.

Typically, we coarsely forward tune the cavity resonance by opening the leak valve in discrete steps, controllably increasing the N_2 gas flow rate, while at the same time monitoring the cavity resonance red shift. We correlate the position setting of the valve (closed valve zero leak-rate, open valve typical leak-rate 10^{-8} mbar*L/s) with cavity resonance λ_c (Figure 5.6 (a)) and with the quality factor of the cavity (Figure 5.6 (b)). In the specific device example presented in Figure 5.6 (a) we coarse forward tune the cavity resonance from initial $\lambda_c = \lambda_{c,i} \approx 612$ nm to $\lambda_c \approx 619$ nm. When the coarse target wavelength is reached, we close the leak valve, stopping the N_2 gas delivery in the vacuum chamber. After the leak valve is fully closed, the N_2 gas in the chamber is fully deposited on the substrate surfaces within a few minutes of latency, further shifting the resonance of the cavity to $\lambda_{c,f} \approx 619.16$ nm. The quality factor measured after cavity resonance tuning (Figure 5.6) $Q_f \approx 9000$) is lower than the value measured after fabrication, indicating that the device geometry is indeed modified by the solidified deposited N_2 , deviating from the optimal fabricated cavity geometry parameters.

Fine-tuning of the cavity resonance with the identified SnV centers emission located within the suspended device, we reverse tune the cavity by locally heating the device with a green laser source (~ 2 μ W at device, 20 s exposure time per pulse).

In order to determine whether the nanophotonic cavity contains embedded SnV centers, prior to the cavity resonance tuning, a PL spectrum is acquired determining the potential SnV center candidates (positioned within the projection of the free-space excitation beam spot size on the cavity region of the device) emission lines. In the specific example shown in Figure 5.6, PL spectrum reveals an SnV center C transition at ~ 618.87 nm.

Once the cavity is coarsely forward tuned, we reverse fine-tune the cavity resonance to the identified SnV centers emission lines. The experiment consists of consecutive sequential PL measurement sequence interleaved with the white light supercontinuum laser source:

this enables simultaneous probing of SnV centers and cavity resonance shift. At the same time, the green excitation laser source at 515 nm serves as both SnV center off-resonant excitation and as laser heating source, aimed at sublimating the deposited N_2 , thus reverse tuning the cavity resonance.

The specific example presented in Figure 5.6 (c) shows an example of the interleaved sequential 60 PL spectra (underlying colored map) with cavity resonance white-light super-continuum laser source probing. The cavity resonance is reverse fine-tuned from 619.65 nm to 618.28 nm, where we precisely monitor the cavity resonance red-shift (overlying, in dashed-gray). When the cavity resonance reaches the previously determined SnV center emission line, an increase in emission intensity is observed at ~ 618.875 nm, indicating that the identified SnV center is presumably located in the cavity region. The increase in emission intensity points towards cavity-SnV center interaction and indicates that the identified SnV center is located within the cavity region of the photonic crystal cavity.

5.5 CONCLUSIONS

In this Chapter, we have shown SnV center embedded diamond cavity devices, fabricated with **250 °C QIE-based** fabrication process (development and methods described in Chapter 2). Specifically, by combining high magnification SEM and AFM topography analysis, we evaluated the effective device geometry. Next, we have optically characterized a subset of fabricated devices at room temperature, followed by cryogenic experiments at 9K in a closed cycle cryostat.

5.5.1 FABRICATED DEVICES AND GEOMETRY

Top-down (0° tilt angle view) high magnification SEM analysis allowed evaluation of the device parameters such as the lattice constant a_n , the circular hole radius r , and the device width w_{wg} . Quantifying these parameters from a device top-facet measurement, we identified a hole radius systematic geometry bias ~ 4 nm (higher than design) and a device width w_{wg} systematic geometry bias ~ 10 nm (lower than design) when compared to the optimal target design parameters, obtained from FEM simulations in COMSOL®, while no deviations from the design lattice constant a_n have been observed. At the same time, when comparing the parameters evaluated on the device top-facet with the same evaluated on device bottom facet, assuming a flat horizontal device bottom topography (plane parallel to top facet), the device sidewall angle is roughly estimated $\approx 3^\circ$.

Complementary AFM analysis of the bottom facet of the device enables evaluation of topography and surface roughness. AFM analysis of both device top-facet and bottom-facet confirms the sidewall angle $\sim 3^\circ$, previously estimated from the high magnification SEM analysis. Topography analysis on the device bottom facet on the device cavity region and waveguide region, respectively, shows that these are characterized by a triangular V-shaped topography with an angle 6° . The topography map of the device taper-end shows a rectangular cross section. The observed device geometry reflects the nature of aspect-ratio QIE undercut dependency, for which the complete upward etch flattening of narrow devices (i.e. design taper-end width of $w_t=50$ nm) takes place earlier in the etch process, when compared to wider devices (i.e., design cavity and waveguide region width of $w_l=275$ nm).

We suspect that the geometry difference between the simulated design and the fabricated devices affects both the cavity resonance and the quality factor of the former. Moreover, from AFM topographic maps we evaluated the root mean square roughness R_q over a linear extent equal to a_n for each of the analyzed device regions, showing values $R_q \sim 3$ nm on average. An increased bottom facet surface roughness is suspected to lower the quality factor of the fabricated devices as well.

Nevertheless, high magnification SEM top-down analysis, combined with quantitative AFM topography analysis, allows us to infer the post-fabrication devices geometry and bottom facet devices surface roughness, shedding light on typical device geometry characteristics achievable with **250 °C QIE-based** fabrication process variant.

On the other hand, within **250 °C QIE-based** fabrication process, control over device thickness precision less than ~ 10 nm remains an outstanding challenge.

5.5.2 CAVITY OPTICAL PERFORMANCE

The room temperature optical characterization of the nanophotonic crystal cavities fabricated with the **250 °C QIE-based variant** fabrication process (process parameters detailed in Table A.4) provides valuable insights into their performance while allowing us to examine how individual cavity resonance and quality factor correlate to fabrication parameter factors variability.

The quantitative analysis on optical device performance is performed on a subset of 146 devices with device scaling factors between 95% and 100% (out of 864 total fabricated devices in the range of scaling factors 95% and 100% on this diamond substrate), where devices are characterized by weak mirror unit cell $M_w = 1$ to 5 ($M_w = 6$ devices that are typically challenging to measure in reflection). Scaling factor devices comprised between 101% and 110% typically show a cavity resonance higher than the spectral region of interest, thus not optically characterized here. The sweep of the scaling factor allows us to obtain devices with cavity resonance between ~ 600 nm and 625 nm, characterized by quality factors ~ 10000 on average.

Analyzing the devices optical properties upon devices location on the diamond substrate, we find that devices in distant quadrants (edge of the diamond substrate and center of the substrate, respectively) and slightly different chiplet layout (no holding bar vs. holding bar) show the same patterned cavity geometry (no variability in the geometry systematic bias) and the same devices thickness (QIE undercut and upward etch is uniform across the sample and across the two chiplet layout variants).

We sweep as well the e-beam exposure dose ($265 \mu\text{C}/\text{cm}^2$ with respect to optimal $275 \mu\text{C}/\text{cm}^2$). We find on average that devices exposed with the optimal e-beam exposure dose ($275 \mu\text{C}/\text{cm}^2$) show on average a ~ 5 nm lower cavity resonance than devices exposed with a lower e-beam exposure dose ($265 \mu\text{C}/\text{cm}^2$), all other QIE-based fabrication process parameters equal. This proves the sensitivity of the cavity resonance upon fabrication process parameters, indicating that an extremely high degree of control over the entire process parameters during the fabrication is critical. On the other hand, no significant difference in the cavities quality factors across the entire diamond substrate is identified, indicating that there is no correlation between the cavity quality factors and the position of the devices on the sample. Thus, we attribute the variability in the determined cavity quality factors to fabrication imperfections.

Finally, from the analyzed subset of measured devices, no clear correlation emerges between the number of weak mirror unit cells M_w , cavity resonance and cavity quality factor.

5.5.3 TOWARDS CAVITY-SnV CENTERS COUPLING

Cryogenic optical cavity characterization shows no significant cavity performance difference with respect to room-temperature operation. Occasionally, non reproducible cavity resonance red-shift occurs when sample temperature is lowered from room temperature to 9K, while no significant difference in cavity quality factor is observed. The observed cavity resonance red-shift is attributed to residual cryostat chamber gas deposition on cavity devices.

Next, we showed a systematic accurate cavity resonance forward tuning employing a N_2 gas source, where the cavity resonance and quality factor are monitored by probing the device with a supercontinuum white light laser source.

Fine cavity resonance reverse tuning is achieved, simultaneously probing the cavity resonance by interleaving PL measurement and supercontinuum white light laser source device resonance monitoring. The employed 520 nm laser source in the PL spectroscopy of embedded SnV centers (identified before tuning) in the cavity region serves as a heating source, thereby sublimating the deposited N_2 gas and precisely reverse tune the cavity resonance. Finally, we observe an increase in emission intensity when cavity resonance intercepts the identified SnV center emission line at ~ 618.875 nm, indicating a potential SnV-cavity interaction. Further experiments, such as resonant excitation of SnV centers, are required to fully confirm and characterize the SnV-cavity interaction.

The presented results and methods prove systematic in situ cavity resonance tuning, whereas photoluminescence (PL) spectroscopy shows successful integration of SnV centers in free-hanging single-sided cavity devices.

5.6 METHODS

5.6.1 FABRICATION

The devices presented in this chapter are fabricated in two main phases, following the methods developed and presented in Chapter 3 and Chapter 2.

| Pre-anneal substrate preparation | | | | Sn implantation | | SnV activation | | |
|----------------------------------|-----------------------|-------------------------------------|---------|--|---------------|-----------------|-------------------|-----------------------------------|
| Step | Clean | Strain relief | Clean | | | Clean | Anneal | Clean |
| Parameter | HF 40% + (2x) Piranha | Ar/Cl ₂ , O ₂ | Piranha | Dose [ions/cm ²] | Implant angle | Tri-acid | Vacuum anneal | Piranha+ Di-acid |
| Value | 20 min + (2x) 20 min | 5 μ m + 6 μ m | 30 min | 3×10^{10} , 1×10^{11} | 7° | 4 hour @ 120 °C | 4 hours @ 1100 °C | 30 min @ 80 °C + 4 hours @ 190 °C |

Table 5.3: **Pre-nanofabrication SnV center integration fabrication main steps and parameters** | Left: **Pre-anneal substrate preparation**, methods described in Chapter 3, Section 3.4.1; | Center: **Sn implantation**, methods described in Section 3.4.2; Right: **SnV center activation** high temperature annealing performed with surface-protected method, described in Section 3.4.4.

SnV centers are generated by ion implantation and high temperature annealing, for

which the main parameters are summarized in Table 5.3. The sample fabrication process starts with pre-implantation surface treatment of a {001} surface oriented electronic grade diamond substrate (ElementSix) (methods presented in Section 3.4.1). The sample substrate is first cleaned in a wet HF 40% inorganic solution at room temperature for 20 minutes, followed by Piranha (ratio 3:1 of H_2SO_4 (95%) : H_2O_2 (31%)) inorganic solution for 20 min at 80 °C. Next, the superficial $\sim 5 \mu\text{m}$ etching via inductively-coupled-plasma reactive-ion-etching (ICP-RIE) Ar/Cl_2 plasma chemistry based recipe in order to remove the residual polishing induced strain from the surface of the substrate follows. An additional $\sim 6 \mu\text{m}$ ICP-RIE O_2 chemistry based plasma etch is performed to remove residual chlorine contamination from the previous etching step [10]. The sample is then inorganically cleaned in a Piranha solution (20 min at 80 °C) and implanted with ^{120}Sn ions (implantation dose 3×10^{10} and 1×10^{11} ions/ cm^2 with an implantation energy of 350 keV, 7° implantation angle). Prior to the activation of the SnV centers by vacuum annealing (1100 °C, surface-protected annealing method, described in Section 3.4.4), a tri-acid cleaning (ratio 1:1:1 of HClO_4 (70%) : HNO_3 (70%) : H_2SO_4 (> 99%), at 120 °C) is performed for 4 hours to remove any residual organic contamination, whereas post-annealing sample undergoes a 30 minutes Piranha cleaning at 80 °C and 4 hour di-acid cleaning (ratio 1:1 of HClO_4 (70%) : H_2SO_4 (> 99%), at 190 °C) to remove any superficial graphite thin film layer formed during the annealing step on the exposed edges of the substrate, as well as to oxygen terminate the graphite-free overall substrate surface. To evaluate the successful activation of the SnV centers, the sample is characterized (prior to the nanofabrication of the suspended structures) at 5 K in a closed-cycle cryostat to identify the activated SnV centers (using PL and PLE measurement sequences).

The nanofabrication of PCC structures follows the **250 °C QIE-based variant** fabrication process, based on the crystal-dependent quasi-isotropic-etch (QIE) undercut method developed in references [5–9] and [10]. A schematic of this process is shown in Figure 2.1, while detailed parameters of the process can be found in Appendix, Table A.4.

Specifically, we start with an extensive inorganic clean for 20 min in HF (40%) at room temperature (Figure 2.1, step 1), followed by double Piranha (ratio 3:1 of H_2SO_4 (95%) : H_2O_2 (31%)) inorganic solution for 20 min at 80 °C each.

Next, deposition and patterning of a thin film layer of hard mask material of $\sim 81 \text{ nm}$ Si_xN_y via inductively-coupled-plasma-chemical-vapour-deposition (ICPCVD) (Figure 2.1, step 2). The design of PCC structures is longitudinally aligned with the $\langle 110 \rangle$ diamond crystallographic orientation and exposed via e-beam lithography of $\sim 220 \text{ nm}$ of AR-P-6200.09 positive tone resist (Figure 2.1, steps 3). In order to avoid the charging effects of the diamond substrate during e-beam exposure, the surface of the e-beam resist is coated with $\sim 40 \text{ nm}$ Electra 92 (AR-PC 5090) conductive polymer. Next, this is developed by immersing the sample in a 60 s gentle stirring in H_2O and N_2 blow-dry (to dissolve Electra 92 and fully dry the residual H_2O), followed by resist development in 60 s pentyl acetate, 5 s ortho-xylene, 60 s isopropyl alcohol (IPA) (Figure 2.1, steps 4). The process proceeds with the transfer pattern into the Si_xN_y hard mask material by means of ICP-RIE etch in a CHF_3/O_2 based plasma chemistry (Figure 2.1, step 5): in this case we proceed with a 67% over-etch (higher than typical 30% over-etch tolerance) in order to ensure full clearing of Si_xN_y , as the exposure dose of $265 \mu\text{C}/\text{cm}^2$ and $275 \mu\text{C}/\text{cm}^2$ yields under-dosed resist in correspondence of smaller exposed circular holes. Next, complete removal of residual

e-beam resist in a two-fold wet step follows: we first proceed with a resist coarse removal in a PRS 3000 positive resist stripper solution, followed by fine removal of resist residues in extensive double Piranha inorganic clean (Figure 2.1, steps 6). Such considerable inorganic cleaning is employed in order to prevent micro-masking within next dry etch steps that can potentially be caused by organic residues on the sample.

The pattern from the Si_xN_y hard mask material is transferred in the diamond substrate by etching top-down in a dry ICP-RIE O_2 anisotropic etch for an extent of $\sim 2.5\times$ the designed thickness of the devices (Figure 2.1, step 7). It is crucial to note that the O_2 dry etch heavily affects the aspect ratio of the patterned Si_xN_y hard mask: we observe the etch rate of Si_xN_y to be higher at the edges of the patterned structures compared to the determined etch rate of Si_xN_y on flat area test samples, leading to enhanced erosion of the Si_xN_y at the edges of the nanostructures. This yields rounded vertical sidewalls with few nanometers of hard mask material at the diamond to Si_xN_y interface [10], as extensively detailed in Chapter 2. This leads to weak points across the top surface of the hard mask that can compromise the integrity of the hard mask in the downstream QIE-based process fabrication steps. We circumvent this challenge by carefully tuning the trade-off between sufficient anisotropic diamond etch and Si_xN_y mask integrity, such that the latter withstands the following ICP-RIE dry etch steps foreseen by the overall QIE-based fabrication process.

Next, conformal atomic layer deposition (ALD) of ~ 25 nm of AlO_x for hard mask coverage of devices vertical sidewalls (Figure 2.1, step 8) and the horizontal coverage of AlO_x is fully removed by ICP-RIE etch in a BCl_3/Cl_2 plasma chemistry etch (Figure 2.1, step 9). This opens access to the diamond substrate: we directly follow with sequential QIE undercut and upward etch steps, interleaved by SEM monitoring. For this, we employ the recipe developed in Section 2.7.1, Table 2.3 (Figure 2.1, steps 10). The full release and upward quasi-isotropic total etch time is considerably shorter (85 minutes) when compared to the 65°C QIE undercut recipe, demonstrated suitable for complete undercut of nanophotonic waveguides [20]. Finally, the hard mask materials are removed in extensive inorganic treatment for 20 min in HF (40%) at room temperature (Figure 2.1, step 11).

The overall qualitative characterization of the fabrication steps presented in this work has been executed on a scanning electron microscope Hitachi SEM Regulus system. The etch rates concerning the fabrication steps 6, 7 and 9 (Figure 2.1) have been pre-characterized on additional test samples, in parallel to the fabrication of the diamond sample employed in this work following same fabrication methods and parameters. Such etch tests have been conducted employing silicon substrate samples, with the thin films of interest deposited in parallel to the diamond substrate (methods and parameters detailed in Chapter 2, Section 2.7.3). Optical parameters and thickness of the employed materials have been determined via spectroscopic ellipsometry method on a Woollam M-2000 (XI-210) tool. The QIE rate has been characterized employing supplementary diamond test samples (fabrication parallel to the sample in this work, methods described in Section 2.8) and analyzed via SEM inspection. Cross-section of obtained diamond devices has been determined from a combination between high magnification SEM (Hitachi SEM Regulus) inspection and atomic force microscopy (Bruker FastScan AFM) topographic analysis.

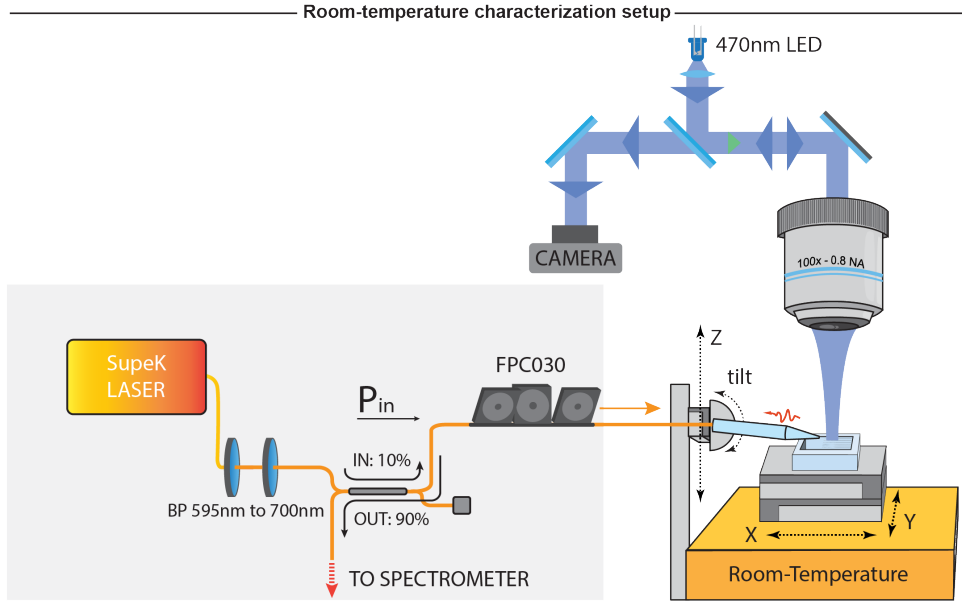


Figure 5.7: **Room temperature characterization setup:** See text for details.

5.6.2 ROOM-TEMPERATURE CHARACTERIZATION SETUP

A schematic of the room temperature single-sided cavity devices characterization setup is shown in Figure 5.7.

The diamond sample is mounted (via carbon tape) on the sample stage, positioned on top of the XY piezo positioner stack (Smaract MCS2-S), allowing sample position control in the XY direction. The tapered optical fiber is mounted on a variable angle (manually set) stage, mounted on a slip-stick Z piezo positioner (Smaract MCS2-S) which allows one to control the vertical position of fiber.

The sample is imaged by illuminating it with a LED at ~ 470 nm using a microscope objective (100X, numerical aperture (NA) 0.8), coupled to a digital camera (CS165CU/M, Thorlabs). This provides enough resolution to optically resolve both the optical fiber tip and the free-hanging cavity devices coupling tapered waveguide.

The input broad-band laser light source (SuperK Compact, NKT Photonics supercontinuum white light source) is delivered adiabatically via the contact coupled tapered optical fiber. This is filtered by cascading a Long Pass and a Short Pass filters, such that the input probing light is comprised between 595 nm and 700 nm, within the cavity resonance spectral region of interest. A 90:10 beam splitter is used to send 10% of the laser light to the input fiber, where we use a Fiber Polarization Controller (FPC030 by Thorlabs) to vary the polarization and match it to the device polarization (set by geometry). The light couples to the single-sided cavity device via the weak mirror region and is reflected back to the same fiber port. The reflected signal (90%) is then sent to the spectrometer detection (SpectraPro HRS-500).

5.6.3 MEASUREMENT SEQUENCES

PL and CR-checked PLE measurement sequences are the same as in Chapter 4 [20]. For cavity resonance monitoring during forward coarse resonance tuning, the PL sequence is interleaved with a broad-band laser light source (SuperK Compact, NKT Photonics supercontinuum white light source).

5.6.4 EXPERIMENTAL SETUP

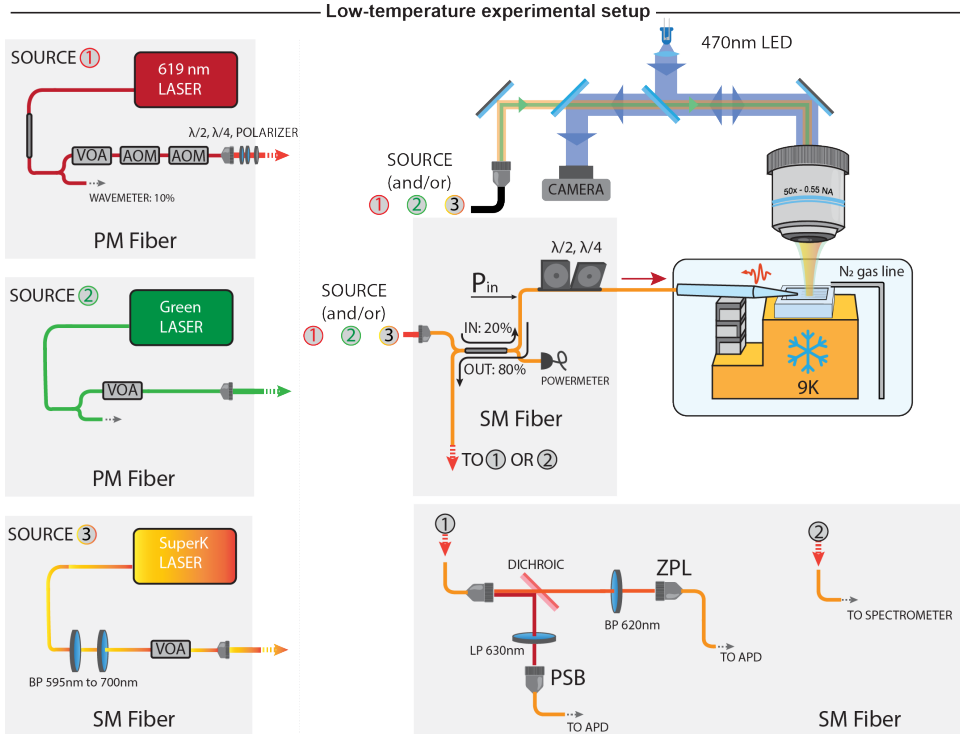


Figure 5.8: **Experimental setup** See text for details.

A schematic of the experimental setup is shown in Figure 5.8. The diamond sample, the XYZ piezo positioner stack (Attocube Systems ANPx51, ANPz51) which allows to control the position of the optical fibers and the N_2 gas tuning line are cooled to 9 K in a closed cycle cryostat (Montana Instruments s50).

The sample is illuminated with an LED at ~ 470 nm and imaged through an optical window in the cryostat using a long working distance objective (Mitutoyo 50X Plan Apochromat, NA: 0.55, WD: 13 mm). This provides enough resolution to optically resolve both the optical fiber tip and the suspended PCC devices.

The white light laser source is delivered via optical fiber, in a lensed fiber configuration into the one-sided photonic crystal cavities, by leaking the laser light through the weak coupling mirror. For off-resonant cavity devices, off-resonant light is reflected by the weak

mirror, inhibiting excitation via fiber. Thus, we probe the off-resonant cavity devices and SnV centers (PL and PLE) in a confocal setup configuration.

In a confocal setup configuration, the same microscope objective is used to deliver the repump laser pulses (Cobolt MLD-06 515 nm, serving as heating source for N_2 sublimation, hence reverse cavity resonance tuning), resonant excitation tunable laser light at 620 nm (Toptica DLCpro) and white light source supercontinuum laser light (SuperK Compact, NKT Photonics, for cavity characterization at 9 K).

A 80:20 beam splitter is used to send 20% of the laser light to the input fiber, where we use motorized polarization paddles to control the input polarization. The remaining 80% is used for calibration and monitoring. The reflected light passes through the beam splitter and is collected in the 80% return port.

The free space setup for filtering and detection of the light is connected to the reflection port, where a dichroic filter (Semrock FF625, short pass ~ 620 nm) separates the PSB and ZPL light. The PSB is further filtered by a Band Pass filter (620 ± 5 nm). In the PSB path, we further filter the excitation laser with two Long Pass tunable filters set approximately at 630 nm. The collected photons are fiber coupled and sent to an avalanche photodiode (APD) single photon detectors (Lasercomponents COUNT) (detection path 1) or to the spectrometer path (SpectraPro HRS-500) (detection path 2). The experiment is run using custom software based on the QMI [22] package.

The N_2 gas is delivered via a customized stainless steel tube (inner diameter 1.58 mm, Quantum Design), located in the immediate vicinity of the sample substrate. The gas tube shape is custom-shaped to allow optimal positioning inside the vacuum chamber and prevent thermal contact with the sample stage. The gas inlet is connected to a digitally controllable vacuum leak-valve (Nenion UHV-Leakvalve ND-3), allowing to operate at leak-rates as low as 10^{-9} mbar*L/s.

ACKNOWLEDGMENTS

We thank the entire SnV-team for fruitful discussions that supported the scientific development presented in this chapter, C.E. Smulders and L.G.C. Wienhoven for fabrication assistance and helpful discussions, T. Turan, D. Bedialauneta Rodríguez and L.G.C. Wienhoven for feedback on this manuscript.

We thank Z. Sadre Momtaz for assistance and helpful discussions, and the entire staff of the Kavli Nanolab Delft for assistance and support.

5.7 REFERENCES

1. Van Leent, T., Bock, M., Fertig, F., Garthoff, R., Eppelt, S., Zhou, Y., Malik, P., Seubert, M., Bauer, T., Rosenfeld, W., Zhang, W., Becher, C. & Weinfurter, H. Entangling single atoms over 33 km telecom fibre. *Nature* **607**, 69–73 (2022).
2. Stolk, A. J., van der Enden, K. L., Slater, M.-C., te Raa-Derckx, I., Botma, P., van Rantwijk, J., Biemond, J. B., Hagen, R. A., Herfst, R. W., Koek, W. D., *et al.* Metropolitan-scale heralded entanglement of solid-state qubits. *Science advances* **10**, eadp6442 (2024).
3. Knaut, C. M., Suleymanzade, A., Wei, Y.-C., Assumpcao, D. R., Stas, P.-J., Huan, Y. Q., Machielse, B., Knall, E. N., Sutula, M., Baranes, G., *et al.* Entanglement of nanophotonic quantum memory nodes in a telecom network. *Nature* **629**, 573–578 (2024).
4. Ruskuc, A., Wu, C.-J., Green, E., Hermans, S., Pajak, W., Choi, J. & Faraon, A. Multiplexed entanglement of multi-emitter quantum network nodes. *Nature*, 1–6 (2025).
5. Khanaliloo, B., Mitchell, M., Hryciw, A. C. & Barclay, P. E. High-Q/V Monolithic Diamond Microdisks Fabricated with Quasi-isotropic Etching. *Nano Letters* **15**, 5131–5136 (2015).
6. Mitchell, M., Lake, D. P. & Barclay, P. E. Realizing $Q > 300\,000$ in diamond microdisks for optomechanics via etch optimization. *APL Photonics* **4**, 016101 (2019).
7. Mouradian, S., Wan, N. H., Schröder, T. & Englund, D. Rectangular Photonic Crystal Nanobeam Cavities in Bulk Diamond. *Applied Physics Letters* **111**, 021103 (2017).
8. Wan, N. H., Lu, T.-J., Chen, K. C., Walsh, M. P., Trusheim, M. E., De Santis, L., Bersin, E. A., Harris, I. B., Mouradian, S. L., Christen, I. R., Bielejec, E. S. & Englund, D. Large-Scale Integration of Artificial Atoms in Hybrid Photonic Circuits. *Nature* **583**, 226–231 (2020).
9. Rugar, A. E., Aghaeimeibodi, S., Riedel, D., Dory, C., Lu, H., McQuade, P. J., Shen, Z.-X., Melosh, N. A. & Vučković, J. Quantum Photonic Interface for Tin-Vacancy Centers in Diamond. *Physical Review X* **11**, 031021 (2021).
10. Ruf, M. *Cavity-enhanced quantum network nodes in diamond* PhD thesis (Delft University of Technology, 2021).
11. Chan, J. *Laser cooling of an optomechanical crystal resonator to its quantum ground state of motion* (California Institute of Technology, 2012).
12. Nguyen, C., Sukachev, D., Bhaskar, M., Machielse, B., Levonian, D., Knall, E., Stroganov, P., Chia, C., Burek, M., Riedinger, R., *et al.* An integrated nanophotonic quantum register based on silicon-vacancy spins in diamond. *Physical Review B* **100**, 165428 (2019).
13. Burek, M. J., Meuwly, C., Evans, R. E., Bhaskar, M. K., Sipahigil, A., Meesala, S., Machielse, B., Sukachev, D. D., Nguyen, C. T., Pacheco, J. L., *et al.* Fiber-coupled diamond quantum nanophotonic interface. *Phys. Rev. Appl.* **8**, 024026 (2017).
14. Chia, C. *Quantum Optomechanics with Color Centers in Diamond* PhD thesis (Harvard University, 2021).

15. Pasini, M. *Nanophotonics with Diamond Color Centers: Quantum Optics and Entanglement Protocols* PhD thesis (Delft University of Technology, 2024).
16. Zeng, B., De-Eknamkul, C., Assumpcao, D., Renaud, D., Wang, Z., Riedel, D., Ha, J., Robens, C., Levonian, D., Lukin, M., *et al.* Cryogenic packaging of nanophotonic devices with a low coupling loss < 1 dB. *Applied physics letters* **123** (2023).
17. Sipahigil, A., Evans, R. E., Sukachev, D. D., Burek, M. J., Borregaard, J., Bhaskar, M. K., Nguyen, C. T., Pacheco, J. L., Atikian, H. A., Meuwly, C., *et al.* An integrated diamond nanophotonics platform for quantum-optical networks. *Science* **354**, 847–850 (2016).
18. Evans, R. E., Bhaskar, M. K., Sukachev, D. D., Nguyen, C. T., Sipahigil, A., Burek, M. J., Machielse, B., Zhang, G. H., Zibrov, A. S., Bielejec, E., *et al.* Photon-mediated interactions between quantum emitters in a diamond nanocavity. *Science* **362**, 662–665 (2018).
19. Kuruma, K., Pingault, B., Chia, C., Renaud, D., Hoffmann, P., Iwamoto, S., Ronning, C. & Lončar, M. Coupling of a single tin-vacancy center to a photonic crystal cavity in diamond. *Applied Physics Letters* **118** (2021).
20. Pasini, M., Codreanu, N., Turan, T., Riera Moral, A., Primavera, C. F., De Santis, L., Beukers, H. K., Brevoord, J. M., Waas, C., Borregaard, J., *et al.* Nonlinear quantum photonics with a tin-vacancy center coupled to a one-dimensional diamond waveguide. *Phys. Rev. Lett.* **133**, 023603 (2024).
21. Brevoord, J. M., De Santis, L., Yamamoto, T., Pasini, M., Codreanu, N., Turan, T., Beukers, H. K., Waas, C. & Hanson, R. Heralded initialization of charge state and optical-transition frequency of diamond tin-vacancy centers. *Phys. Rev. Appl.* **21**, 054047 (2024).
22. Raa, I. T., Ervasti, H. K., Botma, P. J., Visser, L. C., Budhrani, R., van Rantwijk, J. F., Cadot, S. P., Vermeltfoort, J., Pompili, M., Stolk, A. J., Weaver, M. J., van der Enden, K. L., de Leeuw Duarte, D., Teng, M., van Zwieten, J. & Grooteman, F. *QMI - Quantum Measurement Infrastructure, a Python 3 Framework for Controlling Laboratory Equipment* 4TU.ResearchData. 2023.

6

CONCLUSIONS AND OUTLOOK

In this thesis, we reported the experimental results on generation of tin-vacancy (SnV) centers in diamond and further nanophotonic integration in diamond nanophotonic waveguides and photonic crystal cavities. The efforts presented are directed towards realization of SnV center based spin-photon interface for remote entanglement experiments, ultimately as a building block for next-generation quantum networks. Here, we summarize the results and elaborate on open challenges in the systematic generation of SnV centers and the integration in nanophotonic devices. We further elaborate on current challenges and opportunities associated with nanofabrication of such devices and discuss opportunities of integration with conventional nanophotonic platforms.

6.1 SUMMARY

This thesis extensively discussed the generation and nanophotonic integration of SnV centers in diamond as a building block end-node for next-generation quantum networks. The main results can be summarized as follows.

- **Chapter 2** presented the quasi-isotropic-etch (QIE) based nanofabrication process along with its requirements to ensure stable and reproducible outcomes. We then introduced the nanofabrication methods we developed to reliably control the critical process parameters. This was followed by a detailed presentation of the process parameters, nanophotonic device designs, and the performance of the two QIE-based process variants we developed, optimized and implemented throughout this work. Finally, we demonstrated the successful fabrication of all-diamond photonic crystal cavity devices operating in the telecom regime and photonic crystal cavities operating at the SnV center emission wavelength.
- **Chapter 3** presented a brief overview of the state-of-the-art generation and activation of color centers in diamond. We then investigated the challenges associated with the activation of implanted SnV centers upon high temperature vacuum annealing, identifying graphitization of the diamond surface exposed to vacuum annealing chamber conditions as a significant factor in modifying the nanofabricated diamond devices geometry, leading to the complete destruction of cavity resonance. To address the graphitization phenomenon at diamond interfaces challenge, we proposed and discussed in detail an alternative surface-protected high-temperature annealing method. A thorough analysis of the method performance, along with graphitization phenomenon occurring in deliberately exposed diamond surface regions to the vacuum chamber environment, was subsequently carried out via complementary inspection techniques. The analysis confirmed the effectiveness of the proposed method in fully preventing the graphitization phenomenon at the surface-protected diamond interface. This advancement enabled successful activation of implanted Sn ions and generation of SnV centers without modifying the diamond surface and preventing undesirable SnV centers depth modification in a systematic and reliable way.
- **Chapter 4** presented successful integration of SnV centers in nanophotonic waveguides. We then investigated further the interaction between a single SnV center in a fabricated waveguide and a coherent input field. We measured the effect of this interaction on the photon statistics of the transmitted and reflected fields. In the latter, we observed tunable interference between coherently scattered single photons and classical reflections of the driving field, which result in different photon statistics for different interference conditions. We measured an emitter-waveguide coupling factor in agreement with numerical simulations, taking into account the emitter depth resulting from implantation, the lateral offset from the waveguide center and the optical properties of the SnV center zero-phonon line. These results highlight SnV centers integrated in diamond waveguides as a promising platform for the realization of efficient spin-photon interfaces, with significantly reduced fabrication overhead.

- **Chapter 5** presented the results of fabricated SnV-embedded photonic crystal cavity devices. The SnV centers have been fabricated employing the surface-protected high temperature vacuum annealing (development and methods in Chapter 3), whereas the fabrication of photonic crystal cavities employed the 250 °C QIE-based variant fabrication process (development and methods presented in Chapter 2). Here we have analyzed and presented the geometry of typical fabricated SnV-embedded nanophotonic devices, empirically determining the cross-section of the latter via SEM and AFM measurements, along with typical bottom facet surface roughness. We then optically characterized a subset of fabricated devices in a reflection measurement setup at room temperature, determining parameters such as cavity resonance and quality factor. We presented the room temperature characterized device statistics. Finally, we have presented our cavity resonance tuning method at cryogenic temperatures shown successful cavity resonance tuning. These experiments open the path towards further SnV-cavity interaction experiments.

The methods and results presented in this thesis enable further development of SnV center based spin-photon interfaces toward the next generation of quantum network nodes.

In the following sections, we discuss possible improvements and challenges on the path towards successful realization of next generation spin-photon interfaces based on SnV centers in diamond for large scale entanglement-based quantum networks.

6.2 SnV CENTERS AS SPIN-PHOTON INTERFACES

As presented in the Introduction (Section 1.2), SnV centers in diamond offer promising features to realize a scalable and efficient spin-photon interface. The features rendering SnV centers appealing can be mainly articulated from two different converging directions: optical and spin properties and insensitivity to electric field fluctuations. In the following, we briefly discuss the advantages, open challenges, and future prospects.

6.2.1 OPTICAL AND SPIN PROPERTIES

The generation and activation of narrow, close to transform-limited linewidth and stable optical emission SnV centers in diamond represents the first and most important requirement for an optical interface. As discussed in Introduction, a major advantage of the SnV center over other color centers in diamond counterparts is represented by the intrinsic optical properties, i.e. overall efficiency of the optical transition: a high Debye-Waller factor ($\beta_0 = 0.57$) [1] and quantum efficiency ($\eta \approx 0.8$) [2] render the SnV center an overall emission rate into the zero-phonon line of ≈ 0.45 , significantly higher than, e.g. ≈ 0.07 and ≈ 0.24 of SiV and GeV centers, respectively [3]. Taking into account the branching ratio of the SnV center C transition $\alpha \approx 0.8$ [4], this yields a total optical efficiency of the ZPL C transition of $\eta \cdot \beta_0 \cdot \alpha \approx 0.36$. Such high optical efficiency could potentially enable higher spin-photon entanglement generation rates, regardless of the electromagnetic environment surrounding the color center (i.e. the devices the SnV centers are integrated in). At the same time, this higher figure of merit (when compared to other group-IV) significantly relaxes the nanofabrication requirements (in the context of nanophotonic integration), as will be elaborated in Section 6.2.2.

The second substantial advantage of the SnV center is the higher strain-free ground state splitting (measured $\Delta_{GS} \approx 850$ GHz [1]), when compared to e.g. the SiV center (measured $\Delta_{GS} \approx 50$ GHz): The ground state splitting determines the phonon-limited coherence. As described in Section 1.2, for the SnV center, the measured ground state splitting enables operation temperatures in the millisecond range at $T=1.7$ K, higher than other group-IV color centers. This advantage significantly reduces the experimental overhead, characteristic of dilution refrigerators operating in the millikelvin regime required for other group-IV color centers.

6.2.2 NANOPHOTONIC INTEGRATION

First and foremost, the property rendering in general all group-IV color centers extremely appealing candidates as quantum network nodes resides in the insensitivity to electric field fluctuations to the first order. The insensitivity to electric fields fluctuations enables spatial positioning of this type of color centers in the close vicinity to interfaces without compromising the optical stability when integrated in nanophotonic structures. Successful integration of SnV centers in nanophotonic structures has been demonstrated in, e.g., nanopillars [5], nanophotonic one-dimensional waveguides [6–8], one-dimensional photonic crystal cavities [4, 9] and nano-electromechanically actuated devices [9–11].

For the objective of realizing an efficient optical interface, nanophotonic integration offers superior advantages when compared to alternative bulk-like diamond platforms. Advantages associated with nanophotonic integration impact potentially both spin-photon entanglement generation rates (potentially increasing as a result of e.g. improved the spin-photon interface efficiency), and spin-spin entanglement rates (potentially increasing as a result of e.g. improved frequency matching and low-loss routing photonic channels).

Here we briefly discuss the high-end advantages and benefits of nanophotonic integration of color centers in diamond: first, we present the main optical properties advantages of SnV-embedded nanophotonic devices, proceeding with additional capabilities deriving from this approach.

SnV centers in nanophotonic waveguides

Concerning improving the efficiency of the optical interface, in Chapter 4 we have presented the successful integration of SnV centers in nanophotonic waveguides, where a high emitter-to-waveguide coupling has been measured. In such circumstances, the emission into a well-defined mode, combined with optimized off-device photon routing, drastically improves the collection efficiency of the emitted photons. The nanophotonic waveguide taper design, combined with a tapered optical fiber (in lensed mode coupling configuration), drastically improves the collection efficiency of the emitted photons, while at the same time preventing thermal contact between the device and the surrounding environment. The advantage of embedding SnV centers in one-dimensional broadband photonic waveguides resides in the reduced nanofabrication overhead, with device performance characterized by higher tolerances and robustness towards fabrication imperfections. At the same time, two-port devices combined with optical tapered-fiber coupling enable exploration of the emitter-photon interaction, probing the emitter in both transmission and reflection. In addition, the coupling efficiencies at the device taper to the optical tapered-fiber interface, by means of adiabatic evanescent field transfer, have been reported to be as high as up to ~ 90 %

[12, 13], demonstrating highly improved collection efficiencies. Thus, the combination of nanophotonic integration into broad-band devices with efficient off-device photon routing via optical tapered-fiber adiabatic mode transfer will circumvent the challenge of poor collection efficiency, typical of diamond bulk-like devices (e.g. solid-immersion lenses).

SnV centers in photonic crystal cavities

Other advantages of nanophotonic integration include the potential of zero-phonon line emission enhancement: By structuring the electromagnetic environment around the emitter, the light-matter interaction can be dramatically increased. Particularly interesting is the case of nanophotonic crystal cavities, typically characterized by small mode volume ($V \sim (\lambda/n)^3$). High quality factors are desirable in order to enter the high cooperativity regime. In turn, this allows for the realization of efficient single-photon sources [14], demonstrating the potential of such platforms for entanglement-based quantum networks [15], as demonstrated for SiV centers.

In Chapter 5 we demonstrate the successful fabrication of one-dimensional high-quality factor photonic crystal cavity devices (in which SnV centers have been embedded and activated) employing a QIE-based fabrication process. The superior optical properties of the SnV center allow room for higher tolerances over the fabrication imperfections (higher scattering losses can, in principle, be tolerated). However, the lower emission wavelength at ~ 619 nm of the ZPL C transition emission line increases fabrication difficulty and reduces tolerance to imperfections of typical photonic crystal cavity designs. The design of such devices, when calibrated to the SnV center ZPL emission line, are characterized by dimensions much lower when compared with e.g. same designs operating at higher wavelength (e.g. of SiV centers). In turn, photonic crystal cavity designs refractive index modulation features size can be ~ 57 nm [4] (hole radius, hole based design), ~ 40 nm [16] (central vein structure, sawfish design). Such small typical feature size often results challenging to transfer pattern into the diamond substrate. Moreover, resonant cavity devices are extremely sensitive to fabrication imperfections, often requiring additional experimental methods for cavity resonance tuning to the SnV center emission line, for example gas tuning [4, 17], demonstrated in Chapter 5 of this work. The developed and established fabrication process (presented in Chapter 2) systematically and reproducibly yields devices with typical quality factors of $Q \sim 12000$. In principle, such high quality factors, combined with extremely low mode volume yield a cooperativity (simulated) $C \gg 1$ for all possible SnV center dipole orientations. These results provide a cornerstone for upcoming experiments for further investigation of SnV-embedded photonic crystal cavities as a high-efficiency quantum network end node.

SnV center dynamic in-situ frequency tuning

Last but of no less significance, nanophotonic integration provides the opportunity to realize dynamic in-situ frequency tuning [11]. This capability ultimately offers the potential of improving spin-spin entanglement rates.

In situ dynamic strain tuning can be engineered by design and fabrication of micro-electro-mechanically mediated strain control in photonic integrated waveguide devices. In such devices, frequency tuning can be achieved by applying a bias voltage between patterned electrodes that for a capacitive electromechanical actuator. In Ref. [11], we have demonstrated successful fabrication of cantilever-like suspended nanophotonic waveguides

in diamond, using the QIE-based fabrication process (developed and established in Chapter 2 of this thesis work). The fabricated devices show a tunability range >40 GHz, covering a significant range of typical inhomogeneous distribution of the SnV centers in the diamond substrate. In this work, we also demonstrated that the optical stability of the SnV center emission line is guaranteed and 12-fold improved by implementing a strain control feedback loop. The nanophotonic integration of SnV centers in micro-electro-mechanically actuated waveguide strain controlled devices, combined with the stabilized emission frequency control, sets a solid groundwork for future next-generation frequency control nanophotonic integrated devices, which will guarantee overlap between spectrally separate on-chip and spatially remote SnV centers.

Large-scale hybrid integration of SnV center based qubits

Nanophotonic integration also represents a foundational element in the advancement of large-scale heterogeneous hybrid integration with conventional photonic platforms. By combining the advantages of the color centers in diamond as quantum network end-nodes with the on-chip signal processing capabilities guaranteed by conventional photonic integrated circuits (PIC), hybrid integration opens the path towards high-throughput quantum information multiplexing, modularity, and routing. These alleviate current critical barriers to large-scale quantum information processing, such as on-chip quantum information processing, potentially enabled by the integration of multiple processing units [7]. Besides, hybrid integration circumvents the device yield challenge associated with all-diamond architectures, enabling integration of multiple diamond color center based qubits on the same chip [18], for example employing pick-and-place [7] or transfer printing [9] methods. This hybrid approach foresees integration of diamond quantum micro-chiplets (hosting color centers in diamond as spin-photon interfaces) with PIC platforms (constituted by both photonic circuitry for signal routing and electro-mechanical actuators for color center frequency shifting). Such integration will offer the advantage and compatibility of on-chip integration of qubit units (diamond micro-chiplets hosting the spin-photon interfaces) with components such as on-chip electro-optical modulators and superconducting nanowire single-photon (SNSPDs) detectors, required for on-chip photon switching and photon detection, respectively. This hybrid architecture offers the potential of on-chip photon quantum interference, heralded entanglement, frequency tuning and quantum frequency conversion, all constituting paramount capabilities towards the realization of scalable and robust large scale quantum networks [18].

6.2.3 CURRENT CHALLENGES

The same properties that render the SnV center a promising candidate as a quantum node, at the same time come with a specific set of challenges. Here, we elaborate on two interdependent open challenges of SnV centers on the path towards using them as quantum network end-nodes.

Photon indistinguishability

The SnV center insusceptibility to electric field fluctuations materializes in challenging emission frequency tuning. When efficient generation of spin-spin entanglement is considered, one of the fundamental requirements is the photon indistinguishability. Therefore,

considering the typical optical inhomogeneous distribution of SnV centers, the frequency mismatch in SnV centers emission represents a challenge to the indistinguishability requirement.

Dynamical frequency tuning strategies become an enabling tool in order to mitigate for SnV center emission frequency mismatch within higher inhomogeneous distribution. Second-order electric field tuning strategies have been demonstrated employing SnV centers [19–21]. However, the frequency tuning range is limited up to a few GHz range, relatively small when compared to typical inhomogeneous distribution.

One way to mitigate for the above challenge is to address the inhomogeneous distribution by employing an alternative SnV centers creation fabrication method. Ion implantation and subsequent high pressure high temperature annealing (HPHT) have demonstrated an inhomogeneous distribution of SnV centers emission frequencies among the narrowest, as low as ≈ 3 GHz [22]. Narrow inhomogeneous distribution has been achieved by efficiently healing the crystal damage (as a result of high energy ion implantation) employing HPHT annealing, combined with a high ion implantation depth. The latter suppresses the effect of strain and charged defects at the surface [22]. While this strategy yields low inhomogeneous distribution of SnV centers emission frequencies, compatible with e.g. frequency Stark tuning, at the same time it comes at the expense of low lattice strain. As discussed in Introduction, Section 1.2, lattice strain is beneficial and required to enable qubit spin control, thus, low lattice strain might not be advantageous. Additionally, potential diamond graphitization at the surface (extensively discussed in Chapter 3), micrometer range implantation depth [22] and potentially larger implantation straggle [21] are incompatible with nanophotonic integration (requirements are extensively discussed in Chapter 2).

As discussed previously in Section 6.2.2, dynamical frequency tuning strategy by means of strain tuning [9–11] efficiently controls the emission frequency, with demonstrated frequency range as high as >40 GHz for micro-electro-mechanically mediated strain control in photonic integrated waveguide devices [11]. This method covers a significant range of typical inhomogeneous distribution of SnV centers, offering a promising route toward efficient frequency mismatch minimization.

Other frequency tuning strategies are, e.g., quantum frequency conversion (successfully demonstrated for NV centers [23, 24], as well as group IV color centers, e.g., SiV [15]) and shifting the emitted photon frequency by electro-optic modulators [25].

Spin control

Spin control is an essential capability for quantum networks end-node addressability and manipulation of the quantum states. As already stated in Introduction, experimental demonstrations of the SnV center spin control have been shown via all-optical control [26] and via coherent microwave (MW) driving (SnV centers integrated in diamond nanopillars [27], strained diamond membrane [28, 29]) and nuclear spin control (SnV centers in bulk diamond [30]). Specifically, MW driving is a versatile and scalable mechanism for spin control, enabling different decoherence-protected control methods such as dynamically decoupled (DD) and dynamically decoupled radio frequency (DDRF) control [30]. Such methods are paramount for the preservation and extension of both electron spin and nuclear spin coherence, with the goal of establishing coherent quantum gates.

A potential limiting factor in the SnV center MW spin control is the drive-induced heating effects. Conventional materials for the nanofabrication of the MW driving lines, e.g. gold (Au), have proven inadequate for MW driving of electron spin. In fact, applied MW pulses cause excessive heating of the diamond substrate, which in turn decohere the SnV centers [31]. One way to address this challenge is to thermally decouple the MW driving circuitry from the diamond substrate hosting the color centers. A relatively straightforward way is to employ a MW suspended driving bondwire line, in the top side vicinity of diamond substrate [27, 30], avoiding spatial contact between the two. However, spatial alignment of the MW bondwire may result technically challenging, with accuracy limited by the optical microscope inspection tool. Other methods of thermal isolation may be enabled, for example, by hybrid integration.

A parallel route to thermal load management may lead the field to research alternative candidate materials for the MW line delivery fabrication. Superconducting materials have the potential to significantly prevent and mitigate the drive-induced heating directly on-chip, as demonstrated in Ref. [29]. Besides, direct on-chip MW circuitry patterning offers the advantage of high accuracy spatial alignment. This approach advances the efforts and goals of nanophotonic integration, resulting in a straightforward implementation of common superconducting material fabrication methods.

Finally, MW driving susceptibility and operation temperature [32] are enhanced by the high crystal strain environment surrounding the SnV centers. Strain can be induced statically [29, 32] by leveraging thermal expansion coefficient contrast between the diamond and the underlying substrate material, or dynamically employing micro- or nano-electro-mechanical systems (MEMS or NEMS) [9–11]. While the latter method is intrinsically compatible with nanophotonic integration, the former strain-inducing method requires elaborate engineering of nanophotonic devices to prevent strain relaxation in the fabricated devices.

6

6.3 FUTURE PROSPECTS

The exciting challenge lies in combining all the individual features of the SnV center into a single unit that ideally harnesses its full range of advantages. At the same time, it is essential to design, engineer, and fabricate a device that effectively mitigates its weaknesses. The goal is to create an optimized spin-photon interface that can reliably function and satisfy the requirements for a suitable a spin-photon interface in order to operate as a quantum end-node [18].

Future quantum networks require high-rate, long-distance entanglement distribution, where scalability of individual end-nodes is a fundamental requirement. From the point of view of individual end-node requirements, SnV centers in diamond are well-placed as suitable candidates in order to realize spin-photon interfaces, whereas nanophotonic integration addresses scalability and current challenges concurrently via tailored engineering solutions, in a resulting device design as best trade-off.

At the heart of this pathway lies diamond fabrication. This is a young and rapidly advancing field marked by a range of emerging nanoscale processing techniques. In this work, we have systematically studied, developed, and optimized methods for both the generation of SnV centers in diamond and their integration into nanophotonic structures. This work builds upon and extends the current state-of-the-art in diamond nanofabrication.

Generally, to date, the yield of SnV center integrated devices remains a significant challenge. From a fabrication standpoint, it can be primarily attributed to two key factors: the first major contributor is high-yield reliable fabrication of nanophotonic devices, while the second relates to the controlled optimal placement and generation of SnV centers.

In the following, we discuss the current approaches to addressing each of the above challenges, highlighting their respective advantages, limitations, and future prospects.

6.3.1 SnV CENTER GENERATION

As extensively discussed in Chapter 3, generation and activation of color centers in diamond represents the initial prerequisite for successful fabrication of SnV center based devices. In this work we have studied the ion implantation incorporation method, followed by high temperature annealing. This method offers the advantage of control over implantation depth, spatial accuracy, and nature of the implanted species. However, this comes at the cost of crystal damage and generation of implantation-related defects, which upon high temperature annealing treatment can be alleviated, to some extent. Further study of the effects of crystal damage healing, surface charge dynamics and termination on the SnV center optical properties would greatly benefit the field, with the goal of further improving the SnV center spectral stability and linewidth.

Specifically, throughout this work we have employed a substrate-wide uniform implantation process. This method is relatively straightforward, requiring minimal fabrication overhead in preparation for the Sn implantation process and subsequently high temperature annealing for SnV centers activation. However, this process is accompanied by a number of challenges that influence the properties of the resulting SnV centers.

First, ion implantation and high temperature low pressure annealing is typically characterized by high inhomogeneous broadening. Recently, narrow inhomogeneous broadening (comparable to values obtained by HPHT annealing [22]) has been demonstrated by ion implantation along the diamond crystal channel [21]. The resulting narrow inhomogeneous broadening has been attributed to potentially low density of implantation-related defects and crystal damage. Although this efficiently mitigates the spectral SnV centers frequency mismatch challenge, it comes at the cost of a low-strain crystal environment and may thus require alternative strategies for strain engineering. While a recent simulation study on the linewidth broadening and the effects of charge traps in the vicinity of the SnV center has been presented [33], a detailed experimental study on the effect of the implantation crystal damage and created defects is required, with a primary focus on achieving an optimal balance between optical stability, narrow inhomogeneous distribution, and sufficiently high static strain.

Second, the inherent stochastic nature of the implantation process, combined with the moderate Sn-to-SnV conversion yield [2, 34], significantly reduces the likelihood of finding an SnV center that will be optimally coupled to the subsequently fabricated nanophotonic devices. As demonstrated in Chapter 4 this does not pose a significant challenge for optimal coupling of SnV center to broadband devices such as nanophotonic waveguides. Nevertheless, it becomes less suitable when considering SnV center integration in resonant devices such as photonic crystal cavities, requiring device frequency tuning (as demonstrated in Chapter 5). Additionally, high-precision spatial positioning becomes a critical requirement in order to ensure maximum emitter-cavity coupling. Methods such

as focused ion beam (FIB) implantation [35] and masked implantation [36] have been successfully used for the generation of color centers in diamond. Such methods would enable high accuracy three-dimensional placement of Sn ions, which upon successful Sn-to-SnV activation, would maximize emitter-cavity coupling. Yet, the current moderate Sn-to-SnV conversion yield remains a challenge for which heralded SnV center generation approaching near-unit yield is strongly desirable.

6.3.2 NANO-DEVICES FABRICATION

The diamond quasi-isotropic etch (QIE)-based fabrication process offers the advantage of large-scale fabrication of nanophotonic devices: The method supports the fabrication of a large number of devices per substrate, with throughput primarily constrained by the substrate size, currently reaching dimensions on the order of few millimeters. This high device throughput per sample partially overcomes the challenge of limited device yield. The developed methods (presented in Chapter 2) prioritize robustness, with scalability and fabrication fault tolerance as primary objectives. These criteria become especially critical in elaborate multi-step nanofabrication workflows such as QIE-based, where the process design must incorporate sufficient margins to tolerate variations and ensure reliable high yield outcomes.

When viewed within the broader landscape of photonic integration, an essential requirement for the eventual integration of diamond-based components into scalable quantum and classical photonic systems is interconnectivity. Therefore, the ability of arbitrary diamond device designs hosting the SnV center based qubit, combined with ultra-low surface roughness, become necessary requirements to ensure implementation of low-loss on-chip experiment architecture.

Fabrication processes that structure diamond in bulk diamond, such as angled plasma etch [37] and QIE-based [38] have successfully enabled fabrication of one-dimensional nanophotonic devices [39, 40], two-dimensional microdisk resonator devices [41] and photonic crystal cavities [42]. Nevertheless, the device design and layout remain limited in both cases, mainly due to the limiting resulting device cross-section (in case of angled reactive ion etch method) and the crystallographic dependency of the reactive ion etch undercut (in case of QIE-based). For these fabrication methods, typically arbitrary design layouts remain an outstanding challenge, often requiring full process design parameters re-calibration and optimization. Considering QIE-based method, while the crystallographic dependent etch rate enables uniform undercut of devices aligned with crystallographic directions, at the same time this limits the device designs aligned with specific crystallographic directions. Thus, fabrication of device designs characterized by a radius of curvature, e.g. curved waveguides or directional couplers, to date, remains an outstanding challenge.

Emerging diamond fabrication processes, such as "smart-cut" [43], open the path to fabrication of arbitrary device design layout. In this case fabrication of micro- or nano-devices is intrinsically design and aspect-ratio independent, as this method offers the advantage of uniform cross section and high-accuracy tunable thickness across the entire diamond device layer. Moreover, this method offers the advantage of ultra-low surface roughness of the diamond device layer [43]. In fact, to date, the highest optical quality factor of one- and two-dimensional photonic crystal waveguides and cavities [44, 45] has been achieved using this platform.

Diamond membrane transfer and bonding has been successfully demonstrated on a variety of different substrates, including silicon, fused silica, sapphire, thermal oxide, and lithium niobate [32]. This feature comes with the immediate advantage of a different thermal expansion coefficient substrate: MW control of a SnV center spin in a strain-tuned diamond membrane heterostructure [28] has been successfully demonstrated. Beyond the above specific applications, the "smart-cut" method holds significant potential for enabling a broad range of functionalities that extend beyond nanophotonics with color centers in diamond, such as sensing, microfluidics, electronics, and biophysics, potentially demonstrating the unprecedented versatility of this platform.

Nevertheless, while diamond-on-insulator platform offers the potential of scalability and silicon foundry integration, to date this remains in its infancy, warranting continued exploration of alternative diamond fabrication methods.

6.4 EPILOGUE

Color centers in diamond are excellent candidates for long-distance entanglement distribution based quantum networks. Scalability of these systems will potentially be guaranteed by nanophotonic integration. While diamond nanofabrication has historically presented significant challenges, rapid advances in fabrication techniques are opening the path to new opportunities for reliable high-yield device integration. As the field matures, it is time to shift focus toward novel fabrication methods of color centers and multifunctional device designs that will support seamless conventional photonic platforms integration and high-performance operation in the quest to build next-generation high-rate quantum networks.

6.5 DATA AVAILABILITY

The underlying data of this thesis can be found in the repository hosted by 4TU.ResearchData (*Data underlying the doctoral dissertation "Diamond Nanophotonic Devices for Quantum Networks Experiments"*, doi: 10.4121/93d884f9-f862-4ade-8ed4-e32464471507).

6.6 REFERENCES

1. Görlitz, J., Herrmann, D., Thiering, G., Fuchs, P., Gandil, M., Iwasaki, T., Taniguchi, T., Kieschnick, M., Meijer, J., Hatano, M., Gali, A. & Becher, C. Spectroscopic Investigations of Negatively Charged Tin-Vacancy Centres in Diamond. *New Journal of Physics* **22**, 013048 (2020).
2. Iwasaki, T., Miyamoto, Y., Taniguchi, T., Siyushev, P., Metsch, M. H., Jelezko, F. & Hatano, M. Tin-Vacancy Quantum Emitters in Diamond. *Phys. Rev. Lett.* **119**, 253601 (2017).
3. Stramma, A. M. *The tin-vacancy centre in diamond: a coherent spin-photon interface for quantum network nodes* PhD thesis (2024).
4. Rugar, A. E., Aghaeimeibodi, S., Riedel, D., Dory, C., Lu, H., McQuade, P. J., Shen, Z.-X., Melosh, N. A. & Vučković, J. Quantum Photonic Interface for Tin-Vacancy Centers in Diamond. *Physical Review X* **11**, 031021 (2021).
5. Rugar, A. E., Dory, C., Sun, S. & Vučković, J. Characterization of optical and spin properties of single tin-vacancy centers in diamond nanopillars. *Physical Review B* **99**, 205417 (2019).
6. Rugar, A. E., Dory, C., Aghaeimeibodi, S., Lu, H., Sun, S., Mishra, S. D., Shen, Z.-X., Melosh, N. A. & Vučković, J. Narrow-Linewidth Tin-Vacancy Centers in a Diamond Waveguide. *ACS Photonics* **7**, 2356–2361 (2020).
7. Wan, N. H., Lu, T.-J., Chen, K. C., Walsh, M. P., Trusheim, M. E., De Santis, L., Bersin, E. A., Harris, I. B., Mouradian, S. L., Christen, I. R., Bielejec, E. S. & Englund, D. Large-Scale Integration of Artificial Atoms in Hybrid Photonic Circuits. *Nature* **583**, 226–231 (2020).
8. Pasini, M., Codreanu, N., Turan, T., Riera Moral, A., Primavera, C. F., De Santis, L., Beukers, H. K., Brevoord, J. M., Waas, C., Borregaard, J., *et al.* Nonlinear quantum photonics with a tin-vacancy center coupled to a one-dimensional diamond waveguide. *Phys. Rev. Lett.* **133**, 023603 (2024).
9. Li, L., Santis, L. D., Harris, I. B., Chen, K. C., Gao, Y., Christen, I., Choi, H., Trusheim, M., Song, Y., Errando-Herranz, C., *et al.* Heterogeneous integration of spin-photon interfaces with a CMOS platform. *Nature* **630**, 70–76 (2024).
10. Meesala, S., Sohn, Y.-I., Pingault, B., Shao, L., Atikian, H. A., Holzgrafe, J., Gündoğan, M., Stavarakas, C., Sipahigil, A., Chia, C., *et al.* Strain engineering of the silicon-vacancy center in diamond. *Physical Review B* **97**, 205444 (2018).
11. Brevoord, J. M., Wienhoven, L. G., Codreanu, N., Ishiguro, T., van Leeuwen, E., Iuliano, M., De Santis, L., Waas, C., Beukers, H. K., Turan, T., *et al.* Large-Range Tuning and Stabilization of the Optical Transition of Diamond Tin-Vacancy Centers by In-Situ Strain Control. *Appl. Phys. Lett.* **126** (2025).
12. Burek, M. J., Meuwly, C., Evans, R. E., Bhaskar, M. K., Sipahigil, A., Meesala, S., Machielse, B., Sukachev, D. D., Nguyen, C. T., Pacheco, J. L., Bielejec, E., Lukin, M. D. & Lončar, M. Fiber-Coupled Diamond Quantum Nanophotonic Interface. *Phys. Rev. Appl.* **8**, 024026 (2017).

13. Zeng, B., De-Eknamkul, C., Assumpcao, D., Renaud, D., Wang, Z., Riedel, D., Ha, J., Robens, C., Levonian, D., Lukin, M., *et al.* Cryogenic packaging of nanophotonic devices with a low coupling loss < 1 dB. *Applied physics letters* **123** (2023).
14. Knall, E. N., Knaut, C. M., Bekenstein, R., Assumpcao, D. R., Stroganov, P. L., Gong, W., Huan, Y. Q., Stas, P.-J., Machielse, B., Chalupnik, M., *et al.* Efficient source of shaped single photons based on an integrated diamond nanophotonic system. *Phys. Rev. Lett.* **129**, 053603 (2022).
15. Knaut, C. M., Suleymanzade, A., Wei, Y.-C., Assumpcao, D. R., Stas, P.-J., Huan, Y. Q., Machielse, B., Knall, E. N., Sutula, M., Baranes, G., *et al.* Entanglement of nanophotonic quantum memory nodes in a telecom network. *Nature* **629**, 573–578 (2024).
16. Pregnolato, T., Stucki, M. E., Bopp, J. M., Gokhale, A., Krüger, O., Schröder, T., *et al.* Fabrication of Sawfish photonic crystal cavities in bulk diamond. *APL Photonics* **9** (2024).
17. Kuruma, K., Pingault, B., Chia, C., Renaud, D., Hoffmann, P., Iwamoto, S., Ronning, C. & Lončar, M. Coupling of a Single Tin-Vacancy Center to a Photonic Crystal Cavity in Diamond. *Applied Physics Letters* **118**, 230601 (2021).
18. Ruf, M., Wan, N. H., Choi, H., Englund, D. & Hanson, R. Quantum Networks Based on Color Centers in Diamond. *Journal of Applied Physics* **130**, 070901 (2021).
19. De Santis, L., Trusheim, M., Chen, K. & Englund, D. Investigation of the Stark Effect on a Centrosymmetric Quantum Emitter in Diamond. *Phys. Rev. Lett.* **127**, 147402 (2021).
20. Aghaeimeibodi, S., Riedel, D., Rugar, A. E., Dory, C. & Vučković, J. Electrical Tuning of Tin-Vacancy Centers in Diamond. *Phys. Rev. Appl.* **15**, 064010 (2021).
21. Bushmakina, V., von Berg, O., Sauerzapf, C., Jayaram, S., Denisenko, A., Tarín, C., Anders, J., Vorobyov, V., Gerhardt, I., Liu, D., *et al.* Two-Photon Interference of Photons from Remote Tin-Vacancy Centers in Diamond. *arXiv preprint arXiv:2412.17539* (2024).
22. Narita, Y., Wang, P., Ikeda, K., Oba, K., Miyamoto, Y., Taniguchi, T., Onoda, S., Hatano, M. & Iwasaki, T. Multiple tin-vacancy centers in diamond with nearly identical photon frequency and linewidth. *Phys. Rev. Appl.* **19**, 024061 (2023).
23. Stolk, A., van der Enden, K. L., Roehsner, M.-C., Teepe, A., Faes, S. O., Bradley, C., Cadot, S., van Rantwijk, J., Te Raa, I., Hagen, R., *et al.* Telecom-band quantum interference of frequency-converted photons from remote detuned NV centers. *PRX Quantum* **3**, 020359 (2022).
24. Stolk, A. J., van der Enden, K. L., Slater, M.-C., te Raa-Derckx, I., Botma, P., van Rantwijk, J., Biemond, J. B., Hagen, R. A., Herfst, R. W., Koek, W. D., *et al.* Metropolitan-scale heralded entanglement of solid-state qubits. *Science advances* **10**, eadp6442 (2024).
25. Levonian, D., Riedinger, R., Machielse, B., Knall, E., Bhaskar, M., Knaut, C., Bekenstein, R., Park, H., Lončar, M. & Lukin, M. Optical entanglement of distinguishable quantum emitters. *Physical Review Letters* **128**, 213602 (2022).

26. Debroux, R., Michaels, C. P., Purser, C. M., Wan, N., Trusheim, M. E., Arjona Martínez, J., Parker, R. A., Stramma, A. M., Chen, K. C., De Santis, L., *et al.* Quantum control of the tin-vacancy spin qubit in diamond. *Physical Review X* **11**, 041041 (2021).
27. Rosenthal, E. I., Anderson, C. P., Kleidermacher, H. C., Stein, A. J., Lee, H., Grzesik, J., Scuri, G., Rugar, A. E., Riedel, D., Aghaeimeibodi, S., *et al.* Microwave spin control of a tin-vacancy qubit in diamond. *Physical Review X* **13**, 031022 (2023).
28. Guo, X., Stramma, A. M., Li, Z., Roth, W. G., Huang, B., Jin, Y., Parker, R. A., Arjona Martínez, J., Shofer, N., Michaels, C. P., *et al.* Microwave-based quantum control and coherence protection of tin-vacancy spin qubits in a strain-tuned diamond-membrane heterostructure. *Physical Review X* **13**, 041037 (2023).
29. Karapatzakis, I., Resch, J., Schrodin, M., Fuchs, P., Kieschnick, M., Heupel, J., Kussi, L., Sürgers, C., Popov, C., Meijer, J., *et al.* Microwave control of the tin-vacancy spin qubit in diamond with a superconducting waveguide. *Physical Review X* **14**, 031036 (2024).
30. Beukers, H. K., Waas, C., Pasini, M., Van Ommen, H. B., Ademi, Z., Iuliano, M., Codreanu, N., Brevoord, J. M., Turan, T., Taminiau, T. H., *et al.* Control of solid-state nuclear spin qubits using an electron spin-1/2. *Physical Review X* **15**, 021011 (2025).
31. Beukers, H. *Quantum Networks with Diamond Color Centers: Local Control and Multi-Node Entanglement* Dissertation (TU Delft) (Delft University of Technology, 2025). ISBN: 978-94-6384-794-0.
32. Guo, X., Xie, M., Addhya, A., Linder, A., Zvi, U., Wang, S., Yu, X., Deshmukh, T. D., Liu, Y., Hammock, I. N., *et al.* Direct-bonded diamond membranes for heterogeneous quantum and electronic technologies. *Nature communications* **15**, 8788 (2024).
33. Pieplow, G., Torun, C. G., Gurr, C., Munns, J. H., Herrmann, F. M., Thies, A., Pregnolato, T. & Schröder, T. Quantum electrometer for time-resolved material science at the atomic lattice scale. *Nature Communications* **16**, 6435 (2025).
34. Tchernij, S. D., Herzig, T., Forneris, J., Küpper, J., Pezzagna, S., Traina, P., Moreva, E., Degiovanni, I. P., Brida, G., Skukan, N., Genovese, M., Jakšić, M., Meijer, J. & Olivero, P. Single-Photon-Emitting Optical Centers in Diamond Fabricated upon Sn Implantation. *ACS Photonics* **4**, 2580–2586 (2017).
35. Evans, R. E., Bhaskar, M. K., Sukachev, D. D., Nguyen, C. T., Sipahigil, A., Burek, M. J., Machielse, B., Zhang, G. H., Zibrov, A. S., Bielejec, E., *et al.* Photon-mediated interactions between quantum emitters in a diamond nanocavity. *Science* **362**, 662–665 (2018).
36. Schröder, T., Trusheim, M. E., Walsh, M., Li, L., Zheng, J., Schukraft, M., Sipahigil, A., Evans, R. E., Sukachev, D. D., Nguyen, C. T., *et al.* Scalable focused ion beam creation of nearly lifetime-limited single quantum emitters in diamond nanostructures. *Nature communications* **8**, 1–7 (2017).
37. Burek, M. J., De Leon, N. P., Shields, B. J., Hausmann, B. J., Chu, Y., Quan, Q., Zibrov, A. S., Park, H., Lukin, M. D. & Loncar, M. Free-standing mechanical and photonic nanostructures in single-crystal diamond. *Nano letters* **12**, 6084–6089 (2012).

38. Khanaliloo, B., Mitchell, M., Hryciw, A. C. & Barclay, P. E. High-Q/V Monolithic Diamond Microdisks Fabricated with Quasi-isotropic Etching. *Nano Letters* **15**, 5131–5136 (2015).
39. Atikian, H. A., Latawiec, P., Burek, M. J., Sohn, Y.-I., Meesala, S., Gravel, N., Kouki, A. B. & Lončar, M. Freestanding nanostructures via reactive ion beam angled etching. *APL Photonics* **2** (2017).
40. Chia, C., Machielse, B., Shams-Ansari, A. & Lončar, M. Development of hard masks for reactive ion beam angled etching of diamond. *Optics Express* **30**, 14189–14201 (2022).
41. Mitchell, M., Lake, D. P. & Barclay, P. E. Realizing $Q > 300\,000$ in diamond microdisks for optomechanics via etch optimization. *APL Photonics* **4**, 016101 (2019).
42. Wan, N. H., Mouradian, S. & Englund, D. Two-dimensional photonic crystal slab nanocavities on bulk single-crystal diamond. *Applied Physics Letters* **112** (2018).
43. Guo, X., Deegan, N., Karsch, J. C., Li, Z., Liu, T., Shreiner, R., Butcher, A., Awschalom, D. D., Heremans, F. J. & High, A. A. Tunable and transferable diamond membranes for integrated quantum technologies. *Nano Letters* **21**, 10392–10399 (2021).
44. Ding, S. W., Haas, M., Guo, X., Kuruma, K., Jin, C., Li, Z., Awschalom, D. D., Deegan, N., Heremans, F. J., High, A. A., *et al.* High-Q cavity interface for color centers in thin film diamond. *nature communications* **15**, 6358 (2024).
45. Ding, S. W., Jin, C., Kuruma, K., Guo, X., Haas, M., Korzh, B., Beyer, A., Shaw, M. D., Sinclair, N., Awschalom, D. D., *et al.* Purcell-enhanced emissions from diamond color centers in slow light photonic crystal waveguides. *Nano Letters* (2025).

APPENDIX

A.1 ANNEALING FABRICATION STEPS AND TRI-ACID CLEAN

Annealing fabrication steps

| Step name | Parameters | Remarks |
|-------------------------------|--|--|
| 1. Inorganic clean | Double: 20 min Piranha mixture (ratio 3:1 of $\text{H}_2\text{SO}_4(>99\%)$: H_2O_2 (30%)) at temperature 80 °C 1 hour Tri-acid inorganic clean: (ratio 1:1:1 of HNO_3 (65%) : HClO_4 (70%) : $\text{H}_2\text{SO}_4(>99\%)$) at 120 °C; Rinse in de-ionized (DI) water (3x), N_2 blow-dry; | Inorganic cleaning to ensure removal of organic material contaminants; |
| 2. High temperature annealing | Annealing sequence: Ramp up from 20 °C to 400 °C: 4 hours; Constant temperature at 400 °C: 8 hours; Ramp up from 400 °C to 800 °C: 12 hours; Constant temperature at 800 °C: 8 hours; Ramp up from 800 °C to 1100 °C: 12 hours; Constant temperature at 1100 °C: 10 hours; Cooldown: ~8 hours; | High temperature low pressure annealing sequence, starting when the base pressure of the annealing oven is $\sim 1 \times 10^{-6}$ mbar, maintained through the entire sequence. |
| 2. Inorganic clean | 1 hour tri-acid inorganic clean: (ratio 1:1:1 of HNO_3 (65%) : HClO_4 (70%) : $\text{H}_2\text{SO}_4(>99\%)$); Rinse in de-ionized (DI) water (3x), N_2 blow-dry; | Inorganic cleaning to ensure wet etch of graphite from the surface of the diamond substrate |

Table A.1: **Conventional** annealing fabrication steps (illustrated in Figure 3.1 (c), Chapter 3): detailed process parameters.

| Step name | Parameters | Remarks |
|-------------------------------|--|--|
| 1. Inorganic clean | Double: Piranha mixture at temperature 80 °C, 20 minutes each; Tri-acid inorganic clean: (ratio 1:1:1 of HNO_3 (65%) : HClO_4 (70%) : $\text{H}_2\text{SO}_4(>99\%)$) at 120 °C, 1 hour; Rinse in de-ionized (DI) water (3x), N_2 blow-dry; | Inorganic cleaning to ensure removal of organic material contaminants; |
| 2. High temperature annealing | Annealing sequence: Ramp up from 20 °C to 100 °C: 20 minutes; Constant temperature at 100 °C: 4 hours; Ramp up from 100 °C to 400 °C: 6 hours; Constant temperature at 400 °C: 8 hours; Ramp up from 400 °C to 850 °C: 6 hours; Constant temperature at 850 °C: 8 hours; Ramp up from 850 °C to 1100 °C: 6 hours; Constant temperature at 1100 °C: 4 hours; Cooldown: ~8 hours; | High temperature low pressure annealing sequence starting when the base pressure of the annealing oven is $\sim 1 \times 10^{-6}$ mbar. The annealing sequence is modified with respect to the conventional one in Table A.1 with ramp up times shorter as a trade-off between shorter overall duration of the recipe, while at the same time keeping low temperature gradient. |
| 2. Inorganic clean | Double: Piranha mixture at temperature 80 °C, 20 minutes each; Di-acid inorganic clean: (ratio 1:1 of HClO_4 (70%) : $\text{H}_2\text{SO}_4(>99\%)$) at 190 °C, 2 hours; Rinse in de-ionized (DI) water (3x), N_2 blow-dry; | Inorganic cleaning to ensure removal of organic matter and graphite from the surface of the diamond substrate: 1. Piranha clean is performed to ensure removal of organic material contaminants; 2. Di-acid inorganic clean is performed following the protocol described in Ref. [1]. |

Table A.2: **Surface-protected** annealing fabrication steps (schematically illustrated in Figure 3.1 (d), Chapter 3): detailed process parameters. Annealing recipe sequence adapted from [2].

Tri-acid cleaning

The overall post-annealing inorganic cleaning of the substrate is modified with respect to the conventional post-annealing surface treatment. We first proceed with a double

Piranha mixture treatment of 20 minutes each at 80 °C, followed by a di-acid mixture at 190 °C for 2 hours.

Specifically, in the reflux configuration adopted through this study, we find the conventional 1:1:1 of HNO_3 (65%) : HClO_4 (70%) : H_2SO_4 (> 99%) mixture limited in temperature to ~120 °C: the choice of the reflux configuration setup (Figure A.1 (b), Dimroth type condenser) is imposed by the safety regulations, as the risk of explosion is high because of the potential formation of perchlorate salts during the heating of the tri-acid mixture [1]. The recommended tri-acid setup configuration in Ref. [1] (Figure A.1 (a)) is a distilling one, where the HNO_3 part evaporated from the mixture and is separated from the remaining HClO_4 (70 %) : H_2SO_4 (> 99%), whereas in our reflux configuration the evaporated HNO_3 is refluxed back into the mixture flask, hence limiting the overall temperature to empirically measured ~120 °C. This represents a challenge for efficient wet etching of the suspected graphitized layer on top of diamond substrates, as effective perchloric acid oxidation can only be achieved at temperatures of at least 150 °C, as reported by the authors of Ref. [1].

Therefore, in order to achieve efficient wet etching of the suspected graphitized layer on the exposed edges of the diamond substrates, we followed the considerations of Ref. [1], but separated the wet inorganic cleaning of organic traces on our substrates from the graphite wet etch. The separation is as follows: we first remove organic residues by employing a double Piranha cleaning at 80 °C, 20 minutes each, followed by direct di-acid mixture inorganic cleaning (ratio 1:1 of HClO_4 (70%) : H_2SO_4 (> 99%)) at 190 °C for 2 hours. Authors of Ref. [1] recommend to keep the temperature of the tri-acid mixture at 190 °C up until the vigorous bubbling of the mixture (indicative of the presence of organic residues) subsides, followed by an increase the temperature at 205 °C to 210 °C for minimum 10 minutes. We choose to keep the di-acid temperature at 190 °C for the longest duration within the limits of the safety rules (~20 min), reaching however ~200 °C highest temperature.

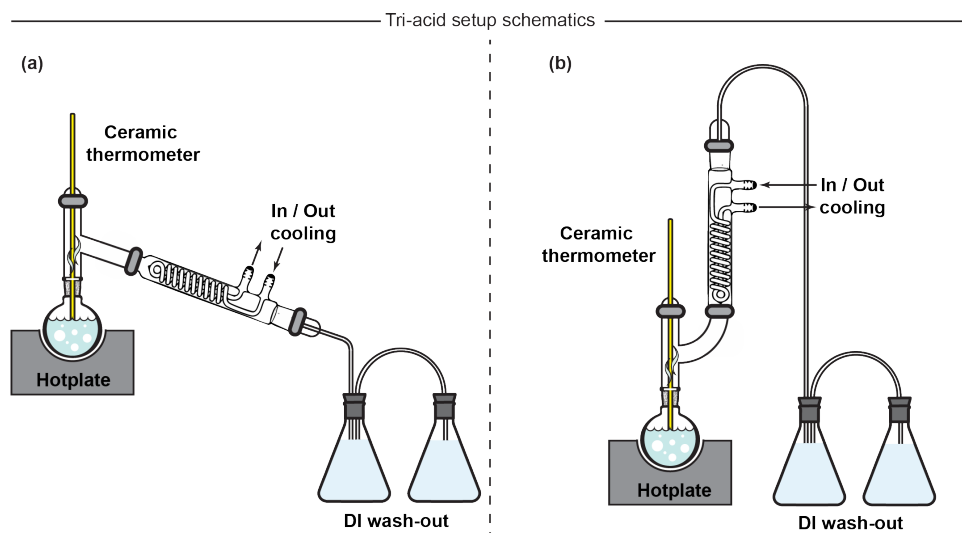


Figure A.1: **Tri-acid setup configuration** | (a) Distillation configuration setup; | (b) Reflux configuration tri-acid wet inorganic clean setup adopted in this work.

A.2 65 °C QIE-BASED FABRICATION PROCESS PARAMETERS

| Step name | Parameters | Remarks |
|---|---|---|
| (1) Inorganic wet clean | Hydrofluoric acid (HF) 40% at room temperature, 20 min Rinse in de-ionized (DI) water (3x) Double: Piranha mixture at 80 °C, 20 min each Rinse in de-ionized (DI) water (3x) N ₂ blow-dry | To obtain an organic free substrate, such that to ensure good adhesion and uniformity of thin film deposition of hard mask material. Piranha mixture: ratio 3:1 of H ₂ SO ₄ (95 %) : H ₂ O ₂ (31 %). |
| (2) Si _x N _y PECVD deposition | Thickness: (~ 221 nm) Plasma chemistry SiH ₄ (20 sccm), NH ₃ (20 sccm), N ₂ (980 sccm) Alternating cycles of LF power (8 s) 20 W, RF (12 s) power 20 W Pressure 650 mTorr, temperature 300 °C | 8 h pre-deposition chamber clean, 5 min chamber conditioning, Deposition tool: Oxford Plasmalab 80 Plus. |
| Mounting the diamond to a Si carrier chip | Pipette drop of PMMA-495-A4 on a Si carrier chip, spin coating at spinning speed 1000 rpm to distribute evenly, sliding diamond sample and silicon coupon samples from side with tweezers, baking time: 2 min at temperature 120 °C | Necessary step for practical handling of the sample. Si coupon samples aligned with diamond sample edges (OM inspection) to prevent resist edge-beating. |
| (3) E-beam resist spin coating | E-beam positive tone resist AR-P-6200.13 Spinning speed 3500 rpm (~ 450 nm) Baking time 3 min at 150 °C | Spinning speed is chosen as optimal trade-off between required resist thickness versus minimization of edge-beating effect. |
| (3) Conductive polymer spin coating | AR-PC-5090, 4000 rpm (~ 40 nm) Baking time 2 min at 90 °C | Top layer protective coating necessary to avoid charging of insulating substrate. |
| (3) E-beam pattern exposure | Exposure dose: variable, optimal dose 350 $\mu\text{C}/\text{cm}^2$ aperture 200 μm , beam spot size ~3 nm, acceleration voltage 100 keV | Proximity effect correction (PEC) simulated and implemented accordingly to the parameters of the stack of materials, exposure tool: Raith EPBG-5200. |
| (4) Development | 60 s DI water, N ₂ blow dry step, 60 s pentyl acetate, 5 s ortho-xylene, 60 s isopropyl alcohol (IPA), N ₂ blow-dry | DI water is necessary to dissolve remove the conductive polymer coating, followed by N ₂ blow-dry. |
| (5) Si _x N _y ICP-RIE etch | Etch rates: Si _x N _y ~ 86 nm/min, AR-P-6200.13 ~ 81 nm / min, Plasma chemistry: CHF ₃ (60 sccm): O ₂ (6 sccm), ICP power 500 W, RF power 50 W, Pressure 1×10^{-7} bar, Table temperature 20 °C | Etch tool: Adixen AMS 100 I-speeder. |
| (6) Resist removal | Positive resist stripper PRS 3000: 12 h soak at room temperature, Ramp-up at 80 °C for 30 min, acetone and IPA rinse for 1 min each at room temperature, N ₂ blow-dry | Long soak at room temperature, followed by ramp-up to high temperature for efficient resist removal. |

Continued from previous page

| Step name | Parameters | Remarks |
|--|---|---|
| (6) Inorganic clean | Double: Piranha mixture at temperature 80 °C for 20 min each, Rinse in de-ionized (DI) water (3x), N ₂ blow-dry | Double inorganic clean necessary for efficient organic residues removal, Piranha mixture: ratio 3:1 of H ₂ SO ₄ (95 %) : H ₂ O ₂ (31 %) at 80 °C. |
| (7) Anisotropic O ₂ etch | Etch rates ~ 10 (~ 300) nm / min for Si _x N _y (diamond), Plasma chemistry O ₂ (50 sccm), RF power 90 W, ICP power 1100 W, Table temperature 20 °C, chamber temperature 60 °C, Pressure 10 μbar Etch depth ~2.5 final device thickness | Pre-etch chamber clean for 10 min SF ₆ /O ₂ plasma chemistry, followed by 30 min O ₂ plasma chemistry, 5 min chamber conditioning, Etch tool: Oxford Plasmalab 100. |
| (8) AlO _x atomic layer deposition (ALD) | Interleaved trimethylaluminium (TMA) (15 ms pulse time, 11 s purge time) H ₂ O (15 ms pulse time, 11 ms purge time), 70 sccm N ₂ , Table temperature 105 °C, AlO _x thickness ~25 nm | Conformal deposition of AlO _x for vertical sidewalls coverage of nanostructures, Deposition tool: Oxford Flexal. |
| (9) AlO _x ICP-RIE etch | Etch rates ~ 36 (10) nm / min for AlO _x (Si _x N _y), Plasma chemistry: BCl ₃ (45 sccm):Cl ₂ (5 sccm), RF power 10 W, ICP power 600 W, Table: 20 °C, Chamber: 60 °C C, Pressure 3 μbar | Pre-etch chamber clean for 10 min SF ₆ /O ₂ plasma chemistry, followed by 30 min O ₂ plasma chemistry, 5 min chamber conditioning, Etch tool: Oxford Plasmalab 100. |
| (10) Quasi-isotropic ICP-RIE etch | Etch rates: ~1.8 nm / min (variable) for Si _x N _y (diamond), Plasma chemistry O ₂ (50 sccm), RF power 0 W, ICP power 2500 W, Pressure 15 μbar, Table temperature 65 °C, chamber temperature 60 °C | Etch tool: Oxford Plasmalab 100 |
| (11) Inorganic wet clean | Double: HF 40% at room temperature, 20 min each, DI water rinse (3x), slow air dry or 80 °C hotplate dry for 30 s | Complete wet etch of hard mask materials. |

Table A.3: **Complete fabrication process of diamond nanophotonic structures: process parameters for quasi-isotropic etch at 65 °C. Schematic illustration in Figure 2.1, Chapter 2.** Fabrication process flow adapted from [3–8]. This table contains the optimized process parameters for quasi-isotropic undercut ICP-RIE etch with table temperature limited at 65 °C. These process parameters allow for successful fabrication of 1550 nm photonic crystal cavity devices and 620 nm nanophotonic waveguide structures.

A.3 250 °C QIE-BASED FABRICATION PROCESS PARAMETERS

| Step name | Parameters | Remarks |
|--|---|--|
| (1) Inorganic wet clean | Hydrofluoric acid (HF) 40% at room temperature, 20 min Rinse in de-ionized (DI) water (3x) Double: Piranha mixture at 80 °C, 20 min each , DI water rinse (3x), N ₂ blow-dry | To obtain an organic free substrate, such that to ensure good adhesion and uniformity of thin film deposition of hard mask material. Piranha mixture: ratio 3:1 of H ₂ SO ₄ (95 %) : H ₂ O ₂ (31 %). |
| (2) Si _x N _y ICPCVD deposition | Thickness: (~ 80 nm to 100 nm) Plasma chemistry SiH ₄ (26 sccm), N ₂ (25 sccm) ICP power 500 W Pressure 10 mTorr, table temperature 400 °C | 10 min chamber conditioning, Deposition tool: Oxford PlasmaPro 100 |
| Mounting the diamond to a Si carrier chip | Pipette drop of PMMA-495-A4 on a Si carrier chip, spin coating at spinning speed 1000 rpm to distribute evenly, sliding diamond sample and silicon coupon samples from side with tweezers, baking time: 2 min at temperature 120 °C | Necessary step for practical handling of the sample. Si coupon samples aligned with diamond sample edges (OM inspection) to prevent resist edge-beating. |
| (3) E-beam resist spin coating | E-beam positive tone resist AR-P-6200.09 Spinning speed 3500 rpm (~ 220 nm) Baking time 3 min at 150 °C | Spinning speed is chosen as optimal trade-off between required resist thickness versus minimization of edge-beating effect. |
| (3) Conductive polymer spin coating | AR-PC-5090, 4000 rpm (~40 nm) Baking time 2 min at 90 °C | Top layer protective coating necessary to avoid charging of insulating substrate, |
| (3) E-beam pattern exposure | Exposure dose: variable, optimal dose 300 $\mu\text{C}/\text{cm}^2$ aperture 200 μm , beam spot size ~3 nm, acceleration voltage 100 keV | Proximity effect correction (PEC) simulated and implemented accordingly to the parameters of the stack of materials, exposure tool: Raith EPBG-5200. |
| (4) Development | 60 s DI water, N ₂ blow dry, 60 s pentyl acetate, 5 s ortho-xylene, 60 s isopropyl alcohol (IPA), N ₂ blow-dry | DI water is necessary to dissolve remove the conductive polymer coating, followed by N ₂ blow-dry. Optical microscope (OM) inspection is strongly advised to confirm absence of H ₂ O residual droplets. Stir gently for the initial ~ 6 sec in pentyl acetate, 5 sec in ortho-xylene and 6 sec in IPA respectively. OM inspection is strongly advised to assert the successful development and absence of residues. |
| (5) Si _x N _y ICP-RIE etch | Etch rates: Si _x N _y ~ 86 nm/min, AR-P-6200.09 ~ 50 nm / min, Plasma chemistry: CHF ₃ (60 sccm): O ₂ (6 sccm), ICP power 500 W, RF power 50 W, Pressure 1×10^{-7} bar, Table temperature 20 °C | Diamond sample is mounted on the Si coupon carrier, glueing with Wakefield thermal paste to the Si carrier wafer. OM inspection is strongly advised to ensure no thermal paste is subsequently exposed to the etching plasma (introduces micromasking). Etch tool: Adixen AMS 100 I-speeder. Over-etch of ~67% to ensure full opening of dense patterns. |

Continued from previous page

| Step name | Parameters | Remarks |
|--|---|---|
| (6) Resist removal | Positive resist stripper PRS 3000: 12 h soak at room temperature, Ramp-up at 80 °C for 30 min, acetone and IPA rinse for 1 min each at room temperature, N ₂ blow-dry | Long soak at room temperature, followed by ramp-up to high temperature for efficient resist removal. |
| (6) Inorganic clean | Double: Piranha mixture at 80 °C for 20 min each, Rinse in de-ionized (DI) water (3x), N ₂ blow-dry | Double inorganic clean necessary for efficient organic residues removal, Piranha mixture: ratio 3:1 of H ₂ SO ₄ (95 %) : H ₂ O ₂ (31 %).. |
| (7) Anisotropic O ₂ etch | Etch rates ~ 10 (~ 219) nm / min for Si _x N _y (diamond), Plasma chemistry O ₂ (50 sccm), RF power 90 W, ICP power 1100 W, Table temperature 20 °C, chamber temperature 60 °C, Pressure 10 μbar Etch depth ~ ×2 to ~ ×2.5 final device thickness | Pre-etch chamber clean for 10 min SF ₆ /O ₂ plasma chemistry, followed by 30 min O ₂ plasma chemistry, 5 min chamber conditioning, Etch tool: Oxford PlasmaPro 100 Cobra. |
| (8) AlO _x atomic layer deposition (ALD) | Interleaved trimethylaluminium (TMA) (15 ms pulse time, 11 s purge time) H ₂ O (15 ms pulse time, 11 ms purge time), 70 sccm N ₂ , Table temperature 105 °C, AlO _x thickness ~25 nm | Conformal deposition of AlO _x for vertical sidewalls coverage of nanostructures, Deposition tool: Oxford Flexal. |
| (9) AlO _x ICP-RIE etch | Etch rates ~ 24 nm / min for AlO _x , Plasma chemistry: BCl ₃ (45 sccm): Cl ₂ (5 sccm), RF power 10 W, ICP power 400 W, Table: 20 °C, Chamber: 60 °C, Pressure 3 μbar | Pre-etch chamber clean for 10 min SF ₆ /O ₂ plasma chemistry, followed by 30 min O ₂ plasma chemistry, 5 min chamber conditioning, Over-etch by 30 % to ensure full clearing of the top layer. Etch tool: Oxford PlasmaPro 100 Cobra. |
| (10) QIE ICP-RIE | Etch rates: ≤ 1.8 nm / min (variable) for Si _x N _y (diamond), Plasma chemistry O ₂ (50 sccm), RF power 0 W, ICP power 3000 W, Pressure 20 μbar, Table temperature 250 °C, chamber temperature 60 °C | Etch tool: Oxford PlasmaPro 100 Cobra. |
| (11) Inorganic wet clean | Double: HF 40% at room temperature, 20 min each, Rinse in de-ionized (DI) water (3x), Slow air dry or 80 °C hotplate dry for 30 s | Complete wet etch of hard mask materials. |

Table A.4: **Complete fabrication process of diamond nanophotonic structures: process parameters for quasi-isotropic etch at 250 °C. Schematic illustration in Figure 2.1, Chapter 2.** Fabrication process flow adapted from [3–8]. This table contains the optimized process parameters for quasi-isotropic undercut ICP-RIE etch with table temperature at 250 °C. These process parameters allow for successful fabrication of 620 nm photonic crystal cavity devices and nanophotonic waveguide structures.

A.4 AlO_x MASK FOR QIE-INSPIRED FABRICATION PROCESS

AlO_x hard mask for QIE-based fabrication process: Si / AlO_x etch tests (Figure A.2) demonstrate high selectivity to anisotropic and quasi-isotropic O_2 ICP-RIE, combined with high accuracy in pattern transfer.

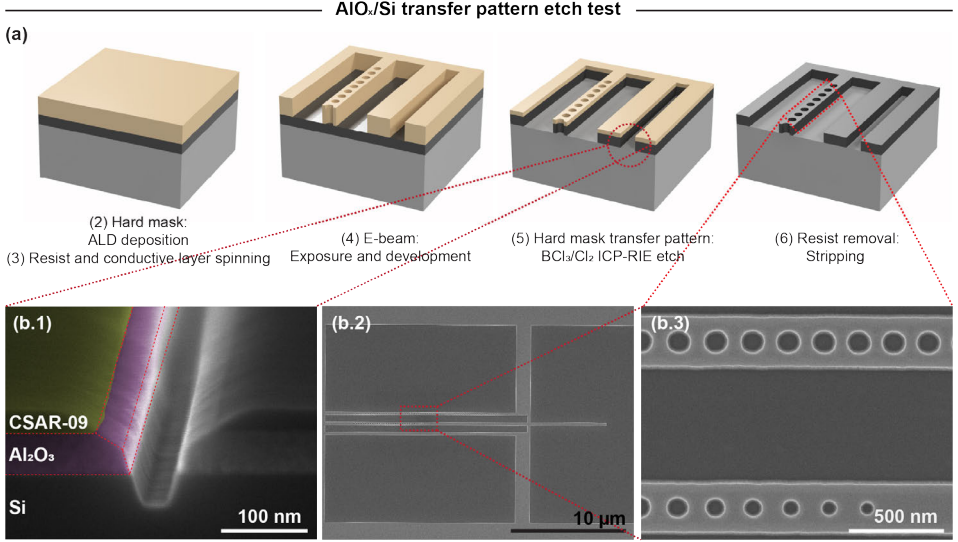


Figure A.2: **Exploring higher selectivity hard mask materials: AlO_x/Si hard mask etch test.** High selectivity hard mask materials ensure both robustness through the full fabrication process, while at the same time allowing for very low aspect ratio: this has the advantage of improving the patterning fidelity. (a) Left to right: fabrication steps foreseen in the $\text{AlO}_x/\text{Si}/\text{Si}$ etch tests with parameters 200 nm CSAR / 50 nm ALD deposited Si_xN_y ; After step (5), the AlO_x/Si samples are cleaved in order to allow investigation on vertical transfer pattern: benchmark etch test lines are patterned with a variable width to test the highest resolution in the pattern transfer; (b.1) SEM pictogram of the vertical cross section of the smallest patterned benchmark etch line; The trench structure shows a non vertical etched profile, with a two-regime inclination: lower regime inclination angle close to 80° sidewalls, proceeding with a 45° profile angle to the top side at the AlO_x/CSAR interface; (b.2) Top view SEM pictogram showing 620 nm patterned nanophotonic triple structure and (b.3) zoom in of the Bragg mirror terminated coupling waveguide (bottom) and photonic crystal cavity (top): maximum lateral transfer pattern bias is up to ~ 10 nm, ensuring accurate patterning of the intended design features.

AlO_x hard mask for QIE-based fabrication process: diamond / AlO_x overall QIE-based, optimized fabrication variant (Figure A.3 (a)) lead to following considerations.

1. **Transfer pattern accuracy:** one-to-one transfer pattern is obtained for low aspect-ratio 200 nm CSAR-09 / 70 nm AlO_x (Figure A.3 (b.1), (b.2) and (b.3), design dimensions overlayed in dashed green). The thickness of AlO_x is chosen considering selectivity of diamond / AlO_x to anisotropic O_2 ICP-RIE is 1:85, and from previous QIE-based variants developed in this work, no etching of AlO_x takes place in O_2 QIE steps. Thus in order to guarantee robustness of the mask, taking into account the tolerance of 30% over-etch in the process, a ~ 30 nm film thickness is required. We decide to adopt the highest AlO_x film thickness, allowing for both accurate transfer

pattern and erosion of the film at the edges (Figure A.2 (b.1)) that would guarantee mask robustness over the entire fabrication process.

2. **Severe micromasking:** even with a BCl_3/Cl_2 ICP-RIE over-etch of 30% that allows for a full clearance of the protective film from the horizontal underlying diamond plane, such that downstream QIE plasma access is guaranteed, after fabrication step (6) (fabrication process steps shown in Figure A.3 (a)) the anisotropic O_2 ICP-RIE in combination with high selectivity AlO_x yields severe dense micromasking. First, any pristine diamond surface imperfections, e.g. diamond pits, act as nucleation points where the AlO_x film thickness may be higher, thus these centers are not efficiently cleared out from the protective film. Given the high selectivity to anisotropic O_2 ICP-RIE, renders the residues of AlO_x film micromasking sources (Figure A.3 (c.1)). Moreover, anisotropic O_2 ICP-RIE leads to enhanced mask erosion at the edges of the devices, whereas the vertical profile of the etched devices shows severe sidewall surface roughness (Figure A.3 (c.2)). At the same time, re-deposition of O_2 etch of AlO_x ICP-RIE non-volatile by-products, as well as small AlO_x particles from the mask itself, that subsequently sputter back on the diamond surface [9], may be the source of extremely dense micromasking around the patterned diamond devices (Figure A.3 (c.3)).
3. **Mask breaking:** even though AlO_x material has a very high selectivity to both anisotropic and QIE O_2 ICP-RIE, severe micromasking and vertical sidewall surface roughness lead to erosion of the protective mask through the QIE undercut step, resulting in complete breaking and delamination of the protective mask (Figure A.3 (d.1), (d.2) and (d.3)). Thus, fabrication of diamond devices with this high selectivity protective material has been unsuccessful.

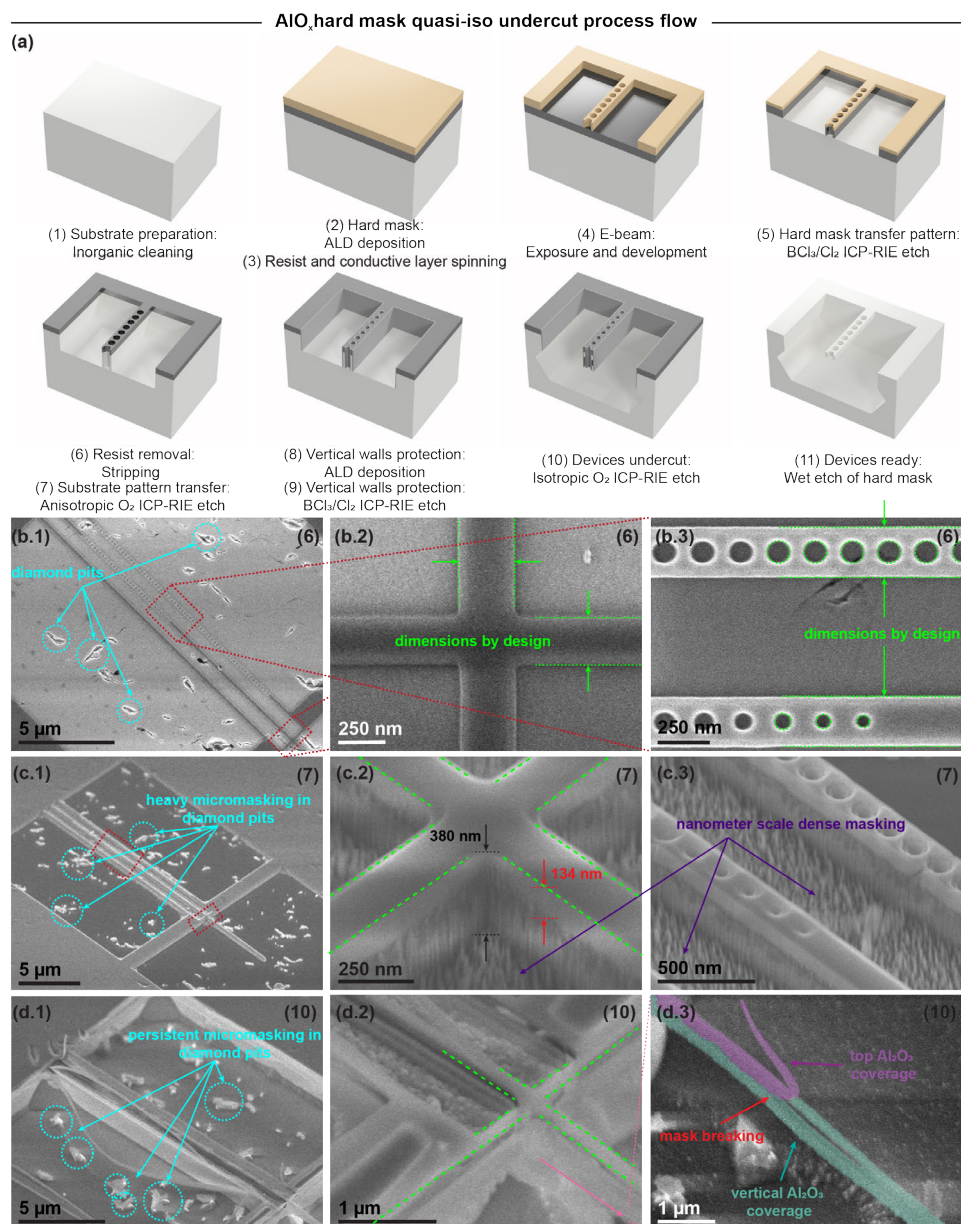


Figure A.3: **AIO_x hard mask based quasi-isotropic undercut fabrication process**: high selectivity hard mask materials present an extremely low tolerance to fabrication process variations, with micromasking and mask breaking due to angled vertical etched profiles constituting major challenges, compromising successful fabrication of suspended diamond devices. | **Top panel:** (a) Quasi-isotropic fabrication process steps: design and adaptation of the fabrication process to the AIO_x hard mask; **Bottom panel:** SEM pictograms showing the monitoring of the fabrication process: (b): Accurate and precise to ~5 nm design feature transfer pattern, after fabrication step (6); (c): detrimental diamond micrometer sized pillars and dense nanoscale pillar as a result of heavy micromasking, after fabrication step (7); (d): complete AIO_x mask breaking mechanism and full etch of diamond structures, after fabrication step (10);

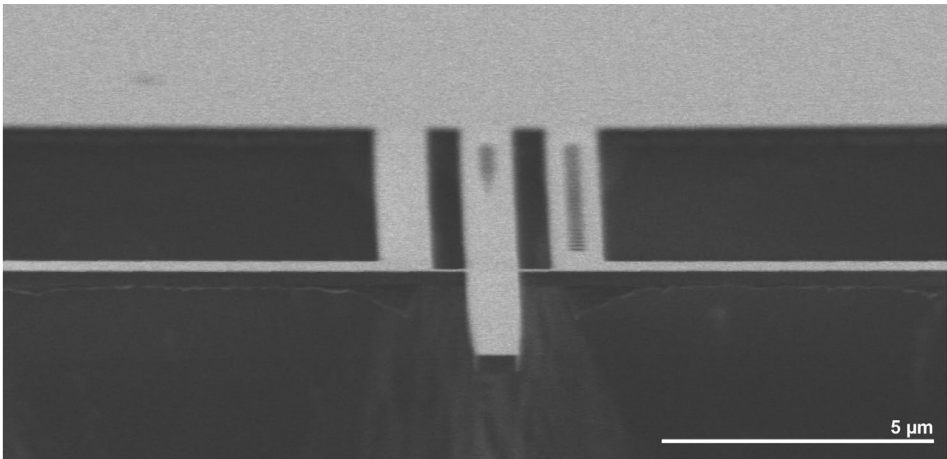
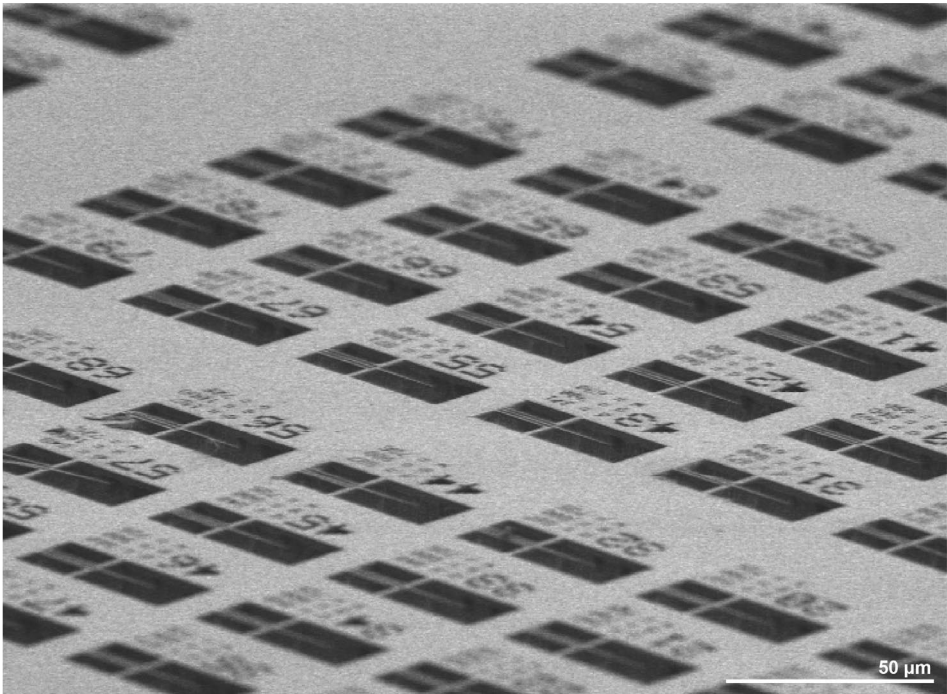
A.5 REFERENCES

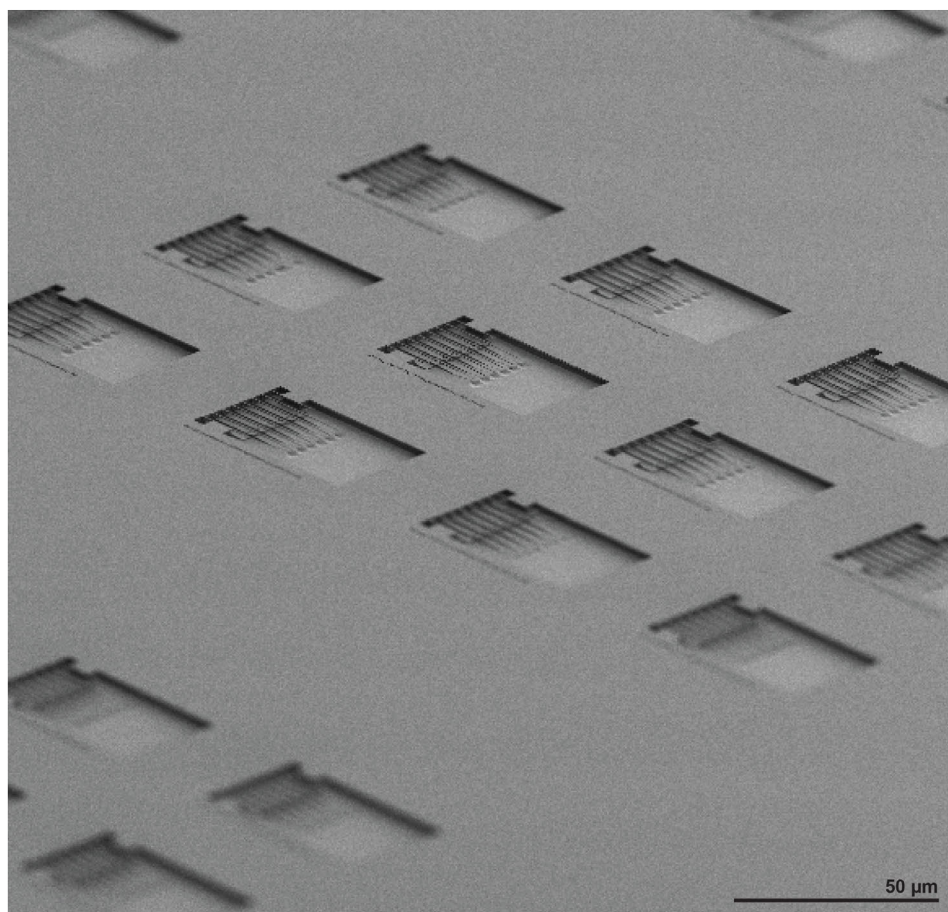
1. Brown, K. J., Chartier, E., Sweet, E. M., Hopper, D. A. & Bassett, L. C. Cleaning diamond surfaces using boiling acid treatment in a standard laboratory chemical hood. *Journal of Chemical Health & Safety* **26**, 40–44 (2019).
2. Sangtawesin, S., Dwyer, B. L., Srinivasan, S., Allred, J. J., Rodgers, L. V., De Greve, K., Stacey, A., Dontschuk, N., O'Donnell, K. M., Hu, D., *et al.* Origins of diamond surface noise probed by correlating single-spin measurements with surface spectroscopy. *Physical Review X* **9**, 031052 (2019).
3. Khanaliloo, B., Mitchell, M., Hryciw, A. C. & Barclay, P. E. High-Q/V Monolithic Diamond Microdisks Fabricated with Quasi-isotropic Etching. *Nano Letters* **15**, 5131–5136 (2015).
4. Mitchell, M., Lake, D. P. & Barclay, P. E. Realizing $Q > 300\,000$ in diamond microdisks for optomechanics via etch optimization. *APL Photonics* **4**, 016101 (2019).
5. Mouradian, S., Wan, N. H., Schröder, T. & Englund, D. Rectangular Photonic Crystal Nanobeam Cavities in Bulk Diamond. *Applied Physics Letters* **111**, 021103 (2017).
6. Wan, N. H., Lu, T.-J., Chen, K. C., Walsh, M. P., Trusheim, M. E., De Santis, L., Bersin, E. A., Harris, I. B., Mouradian, S. L., Christen, I. R., Bielejec, E. S. & Englund, D. Large-Scale Integration of Artificial Atoms in Hybrid Photonic Circuits. *Nature* **583**, 226–231 (2020).
7. Rugar, A. E., Aghaeimeibodi, S., Riedel, D., Dory, C., Lu, H., McQuade, P. J., Shen, Z.-X., Melosh, N. A. & Vučković, J. Quantum Photonic Interface for Tin-Vacancy Centers in Diamond. *Physical Review X* **11**, 031021 (2021).
8. Ruf, M. *Cavity-enhanced quantum network nodes in diamond* PhD thesis (Delft University of Technology, 2021).
9. Hicks, M.-L., Pakpour-Tabrizi, A. C. & Jackman, R. B. Polishing, preparation and patterning of diamond for device applications. *Diamond and Related Materials* **97**, 107424 (2019).

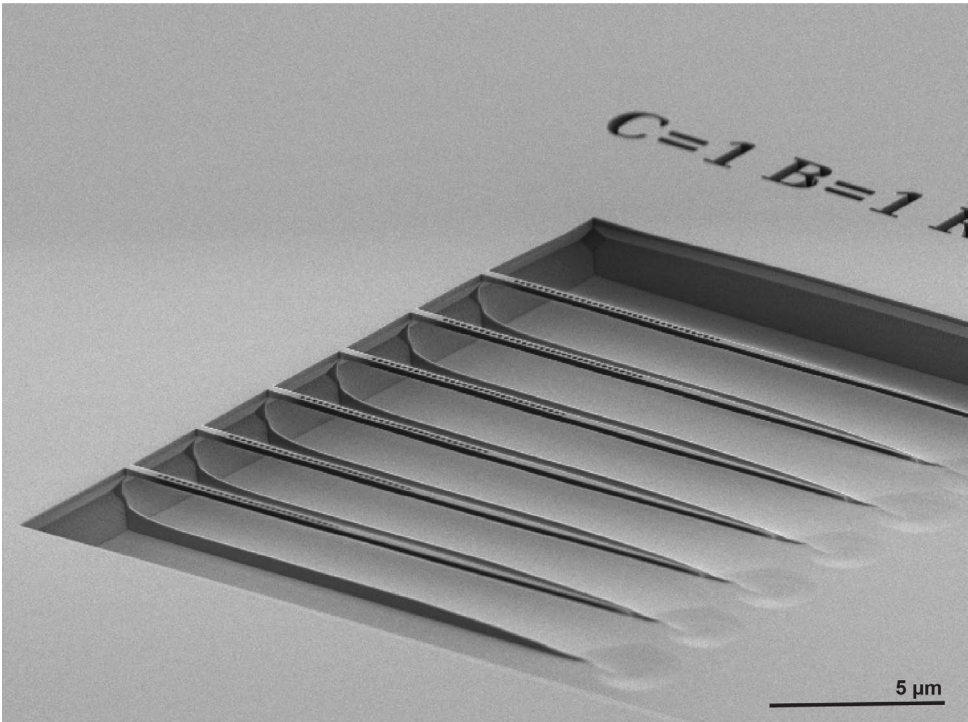
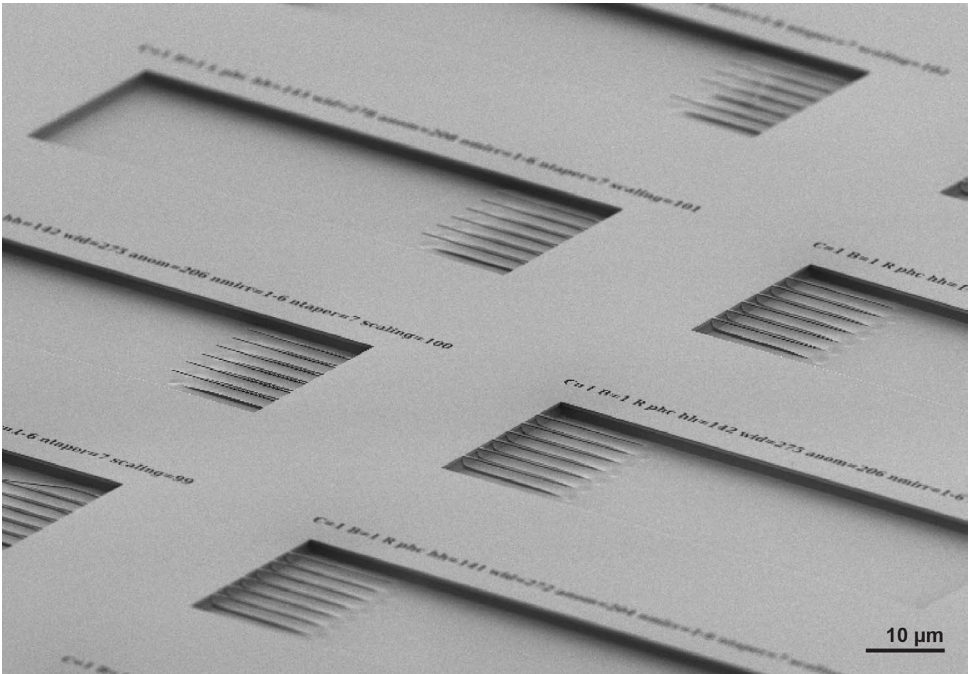
GALLERY

E nel percorso, fermati e ammira la bellezza che ti circonda



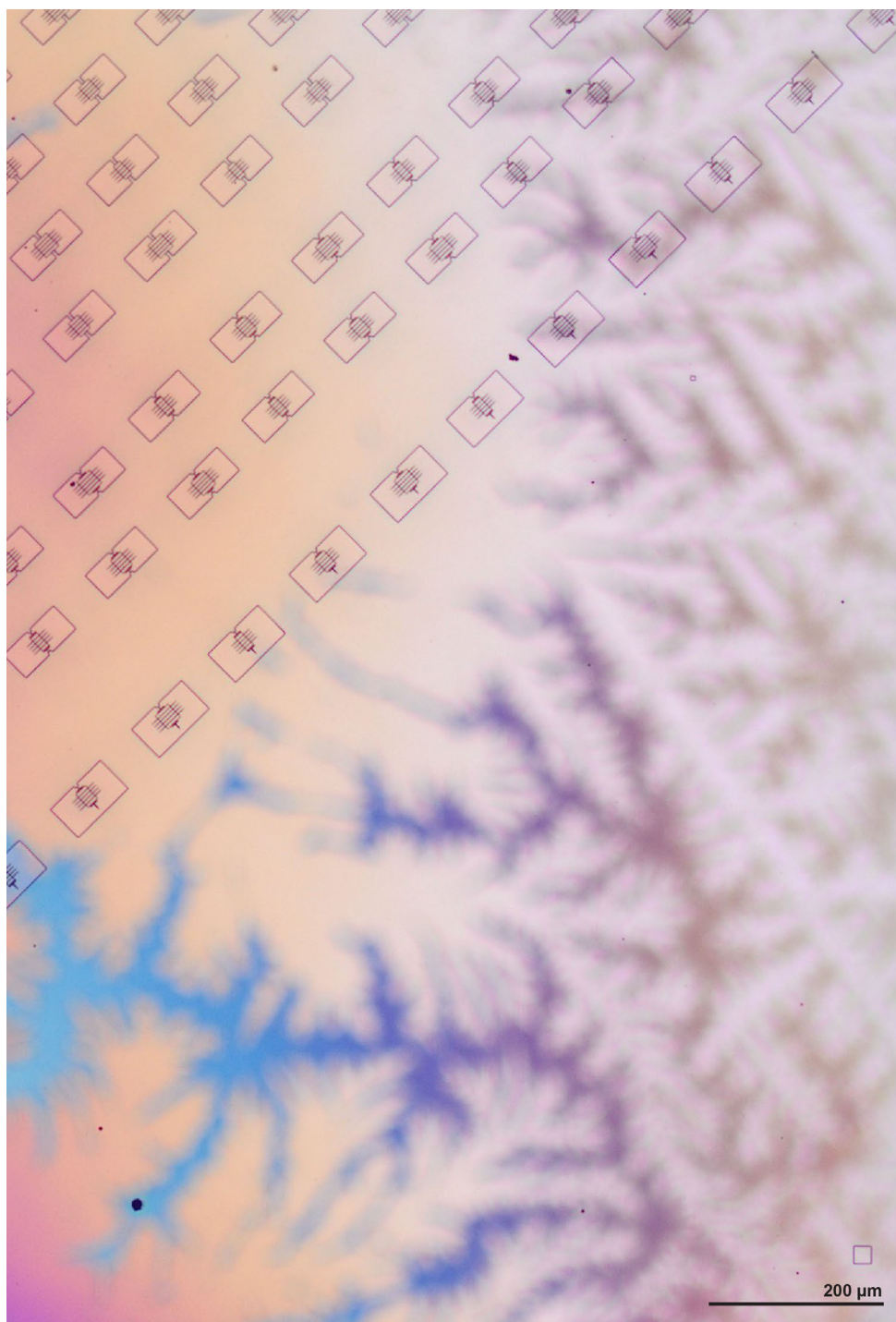












ACKNOWLEDGMENTS

My most esteemed reader,

This section of the thesis is less scientific and more about the environment, the vibrant community, and the many people who have made this PhD journey so special and life-changing. This story began in early 2020, when a strange flu was spreading throughout the world and most of us believed "in two weeks it will be over and life will return to normal". At that time, I was in the final stage of my Master's project at Politecnico di Milano, immersed in the familiar rhythm of lab work and wondering, as any student would, where I should go next. During those ordinary days, I learned about the Casimir Open Days, to which I submitted my application, hoping simply to explore Delft and Leiden, in the very spirit of the program. Little did I know that this opportunity, moved online just as the world went into lockdown, would set in motion the journey that brought me here. That was how I found my way into a PhD in Delft, in a country I had never visited before, and into a program that allowed me to do what I love most: work in a *spaceship* cleanroom. I am convinced that the wisdom of the proverb, "It takes a village to raise a child," also holds true for the scientific growth of a PhD candidate: "It takes a team to raise a scientist." Throughout these years, I have been guided, supported, and inspired by many such villages, and to all of you I owe my deepest gratitude.

Ronald, I must admit that when I received your first email, I double-checked the sender. Coming from a background in Engineering Physics, I struggled at the time to see myself as a natural fit in a Quantum Networks group, and I was curious to understand what had drawn your interest. In retrospect, looking at the work presented in this thesis and the direction of the group towards diamond nanophotonic integration, it all makes perfect sense, and I realize how fortunate I have been to have your guidance throughout this journey. Your unique combination of qualities, an exceptional scientist, a natural leader, and a kind person, makes you an ideal promotor for any young researcher. You consistently inspire in us both freedom and curiosity in science. Words cannot fully express my gratitude for your support, your trust, and the many opportunities you have given me, all to which I owe you my growth as a scientist. Thank you for your guidance, your encouragement and the privilege of being part of your group.

Simon, you equally welcomed me into your group and encouraged me to pursue ambitious projects. In GLab, I received considerable training and supervision at the start of my PhD journey, which laid the foundation for my nanofabrication becoming. You combined generous guidance with freedom to explore, conduct research, and experiment, which was essential to building my independence. The skills I gained under your supervision enabled me to carry this expertise forward and develop the diamond nanofabrication processes on which this thesis is largely based. You have played an essential role in shaping my scientific path, supporting me with generous knowledge, guidance, and skill. I am deeply grateful for your mentorship, your encouragement, and the opportunity to work closely with you and your group.

I also thank all the committee members for agreeing to evaluate this thesis: **Sonia Conesa Boj**, **Toeno van der Sar**, **Paul Barclay** and **Alex High**. I really look forward to an exciting discussion on the defense day.

The two people standing next to me on the defense day have been doing so throughout their entire own journeys here in Delft. **Davide**, we began this journey almost at the same time and have shared countless memorable moments, both inside the cleanroom and beyond. Thank you for your constant support, for our Sunday afternoon tea and cake, and for always making this journey brighter through your solid sense of humor. Thank you for being my damigella today. **MG**, I was very happy when you joined our group. You are an exceptionally talented scientist, only a true force of nature like you could have brought the three-node setup to new glory days with such elegance and grace! Thank you for being here today, as always for your support, your encouragement, and for bringing the Taylor Swift kind of energy into every day.

At the start of my PhD, I trained in both the GLab and the Hanson Lab, each offering me a different perspective and expertise. In Hanson Lab, **Max**, you welcomed me as your protégé and introduced me to the world of diamond nanofabrication and nanophotonic devices. The very first telecom-operating diamond nanocavities had just been measured by you and **Chris**, and that milestone only amplified the excitement to dive into the development and optimization of the process without hesitation. From there, we embarked on an exciting path, gradually uncovering the many facets of fabrication and learning how to reliably fabricate telecom nanophotonic cavities. I deeply value the scientific discussions we shared in those early days and have done my best in the years since to build on the knowledge we developed together. Your scientific insight and leadership have profoundly shaped my PhD journey. Thank you for your guidance and advice. I look forward to hear about your current adventures!

Bas, you generously supported me with scientific discussions, training, and mentoring. It was a pleasure to work with you and GLab on the NVNB project. You patiently taught me not only the theoretical and experimental aspects but also but also the importance of efficiency and effective time management. I am eager to see the exciting results that will come from your lab in Leiden.

I was fortunate to spend most of my PhD working closely within the **SnV team**. To each of you, it has truly been an incredible journey! **Matteo Jr.**, we handed you a diamond waveguide, and you gave us back some of the coolest physics of the tin-vacancies. Thank you for all the scientific discussions, the countless risottos, and the live music. I look forward to hearing about the exciting physics you are exploring in Barcelona! **Hans**, I really always appreciated and enjoyed your input and advice. I was excited to walk you through the stripline fabrication in the cleanroom. You taught me the importance of constructive feedback and how good supervision can truly make a difference. I think the “see one, do one, teach one” motto will long live in Team Diamond. Good luck, and I am sure you will have a great time in Switzerland together with **Sophie** and **Hannah**! **Chris**, that evening when you called me out of cleanroom and we saw the stable tins is one of the dearest highs of my PhD. Your expertise and resilience are inspiring. I am looking forward to the exciting outcome of your project! **Julia** your enthusiasm is always palpable! Thank you for the great times in Hawaii, as well as at all conferences we attended together. **Lorenzo**, it was really nice to work together, both in the lab and in the cleanroom. I appreciated

your support and advice. **Tim**, it was great to learn the lab ropes from you, and your grounded positivity has influenced me many times along the way. **Dani**, keep nurturing your talent for simulating hole based design, or any future kind of cavity devices! I am looking forward to fancy cavity designs the group will fabricate! Thanks for the fun time in the lab, tuning the cavities was super exciting! **Leo**, from the very beginning, working together felt like a partnership, and your enthusiasm always brightened (in safe yellow light) our cleanroom days. I am confident that you will take diamond nanofabrication into new and exciting directions. Thank you for your help, support, and generous feedback on this thesis! **Niv**, you joined a fully experimental group bringing *theory land* to us. I admire your courage and look forward to seeing how your perspective will shape exciting experiments ahead. **Alex**, your knowledge and skills were a very welcome addition to the tin-team. I look forward to the next cool experiments in the lab and hear about your next impressive cycling adventures outside it! Thank you as well for your extensive feedback on this thesis manuscript. **Timo**, it's exciting to see you at the beginning of your PhD journey. I look forward to see your work take shape in the coming years and wish you the best of luck along the way!

The Big Cavity Boys: When you need an emitter to shine just right, a big cavity keeps it nice and bright! **Yanik**, you started just two weeks before me (which still makes you the one to decide who speaks first at the stand-up), and we have shared the PhD journey ever since. It's impressive how you built and set up the cavity lab: Your attention to detail and organization are clearly reflected in it and are much appreciated within Team Diamond. It was fun to co-supervise together and to set the basis for the research practicum. Thank you for your support over the years, your valuable feedback on this thesis, and, of course, the diamond stickers. Wishing you all the best for your defense day and the adventures ahead! **Julius**, your openness and willingness to help have always made a difference in the group. Thank you for organizing the Diamond Cup, for taking us to Stuggy, and for the great times during the many trips we shared. Best of luck with your own defense and what comes next! **Stijn**, the fiber whisperer, thank you for the best splice RTNano has ever seen. Success in your PhD journey! **Christian**, starting an entire new project has its own challenges, I am confident that you are the right person for that! Looking forward to exciting experiments.

I also had the privilege of supervising and mentoring bright students along the way, and I learned a lot in the process. **Sezer**, you were my first student, shared between the Hanson and Gröblacher groups. It was a challenging experience to explore a new fabrication process from scratch together, and I think you've showed a lot of courage to jump on it! We certainly learned a lot about the limits of diamond etching. I wish you much success at ASML. **Caroline**, together we convincingly demonstrated some of the extreme possibilities of advanced diamond nanofabrication, and I also greatly enjoyed the fun moments along the way. We spent many hours side by side, and I was really impressed by the precision and skill with which you handled those tiny membranes! **Leo**, the fact that you are mentioned twice in this thesis section hints towards the time extent you've been in Team Diamond, you are competing fiercely with Ronald on this! Supervising you during your master's was where we began working together, and I am happy we are continuing since then. **Elvis**, even though you were Julia's master student, I always enjoyed debugging the diamond nanofab with you and discuss your project. Thank you all for being part of Diamond Fab

Team!

Thanks to the old guard of Team Diamond. **Arian**, we've always worked on almost diagonally opposed topics in the group, and so I was always mega curious to hear from you about the unprecedented challenges you have faced in the Delft - The Hague project. Thanks for the fun moments, in the group and partying! Success with your next adventure, I am sure that with **Vincy** on your side this will be a certain life-changing experience. **Kian**, bringing the technological and commercial applications resulted in a unique thesis. Also, together with Arian, you really went for it: I think we all better grasped how long the distance was when we all cycled it, especially some of us on a not-so-good bike! Thank you for the discovery of the coffee creamer, it made my days sweeter! Success in your Canadian adventure! **Sophie**, it is very nice to have you back in QuTech. We are all very excited to see the novel research that will come out of your lab. Your leadership, talent, and kindness are inspiring! **Matteo Sr.**, some years ago you already predicted what the cover of this thesis would look like! It was nice to have you in the group! Success with your projects and hope to catch up at a next conference soon! **Marie-Christine**, it was amazing to have you in the group! I am sure anyone who works with you can count themselves fortunate. Your wedding in Vienna truly felt like being part of a fairytale, and thank you for sharing your special day with us. **Matthew**, it was very nice to work with you at the beginning of my PhD. Lots of success in QPhoX, I am sure your impact is greatly appreciated! **Alejandro**, conversations with you have always been edge-unhinged, your sense of humor is admirable. I hope you enjoy the view (through your sparkling diamond shaped sunglasses) from the top floors of HSBC!

The amazing GLab team: thank you for all the years of exciting science and shared moments. **Parsa**, your talent, patience, and empathy make you both a great scientist and a wonderful person. You have been there for me since the very beginning. Thank you not only for your scientific advice and support, but above all for your friendship. I wish you every success in your PostDoc adventure! **Yong**, even though our time together was short, I was blessed with your day-to-day PostDoc wisdom. Learning the ropes of an in-fiber optical setup would have been far less fun without your infinite patience. You showed me that no matter how complicated a problem may seem, its origin is often quite simple. It was a pleasure to work with you, and I wish you all the best with your newly established group. **Jingkun**, your dedication was inspiring, thank you for the fabrication advice and for all the fun in the office. **Matthijs**, it was an honor to be your paronymph and to share the PhD experience with you. I am sure your projects are going even better than you expected. **Nico**, your energy is unmatched, and so have been the pastas you cooked for us. Enjoy your overseas adventure. **Rob**, thank you for the scientific conversations and your support during my first steps. QPhoX is lucky to have you. **Liu**, your dedication is admirable. Thank you for the support and the relaxing brunches we've had, I hope they continue coming! Wishing you all the best for your big day soon. **Alex**, Doctor Alex, congratulations on this great achievement, and much success in your next chapter. The rare-earth ions team: **Gaia**, thank you for your kindness; it was great to share an office with you and **Emanuele**. **Jana**, I admire your courage, fierceness and resilience, which combined with your knowledge I am confident that it will result in a successful PhD. Thank you for your friendship. **Boris**, it was really nice to supervise you together with Yanik during your bachelor's practicum project. I was delighted when you joined GLab for your

master's and now your PhD! **Jan, Jin, Xiong, Luca, Harmen**, and the rest of the team: keep up the amazing work that makes GLab such a successful and great team to be part of.

The other half of Team Diamond cannot be missed. **Gerben**, the SiC fab king! It has been great to see your beginnings and how far you have come. Our fabrication discussions were always both fun and insightful. Veel succes with the alligator cavities! **Jiwon**, I really enjoyed the California road trip with you and Yanik. The K-pop playlist combined with the german schlager, and the endless supply of beef jerky made it even more memorable. **Laurens**, it was a pleasure to be part of the NanoArt Collective with you, thank you for encouraging and nurturing my cleanroom artistic side, of which a small part is shown in the gallery section here. It was fun to hike the Hollywood hills with you, **Ben**, and **Margriet**. To you all, and to **Madhu, Christina, Nic**, good luck with your PhD journeys. **Tobi**, your kindness, positivity, and encouraging words always bring a smile. I am sure you will do great on your PhD adventure! **Conor**, it is great to have you back at QuTech. I have always enjoyed our scientific conversations, as well as career-development ones. Your advice is greatly appreciated. **Sjoerd**, it is always fun and stimulating to debate with you. You always bring a different and interesting perspective! I really enjoyed the Grand Canyon trip with you and a big part of Team Diamond!

Carlos, I look forward to exciting experiments coming from your group! **Jan**, you have been the first to join Carlos' group and I have great admiration for your dedication and work. Setting up an experimental lab is a huge milestone, I am confident that many amazing results will come out of it. **Elena**, it was great to work with you on device designs and I really enjoyed our conversations. Much success with your PhD. **Matteo**, although we briefly crossed paths, I enjoyed our conversations about silicon fab. Looking forward to fancy devices and experiments! **Lin**, your enthusiasm for science is inspiring. I really enjoyed our conversations about diamond nanofabrication from the very first day we met. Thank you for that!

While a PhD can often be perceived as a lonely journey, I was fortunate to experience quite the opposite. I was fortunate to work within several fruitful collaborations. **Ryoichi, Salahuddin, Kenichi, Tetsuro**, and the rest of Fujitsu collaboration team, thank you for the stimulating scientific conversations. Wishing you success with the next projects.

To the extended Diamond NanoFab team: **Richard**, it was really exciting to explore the early stages of diamond nanofabrication with you. Thank you for your advice and help. **Yufan**, we started almost at the same time. Thank you for your help and dedication. It was always exciting to discuss and debug the fab details together. **Gesa**, it was always nice to discuss science together. Those long tri-acid procedure days would have been much less fun without you! Good luck with your scientific adventure! The device nanofabrication process, in reality, is much longer than the steps schematically illustrated in this thesis, the support of which requires a considerable amount of preparation and work: special thanks **Zahra Sadre Momtaz** and the TNO team. Your help has often accelerated the execution of the diamond fabrication runs.

The high temperature annealing process proved less trivial than it would seem when written down in a fabrication protocol: **Patrick Maletinsky**, although we have not had the opportunity to meet in person, thank you for hosting us and generously lending us the equipment in your group. Special thanks to **Silvia Ruffieux**, for the scientific discussions and help with diamond annealing.

I would like to thank the entire Kavli Nanolab Staff. With great kindness, you welcomed me and offered your support and help throughout the years of my PhD. **Eugene**, thank you for your patience, your critical eye, and your ever-watchful presence over the shoulder. Your scientific advice and deep knowledge have been invaluable in developing the wet inorganic protocols in this thesis. Cheers to September 29th: wishing you a fulfilling and well-deserved retirement ahead! **Charles**, your kindness, help, and advice are unmeasurable. Transitioning etchers would not have been that smooth without your knowledge and skill. Thank you! **Hozanna**, I learned the art of wonderful SEM imaging from you. Thank you for your support, and the exciting trip to Germany. **Lodi**, I really enjoyed adventuring into AFM scanning crazy positioned samples with you. **Arnold** and **Anja**, thank you for all the help in figuring out the e-beam on diamond with us. **Esther**, it was really exciting to set up a new tri-acid system with you. **Brian**, thank you for your help and always good advice on any wet chemistry related process. **Bas**, your excitement for developing new processes was contagious. **Roald**, your enthusiasm and scientific curiosity made a PhD adventure unavoidable for you! Much success ahead! **Marinus**, **Marco**(2x), **Ewan**, **Pauline** thank you for your help over the years. **Marc**, your leadership and openness are inspiring, attending CRUM meetings was always exciting, whether for ongoing equipment updates or a new sophisticated one. Thank you all for your advice and support and for keeping the cleanroom up and running at all times with endless positivity and patience.

Some of the highest risk cleanroom activities would not have been that straightforward without the help of QuTech's Fine Precision Engineering team: thank you **Nico Alberts** and **Ronald Bode** for all the sketches and parts you crafted for us. Many thanks as well to the Cryogenics Team, for your support and continuous training, in particular **Jason**, **Olaf** and **Tom**. **Hitham** and **Regis**, thank you for keeping the work environment safe! I owe a special thanks to our management assistants **Chantal**, **Esther**, **Sara** for promptly taking care of any matter and **Maria Roodenburg-van Dijk** for taking care of my initial settling in Delft. **Shannon**, **Cansin** and **Rodica** thank you for thoroughly taking care of any administrative aspect of the Fujitsu collaboration and for your kind and always fast feedback.

To the greater Quantum Nanoscience community and the QN Culture & Community Council : thank you for the great scientific environment and all the nice social activities you organize. In particular, many thanks to **Michael**, **Brecht**, **Iacopo**, **Samer**, **Irina**, **Sabrya** for the company and interesting conversations over the years. Good luck with your current and future adventures!

Many thanks also to the great QuTech community for constantly creating a fun environment and for the amazing Uitjes, for your openness to help and discuss science on any possible occasion. **Scarlett**, **Tzula**, **Giordano**, **Alberto**(2x), **Hanifa**, **Irene**, **Zarije**, **Pepijn**, **Damian**, **Benjamin**, **Guido**, **Vicky**, **Fenglei**, **Kilian** thank you all for the interesting discussions and company over a coffee or lunch. **Pablo** and **Uri**, together with **Ralf**, thank you for the spontaneous brunches and always a good word of mutual support. **Anta** thanks for the cool-cool office much needed light-hearted office conversations after long cleanroom days, and **Hemant** for genuine support, fun, the warm ramen soups and good advice on many cold Boston days.

Un ringraziamento speciale ai miei amici: gli anni di scuola ci hanno formati e fatti crescere, e io sono stata fortunata a dividerli con voi. Grazie a tutti. **Aloisia**, la mia

stella: il tuo supporto e affetto incondizionato non sono mai mancati. Anche se in questi anni ci siamo spesso trovate lontane, non c'è stato un momento in cui non fossimo lo specchio l'una dell'altra. Sei una forza! **Giulia**, pur vivendo in paesi diversi, siamo sempre rimaste unite: grazie per il tuo supporto, la tua saggezza e i tuoi consigli, sempre preziosi. **Nico**, da due percorsi paralleli abbiamo condiviso gli alti e bassi del dottorato e ci siamo sostenuti a vicenda. **Riccardo**, il tuo sostegno e la tua costante presenza mi hanno spinto innumerevoli volte a vedere il lato positivo. Il *tentativo quantistico*: **Ciro** e **Andrea**, grazie per il vostro supporto in tutti questi anni. Il vostro incoraggiamento a esplorare i paesi nordici mi ha portata questa volta verso la scelta giusta! **Vale**, una costante sin dalle prime parole che io abbia mai pronunciato in italiano: la tua resilienza e tenacia sono contagiose. Grazie per la tua amicizia e per il supporto incondizionato in tutti questi anni. Abbiamo condiviso liceo e università e, anche quando le nostre strade si sono allontanate, insieme a **Monia** siete sempre riuscite a starmi vicine, ovunque io mi trovassi. Con tutti voi accanto, io sono sempre a casa.

There is a set of wonderful people that I am truly lucky to have met during my time here in Delft. COVID and social distancing have been no challenge for you, **Sonakshi**: you are the social fairy that brought us all together, welcoming me in Quantum Nanoscience and into your life. On the days when the etchers went down or I went through yet another existential crisis, you and **Luigi** always had the right words and encouragement. I am happy to share this day with you. **Nicole** and **Quentin**, you bring a special energy into the group. **Deni**, your discipline is inspiring, thank you for your steady pragmatism. **Tina** and **Milan**, you always have a kind word of encouragement. **Luca**, your perspective is always much appreciated. **Stephan**, I enjoy our conversations, which somehow, more often than not, find their way back to science. **Eleni**, it turns out we share many cultural traits, and **Manon**, our discussions are always interesting, I especially enjoyed defending one of the propositions of this thesis with you. You all have been there for me, through the most challenging lows and the happiest highs, and everything in between. **Sofia**, **Clemence**, **Mark**, **Natasha**, **Tanja**, and **Nils**, I treasure the time when we are all here in Delft and could enjoy fun activities together with **Lola**. Thank you for your support and kindness.

Acasă alături de familia mea am învățat multe dintre valorile care mă definesc zi de zi și care mi-au permis să ajung la această etapă. **Tăticu** și **Mămica**, prin exemplul vostru mi-ați arătat cum să privesc viața cu onestitate, perseverență și sensibilitate. Împreună mi-ați arătat că acasă poate fi oriunde și că a trăi între țări te face cu adevărat un cetățean al lumii. **Diana**, surioara mea mai mare, rămâi pentru mine un exemplu de reziliență și iubire, alături de **Adrian**. **Darius** și **Damian**, prin felul minunat în care creșteți, îmi reamintiți zi de zi cât de prețios este timpul. Vă mulțumesc din suflet tuturor.

Heartfelt thank you social fairy for introducing me to **Stefan**. That first conversation on scientific integrity was the start of a continuous exchange of ideas on the universe of topics that define our lives together. I am endlessly grateful for your support, for making every day colorful, and I am excited for all our future adventures ahead.


And to you, my most esteemed reader, thank you for taking the time to read these words. I hope I have remembered to mention you, and if not, please accept my heartfelt thanks all the same.

Nina
Delft, September 2025

LIST OF PUBLICATIONS

JOURNAL PUBLICATIONS AND PREPRINTS

9. **N. Codreanu**^{*}, T. Turan^{*}, D. Bedialauneta Rodriguez^{*}, *et al.*, "Above-Unity Coherent Cooperativity of Tin-Vacancy Centers in Diamond Photonic Crystal Cavities" *in preparation*
8. **N. Codreanu**, *et al.*, "Fabrication of Tin-Vacancy Centers in Diamond: Surface-Protected Annealing Method and Graphitization Analysis" *in preparation*
7. J. M. Brevoord^{*}, J. F. Geus^{*}, T. Turan, M. G. Romero, D. Bedialauneta Rodríguez, **N. Codreanu**, A. M. Stramma, R. Hanson, F. Elsen, B. Jungbluth, "Quantum Frequency Conversion of Single Photons from a Tin-Vacancy Center in Diamond" arXiv preprint, (2025)
6. Y. Herrmann^{*}, J. M. Brevoord^{*}, J. Fischer^{*}, S. Scheijen, C. Sauerzapf, **N. Codreanu**, L. G. Wienhoven, Y. M. Q. van der Graaf, C. F. J. Wolfs, R. Méjard, M. Ruf, N. de Jong, R. Hanson, "Laser-cut Patterned, Micrometer-thin Diamond Membranes with Coherent Color Centers for Open Microcavities" *Mater. Quantum. Technol.* 5 035001, (2025)
5. J. M. Brevoord, L. G. C. Wienhoven, **N. Codreanu**, T. Ishiguro, E. van Leeuwen, M. Iuliano, L. De Santis, C. Waas, H. K. C. Beukers, T. Turan, C. Errando-Herranz, K. Kawaguchi, R. Hanson, "Large-Range Tuning and Stabilization of the Optical Transition of Diamond Tin-Vacancy Centers by In-Situ Strain Control" *Applied Physics Letters* **126**, 174001, (2025)
4. H. K. C. Beukers^{*}, C. Waas^{*}, M. Pasini, H. B. van Ommen, Z. Ademi, M. Iuliano, **N. Codreanu**, J. M. Brevoord, T. Turan, T. H. Taminiau, R. Hanson, "Control of Solid-State Nuclear Spin Qubits Using an Electron Spin-1/2" *Physical Review X* **15**, 021011, (2025)
3. M. Pasini, **N. Codreanu**, T. Turan, A. Riera-Moral, C.F. Primavera, L. De Santis, H. K. C. Beukers, J. M. Brevoord, C. Waas, J. Borregaard, and R. Hanson, "Nonlinear Quantum Photonics with a Tin-Vacancy Center Coupled to a One-Dimensional Diamond Waveguide", *Physical Review Letters*, **133**, 023603, (2024).
2. J. M. Brevoord^{*}, L. De Santis^{*}, T. Yamamoto, M. Pasini, **N. Codreanu**, T. Turan, H. K. C. Beukers, C. Waas, and R. Hanson, "Heralded initialization of charge state and optical-transition frequency of diamond tin-vacancy centers", *Physical Review Applied*, **21**, 054047, (2024)
1. Y. Li, F. A. Gerritsma, S. Kurdi, **N. Codreanu**, S. Gröblacher, R. Hanson, R. Norte, T. van der Sar, "A Fiber-Coupled Scanning Magnetometer with Nitrogen-Vacancy Spins in a Diamond Nanobeam", *ACS Photonics*, **10**, 6, 1859–1865, (2023)

 (Partially) included in this thesis.

^{*}Equally contributing authors

CURRICULUM VITÆ

Nina CODREANU

January 31st, 1993, Leuseni, Republic of Moldova

- 2020-2025** **PhD in Physics**
Delft University of Technology, Delft, The Netherlands
Thesis: *"Diamond Nanophotonic Devices for Quantum Networks Experiments"*
Promotors: Prof.dr.ir. R. Hanson and Prof.dr. S. Gröblacher
- 2018-2020** **Master of Science in Engineering Physics**
Politecnico di Milano, Milano, Italy
School of Industrial and Information Engineering, Engineering Physics (486), Nanophysics and Nanotechnology (F2B)
Thesis: *"Amorphous Silicon Photodetector for Integrated Photonics Applications"*
Dipartimento di Elettronica, Informazione e Bioingegneria
Photonic Devices Group
Supervisors: Prof. Francesco Morichetti and Prof. Andrea Ivano Melloni
- 2013-2018** **Bachelor of Science in Physics Engineering**
Politecnico di Milano, Milano, Italy
School of Industrial and Information Engineering, Physics Engineering (366, FPN)
Thesis: *"Characterization of the Metal Assisted Chemical Etching on Si and Ge Substrates"*
Department of Physics and Laboratory for Nanostructure Epitaxy and Spintronics on Silicon
Supervisor: Dr. Monica Bollani
- 2010-2013** **Scientific High School Diploma**
Liceo Scientifico Tecnologico "Primo Levi", Bollate (MI), Italy



 **TU Delft**

ISBN: 978-94-6518-130-1

